University of Sussex

An Experimental Study of Windage due to Rotating and Static Bolts in an Enclosed Rotor-Stator System.

Anna Miles

Submitted for the degree of Doctor of Philosophy

Thermo-Fluid Mechanics Research Centre

University of Sussex

September 2011

Declaration

I hereby declare that this thesis has not been and will not be, submitted in whole or in part to another University for the award of any other degree.

Signature.....

Anna Miles

September 2011

Acknowledgements

I would like to thank my supervisors Professor Peter Childs, Dr Christopher Long and Dr Daniel Coren for their advice and support during the course of this D.Phil. The research was funded by Rolls-Royce plc. and I would like to thank in particular Dr. Torsten Geis and Dr. Timothy Scanon for their guidance throughout the experimental programme.

I would also like to give a very special thank you to the technicians Tony Martin and Glen Downs, who were both vital in helping me fulfil my testing requirements with a functioning test rig and with the all necessary components available when they were needed.

Finally, I could not have completed this D.Phil without the support and encouragement from my family and friends. My Mum, Dad and Adam Cooke all deserve a mention for providing their proof reading skills, but a special thanks go to James Turner without whom I may not have reached the end.

University of Sussex

Anna Miles

Submitted for the degree of Doctor of Philosophy

An Experimental Study of Windage due to Features in an Enclosed Rotor-Stator System.

Summary

The cooling air in a gas turbine engine is subject to windage as it flows through the internal air system. The work in this thesis focuses on the windage generated as the cooling air passes over the rotor surface, particularly for case where bolts are encountered. Reducing windage heating of the cooling air is of great importance to turbomachinery engineers, particularly in the aerospace industry, since the use of compressor air for cooling greatly reduces the thrust potential of an engine. The ability to accurately predict windage can help reduce the quantity of cooling air required, resulting in increased efficiency.

A purpose built rig was used to measure both windage and rotor surface temperature as air passes through an enclosed rotor-stator cavity. A wide range of flow conditions were tested with some being close to those found in a modern gas turbine engine. A variety of both stator and rotor mounted bolts were investigated, of varying size and shape, as well as cavities in the disc surface. In addition, PIV measurements of the core tangential velocity were obtained.

Test results show that windage is increased substantially with rotor bolts present, compared with a plain disc, and that it increases with increasing bolt size. For hexagonal rotor bolts a new correlation was produced between the moment coefficient and bolt diameter to pitch ratio for a range of flow conditions, characterised by the rotational and throughflow

Reynolds numbers. Stator bolts were shown to generate a large increase in disc surface temperature compared with the plain disc at engine representative conditions.

PIV measurements of the core tangential velocity showed an increase of up to 80% above the plain disc with rotor bolts present and no superimposed flow. When throughflow was introduced, the increase was around 300%. These measurements also demonstrate a local increase in tangential velocity in the region close to the bolt.

List of Figures

Nomenclature

A	Cross sectional area	m^2
a	Disc inner radius	m
b	Disc outer radius	m
C	Experimental constant	
C_D	Drag coefficient ($C_D = 2d/\rho u_0^2 A$)	
C_p	Specific heat at constant pressure	J/kg K
C_w	Throughflow Reynolds number	
D	Diameter of bolts	m
d	Drag force	kgm/s^2
F	Form drag correction factor	
G	Gap ratio ($G = s/b$)	
G_a	Axial clearance ratio ($G_a = s_a/b$)	
G_r	Radial clearance ratio ($G_r = s_r/b$)	
H	Windage heating	kW
k	Mean grit size	m
k_{lim}	Roughness limitation	m
M	Torque	N m
$\dot{m}$	Mass flow rate	kg/s
m_m	Molar mass	kg/mol
N	Rotational Speed	rev/min
n	Number of bolts	
n_f	Number of seal fins	
P	Pumping losses	W
p	Bolt pitch	
p_s	Surface pressure	N/m^2
p_0	Static pressure	N/m^2
R	Gas constant	J/kg K
r	Local radius	m
r_b	Bolt radius	m

$\Re$	Universal gas constant	J/mol K
Ro	Rossby number ($\dot{m}/2\pi\rho bG_r\omega$)	
S	Scale factor	
s	Axial gap between the discs	m
s_a	Axial clearance between rotor/stator and shroud	m
s_r	Radial clearance between rotor/stator and shroud	m
T	Temperature	K
T_0	Total temperature	K
U_s	Free stream velocity	m/s
u	Time averaged velocity in boundary layer	
V	Voltage	V
V_r	Radial velocity	m/s
V_ϕ	Tangential velocity	m/s
w	Absolute uncertainty	
x_c	Radial location where source region ends	

Greek Symbols

β	Core velocity ratio with throughflow ($\beta = V_\phi/\omega r$)	
β^*	Core velocity ratio with no throughflow	
γ	Heat capacity ratio ($\gamma = C_p/C_v$)	
δ	Boundary layer thickness	m
ε	Expansibility factor	
φ	Angle of attack	°
μ	Dynamic viscosity	kg/m s
ν	Kinematic viscosity	m^2/s
π	pi = 3.142	
θ	Momentum thickness	
τ_0	Shear stress of fluid due to the disc	N/m^2
τ_p	Shear stress of fluid due to the protrusions	N/m^2
ρ	Density	kg/m^3
ω	Rotational speed	rad/s

Dimensionless Groups

Moment coefficient: $C_m = \dfrac{M}{\frac{1}{2}\rho\omega^2 b^5}$

Rotational Reynolds number: $\mathrm{Re}_\phi = \dfrac{\rho\omega b^2}{\mu}$

Throughflow Reynolds number: $C_w = \dfrac{\dot{m}}{\mu b}$

Turbulent flow parameter: $\lambda_T = \dfrac{C_w}{\mathrm{Re}_\phi^{0.8}}$

Gap ratio: $G = \dfrac{s}{b}$

Subscripts

0	Total
atm	Atmospheric
av	Average
g	gauge
HG	Mercury
i	Inner
in	Inlet
o	Outer
out	Outlet
PRT	Platinum resistance thermometer
r	Radial
ϕ	Tangential
TC	Thermocouple
∞	Outside the boundary layer

Acronyms

CCD	Charged Coupled Device
DVM	Digital Volt Meter
LDA	Laser Doppler Anemometry
PIV	Particle Image Velocimetry
PRT	Platinum Resistance Thermometer
RSS	Root Sum Square
SPRT	Standard Platinum Resistance Thermometer

Chapter 1. Introduction

1.1 Background

The first ever jet powered aeroplane flew in 1939. By the 1950s the use of jet engines was almost universal in combat aircraft and by the 1960s most large civilian aircraft were also jet powered. The use of jet engines in civil aviation sparked massive growth in overseas travel as journey times plummeted. In 1947 the "Kangaroo Route", operated by Quantas between London and Sydney, would have taken four days including two overnight stops and 55 hours in the air. A return ticket would have cost £585, equivalent to 85 times the average weekly wage in Australia, or half the value of a suburban house (**Marks 2007**). Today this journey, with the same airline, would take 23 hours including one refuelling stop, and cost around £1000, a little more than the current average weekly wage in Australia (~£900).

This massive growth in the aviation industry has meant that legislation around the world is becoming ever more stringent in setting emissions targets for new engines. From 2012 any airline wishing to take off or land in the E.U. will have to join the Emissions Trading Scheme (ETS). This scheme allows airlines only 85% of the target emissions certificates for free (target CO_2 emission will initially be set to 97% of the average 2004 to 2006 levels) the rest they will have to buy. It is therefore essential for airlines to reduce their emissions considerably in order to viably operate in the current highly competitive market. The most effective way of reducing emissions is to reduce fuel consumption by increasing engine efficiency.

Engine performance and efficiency have typically been gained by increasing both the compressor pressure ratio and turbine entry temperature (TET). For example, a typical jet engine of the 1940s had a pressure ratio of 6:1 and TET of 800 °C, whereas in a modern Rolls Royce Trent engine they are over 50:1 and 1700 °C. This has been made

possible mainly due to advances in material technologies and the development of complex cooling systems. Even using advanced materials, however, components that come into contact with the mainstream gas, most notably the turbine blades and nozzle guide vanes (NGVs), would quickly exceed their creep and fatigue limits at temperatures of 1700 °C. It is only with the complex internal cooling systems that it is viable to run at such temperatures.

Improvements in performance and efficiency from higher pressure ratios and TETs are now becoming less significant, consequently the research focus in gas turbine technology is increasingly moving towards what is referred to as the internal air system.

1.2 Cooling

The term ‘internal air system’ refers to air that does not directly contribute to the thrust of the engine. This includes air used for cooling, as well as sealing bearing chambers, balancing axial loads and preventing ingress of the mainstream gas through pressurisation of the turbine cavities. The air is bled from various stages of the compressor and directed to the turbine stages to cool the hot components such as the turbine discs, blades and NGVs. A diagram of the internal air system of a gas turbine engine is shown in Figure 1.1.

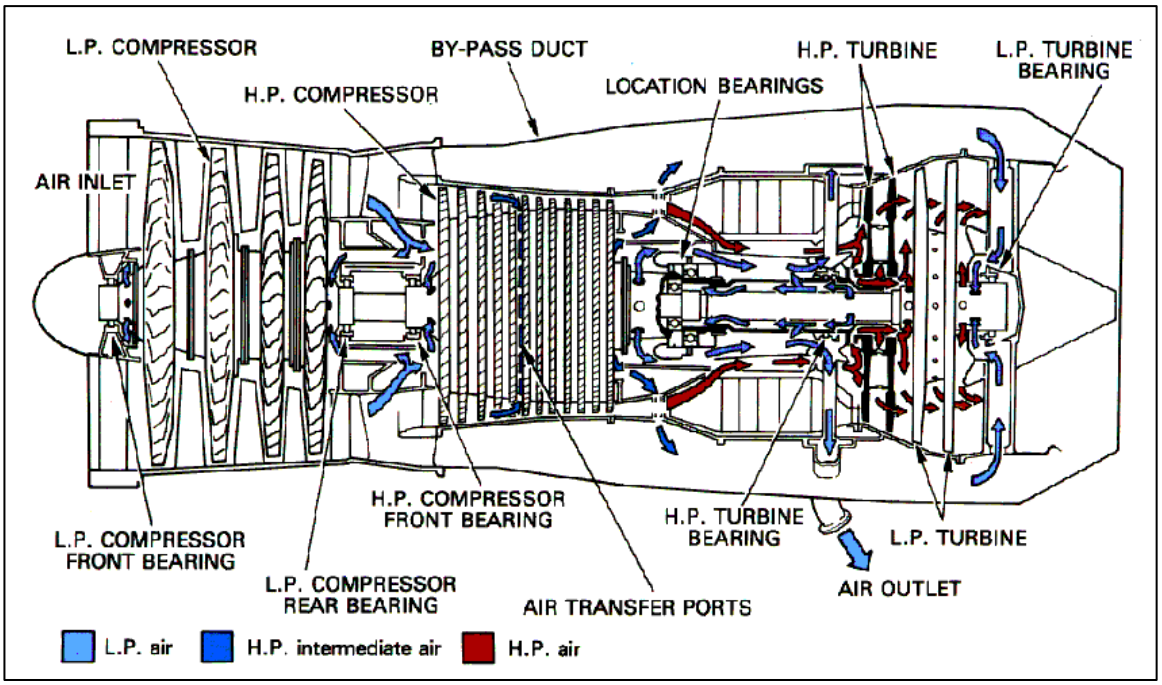

Figure 1.1 – The internal air system of a gas turbine engine (courtesy of Rolls Royce plc).

In some cases up to 20% (**Rolls-Royce (2005)**) of the compressor air passes through the internal air system, this greatly reduces the thrust potential of the engine by removing air that would otherwise be passing through the combustion system. It is therefore important for turbomachinery engineers to minimise the quantity of compressor air used for the internal air system, though this must be achieved without compromising the integrity of the engine components. A second loss component resulting from the internal air system is the retarding force, known as windage, resulting primarily from the air passing over the surfaces of the turbine discs.

With the aim of reducing the quantity of compressor air used in the internal air system, engineers invest a lot of time investigating the effects of this retarding force, and also the temperature rise of the air, due to windage. Owing to the massively increased pressure ratios in modern engines, the cooling air is already at around 700 °C (**Rolls-Royce (2005)**) as it leaves the compressor stages. Therefore it is vital that there is minimal further increase of the temperature, before it reaches the hot components. If windage is reduced, the temperature of the cooling air is lower when it reaches the hot components, leading to a reduction in the mass flow of air required. Decreasing

windage also reduces the retarding force acting on the turbine discs. As such, accurate quantification of windage in all areas of the internal air system is desired.

Windage heating within the cavities between the turbine discs, and between the discs and stationary components, contributes a substantial proportion of the heat rise in the cooling air. This windage not only increases the temperature of the cooling air, which is undesirable as already discussed, but also that of the turbine disc. The turbine disc is a highly stressed component, rotating at speeds of up to 11,000 rpm in the high pressure turbine stage. Therefore any decrease in disc temperature, however small, can play a significant part in increasing the life of the disc. This could result in longer intervals between services, thereby reducing running costs, but more importantly reduces the risk of failure during operation which could have devastating consequences.

1.3 Windage

It is appropriate at this point to properly define the term windage, and the way in which it is determined and used within this thesis. Windage is defined as a force caused by the relative motion between a fluid and an object. In this thesis the focus is on windage occurring due to a fluid, air, passing through a rotor-stator cavity. This is primarily measured as a retarding torque on the rotor using an inline torquemeter within the driveline.

For the purposes of the work in this thesis, the term windage includes three loss components: viscous friction; form drag; and pumping losses. Viscous friction arises due to shear stresses within the boundary layer on the surface of either the rotor or the stator. The shear stresses are a result of the relative velocity between the fluid and both the rotor and stator surfaces. Form drag occurs due to separation of the air, as it passes over features present within the cavity, and the resulting wake formation. Pumping losses are the result of the work done by these features in changing the angular momentum of the fluid. For the particular case of a smooth rotor surface, the term windage will naturally only refer to losses due to viscous friction.

1.4 Scope of work

In order to develop the current understanding of windage in rotor-stator systems, the tests presented in this thesis have been carried out to quantify the windage effects of a variety of features present within a rotor-stator cavity. The investigation used a special purpose rig, shown in Figure 1.2, designed to rotate a disc between two stationary surfaces at speeds of up to 12000 rev/min. Air is introduced axially at varying rates in order to represent a variety of flow conditions. A detailed description of the test facility can be found in Chapter 3.

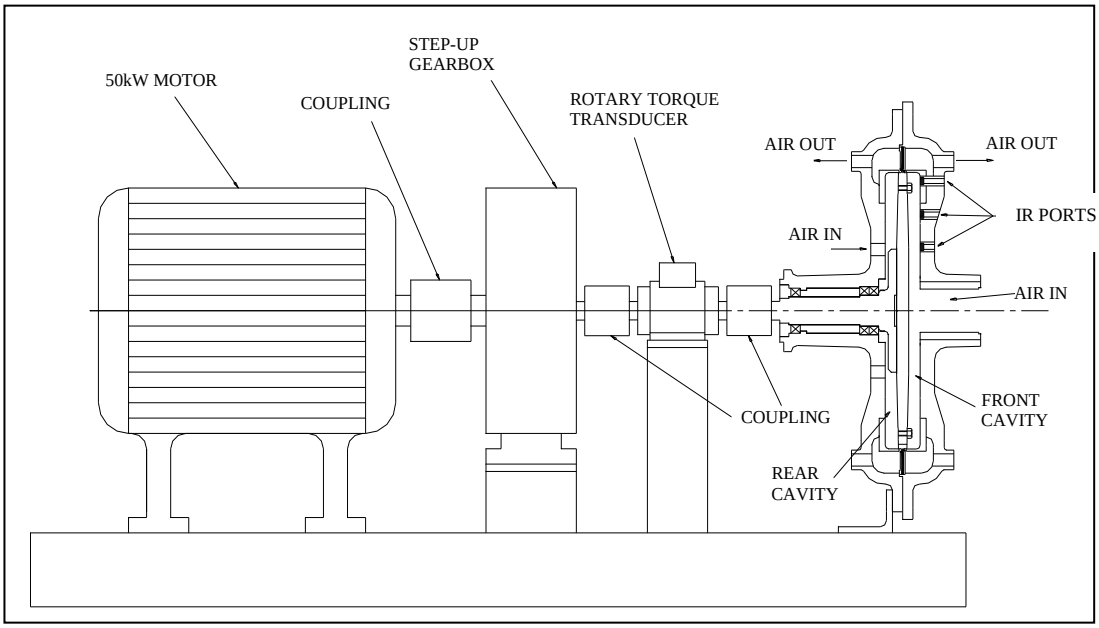

Figure 1.2 – Special purpose bolt windage test rig.

The rotor-stator cavity can be found in a number of places within a gas turbine engine. One example is between the high pressure turbine disc and the vane support, illustrated in Figure 1.3. Both rotating and static features, such as bolts, are necessary for the assembly of a gas turbine engine, again shown in Figure 1.3, necessitating the investigation of their effects on windage.

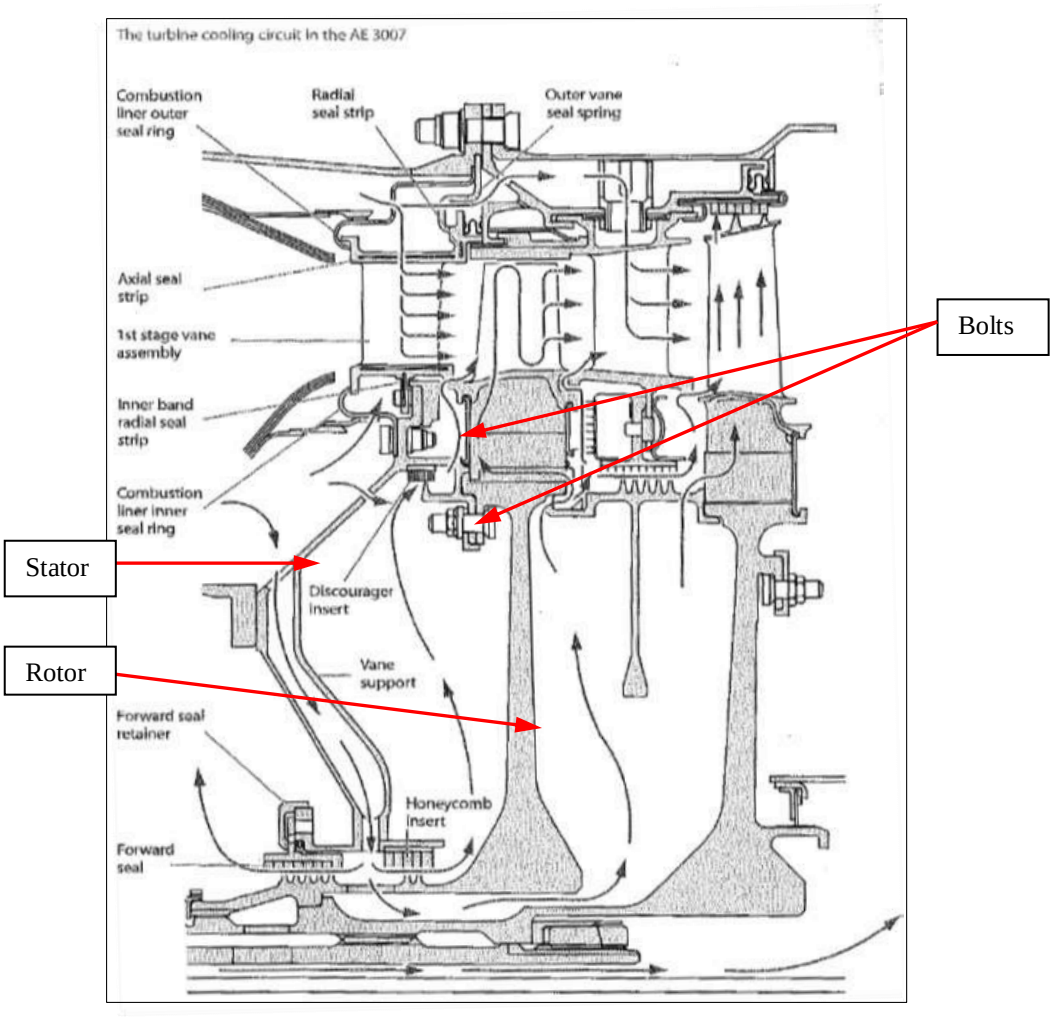

Figure 1.3 – Picture showing the turbine cooling circuit of a gas turbine engine (Courtesy of Rolls Royce Plc).

The purpose built test rig shown in Figure 1.2 had previously been used by **Coren (2007)** to investigate the effect of spacing and radial location of 16 mm hexagonal bolts on windage. As a result of this work, it is now understood that rotor bolts at a high radius contribute substantially more than low radius bolts, to total windage when two rows of bolts are present. Stator bolts tests on the other hand showed that two rows of bolts produces lower values of windage than the plain disc, whereas a single row at high radius gave either similar or higher than plain disc values. It was also shown that the number of rotor bolts, and consequently the circumferential spacing, has a significant effect on the measured windage.

The experimental investigation presented in this thesis follows on from the work by Coren and aims to determine the effect on both windage and rotor surface temperature of the following:

- Varying the diameter (10 mm, 13 mm and 16 mm) of hexagonal rotor bolts at a single radius $r_b/b = 0.89$. These measurements are obtained with the intention of creating a correlation between the moment coefficient and bolt diameter to pitch ratio, for a range of flow conditions characterised by the rotational and throughflow Reynolds numbers.
- A single row of 16 mm hexagonal stator bolts at a radius $r_b/b = 0.89$. Although windage measurements have already been obtained, the rotor surface temperature measurements have not. Any increase in rotor temperature due to stator bolts can have a significant effect on component life, therefore these measurements have significant industrial relevance.
- A comparison of 13 mm bi-hexagonal bolts with 13 mm hexagonal bolts. The hexagonal bolt is representative of a large portion of the protrusions found in a variety of gas turbine applications. Bi-hexagonal bolts, however, are commonly used in gas turbines for aero applications. It is therefore important to quantify any variation there may be between the two bolt shapes.
- Cavities in the rotor surface, of varying diameter and depth. These cavities aim to represent the use of large cap screws, which are sometimes used within the internal system of a gas turbine engine. The cavity represents the recess into which an Allen key would be inserted.

In addition to the windage and temperature measurements, Particle Image Velocimetry (PIV) measurements aim to investigate the variation in tangential velocity of the core flow within the cavity as a result of both rotor and stator bolts. Laser Doppler Annemometry (LDA) measurements were obtained by Coren for the plain disc as well as with rotor bolts, showing the tangential velocity to increase with bolts present. The measurements, however, did not extend to the radius of the bolt and so local effects of the bolts were not measured. Stator bolts were also not covered in this investigation. The PIV measurements in the current investigation intends to extend the current knowledge by including the region around the bolts in the measurements, as well as measuring the, currently assumed, retardation of the core flow due to stator bolts.

1.5 Thesis Structure

The published literature relevant to the subject of rotor-stator systems, windage investigations in particular, is discussed in Chapter 2 of this thesis. Chapter 3 outlines the test facility and instrumentation used to obtain the measurements, and Chapter 4 the method used to analyse the results, as well as the uncertainty analysis. Chapters 5 to 9 present the experimental results. Chapter 5 introduces the plain disc tests, carried out to give a baseline so that the windage effects of the features investigated can be quantified. Chapter 6 details the experiments with hexagonal stator bolts and Chapter 7, hexagonal rotor bolts. Chapter 8 presents the results for bi-hexagonal rather than hexagonal rotor bolts and also discusses the rotor surface cavity results. Chapter 9 examines the use of Particle Image Velocimetry to measure the core velocity for both a smooth disc and with hexagonal rotor bolts. Finally, Chapter 10 presents the conclusions which were derived from the results and some recommendations for further work are suggested.

Chapter 2. Literature Review

2.1 Introduction

The purpose of this chapter is to provide an overview of the current state of understanding of the fluid mechanics relevant to the study of windage in a rotor-stator system. Initially, the general rotor-stator problem is considered. Focus is then directed toward research on features relevant to the work in this thesis, such as the effects that protrusions and surface cavities have on windage.

Section 2.2 of this chapter considers the free disc, which provides a useful starting point for rotor-stator flows. Section 2.3 explains the different types of rotor-stator configurations and the relevant research that has been carried out to date on those systems. Section 2.4 discusses rotor-stator systems with a superimposed throughflow of fluid and then, Section 2.5, systems with protrusions in the cavity. Section 2.6 looks at the effects of surface roughness on windage. It may initially seem that surface roughness is not directly related to the problem of protrusion windage. However, the similarity between the effects of discrete protrusions and general roughness of the rotor or stator surface are compelling enough for this research to be considered. Section 2.7 looks at research into the effects of surface cavities on windage and Section 2.8, the effects of seal geometry.

2.2 Free Disc

A useful starting point for rotating flow theory is the so called free disc. This is a disc of radius, b, rotating at a speed, ω, in an initially stationary fluid of density, ρ, and dynamic viscosity, μ. Figure 2.1 below shows the boundary layer flow associated with the free disc

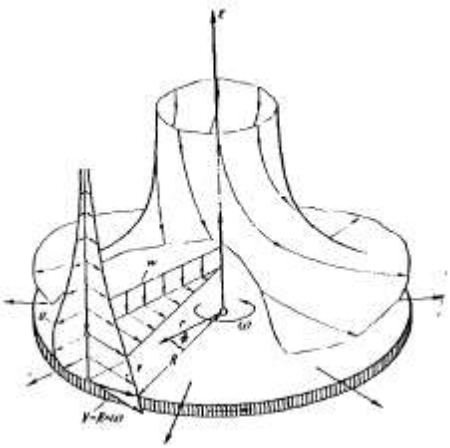

Figure 2.1 – Boundary layer flow on a free disc taken from **Schlichting (1979)**

Centrifugal acceleration, induced by the rotation of the disc, causes a radially outward motion of the fluid entrained within its boundary layer, due to viscous friction. This is often referred to as disc pumping. In order to replace this fluid and comply with conservation of mass, fluid is entrained axially into the boundary layer.

Rotating flows are often characterised by two main non-dimensional parameters: the rotational Reynolds number, Re_ϕ, and the throughflow Reynolds number, C_w. The rotational Reynolds number is defined in Equation 2.1.

$$\mathrm{Re}_\phi = \frac{\rho \omega b^2}{\mu} \qquad \textbf{(2.1)}$$

Free disc flow is laminar where $\mathrm{Re}_\phi < 2 \times 10^5$, at which point the flow becomes transitional. The flow becomes turbulent where $\mathrm{Re}_\phi > 3 \times 10^5$.

Radial flow, whether it is induced by rotation only or purposely superimposed into a rotor-stator cavity (as discussed in Section 2.4), is described by the throughflow Reynolds number, C_w, defined in Equation 2.2, where $\dot{m}$ is the mass flow rate of fluid.

$$C_w = \frac{\dot{m}}{\mu b} \qquad \textbf{(2.2)}$$

The moment coefficient, C_m, is the non-dimensional parameter frequently used to quantify windage. This is shown in Equation 2.3, where M is the windage torque.

$$C_m = \frac{M}{\frac{1}{2}\rho\omega^2 b^5} \qquad \textbf{(2.3)}$$

Some authors define the moment coefficient based on the frictional torque over a single face of the disc, others as over both faces. For practical turbomachinery applications, to assess windage over a single face of a disc makes particular sense, since geometries are rarely equal on both sides. However, the moment coefficient data presented in the results chapters of this thesis is based on torque measurements accounting for both faces of the disc. Consequently, unless otherwise stated, all values of moment coefficient presented in this chapter account for both sides of the disc.

von Kármán (1921) developed analytical expressions for the moment coefficient and boundary layer thickness for a free disc in both laminar and turbulent flow. He used a $1/7^{th}$ power law to describe the velocity profile in the rotor boundary layer for axisymmetric flow. The relationships for moment coefficient, C_m, are shown in Equations 2.4 and 2.5 for laminar and turbulent flow respectively. These are only valid where the radius of the disc is large compared to the thickness of the boundary layer, therefore edge effects can be neglected.

$$C_m = 3.68\,\mathrm{Re}_\phi^{-0.5} \qquad \textbf{(2.4)}$$

$$C_m = 0.146\,\mathrm{Re}_\phi^{-0.2} \qquad \textbf{(2.5)}$$

The relationships for boundary layer thickness, δ, for laminar and turbulent flows respectively are shown in Equations 2.6 and 2.7, where ν is the kinematic viscosity ($\nu = \mu/\rho$) and r is the local radius.

$$\delta = 2.58\sqrt{\frac{\nu}{\omega}} \qquad \textbf{(2.6)}$$

$$\delta = 0.462r\,\mathrm{Re}_{\phi}^{-0.2} \qquad \textbf{(2.7)}$$

von Kármán also obtained a relationship for the entrained mass flow of fluid, due to disc pumping, in the rotor boundary layer. This is expressed in non-dimensional form, as shown in Equation 2.8. The relationship accounts for entrainment on one side of the disc and is valid for turbulent flows only.

$$C_{w,ent} = 0.219\,\mathrm{Re}_{\phi}^{0.8} \qquad \textbf{(2.8)}$$

Cochran (1934) developed the work by von Kármán and corrected errors in his calculations to produce the equation for the moment coefficient for laminar flow, shown in Equation 2.9

$$C_m = 3.87\,\mathrm{Re}_{\phi}^{-0.5} \qquad \textbf{(2.9)}$$

Goldstein (1935) performed an analytical analysis to calculate the moment coefficient for a free disc. The analysis is valid for turbulent flow and a logarithmic boundary layer velocity profile is assumed, rather than the $1/7^{th}$ power law used by von Kármán. The correlation produced is shown in Equation 2.10.

$$\frac{1}{C_m^{0.5}} = 2.78\log_{10}\left(\mathrm{Re}_{\phi}\,C_m^{0.5}\right) + 0.46 \qquad \textbf{(2.10)}$$

Theodorsen and Regier (1944) carried out experiments to measure windage on rotating discs. Using a disc of diameter D = 0.61 m, they tested up to rotational Reynolds numbers of $\mathrm{Re}_{\phi} = 7 \times 10^6$ and Mach numbers (in the tangential direction) of 1.69, by using Freon 12 as the working fluid. The data presented validated von Kármán's free disc theory for the moment coefficient on both sides of a free disc beyond the range that had previously been achieved. They also found that the moment coefficient, C_m, is a function of rotational Reynolds number only and is totally independent of Mach number.

Batchelor (1950) used an analytical approach to look at flows associated with a single rotating disc and found there to be three different cases. The first case, where the tangential velocity of the fluid is higher than the disc, the fluid was found to flow radially inwards near to the disc surface and then away from the disc along the axis of rotation. The second case, where the tangential velocity of the disc is higher than the fluid, the fluid was found to flow toward the disc along the axis of rotation and then radially outwards near to the disc surface. The extreme case of this, where the fluid away from the disc is stationary, represents a free disc. The third case is where the fluid and the disc rotate in opposite directions. Here the flow is radially outward close to the disc but radially inward elsewhere.

Dorfman (1957) used analytical methods to calculate the moment coefficient of a free disc using a logarithmic boundary layer velocity profile. He initially found a separate relationship for three different ranges of Re_ϕ: $10^4 \leq \mathrm{Re}_\phi \leq 9 \times 10^4$; $9 \times 10^4 \leq \mathrm{Re}_\phi \leq 9 \times 10^6$ and $6.4 \times 10^7 \leq \mathrm{Re}_\phi \leq 3.3 \times 10^9$. These were then combined to give the general formula shown in Equation 2.11.

$$C_m = 0.982(\log_{10} \mathrm{Re}_\phi)^{-2.58} \qquad \textbf{(2.11)}$$

Similarly, a general equation for the boundary layer thickness was found, which is shown in Equation 2.12.

$$\frac{\delta}{r} = 0.05 + 5(\log \mathrm{Re}_\phi)^{-2.7} \qquad \textbf{(2.12)}$$

Bayley and Owen (1969) performed experiments on a single disc, with a diameter D = 0.762 m, rotating at speeds of up to 4500 rev/min. The frictional torque was measured using an optical torquemeter built into the driveshaft. The resulting torque measurements were correlated to find the relationship between the moment coefficient and the rotational Reynolds number. This correlation for the moment coefficient, accounting for both sides of the disc, is shown in Equation 2.13.

$$C_m = 0.131\mathrm{Re}_\phi^{-0.186} \qquad \textbf{(2.13)}$$

This correlation was found to give values that corresponded closely with the numerical predictions of **Dorfman (1957)**.

2.3 Rotor-Stator Systems

'Rotor-stator systems' describes a variety of different configurations of rotating and stationary discs. Figure 2.2(a) shows the basic rotor-stator configuration which comprises a rotating disc adjacent to a stationary one, separated by an axial gap, *s*. This can be extended to have a stationary or a rotating shroud attached at the periphery (Figures 2.2(b) and 2.2(c) respectively). These rotor-stator systems with shrouding, rotating or stationary, can have either an axial or a radial gap between shroud and disc. Figures 2.2(b) and 2.2(c) show a stationary and a rotating shroud respectively, with an axial clearance, s_a.

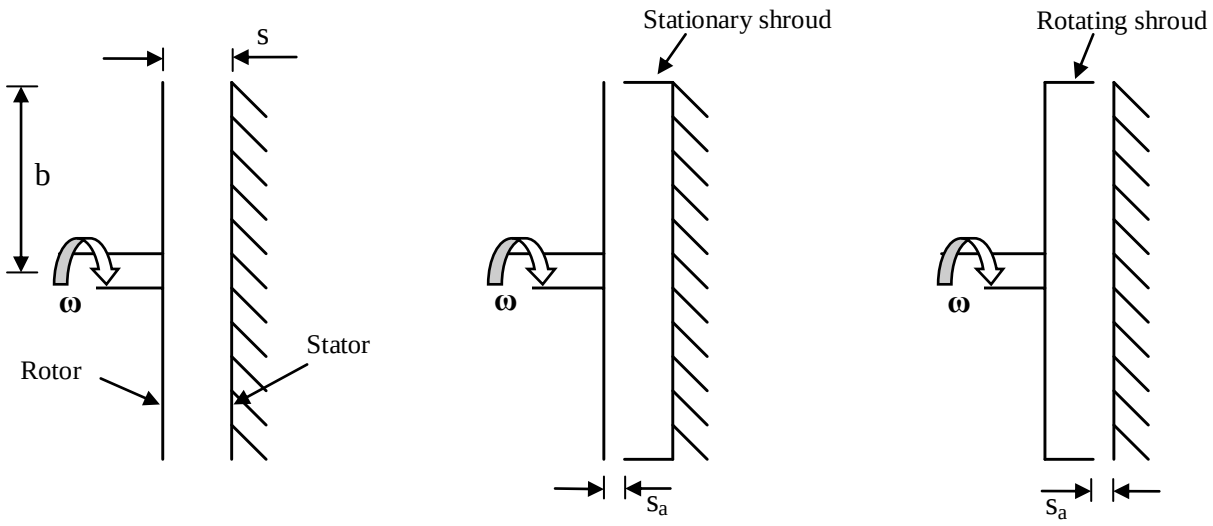

Figure 2.2 – (a) basic rotor-stator configuration, (b) rotor-stator with stationary shroud, (c) rotor-stator with rotating shroud

These classifications can be extended to allow for superimposed radial inflow or outflow. Figures 2.3(a) and (b), show the radial outflow and radial inflow cases respectively for a rotor-stator system with stationary shrouding.

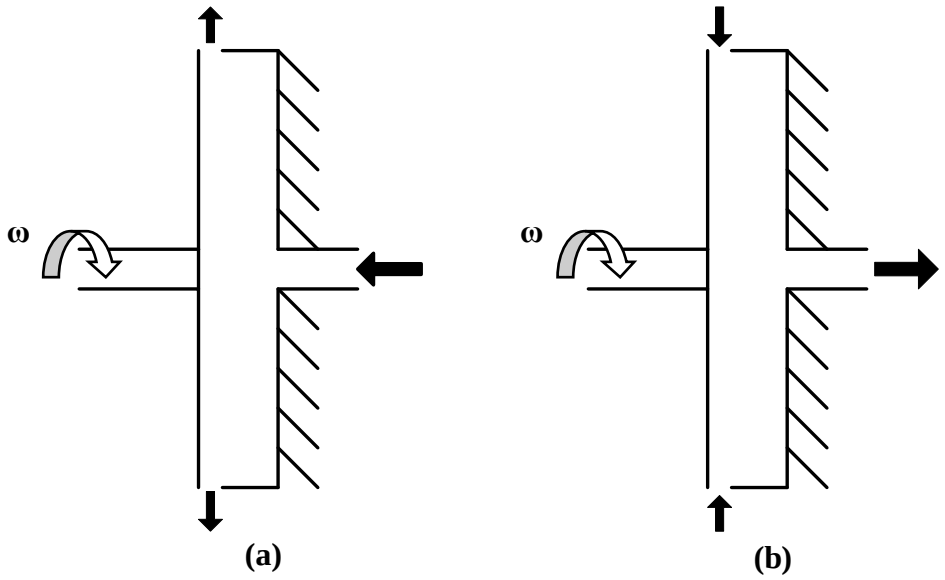

Figure 2.3 – Rotor-stator cavity with stationary shroud and (a) radial outflow, (b) radial inflow

Much of the work on rotor-stator systems is driven by research into gas turbine internal air systems. Within this field there are also systems with co-rotating and counter-rotating discs. These configurations are introduced in Figure 2.4. Figure 2.4(a), shows the co-rotating discs and 2.4(b) counter-rotating discs. These configurations can also have superimposed radial inflow or outflow, in addition to various shroud configurations.

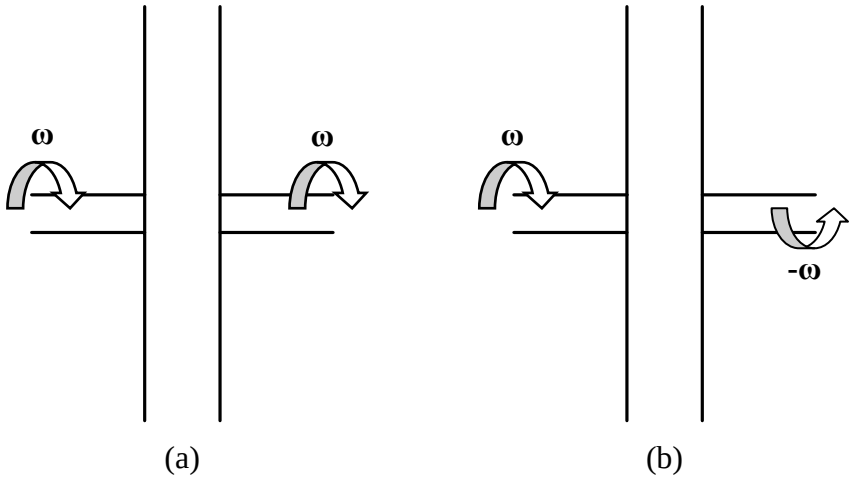

Figure 2.4 – (a) co-rotating discs, (b) counter-rotating discs

The non-dimensional parameters, commonly used to describe the dimensions of a rotor-stator system, are as follows:

The gap ratio, *G*, represents the non-dimensional parameter used to describe the aspect ratio of the rotor-stator spacing to disc radius. This is defined in Equation 2.14, where *s* is the axial gap between the discs and *b* is the disc radius.

$$G = \frac{s}{b} \qquad \textbf{(2.14)}$$

The axial clearance ratio, G_a, describes the ratio of axial spacing between the shroud and either the rotor or the stator, to the disc radius. This is defined in Equation 2.15, where s_a is the axial clearance between the shroud and the appropriate surface of either the rotor or stator.

$$G_a = \frac{s_a}{b} \qquad \textbf{(2.15)}$$

Similarly, the radial clearance ratio, G_r, is defined in Equation 2.16, where s_r is the radial gap between the shroud and the appropriate surface of either the rotor or the stator.

$$G_r = \frac{s_r}{b} \qquad \textbf{(2.16)}$$

Schultz-Grunow (1935) carried out experimental work on a rotor-stator system using a polished aluminium disc of diameter D = 200 mm. The disc was enclosed in a stationary cylindrical housing, of diameter D = 206 mm, with circular end plates on either side of the disc to act as stators. The gap between rotor and stator could be altered by using a different width cylindrical housing. The disc was capable of rotating at speeds of up to 10000 rev/min.

Using analytical methods, the author predicted that the moment coefficient, accounting for both sides of a disc rotating in laminar flow conditions, was as shown in Equation 2.17.

$$C_m = 1.334\,\mathrm{Re}_\phi^{-0.5} \qquad \textbf{(2.17)}$$

This prediction compared well with the experimental results. For turbulent flow, using a $1/7^{th}$ power law for the boundary layer velocity profile, Schultz-Grunow predicted the moment coefficient, accounting for both sides of the disc. This is shown in Equation 2.18.

$$C_m = 0.0311\,\mathrm{Re}_\phi^{-0.2} \qquad \textbf{(2.18)}$$

(N.B. The value of the index in Equation 2.18 could not be established from the copy of this paper that was acquired, hence the value of -0.2 is taken from **Coren (2007)** who also reviewed this paper.)

At first glance, it may seem that the constant 0.0311 in Equation 2.18 is small when compared to the correlation developed by von Kármán for a free disc (Equation 2.5). However, it is accepted that the free disc, in principle, should give rise to a higher moment coefficient than a rotor-stator system, since the air far away from the free disc is stationary. In a rotor-stator system the air is rotating at a fraction of disc speed, resulting in a smaller relative velocity between the disc and the core. This leads to a reduced moment coefficient as a result of reduced viscous friction. (A detailed comparison of the free disc and the rotor-stator system can be found in Section 5.5.2). Shultz-Grunow's analysis is based on the assumption that the gap ratio, G, is very small in order to neglect the effects of the cylindrical shroud, which will result in a lower prediction of moment coefficient. Comparing Equation 2.18 with a correlation later developed by **Daily and Nece (1960)** for a similar flow condition (Equation 2.20, discussed later in this section) suggests the constant used in Schultz-Grunow's correlation is not excessively small, since the moment coefficient predicted by Daily and Nece is smaller still.

Figure 2.5 shows the variation of C_m with Re_ϕ for Schultz-Grunow's correlation (Equation 2.18) with that of Daily and Nece (Equation 2.20), and von Kármán's correlation for a free disc (Equation 2.5). It can be seen that although the moment coefficient predicted by Equation 2.18 is roughly a quarter that predicted by Equation

2.5, it is higher than that predicted by Daily and Nece for turbulent flow with merged boundary layers.

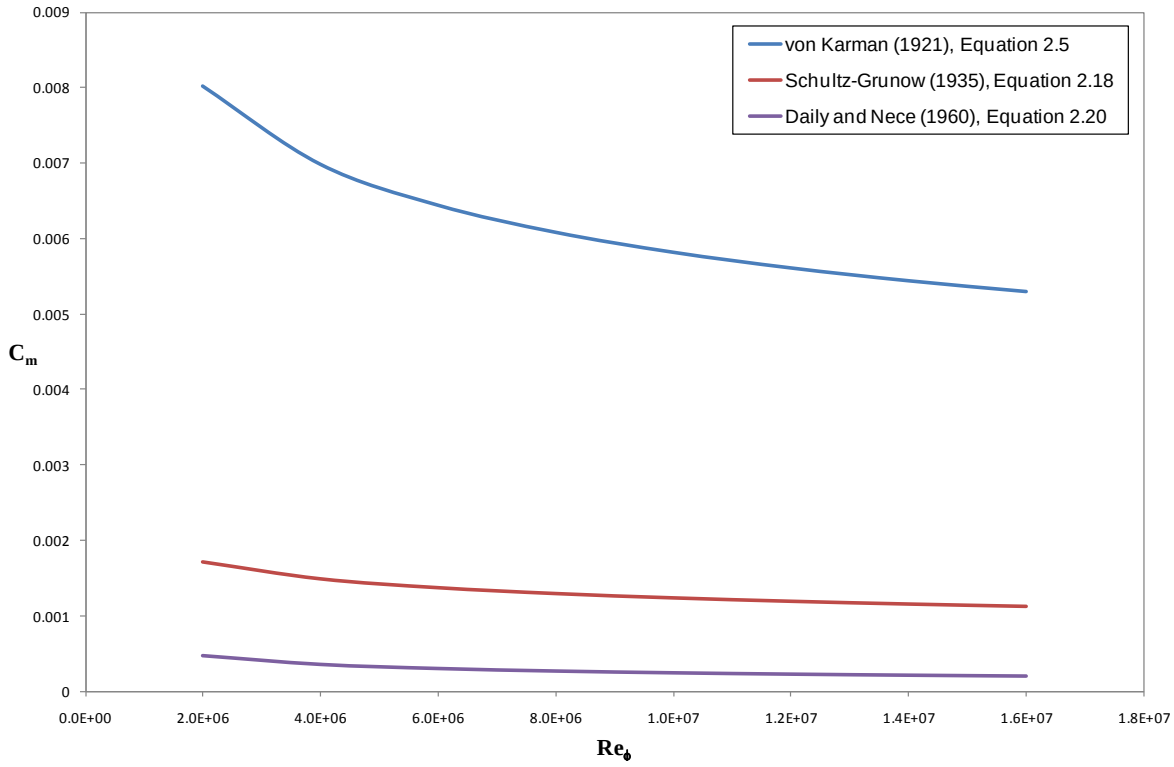

Figure 2.5 – Variation of C_m with Re_ϕ for the rotor-stator correlations of Schultz-Grunow (Equation 2.18), Daily and Nece (Equation 2.20) and the free disc correlation of von Kármán (Equation 2.5).

Schultz-Grunow stated that Equation 2.18 tended to under predict the experimental results by about 17% and that the cause was likely due to a combination of two factors. Firstly, the cylindrical wall friction is not accounted for in the analysis, although it was measured as a consequence of the experimental configuration. Secondly, the wall shear stress for the disc was approximated from experiments on a straight circular section tube and therefore may not reproduce the disc shear stresses accurately.

Schultz-Grunow found that, at higher values of Re_ϕ, a body of fluid rotates between the boundary layers on the rotor and stator surfaces as if it were a solid body. The angular velocity of this body of fluid, and hence its frictional resistance, were found to be independent of the rotor-stator gap. He also found that it is immaterial to the value of moment coefficient whether the axial gap, *s*, is the same on both sides of the rotor, as

long as *s* is small enough for the contribution of the cylindrical wall friction to be negligible.

Batchelor (1950) used an analytical approach to show that the flow between two discs, rotating in the same direction at different speeds, will be radially outwards near to the faster disc and inwards near to the slower rotating disc. As the rotational Reynolds number becomes very large, the boundary layers on the discs become thin in relation to the axial gap that separates them. In between these boundary layers, the fluid can be approximated as inviscid.

If the discs are rotating in opposite directions, the radial flow close to both discs will be outward. There are two regions of inviscid fluid in between the discs, each with uniform axial and tangential velocity but rotating in opposite directions. In between these would be a transitional region of radially inward flowing fluid. Within this transitional region there are changes in the direction of both axial and tangential velocity.

Stewartson (1952) studied, both analytically and experimentally, the motion of fluid between two coaxial discs rotating in the same direction, the opposite direction and with one disc stationary. The experimental set up was basic, using cardboard discs of diameter $D = 0.152$ m at very low rotational Reynolds numbers, $\mathrm{Re}_\phi \approx 100$.

With both discs rotating in the same direction, the flow is substantially as **Batchelor (1950)** predicted. However, with the disc moving in opposite directions, he disagrees with Batchelor and predicts that the fluid between the discs will be largely undisturbed. Similarly with one disc stationary, Stewartson concludes that the main body of fluid between the rotor and stator is largely unaffected by the rotating disc.

Picha and Eckert (1958) carried out an experimental study of the flow between two coaxial discs of diameter $D = 0.458$ m. The two discs were mounted on separate frames which could be moved in the axial direction in order to vary the gap ratio between $0.111 \leq G \leq 0.444$. The discs had independent drives, both with variable speed, adjusted in five steps between 800 rev/min $\leq N \leq$ 3600 rev/min. Tests were performed both with, and without, a clear plastic cylindrical shroud. The radial clearance ratio between the

discs and the shroud was $G_r = 7 \times 10^{-3}$. A Prandtl probe was used for measuring the tangential velocities within the cavity between the discs, which could be moved axially and radially, and smoke was used for flow visualisation.

The results of the flow visualisation showed that, for the rotor-stator configuration when the discs were un-shrouded, there was no discernable tangential velocity within the core of fluid between the discs. However, when shrouding was introduced, they observed a definite tangential velocity component.

The velocity measurements for the un-shrouded rotor-stator system showed a time averaged tangential velocity in the core of practically zero, agreeing with the flow visualisation observations. Only at the two smallest gap ratios, $G = 0.111$ and 0.222, could a slight rotation be observed. For the shrouded discs a definite rotation was detected, again agreeing with flow visualisation observations. It was also observed that the tangential velocities at the outer radii increased with decreasing gap ratio. The measurements at $G = 0.111$ almost coincide with those made by Schultz-Grunow.

Daily and Nece (1960) performed experiments using an enclosed rotor-stator system with a disc of diameter $D = 0.498$ m, and thickness of either 12.7 mm or 6.35 mm. The disc was housed within a cylindrical stationary shroud with circular cover plates either side of the disc to act as stators. The gap ratio was varied between $0.0127 \leq G \leq 0.217$ with the use of spacers mounted in the cylindrical casing. The radial tip clearance was constant at $G_r = 6.4 \times 10^{-3}$. The working fluids were water in addition to four different lubricating oils, allowing testing to rotational Reynolds numbers of up to $\mathrm{Re}_\phi = 10^7$. Torque was measured using four strain gauges mounted within the shaft at 45 ° to the centre line. Radial and tangential velocities were measured at three radii using a 2-hole cobra probe and a pitot-static tube.

Their experimental results showed that, by altering G and Re_ϕ, there are four distinct flow regimes possible within the rotor-stator cavity. If the axial gap, s, is smaller than the combined thickness of the boundary layers, they merge to form a single boundary layer. If s is larger than this, two separate boundary layers occur, one on each surface, and a core of rotating fluid forms between them. These two states can be achieved with either laminar or turbulent flow, hence the four possible flow regimes. From the torque

data obtained, it was possible to find the correlations for moment coefficient, shown in Equations 2.19 to 2.21, for three of the four regimes. These correlations account for windage on both sides of the disc.

Turbulent flow, separate boundary layers:

$$C_m = 0.102 G^{0.1} \mathrm{Re}_\phi^{-0.2} \qquad \textbf{(2.19)}$$

Turbulent flow, merged boundary layers:

$$C_m = 0.08 G^{-0.17} \mathrm{Re}_\phi^{-0.4} \qquad \textbf{(2.20)}$$

Laminar flow, separate boundary layers:

$$C_m = 3.7 G^{0.1} \mathrm{Re}_\phi^{-0.5} \qquad \textbf{(2.21)}$$

For the remaining flow regime the relationship in Equation 2.22 was established analytically, again accounting for the torque on both sides of the disc.

Laminar flow, merged boundary layers:

$$C_m = \frac{2\pi}{G \mathrm{Re}_\phi} \qquad \textbf{(2.22)}$$

Velocity measurements showed that the magnitude of the core tangential velocity decreased with increasing gap ratio, *G*. They also measured a small radial outflow in the core region, which increased with decreasing *G*. To satisfy continuity this net outward flow in the core, plus the radial outflow in the rotor boundary layer, must be matched by the radial inflow in the stator boundary layer. This was observed in the measurements, which showed the stator boundary layer to be thicker than the rotor boundary layer.

Cheah *et al.* (1994) employed three techniques to measure the variation of radial and tangential velocity components across an enclosed rotor-stator cavity with gap ratio, $G = 0.127$. The techniques used were: laser-doppler anemometry (LDA); hot-film velocimetry; and the yaw tube method. Water was employed as the working fluid and the tests covered the range of rotational Reynolds numbers $0.3 \times 10^6 \leq Re_\phi \leq 1.6 \times 10^6$.

The results showed that, at the higher rotational speeds, the rotor boundary layer is laminar close to the axis of rotation but, as radial distance increases, the flow becomes turbulent. At the lowest rotational Reynolds number however, the rotor boundary layer remains laminar for almost the entire radius. The stator boundary layer, on the other hand, is turbulent throughout the complete range of Reynolds numbers. Even when the rotor boundary layer is turbulent, the stator boundary layer is shown to have differing properties to the rotor boundary layer. These results support their theory that the differences in the turbulent boundary layers can be attributed to the upstream history, such as the turning of the flow on the shroud.

Gan and Macgregor (1995) conducted an experimental investigation using LDA. Radial and tangential velocity measurements were obtained in order to identify the flow structure between rotor-stator and counter-rotating discs, with a gap ratio $G = 0.12$ and shrouding on both discs.

For the rotor-stator geometry a Batchelor type flow was observed, where a central core of fluid is found between the two boundary layers rotating at approximately 40% of the disc speed. The angular velocity of the core is shown to increase slightly with increasing radius.

The counter-rotating discs, on the other hand, show a Stewartson type flow. There is a single core between the boundary layers (rather than the dual core predicted by Batchelor) with virtually no rotation. The results also show that there is early transition to turbulence occurring within the core, at values as low as $(r/b)^2 Re_\phi = 3.8 \times 10^4$ (where r is the local radius and b is the disc radius), whereas the boundary layer flow remains laminar up to $(r/b)^2 Re_\phi = 1.1 \times 10^5$.

Soong *et al.* (2002) investigated the flow structure between two independently rotating, co-axial discs using flow visualisation with smoke. Three modes of rotation were tested: co-rotation, rotor-stator and counter-rotation, both with and without symmetric shrouds. Tests covered the following ranges of non-dimensional conditions: $4.7 \times 10^3 \leq Re_\phi \leq 14.1 \times 10^4$, $0.08 \leq G \leq 0.133$ and $-1.2 \leq \Gamma \leq 1.2$ (where Γ is the rotation ratio between the two discs).

The results for an open rotor-stator configuration showed that at the lowest rotation rate concentric stripes appear, particularly in the region near the hub. As rotation increases, the region of axisymmetric concentric stripes travels radially inwards and a spiral wave pattern appears in the outer region. With rotation constant but varying gap ratio, the region of spiral waves decreases with decreasing gap ratio. The flow in the cavity was shown to be radially outward on the rotor, with external air ingested along the stator disc. A small vortex region was also noted near the rotor disc rim, which becomes more unstable with both increasing rotation and gap ratio.

Co-rotating discs were shown to be characterised by an inboard region of near solid body rotation and an outboard region, where vortex chains form adjacent to the disc boundary layers. As rotation increases, these vortex chains were shown to decrease and with increasing gap ratio, the vorticies were of larger scale but weaker strength. The flow in counter-rotating disc cavities was shown to be far more turbulent than co-rotating and rotor-stator discs. This turbulence increases with both increasing rotation and gap ratio.

The introduction of symmetric shrouds can significantly alter the flow field in the outboard region. For the rotor-stator case the spiral wave pattern can only be observed at very high rates of rotation, suggesting that the flow in a shrouded system is more stable than an open one. A similar result was also observed for the counter rotating system, although co-rotating discs with the symmetric shrouds were shown to be similar in nature to the un-shrouded discs.

Launder *et al.* (2009) provided a review of the current understanding of instability patterns that are created in rotor-stator cavities leading to transition and eventually turbulence. Attention is focussed on radially elongated cavities with a gap ratio $G < 1$.

The review summarises that laminar flow in a rotor-stator cavity is axisymmetric and three-dimensional due to the recirculation created in the radial-axial plane by disc rotation. The stability of the flow is governed by the boundary layers and as such the flow is closely connected to that of a single, infinite rotating disc. The first instability observed is characterised by a circular wave on the stator boundary layer, propagating in the flow direction. As rotation increases the axisymmetry of the flow is broken and spiral waves develop. In the transition to turbulence, turbulent spirals are periodically formed around the disc and finally invade the whole cavity as the rotation rate increases. Stability on the rotor boundary layer is less well documented than that on the stator. Experimentally measurements are technically much more difficult than those on the stator and numerically, the instabilities at large rotation rates involve large computational costs due to resolution requirements.

Until recently the turbulent flow regime has been treated as though the flow in the disc cavity is axisymmetric, both in experiment and computation. Currently, whilst large eddy simulations of the vortex structures close to the discs are well resolved, large scale vortex structures in the core flow have not yet been satisfactorily captured by computations.

2.4 Rotor-stator systems with superimposed throughflow

In this section, the addition of throughflow in a rotor-stator cavity is investigated. It is necessary to first introduce a new relationship, commonly used with reference to this type of system. The rotational Reynolds number, Re_ϕ, and throughflow Reynolds number, C_w, are defined in Equations 2.1 and 2.2. The relationship between these two parameters is often used and is referred to as the turbulent flow parameter, shown in Equation 2.23.

$$\lambda_T = \frac{C_w}{\mathrm{Re}_\phi^{0.8}} \qquad \textbf{(2.23)}$$

The turbulent flow parameter, λ_T, gives an indication of the dominant flow mechanism in a rotor-stator cavity. This parameter was developed by **Owen and Rogers (1989)** from von Kármán's solution for the mass flow entrainment rate for a free disc (Equation 2.8). For $\lambda_T < 0.219$, all the fluid is entrained into the boundary layer of the disc and the flow is said to be rotationally dominant. For $\lambda_T > 0.219$, the flow is dominated by the superimposed flow and is said to be radially dominant. Figure 2.6 shows these flow structures within the rotor-stator cavity. Figure 2.6 (a) shows the case where there is no throughflow, Figure 2.6 (b) the case with throughflow and $\lambda_T < 0.219$ and Figure 2.6 (c) the case with throughflow and $\lambda_T > 0.219$.

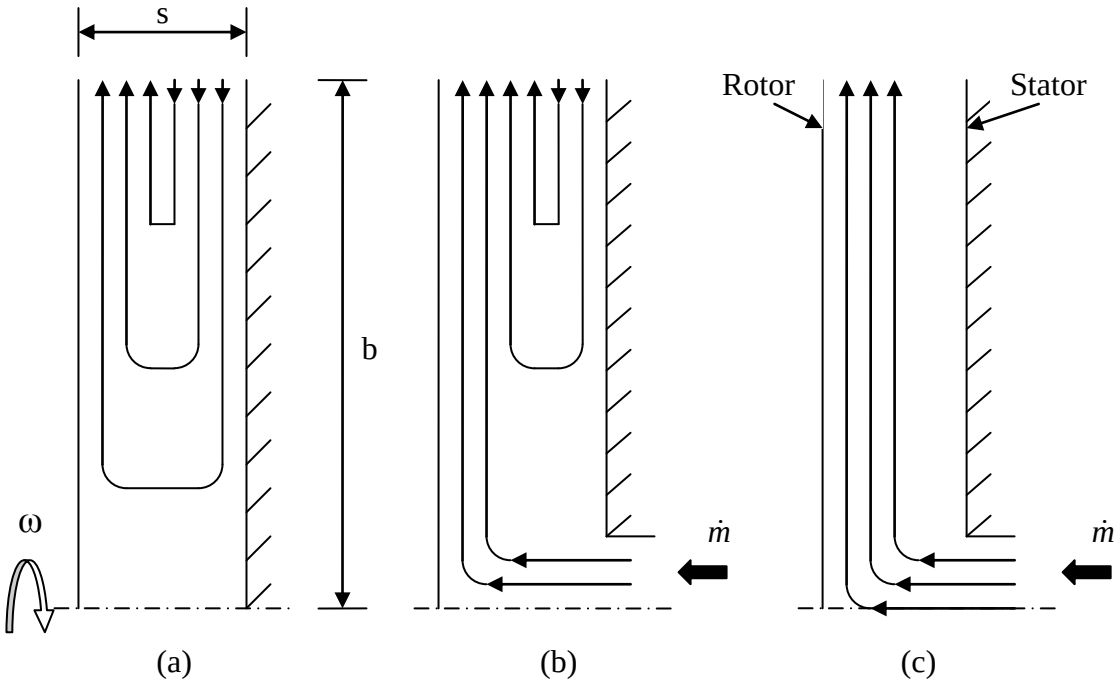

Figure 2.6 – Diagram showing the flow structure inside a rotor-stator cavity with (a) no throughflow, (b) with throughflow, $\lambda_T < 0.219$ and (c) with throughflow, $\lambda_T > 0.219$

Daily *et al.* (1964) performed analytical and experimental analyses to determine the moment coefficient of a rotor-stator system with superimposed throughflow, as a function of the core rotation velocity. The experimental set up included a rotor with a diameter $D = 0.46$ m and a thickness of either 12.7 mm or 6.35 mm. A cylindrical housing allowed variable axial length between $0.01 \leq G \leq 0.1$, with a radial clearance of $G_r = 7 \times 10^{-3}$. Superimposed throughflow of both water and air could be introduced axially to the rotor-stator cavity and rotational Reynolds numbers of up to $Re_\phi = 10^6$ could be reached. Radial and tangential velocities were measured using pitot tubes, in

addition to hot wire probes. Pressure measurements were taken at four radii, and also in the cylindrical housing. Shaft torque was measured using strain gauges and smoke (for flow visualisation) was introduced to the flow through ports angled at 30° to the surface of the disc at three radii.

The radial velocity profile measurements showed a radial outflow on the rotor and radial inflow on the stator. When the rotor-stator gap increases, there is a core of fluid between the rotor and stator which has no radial flow and a constant tangential velocity. When throughflow is introduced, the boundary layer thickness increases and the core velocity is reduced, more substantially at low radius. Equation 2.24 shows the relationship for calculating the relative velocity of the core speed to rotor speed, β. The parameter β^* in Equation 2.24 is the theoretical maximum relative core speed when there is no throughflow (β^* is dependent on the gap ratio of the rotor-stator cavity and can be found from data produced by **Daily and Nece (1960)**). For the current experimental set up, where $G = 0.1$, β^* is found to be 0.431.

$$\beta = \beta^* \left[1 + \frac{C\lambda_T}{\left(r/b\right)^{2.6}} \right]^{-1} \qquad \textbf{(2.24)}$$

In this equation C is a constant, chosen to be 12.74 by Daily *et al.* to match experimental data at $r/b = 0.648$.

Torque measurements showed that moment coefficient increased with increasing throughflow. The correlation shown in Equation 2.25 was produced to calculate the moment coefficient. The parameter C_m^* is the moment coefficient with no throughflow, calculated by Daily and Nece (Equations 2.19 to 2.22, depending on the geometry and flow conditions)

$$C_m = C_m^* \left(1 + 13.9\beta^* \lambda_T G^{-\frac{1}{8}} \right) \qquad \textbf{(2.25)}$$

Daily *et al.* also performed an analytical analysis to predict the moment coefficient as a function of the core rotational velocity. Calculating β using Equation 2.24, the moment coefficient can be found using Equation 2.26.

$$C_m = \left[\frac{0.663}{b^{\frac{23}{5}} \, \mathrm{Re}_\phi^{\frac{1}{5}}} \right] \int_0^b r^{\frac{18}{5}} (1-\beta)^{\frac{5}{4}} \left[1 + \left(\frac{0.162}{1-\beta} \right)^2 \right]^{\frac{3}{8}} dr \qquad \textbf{(2.26)}$$

Bayley and Conway (1964) carried out experiments on a rotor-stator system with radial inflow. Two discs with diameters D = 0.762 m were used, one of which was rotated at speeds up to 4000 rev/min. The gap ratio for the experiments varied from $2 \times 10^{-3} \leq G \leq 30 \times 10^{-3}$. Radial inflow was achieved by attaching the suction side of a compressor to a hole in the centre of the stator. The flow rate was measured by a venturi on the compressor outlet and the radial pressure gradient was measured using static pressure tappings in the stationary disc. Torque was measured on the stationary disc, rather than the rotating disc, under the assumption that it would be the same as rotor torque for the gap ratios tested and they would gain a more accurate measurement. The method used was to apply weights to a lever arm attached to the shaft.

They observed that, as G decreased, the sensitivity of the torque to variations in G also decreased, eventually leaving the moment coefficient as a function of Re_ϕ and C_w only. It was also noted that, as either Re_ϕ decreased or C_w increased, the value of G, below which it becomes inconsequential to the measured torque, increased. Increasing the radial inflow was found to increase C_m, and the majority of the increase was found to occur predominantly within the range of $10^3 \leq C_w \leq 10^4$.

Their observations of radial pressure distribution showed that similar trends occur with both increasing Re_ϕ and decreasing G. This suggests that decreasing the gap ratio leads to an increase in tangential velocity of the fluid. With no radial inflow, the pressure distribution is determined solely by the high tangential velocities towards the outer radius of the cavity. However, increasing radial inflow increases the tangential velocities towards the inner radius, which starts to change the overall pressure distribution within the cavity.

Alongside the pressure and torque measurements, were observations of the flow pattern within the cavity by way of both a claw-type yaw-meter and a total head tube. These results showed there to be a core of fluid rotating, almost uniformly, at roughly 40% of the disc speed. The core occupied 80% - 90% of the axial distance between the rotor and stator. The motion of the fluid falls in between free vortex flow and forced vortex flow, but as either radial inflow increased, or radius and rotational speed decreased, it tends towards free vortex flow.

Bayley and Owen (1970) also looked at the effects of a superimposed radial outflow, on both windage and pressure distribution, within a rotor-stator system. They used a disc of diameter D = 0.762 m, rotating up to speeds of 4500 rev/min, with a stationary Perspex shroud. The tests covered the range of rotational Reynolds numbers $4 \times 10^5 \leq Re_\phi \leq 4 \times 10^6$. Three gap ratios were used: G = 0.06; 0.12 and 0.18, with axial clearance ratios of G_a = 0.0033 and 0.0067. The windage torque on the disc was measured using a shaft mounted optical torque meter. Axial and radial static pressure tappings recorded the pressure distribution within the cavity.

There were found to be two factors affecting drag on the rotor due to shrouding, in the absence of superimposed radial outflow. The shrouding restricts the flow area at the periphery, increasing the radial velocity, which in turn increases the viscid shear in a region where it has greatest effect. Shrouding also restricts the ingress of fluid, therefore conserving the angular momentum of the fluid within the cavity. This decreases the relative motion between the core and the disc, which decreases drag on the rotor.

For a shrouded system with no superimposed throughflow, the results show that at low rotational Reynolds numbers, where ingress of fluid is expected to be small, the windage is increased compared to an un-shrouded disc. But, at high Reynolds numbers, the opposite applies. As the gap ratio increases, the point at which the drag of a shrouded system falls below that of the un-shrouded system moves to lower Reynolds numbers. At G = 0.18 the rotational Reynolds number at which the drag of a shrouded system falls below that of the un-shrouded system is $Re_\phi = 5 \times 10^5$. The effect, therefore, of shrouding is to decrease windage on the rotor, except at very low Reynolds numbers.

With superposition of throughflow the opposite occurs, as the effect of the shroud accelerating the flow at the periphery is dominant. Windage is, therefore, consistently higher than in an open system with no shroud. The axial gap between rotor and stator is largely insignificant but axial clearance between the rotor and shroud is not. Smaller axial clearance ratios, G_a, give higher values of windage.

With no shrouding, the pressure between the discs is slightly below atmospheric. With a stationary shroud, where $G_a = 0.0067$, this turns into a large positive pressure gradient (towards the axis of rotation), even with the pumping effects associated with high rotational Reynolds numbers.

Dibelius *et al.* (1984) carried out tests on a variable geometry, shrouded rotor-stator system, with a disc of diameter $D = 0.8$ m. It had the capacity for both radial inflow and radial outflow of superimposed air of up to $C_w = 14 \times 10^4$. Measurements were obtained for the static pressure, velocity distribution and windage torque of the rotating disc. The range of rotational Reynolds numbers tested was $2 \times 10^6 \leq \mathrm{Re}_\phi \leq 3 \times 10^7$.

Without throughflow, increasing the radial clearance ratio, G_r, between the shroud and the rim of the disc is shown to make the tangential velocity of the core decrease as disc radius increased. With $G_r \approx 0$, the tangential velocity is almost constant with radius. The effect of radial gap on tangential velocity was found to decrease with decreasing gap ratio, G. The introduction of radially inward throughflow, with swirl, causes the core rotation to increase. Since the angular momentum of the throughflow is maintained towards the axis of rotation, the tangential velocity increases and surpasses that of the disc on approaching the axis of rotation.

Pressure distribution within the cavity is shown to depend mainly on the core rotation, with diffuser effects from the variation of radial velocity being small. With increasing throughflow, the pressure first increases and then decreases, and pressure decreases with increasing swirl. Measurements showed that the maximum pressure for radial outflow, without swirl, is close to the critical flow to prevent ingress at the rim.

The windage torque measurements showed that the moment coefficient for radial outflow exceeds that for radial inflow. Positive swirl decreases the frictional torque for both radial inflow and outflow. Where $G_r \approx 0$, the torque measurements were in agreement with Daily and Nece (1960). Increasing the radial gap decreases the core rotation, which results in increasing measured torque.

Owen (1987) used an analytical approach to find an expression for the moment coefficient within a shrouded rotor-stator system with a superimposed radial outflow. Owen divides his work into two different flow regimes, depending on the value of λ_T, (Equation 2.16).

In the solution for the rotationally dominant flow regime where $\lambda_T < 0.219$, Owen distinguishes between the source region close to the axis of rotation and the core region radially outward of the source region. The total moment coefficient can be found from Equation 2.27,

$$C_m = C_{m1} + C_{m2} \qquad \textbf{(2.27)}$$

where C_{m1} and C_{m2} are the moment coefficients for the source and core regions respectively. These are obtained from Equations 2.28 and 2.29, where x_c is defined as the radial location at which the source region ends and core rotation begins, and can be calculated using Equation 2.30.

$$C_{m1} = 0.146\,\mathrm{Re}_\phi^{-\frac{1}{5}}\, x_c^{\frac{23}{5}} \qquad \textbf{(2.28)}$$

$$C_{m2} = 0.0796\,\mathrm{Re}_\phi^{-\frac{1}{5}}\left[\left(1 - x_c^{\frac{23}{5}}\right) + 14.7\lambda_T\left(1 - x_c^2\right) + 90.4\lambda_T^2\left(1 - x_c^{-\frac{3}{5}}\right)\right] \qquad \textbf{(2.29)}$$

$$x_c = 1.79\lambda_T^{\frac{5}{13}} \qquad \textbf{(2.30)}$$

It can be seen that C_{m1} is the same as von Kármán's free disc solution. For the case where $\lambda_T > 0.219$, the source region is assumed to apply for the whole rotor-stator cavity

($x_c > 1$). However, the free disc solution is inapplicable therefore, in this case, the moment coefficient, C_m, is calculated from Equation 2.31.

$$C_m = 0.666 C_w \, \mathrm{Re}_\phi^{-1} \qquad \textbf{(2.31)}$$

Gartner (1997) used an analytical approach to extend Owen's correlations for the frictional torque, in a shrouded rotor-stator system with radial outflow, to include the effects of the cylindrical shrouding. The correlations produced by **Owen (1987)** (Equations 2.27 and 2.31) were established and widely used. However, Equation 2.31 had a tendency to over predict frictional torque at high throughflow rates. Gartner's new correlations were compared to the experimental data obtained by **Daily *et al.* (1964)** (Equation 2.25), as well as to data obtained by **Dibelius *et al.* (1984)** and **Zimmermann *et al.* (1986)** (both of which are discussed in Section 2.5 of this chapter).

For the case where $\lambda_T < 0.219$, Gartner added a third term, C_{m3}, to Owen's solution, which represents the moment coefficient due to the cylindrical shroud. The expression for C_{m3} can be seen in Equation 2.32. This correlation showed a small improvement on Owen's correlation in its agreement with the experimental data.

$$C_{m3} = 0.36 G \gamma^{-\frac{1}{4}} \beta^{\frac{7}{4}} (1-\beta)^{-\frac{3}{20}} \mathrm{Re}_\phi^{-\frac{1}{5}} \qquad \textbf{(2.32)}$$

The core rotation factor, β, is calculated using Equation 2.33, where β^* is the core rotation with no throughflow.

$$\beta = 0.087 \beta^* \left\{ \exp\left[5.2 (0.486 - \lambda_T) - 1 \right] \right\} \qquad \textbf{(2.33)}$$

The value of β^* is calculated from the expression shown in Equation 2.34, which is a regression calculated from values of β^* quoted by **Daily *et al.* (1964)** for varying gap ratios.

$$\beta^* = 0.49 - 0.57 \frac{s}{b} \qquad \textbf{(2.34)}$$

The parameter γ, in Equation 2.32, is defined in Equation 2.35, where α is as defined in Equation 2.36.

$$\gamma = \left[\frac{81\left(1+\alpha^2\right)^{\frac{3}{8}}}{49\left(23+37\beta\right)\alpha} \right]^{\frac{4}{5}} \qquad \textbf{(2.35)}$$

$$\alpha = \left[\frac{2300\left(1+8\beta\right)}{49\left(1789-409\beta\right)} \right]^{\frac{1}{2}} \qquad \textbf{(2.36)}$$

The total moment coefficient is represented by Equation 2.37, where C_{m1} and C_{m2} are as Owen calculated and are given in Equations 2.28 and 2.29.

$$C_m = C_{m1} + C_{m2} + C_{m3} \qquad \textbf{(2.37)}$$

Equation 2.37 shows good agreement with the experimental results for the higher throughflow rates. For the case where $\lambda_T > 0.219$, Gartner's expression for the frictional torque is given by Equation 2.38.

$$C_m = 0.565\,\mathrm{Re}_\phi^{-\frac{1}{4}}\, G^{-\frac{1}{4}} \int_0^b \left(\frac{r}{b}\right)^{\frac{15}{4}} \left[1 + \frac{0.02533\lambda_T^2\,\mathrm{Re}_\phi^{-0.08}\,G^{1.14}}{\left(0.0017+0.0162\lambda_T\right)^2} \left(\frac{r}{b}\right)^{-4} \right]^{\frac{3}{8}} \frac{1}{b}\,dr \qquad \textbf{(2.38)}$$

Poncet *et al.* (2005) investigated the flow structure within a rotor-stator cavity, with gap ratio $G = 0.036$, using a test rig with the capability to superimpose water into the cavity. The radial clearance between the rotor and shroud was fixed at $G_r = 0.012$. LDA was used to measure the radial and tangential velocities, and also the Reynolds stress tensor components. Pressure was measured on the stator at six radial locations using piezoresistive transducers. Three values of throughflow Reynolds number were tested for both radial inflow (positive values) and radial outflow (negative values) $C_w = \pm 1976$, ± 5929 and ± 9881. Measurements were recorded at two rotational Reynolds numbers, $\mathrm{Re}_\phi = 10^6$ and 4.15×10^6.

For the case without superimposed throughflow and a rotational Reynolds number $Re_\phi = 10^6$, Batchelor type flow was observed. This consists of a radial outflow of fluid in the rotor boundary layer and radial inflow in the stator boundary layer, with a central core of rotating fluid. The results showed that the core tangential velocity increases slightly with increasing radius but the axial extent of the core decreases due to thickening of the boundary layers towards the outer radius of the disc. Increasing the rotational Reynolds number does not change the flow significantly, however, the maximum radial velocity in the rotor boundary layer decreases. Pressure is shown to decrease towards the axis of rotation. The turbulent intensity is concentrated in the boundary layers: on the rotor boundary layer more than the stator boundary layer, and there is no turbulent shear stress in the core.

With a superimposed radial inflow of fluid $C_w = 5929$, the rotor boundary layer changes from flowing radially outward at $r/b = 0.8$ to radially inward at $r/b = 0.44$ and the core tangential velocity increases above that of the rotor. Increasing the rotational Reynolds number decreases the core velocity to below that of the rotor and the rotor boundary layer flows radially outward again over the whole surface. Pressure again decreases towards the axis of rotation and absolute values of pressure increase with increasing radial inflow. Flow was found to be more turbulent close to the axis of rotation and, in this case, the stator boundary layer is more turbulent than the rotor boundary layer. As throughflow increases, turbulent intensities increase.

Superimposed radial outflow also produced Batchelor type flow, as in the case without throughflow, with a core velocity slower than that of the disc. However, towards the axis of rotation there is a similarity to Stewartson type flow, where there is no central core and the stator boundary layer flows radially outwards. Increasing the rotational Reynolds number causes the Batchelor type flow to extend further towards the axis of rotation. The transition between Batchelor and Stewartson type flow is characterised by the relationship between Rossby number, *Ro*, (defined in Equation 2.39) and radial location.

$$Ro = \frac{\dot{m}}{2\pi\rho b^2 G_r \omega} \qquad \textbf{(2.39)}$$

For the highest value of superimposed radial outflow, C_w = -9881, the radial velocity profile across the cavity becomes similar to that of fully developed channel flow.

With radial outflow, pressure decreases towards the axis of rotation and absolute values of pressure decrease with increasing throughflow, the opposite of radial inflow. In this case, the maximum turbulent intensity is again in the rotor boundary layer and the influence of throughflow on the turbulent field is negligible.

Coren *et al.* (2008) investigated windage in a shrouded rotor-stator system with superimposed throughflow. A smooth disc of radius b = 0.225 m was encased in a sealed casing with a gap ratio G = 0.1 on both sides of the disc. Air was introduced to the cavity axially and exited radially. The range of non-dimensional parameters tested were: $2.5 \times 10^6 < \mathrm{Re}_\phi < 2.5 \times 10^7$; $3 \times 10^4 < C_w < 10^7$ and $0.05 < \lambda_T < 0.5$. As well as windage measurements, obtained using an in-line shaft torquemeter, LDA measurements of core velocity were obtained and infra red sensors acquired disc surface temperatures.

The acquired data was first compared with existing free disc correlations and some significant variations were observed. When taking only the data from $\lambda_T \approx 0.2$, however, where the flow regime can be considered similar to the free disc, there was good agreement.

Coren *et al.* then went on to compare the data to existing correlations for rotor-stator systems without superimposed throughflow. Their data showed significantly larger moment coefficients than predicted by existing correlations, indicating that superimposed throughflow has a profound effect on the flow structure within the cavity. Comparison against existing correlations for systems with throughflow generally showed good agreement within the ranges appropriate for each correlation.

From the results obtained, Coren at al produced a correlation giving the moment coefficient in terms of Re_ϕ and C_w. This correlation is shown in Equation 2.40

$$C_m = 0.52 C_w^{0.37}\, \mathrm{Re}_\phi^{-0.57} + 0.0028 \qquad \textbf{\textit{(2.40)}}$$

A comparison with the existing correlations of **Owen (1987)** and **Gartner (1997)** showed there to be good agreement, particularly at low superimposed flow rates.

The LDA measurements showed that for radially dominant flow the velocity decreases with increasing axial distance from the rotor surface. The rate of rotation reaches a maximum of about 10% of rotor speed close to the rotor surface. For rotationally dominant flow the rotation reaches 25% of rotor speed at $r/b = 0.82$ and is shown to be fairly constant with distance from the rotor surface. Infra red rotor surface temperature measurements showed that for radially dominant flow conditions the increase in temperature due to increasing radius was around 2 °C, whereas for rotationally dominant flow the increase was 20 °C

2.5 Systems with protrusions

Taniguchi *et al.* (1981) researched circular cylinders of finite height in order to correlate the drag coefficient, C_D, of a cylinder in a turbulent boundary layer. The experiments were carried out in a wind tunnel with the cylinder vertically mounted on a flat plane. The height to diameter ratio of the cylinders tested ranged from $0.75 \leq h/D \leq 5$. Holes were drilled vertically down the height of the cylinder, which could be rotated around its vertical axis to allow measurement of pressure distribution over the whole surface. From their measurements they determined that the drag coefficient can be approximated from pressure forces only, since the viscous forces are an order of magnitude smaller, therefore the local drag coefficient, C_{Dy}, can be obtained using Equation 2.41.

$$C_{Dy} = \int_0^D \frac{p_s - p_0}{\frac{1}{2}\rho U_0^2} \cos\theta d\theta \qquad \textbf{(2.41)}$$

Here, p_s is the surface pressure and p_0 the static pressure of the free stream, U_0 is the free stream velocity and θ is the momentum thickness, which is defined in Equation 2.42 with u being the time averaged local velocity in the boundary layer.

$$\theta = \int_0^{\infty} \left(1 - \frac{u}{U_0}\right)\left(\frac{u}{U_0}\right) dy \qquad \textbf{(2.42)}$$

The total pressure drag coefficient can then be found using Equation 2.43, where h is the height of the cylinder and y is the local height.

$$C_D = \int_0^1 C_{Dy} D\left(\frac{y}{h}\right) \qquad \textbf{(2.43)}$$

Taniguchi *et al.* (1982) also researched the interference between two circular cylinders of finite height. Two cylinders, of height h = 45 mm and diameter D = 15 mm, were placed in a fully developed turbulent boundary layer in a wind tunnel. The cylinders were attached to a turntable in order to allow changes in the angle of attack, φ, between 0° and 180°. The spacing, s, between the two cylinders was adjustable between s/D =1.2 and 4. One cylinder was able to rotate on its vertical axis and pressure was measured from ten, vertically equidistant, piezometric holes on the surface. This allowed the pressure distribution over the whole surface to be measured. Figure 2.7 shows the layout of the equipment.

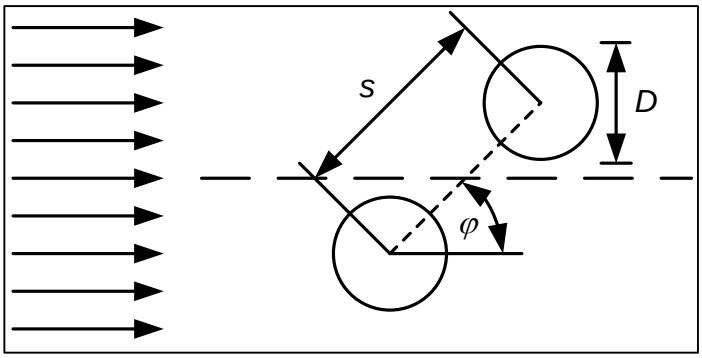

Figure 2.7 – Sketch of two circular cylinders in turbulent flow.

From the measurements obtained, both the drag and lift characteristics were classified into three regions, namely $0° \leq \varphi \leq 30°$, $30° \leq \varphi \leq 120°$ and $120° \leq \varphi \leq 180°$. In the first, $0° \leq \varphi \leq 30°$, lift was found to be positive (towards the gap between the cylinders) and increasing as spacing decreased. Drag variation was very small in this region. In the second region, $30° \leq \varphi \leq 120°$, a negative value of lift was found with the absolute

value increasing as spacing decreased. Drag was also found to increase as spacing decreased. In the third region, $120° \leq \varphi \leq 180°$, the lift was again positive.

It was concluded that, in the region $0° \leq \varphi \leq 135°$ and when $s/D \geq 4$, the effect of interference between the two cylinders is negligible and the time averaged fluid forces of the two cylinders are similar to those of a single cylinder.

Dibelius *et al.* (1984) carried out tests on a variable geometry, shrouded rotor-stator system, with a disc of diameter $D = 0.8$ m. The test facility had the capacity for both radial inflow and radial outflow of superimposed air, up to $C_w = 14 \times 10^4$. Measurements were obtained for the static pressure, velocity distribution and windage torque of the rotating disc, both with and without discrete protrusions (8 socket head cap screws at $r/b = 0.75$, $h = 20$ mm). The range of rotational Reynolds numbers tested was $2 \times 10^6 \leq \mathrm{Re}_\phi \leq 3 \times 10^7$. Details of the measurements without protrusions can be found in Section 2.4.

The windage torque measurements showed that, at $\mathrm{Re}_\phi = 4.2 \times 10^6$, the cap screws caused a 40% increase in moment coefficient when there was no superimposed throughflow. In the cases with throughflow, there was a 100% increase. Pressure measurements showed that, with no throughflow, the presence of cap screws decreases the pressure within the cavity. However, the influence they have on pressure decreases with increasing throughflow.

Zimmerman *et al.*. (1986) also researched the effect of protrusions on windage. The test configurations included staged bolts of height, h, and cross sectional area, A, and also cylindrical bolts with the same projected area as the staged bolts, A, but of smaller height and larger diameter, D. The staged and cylindrical bolt shapes are shown in Figure 2.8. Also tested were fully and partially shrouded bolts and, for comparison, a plain disc.

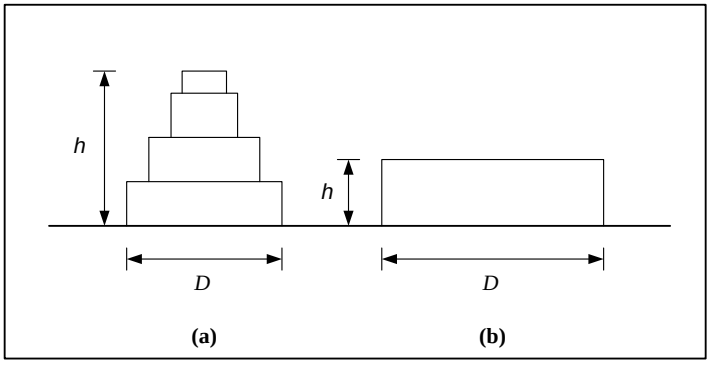

Figure 2.8 – Diagram showing (a) staged bolts, (b) cylindrical bolts

It was found that eighteen staged bolts on a disc placed at a non-dimensional radius of $r_b/b = 0.75$ (where r_b is the bolt radius) increased the windage torque by a factor of 2.5 over that of a plain disc. There were further increases for cylindrical shaped bolts. A partial shroud around the bolts, which was thought to decrease the pumping effect, had little effect on windage, compared to the uncovered bolts. Fully covered bolts, however, only increased torque above that of a plain disc by 25%. A superimposed radial outflow of $C_w = 2.6 \times 10^4$ increased the windage by 50% for all configurations.

Using the plain disc test results, Zimmermann *et al.* applied an empirical correction factor to von Kármán's free disc relationship between moment coefficient and rotational Reynolds number for one side of the disc. The resulting relationship, shown in Equation 2.44, where *a* and *b* are the disc inner and outer radii respectively, predicts the moment coefficient for a rotor-stator system with a superimposed throughflow.

$$C_m = 0.073\,\mathrm{Re}_\phi^{-0.2}\left[1+10^{-4}C_w\left(4.1\mathrm{Re}_\phi^{-0.16}-0.32\right)\right]\left[1-\left(\frac{a}{b}\right)^{5.7}\right]^{0.8} \qquad \textbf{(2.44)}$$

For protruding bolts, the authors attributed the increased windage due to protrusions to three elements: form drag; boundary layer losses and pumping losses. The contribution from form drag is calculated from Equation 2.45.

$$\Delta C_m = nC_D(1-\beta)^2\left(\frac{r_b}{b}\right)^3\frac{hD}{b^2}F \qquad \textbf{(2.45)}$$

Where ΔC_m is the increase in moment coefficient above that of a plain disc, n is the number of bolts, β is the core velocity ratio (taken here as $\beta = V_\phi/\omega r$ where V_ϕ is the core tangential velocity), F is a form drag correction factor (as described by **Taniguchi *et al.* (1981)**), and C_D is the drag coefficient of the bolts (calculated from Equation 2.43 by Taniguchi *et al.*).

Boundary layer losses occur due to bolt heads interrupting the boundary layer developing on the surface of the disc. The boundary layer losses for a circular ring can be calculated from Equation 2.46, where r_i and r_o are inner and outer radii of the boundary layer. The total boundary layer losses can then be found by adding the losses from three individual sections: From the inner radius of the disc, a, to the inner radius of the bolts, from the inner to the outer radius of the bolts and from the outer radius of the bolts to the disc outer radius, b.

$$C_m = 0.073 \mathrm{Re}_\phi^{-0.2} \left(\frac{r_o}{b}\right)^{4.6} \left[1 - \left(\frac{r_i}{r_o}\right)^{5.7}\right]^{0.8} \qquad \textbf{(2.46)}$$

The pumping losses can be calculated from Equation 2.47, where r_i and r_o are the inner and outer radius of the bolts and $V_{\phi,i}$ and $V_{\phi,o}$ are the inner and outer tangential velocities of the bolt driven fluid. The mass flow of fluid pumped by the bolt heads is given by $\dot{m}$.

Pumping losses: $P = \omega \dot{m} \left(V_{\phi,o} r_o - V_{\phi,i} r_i\right)$ **(2.47)**

Zimmerman *et al.*. argue that the additional windage, above that of a plain disc, can be obtained by adding these three loss components.

Millward and Robinson (1989) also investigated the influence of protrusions within the rotor-stator cavity. Their experiments involved a varying number of bolts, n, of diameter, D, pitch, p, and cross sectional area, A, attached to either the rotating disc or the stationary casing. They used an enthalpy balance to obtain the windage for rotor bolts. Their results can be rewritten in terms of moment coefficient, as shown in Equation 2.48, where a is the inner radius of the disc and r is the local radius.

$$C_m = 2.3\left(\frac{C_w}{\mathrm{Re}_\phi}\left(\frac{b}{r}\right)^3\right)^{\left(1.4-\frac{1}{3}\frac{r}{a}\right)}\left(\frac{p}{D}\right)^{0.44}\frac{r^3 An}{b^5} \qquad \textbf{(2.48)}$$

The limits of this correlation are:

$$1.5 < (r/a) < 2.25$$

$$3 < (p/D) < 20$$

$$0.001 < \frac{C_w}{\mathrm{Re}_\phi}\left(\frac{b}{r}\right)^3 < 0.1$$

$$2.3\left(\frac{C_w}{\mathrm{Re}_\phi}\left(\frac{b}{r}\right)^3\right)^{\left(1.4-\frac{1}{3}\frac{r}{a}\right)}\left(\frac{p}{D}\right)^{0.44} \leq 1$$

The authors noted that the windage, due to bolts located towards the outer radius of the disc, was significant whereas, those located towards the inner radius had little effect. For protrusions on the stator there was insufficient data to derive a correlation, although a recommendation was made that stator bolts contributed one third less windage than the corresponding rotor bolts.

Tests were also carried out to find the effect of full and partial shrouding, of both stator and rotor bolts, on windage. No measurable effect was found from partial shrouding of the rotor bolts, but with partial shrouding of the stator bolts there was a reduction in windage at high mass flows. When either the rotor or stator bolts were fully shrouded, there was no indication of additional windage compared with that of a plain disc. In fact a reduction in windage was observed for most flow conditions tested where there was full rotor bolt shrouding.

Daniels *et al.* (1991) conducted experiments to determine torque and aerodynamic characteristics of adjacent rotating discs, enclosed in a stationary shroud. Torque and pressure measurements were obtained, for both discs, in the rotating frame of reference for the co-rotating, counter-rotating and rotor-stator conditions. Superimposed throughflow could be introduced into the cavity, from either the hub or the disc rim, with swirl. Four different disc models were tested; smooth flat disc, smooth turbine

disc, turbine disc with bolts (40 equally spaced 10-24NC socket head cap screws, at a non-dimensional radius of $r/b = 0.88$) and turbine disc with partially covered bolts. Tests were conducted for the range of rotational Reynolds numbers $0.4 \times 10^7 \leq Re_\phi \leq 1.6 \times 10^7$ and throughflow Reynolds numbers $-12 \times 10^3 \leq C_w \leq 12 \times 10^3$, where a positive C_w is radially outward flow and a negative C_w is radially inward flow.

It was found, from the experiments with the turbine disc, that the increased windage due to the presence of bolts was roughly a factor of two over that of a plain disc. The partial covering led to windage measurements of only 5% to 10% less than with the uncovered bolts. This is comparable to the results obtained by **Zimmermann *et al.* (1986)**. When the disc spacing was reduced from $G = 0.328$ to $G = 0.233$, it was found that, for the co-rotating and the rotor-stator configurations, the moment coefficient remained the same. For counter-rotating discs the windage increased slightly.

Throughout the experiments the torque was measured separately on both discs. With the rotor-stator configuration, the moment coefficient for the rotating plain turbine disc was recorded as two to three times greater than that of the static disc. This difference in torque was attributed to the stationary shroud around the periphery.

For the flat disc, measurements were taken with both radial inflow and radial outflow of air. The results indicated that C_m is highest for counter-rotating discs and lowest for co-rotating discs. For co-rotating and the rotor-stator configuration, C_m increases as flow rate increases for radially outward flow and decreases as flow rate increases for radially inward flow. For counter-rotating discs, C_m is independent of both flow rate and direction. The turbine disc was tested with radially inward flow only. The results indicate that the moment coefficient for the turbine disc is greater than for the flat disc at all conditions. This increase was attributed to increased surface area (around 15% more than the flat disc) and not to a change in flow structure within the cavity.

Gartner (1998) used a momentum integral method to predict the frictional torque of a disc with protruding bolts. Experiments were also carried out on a disc of diameter $D = 0.8$ m, with the range of rotational Reynolds numbers $2 \times 10^6 \leq Re_\phi \leq 5 \times 10^6$, using three different bolt configurations. Configuration A consisted of 18 or 36 staged bolts (See Figure 2.8 (a)), with a diameter at the base $D = 45$ mm and height $h = 46$ mm, at

r/b = 0.75. Configuration B consisted of 6 or 18 staged bolts at *r/b* = 0.52 and configuration C with 18 cylindrical bolts (See Figure 2.8 (b)) with a diameter *D* = 30 mm and height *h* = 50.6 mm, at a radius *r/b* = 0.75. The momentum integral equations used in the analysis are shown in Equations 2.49 and 2.50.

$$\frac{1}{r}\frac{d}{dr}\int_0^{\delta} rV_r^2 dz = \frac{1}{r}\int_0^{\delta}\left(V_{\phi}^2 - V_{\phi,\infty}^2\right)dz - \frac{1}{\rho}\left(\tau_{0,r} + \tau_{p,r}\right) \qquad \textbf{(2.49)}$$

$$\frac{1}{r}\frac{d}{dr}\int_0^{\delta} r^2 V_r V_{\phi} dz - V_{\phi,\infty}\frac{d}{dr}\int_0^{\delta} rV_r dz = -\frac{r}{\rho}\left(\tau_{0,\phi} + \tau_{p,\phi}\right) \qquad \textbf{(2.50)}$$

In these equations, δ is the boundary layer thickness, $V_{\phi,\infty}$ is the tangential velocity outside the boundary layer. The radial and tangential velocities of the fluid within the boundary layer are given by V_r and V_{ϕ} respectively; $\tau_{0,r}$ and $\tau_{0,\phi}$ are the radial and tangential components of shear stress caused by the disc and $\tau_{p,r}$ and $\tau_{p,\phi}$ are the radial and tangential components of shear stress caused by the protrusions. It is assumed that the velocity profile within the boundary layer (for both radial and tangential components) follows the $1/7^{th}$ power law.

Using Equations 2.49 and 2.50, Gartner showed that the predicted boundary layer thickness increases rapidly to a maximum, similar in magnitude to the radius of the disc, when bolts are encountered. It then decreases to approach smooth disc values again. The predicted radial velocity decreases as the bolts are encountered but then increases to higher values than the plain disc. The predicted frictional torque is generally close to the measured values except in the case of configuration A, with 36 bolts. This is due to the large number of bolts approaching the limiting value, where discrete bolts act like a ring. **Zimmerman *et al.* (1986)** found that, when *p/D* > 6 (*p/D* is the bolt pitch to diameter ratio), the moment coefficient for a rotating disc, with bolts, increases as number of bolts increases. Where *p/D* < 6, interference between a bolt and the wake of the preceding bolt begins to affect the moment coefficient and, when *p/D* < 4, the total moment coefficient starts to decrease with increasing number of bolts. For Gartner's experiments, configuration A has a value of *p/D* = 1.2. This means that the interactions

between a bolt and the wake of the preceding bolt are strong and consequently the prediction of the drag coefficient, C_D, for a single cylinder is poor.

For configuration C, a simplified method is also used where the torque, caused by the drag of the bolt heads, is added to Dorfman's correlation for the windage torque for a plain disc. In the range of Reynolds numbers applied, the bolt Reynolds number is in the transition region between laminar and turbulent flow. Consequently, there is an uncertainty in the predicted drag coefficient. Two values of drag coefficient were used in this simplified method for predicting windage torque but, on both occasions, the torque was over predicted.

Coren (2007) carried out an experimental investigation of protrusions in a shrouded rotor-stator system with superimposed throughflow. Up to 18 bolts, of diameter D = 16 mm, were positioned on both the rotor and stator surfaces at two radii: r_b = 0.135 and r_b = 0.2. Radial ribs were also tested on the stator surface and plain disc measurements were obtained as a baseline. The range of rotational Reynolds number tested was $0.17 \times 10^6 \leq \mathrm{Re}_\phi \leq 2 \times 10^7$, and throughflow Reynolds number $2.5 \times 10^4 \leq C_w \leq 10^5$, giving a range of turbulent flow parameter $0.05 \leq \lambda_T \leq 0.6$. Torque measurements were obtained using an in-line shaft torquemeter. Infra red measurements of the disc surface temperature were obtained as well as LDA measurements of the velocity of the fluid within the cavity.

The radial ribs on stator measurements showed that where $\lambda_T < 0.15$ the moment coefficient was increased compared with the plain disc, however where $\lambda_T > 0.2$ lower than plain disc moment coefficients were observed. The dual row of stator bolts showed a similar trend to the radial ribs, whereas a single row of stator bolts at r = 0.2 showed similar or slightly higher moment coefficients than the plain disc for all values of λ_T. The lower than plain disc moment coefficients where $\lambda_T > 0.2$, is thought to be linked to source region instabilities. The rotor bolt measurements showed that the dual row of bolts only increased moment coefficient by about 10% compared with the single row at r = 0.2. The measurements also showed that the moment coefficient is increased significantly with an increasing number of bolts.

From the data obtained, correlations were produced for windage in a rotor-stator system with bolts present and for the windage due to the bolts in isolation. These are shown in Equations 2.51 and 2.52 respectively.

$$C_m = C\left(0.115 C_w^{0.63}\,\mathrm{Re}_\phi^{-0.57}\left(\frac{r_b}{p}\right)^{0.38} + 0.005\right) \qquad \textbf{(2.51)}$$

$$C_m = C\left(0.115 C_w^{0.47}\,\mathrm{Re}_\phi^{-0.3504}\left(\frac{r_b}{p}\right)^{0.34} - 0.00179\right) \qquad \textbf{(2.52)}$$

In Equation 2.51 the value of C is 1 for rotor bolts and 0.032 for stator bolts. In Equation 2.52 the value of C is again 1 for rotor bolts but 0.031 for stator bolts.

Infra red disc surface temperature measurements showed that the temperature gradient across the disc is strongly influenced by the flow conditions. With radially dominant flow the temperature increased by 2 °C with increasing radius from r = 0.098 to r = 0.21, but with rotationally dominant flow the temperature increased by approximately 20 °C. The tests with rotor bolts showed an additional localised heating of the disc around the radius of the bolt, which also results in conduction toward the mid-radius of the disc.

LDA measurements showed that for radially dominant flow the tangential velocity of the core increased from around 6% of rotor speed for the plain disc to up to 30% with 18 rotor bolts present, at the highest measured radius r = 0.185. For the rotationally dominant flow condition, the increase was from 25% for the plain disc to up to 80% with 18 bolts. The radial velocity was shown to decrease with increasing radius for all conditions. For radially dominant flow the radial velocity did not vary greatly with bolts present compared with the plain disc. For rotationally dominant flow, however, an increase in radial velocity with increasing radius was found. It was suggested this could be due to the radial pumping of fluid due to the bolts.

Moghaddam *et al.* (2011) carried out a numerical study of the effect of bolts on the rotor surface, on moment coefficient and the flow structure, in a shrouded rotor-stator

system with superimposed throughflow. Varying number of bolts between $0 < N < 60$ were investigated, as well as a continuous ring, at $Re_\phi = 6.8 \times 10^6$ and $C_w = 10^5$, giving a value of turbulent flow parameter $\lambda_T = 0.35$.

After carrying out two validation cases against experimental data from open literature, a comparison was made between the data from the experimental test rig with 3, 9 and 18 bolts and the numerical model. The numerical model showed that moment coefficient increases significantly with an increasing number of bolts. These results showed good agreement with the experimental data which gave confidence in the numerical model. Further simulations were then carried out extending the number of bolts as well as modelling a continuous ring. The continuous ring was shown to be approximately the same as the plain disc, in agreement with **Millward and Robinson (1989)**. The tangential velocity was shown to increase significantly from $\beta = 0.2$ to $\beta = 0.7$ increasing from 9 to 45 bolts. Above 45, however, increasing the number of bolts was shown to have little effect on the core velocity. The study also showed that the pressure related contributions to overall moment coefficient (from form drag and pumping losses) were much larger than the contribution from skin friction.

2.6 Systems with surface roughness

Theodorsen and Regier (1944) carried out experiments measuring the drag force on a rotating disc in fluid. The tests included an investigation into the effects of surface roughness. Using a disc of diameter $D = 0.61$ m, they tested up to rotational Reynolds numbers of $Re_\phi = 7 \times 10^6$ and Mach numbers (in the tangential direction) of 1.69 by using Freon 12 as the working fluid.

The transition from laminar to turbulent flow on a smooth disc was found to occur at a rotational Reynolds number of 3.1×10^5 and could not be increased beyond this no matter how highly polished the disc was. With the application of 60 mesh coarse sand to the disc the transition Reynolds number was reduced from 3.1×10^5 to 2.2×10^5. This roughness on the surface of the disc also had a significant effect on moment coefficient, increasing it by 25% compared to the smooth disc.

The study also looked at the influence of initial turbulence on transition by introducing a small high pressure jet near the centre of the disc. This brought the transition Reynolds number close to the intersection of von Kármán's moment coefficient correlations for laminar and turbulent flow, which is the theoretical minimum it could be. From Equations 2.4 and 2.5, this occurs when $Re_\phi = 5.6 \times 10^4$.

Dorfman (1958) used analytical methods to calculate the windage generated by a free disc with varying surface roughness. The calculation is based on the assumption that the roughness consists of grains of uniform size. Equation 2.53 below shows the correlation for the moment coefficient produced, where *h* is the height of the roughness.

$$C_m = 0.108\left(\frac{h}{b}\right)^{0.272} \qquad \textbf{(2.53)}$$

Dorfman also applied this method of analysis to the rotor-stator problem. Using the ratio, shown in Equation 2.54, between the minimum moment coefficient for a rough disc in an enclosed space, $C_{m,min}$, and the value for a free disc, C_m, (as described in Equation 2.53), he derived the formula shown in Equation 2.55 for the minimum moment coefficient for a rough disc in an enclosed space.

$$\frac{C_{m_{\min}}}{C_m} \approx 0.474 \qquad \textbf{(2.54)}$$

$$C_{m_{\min}} \approx 0.051\left(\frac{h}{b}\right)^{0.272} \qquad \textbf{(2.55)}$$

Nece and Daily (1960) acquired torque data for varying surface roughness in an enclosed rotor-stator system. For the case where there was equal roughness on both the rotor and the stator, three gap ratios were tested: $G = 0.0227$, 0.0609 and 0.112, with three values of relative roughness: $b/k = 1000$, 2000 and 3000 (where *b* is the disc radius and *k* is the mean grit size, measured using a roughness indicator). The case of a rough rotor and smooth stator was also tested for three comparable gap ratios but only with $b/k = 1000$. The cylindrical shroud was smooth for all runs and the moment coefficient

attributed to the shroud was deducted from the total so that the moment coefficient results presented are due solely to the rotor and the stator. The working fluids used were water along with three commercial lubricating oils. Using a speed range of 125 rev/min $\leq N \leq$ 2000 rev/min, the range of rotational Reynolds numbers tested is 4 x 10^3 $\leq \mathrm{Re}_\phi \leq$ 6 x 10^6.

The results of these tests showed that, within the laminar flow regimes ($\mathrm{Re}_\phi < 2 \times 10^5$), roughness has no effect, therefore the variations in C_m are the same as those for the smooth rotor-stator case. For turbulent flow, two terms were developed to describe the transition zone between smooth disc and rough disc behaviour. The first term is the upper limit of 'smooth disc performance', where roughness effects first become visible. This is calculated as shown in Equation 2.56. Beyond this, the measured values of C_m are greater than for the corresponding smooth disc case.

$$\mathrm{Re}_\phi \sqrt{C_m} = 1.1 \times 10^3 \left(\frac{b}{k}\right)^{\frac{2}{5}} \qquad \textbf{(2.56)}$$

The second term is the lower limit of 'fully rough flow', shown in Equation 2.57, beyond which the value of C_m is constant and can be predicted by Equation 2.58.

$$\mathrm{Re}_\phi \sqrt{C_m} = 1.15 \times 10^4 \left(\frac{b}{k}\right)^{\frac{1}{10}} \qquad \textbf{(2.57)}$$

$$\frac{1}{\sqrt{C_m}} = 3.8 \log_{10}\left(\frac{b}{k}\right) - 2.4 G^{\frac{1}{4}} \qquad \textbf{(2.58)}$$

Kurokawa *et al.*. (1978) undertook research into the effects of surface roughness on the three dimensional boundary layer flow in a rotor-stator cavity. Testing took place using a smooth disc, with a diameter D = 0.328 m, in a closed cavity with a gap ratio G = 0.078 and water as the working fluid. The varying surface roughness was obtained using commercial waterproof grit papers attached to either the disc, the stationary enclosure or both. Static pressure measurements were obtained in addition to velocity measurements, using pitot tubes, at a constant speed of 850 rev/min (Re_ϕ = 3.1 x 10^6).

Measurements were made for: smooth-disc, smooth-enclosure; smooth-disc, rough-enclosure; rough-disc, smooth-enclosure; and rough-disc, rough-enclosure.

The results from these tests showed that increasing the roughness of the rotating disc increases the core flow velocity. It also considerably increases the pressure drop towards the axis of rotation. An increase in the roughness of the stationary enclosure results in the opposite effect: core velocity slows and the pressure drop towards the centre of the disc decreases. The three-dimensional boundary layer on a rotating disc, with no superimposed throughflow, gets thinner towards the outer radius, unlike that of two-dimensional boundary layer flow. As a result, the effects of roughness first appear at the outer radius resulting in varying radial distribution of the core tangential velocity. As roughness increases, its effects extend towards the inner radii, allowing the core to rotate with almost constant tangential velocity in the radial direction. When there is equal roughness on both the disc and stationary enclosure, the core tangential velocity is almost the same as when both surfaces are smooth.

Equation 2.59 gives the roughness limitation, k_{lim}, in the hydraulically smooth region of a two dimensional boundary layer that was developed by **Schlichting (1979)**, where ν is the kinematic viscosity and β is the fluid to disc tangential velocity ratio.

$$k_{\text{lim}} = \frac{100\nu}{(1-\beta)r\omega} \qquad \textbf{\textit{(2.59)}}$$

Kurokawa *et al.* confirmed that this formula can also be effective for three dimensional boundary layer flow. This reason for this is that the velocity of the secondary, axial, flow is much smaller than the velocity of the main, tangential and radial, flows in the immediate vicinity of the wall. The secondary flow, therefore, has minimal influence on the main flow, so the viscous sublayer along a rotating disc shows almost the same behaviour as one in two dimensional flow.

2.7 Systems with surface cavities

Roshko (1955) investigated the flow in a rectangular surface cavity. A variable depth box, recessed into the floor of a wind tunnel, was used, of fixed width $W = 0.81$ m, and breadth (in the streamwise direction) $B = 0.1$ m. Pressure and velocity measurements were made on the cavity walls for the varying depth-breadth ratios.

The main conclusions of this work were that the drag increment on the free stream due to the cavity is almost entirely accounted for by the pressure on the cavity walls. Not, as had been previously supposed, due to the change in friction on the external flow. Moreover, the variations of drag with varying depth are analogous to the variations of pressure at the downstream edge. It is here that deflection of the separated boundary layer into the cavity occurs, resulting in the formation of a vortex. It does not seem likely from these tests, however, that drag can be calculated accurately by only considering the downstream edge pressure.

Kistler and Tan (1967) carried out an experimental investigation to determine the principal mechanisms controlling the transport process between a rectangular surface cavity and an adjacent uniform stream. Measurements were made on three sides of a cut out, of variable depth and breadth, on the floor of a wind tunnel. The cavity was 0.6 m wide, the breadth, in the stream direction, could be varied between $0 \leq B \leq 0.3$ m, and the depth was variable between $0 \leq d \leq 0.6$ m. The boundary layer thickness of the free stream was 15 mm and fully turbulent, due to forced transition of the flow 0.3 m upstream of the cavity.

Distinct differences in the internal flows of the cavity were found when $d < 2.5\,B$ and $d > 2.5\,B$. For $d < 2.5\,B$, the flow was found to be distinctly three-dimensional and a cellular structure was observed. For $d > 2.5\,B$ the flow was found to be essentially two-dimensional. Measurements showed that the intrinsic properties of the free stream are not strongly influenced by the details of the particular flow within the cavity. However, the free stream is warped by the internal cavity flow which results in external flow entering the cavity. The effect of this is to increase drag in the free stream above the value predicted for a two-dimensional flow. This is dependent on the strength of the

three-dimensional flow in the cavity, although the actual size of the effect could not be calculated from the measurements taken. Preliminary measurements suggested that changing the internal flow in the cavity, by such things as surface roughness or an obstruction to the flow, could have large effects on free stream drag.

Geis *et al.* (2001) investigated the effects of rotor surface cavities on the fluid velocities and moment coefficient in a rotor-stator system, as compared with a plain disc. These tests were carried out using a stationary shrouded, rotor-stator system with radially outward superimposed throughflow. The rotor had a diameter D = 0.496 m and could be rotated at speeds of up to 10000 rev/min. The maximum rotational Reynolds number achieved was $Re_\phi = 4.2 \times 10^6$ and the range of superimposed throughflow was $1.1 \times 10^4 \leq C_w \leq 6.6 \times 10^4$. There were 93 surface cavities, of cross section 8 mm by 10 mm (10 mm in the radial direction) and 20 mm depth, machined into the rotor surface just underneath the disc rim. There was a combined axial and radial seal which divided the space between the rotor and stator into an inner cavity (close to the axis of rotation) and an outer cavity (radially outwards of the inner cavity). A three-component LDA system was used within the outer cavity to measure the radial, axial and tangential velocities. Static pressure taps, in addition to thermocouples, were located on the stator surface in both the outer and inner cavities between r/b = 0.37 and 0.98.

The LDA results showed that there are higher tangential velocities in the core region when surface cavities are present than with a plain disc, in addition to a strong tangential acceleration. Close to the rotating disc, there are small axial deflections of the radial flow that are synchronous to the position of the surface cavities, but there are no vortex structures shed into the flow away from the disc surface. Despite the fact that these deflections in the axial direction are weak, they are responsible for an enhanced transfer of momentum within the outer rotor-stator cavity. This induces higher shear stresses between the rotor boundary layer and the main flow, and also higher tangential velocities within the core.

Frictional torque was also measured using a torquemeter placed between the motor and the disc. These measurements showed that there is an increase in the moment coefficient of up to 60% over that of the plain disc, although the effect of the surface cavities diminishes as rotational speed increases. This leads to the assumption that the

deflections seen in the rotor boundary layer, are weaker at these higher rotational speeds. However, a 20% increase in moment coefficient is observed even at the higher speed conditions.

2.8 Systems with labyrinth rim seals

Millward and Edwards (1994) carried out experimental work to establish the effects of the geometric parameters of seals on windage losses in a rotor-stator system. It is assumed that, in an adiabatic system, all windage power absorbed by a rotor-stator system must be dissipated into the cooling air as heat. Millward and Edwards, therefore, measured the overall heat pick up through the seal in order to calculate the enthalpy change of the system. Temperature measurements were made by placing individually calibrated thermocouples directly before and after the air entered and exited the seal. Four basic types of seal were tested: straight through, radial fins; straight through, inclined fins; stepped, radial fins and two stage brush seals.

From the experimental data, the relationship shown in Equation 2.60, for calculating the windage heating, H (in kW), was found. This relationship estimates the windage data to within ±25%.

$$H = C_{m,seal}\pi L\rho\omega^3 b^4 \qquad \textbf{(2.60)}$$

In this equation L is the length of the seal surface and $C_{m,seal}$ is the seal moment coefficient obtained from Equation 2.61, where n_f is the number of seal fins.

$$C_{m,seal} = 0.06\left(\frac{C_w}{\mathrm{Re}_\phi}\right)^{0.55} n_f^{-0.65} \qquad \textbf{(2.61)}$$

2.9 Summary

From the review of current literature it is clear that significant research has focussed on windage effects and flow structure of rotor-stator systems, both with and without throughflow, therefore the subject is generally well understood. Similarly the windage effect of rotor bolts has been well researched, however the ability to predict windage in a rotor stator system is still limited. Stator bolt measurements have to date only been obtained by **Millward and Robinson (1989)** and **Coren (2007)**. Similarities, however, are found between discrete protrusions and surface roughness. Research by **Kurokawa *et al.* (1978)**, therefore, does give some insight into the effect of stator bolts on the core flow between the rotor and stator surfaces. Measurements of core velocity with rotor bolts have been carried out using a variety of methods therefore their effects on core velocity are generally understood. To date, however, the data is restricted to core flow in general and has never focussed directly on flow local to the bolts. Measurements of core velocity with stator bolts have not yet been undertaken. Experimental data of surface cavities in rotating flow has only previously been obtained by **Geis *et al.*** and so the understanding of their effects on windage and core flow is limited. The experimental investigation described in this thesis aims to address the above limitations in the current knowledge base.

Chapter 3. Test Rig

3.1 Introduction

This chapter contains a detailed description of the test facility used to conduct the research. Section 3.2 describes the air supply system for the test facility. Section 3.3 provides details of the drivetrain components; the motor, gearbox and torquemeter. In Section 3.4 is a detailed description of the pressurised casing and turbine disc. Section 3.5 describes the methods used for temperature measurement, and Section 3.6 the pressure measurements. Section 3.7 provides a description of the data acquisition system, and Section 3.8 describes the Particle Image Velocimetry (PIV) system.

During the test program the data acquisition system was upgraded. The upgrade was carried out early in the test program and, as such, the current instrumentation and data acquisition system was used for the majority of the testing. This set-up is described first in each section. The original instrumentation and data acquisition system, used only for the nine and eighteen stator bolt tests (see chapter 6), will be described subsequently in the relevant sections.

3.2 Air Supply System

3.2.1 Air Compressor

The main air supply comes from an Atlas Copco ZT250 screw type compressor, which is able to supply air to the test rig at up to 7.5 bar (absolute) and 0.85 kg/s. The compressor uses two helical rotors that turn into each other, one has four ‘lobes’ and the other has six ‘flutes’ to accommodate the lobes. The lobed rotor turns 50% faster than the fluted rotor. As the rotors turn, the compartment between the lobe and flute gets

smaller, thereby compressing the air within it. The intermeshing rotors never touch, which reduces wear and also requires no lubrication. As a result of this, and good sealing, the compressed air is completely oil free. A flow diagram of the compressor is shown in Figure 3.1.

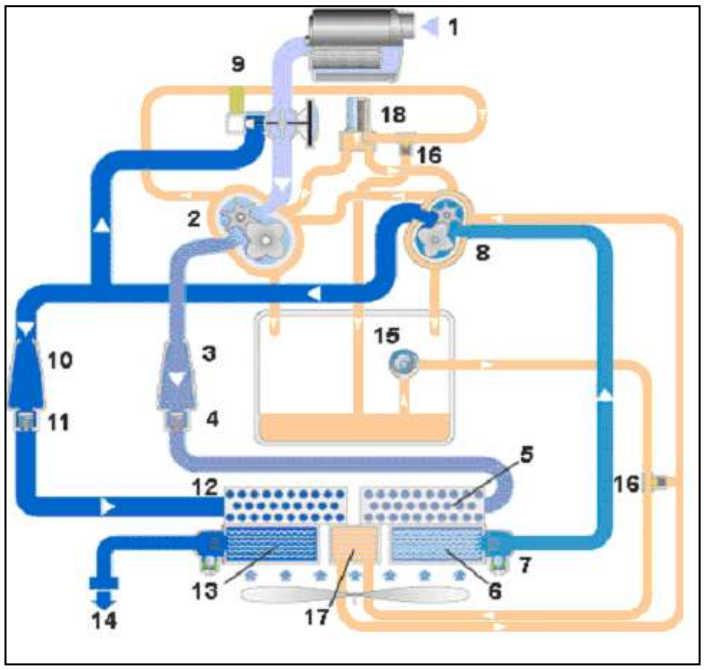

Figure 3.1 – Flow diagram for Atlas Copco ZT250 air compressor

1 – Air inlet, air filter and silencer
2 – Low pressure element
3 – Silencer
4 – Check valve
5 – Pre-cooler
6 – Intercooler
7 – Water separator and drain
8 – High pressure element
9 – Full load/no load regulator, blow-off valve and silencer
10 – Silencer
11 – Check valve
12 – Pre-cooler
13 – After-cooler
14 – Compressed air outlet
15 – Oil pump
16 – Oil bypass valve
17 – Oil-cooler
18 – Oil filter

3.2.2 Air Dryer

The Atlas Copco FD 700 air dryer, ensures that the compressed air is free of moisture upon reaching the test rig. It also provides a stable inlet air temperature. The drying process involves lowering the temperature of the compressed air from the Atlas Copco ZT250 to close to its freezing point. It does this in two stages. Initially the compressed air passes through an air-air heat exchanger, where the outgoing cold, dried air starts the

cooling process. The compressed air is then passed through an air-refrigerant heat exchanger where the evaporation of the refrigerant withdraws heat and the water particles condense. Next the air flows through a separator to remove the condensed water, which is subsequently drained away. The air is then reheated, as it flows back through the air-air heat exchanger, to about 10 °C below the compressed air inlet temperature before leaving the dryer.

3.3 Drivetrain

3.3.1 Motor

The power to rotate the test rig comes from a 55 kW, three phase motor, which can run at speeds of up to 3000 rev/min. The motor is controlled by an Optidrive control unit which in turn is controlled manually via a potentiometer. Although the motor is capable of running at speeds of up to 3000 rev/min, the maximum loading is 35 N m of torque, at which point the motor will cut out as a safety precaution. Steps were taken to ensure this limit was not exceeded, as some of the test conditions produced a windage torque close to the maximum load allowed on the motor. During these tests, care was taken to obtain the required speed slowly, ensuring the maximum load was not exceeded.

3.3.2 Gearbox

The output of the motor is directed through a 5:1 step up gearbox in order for the rotor to be able to rotate at speeds of up to 15000 rev/min. The gearbox is shown in Figure 3.2 (a), part way through a rebuild which was necessary due to oil leakage problems. An oil pump system feeds oil through the gearbox by way of the feed pipes indicated in Figure 3.2 (a). The oil is collected from the bottom of the casing and re-circulated through the system. The oil pump system is shown in Figure 3.2 (b).

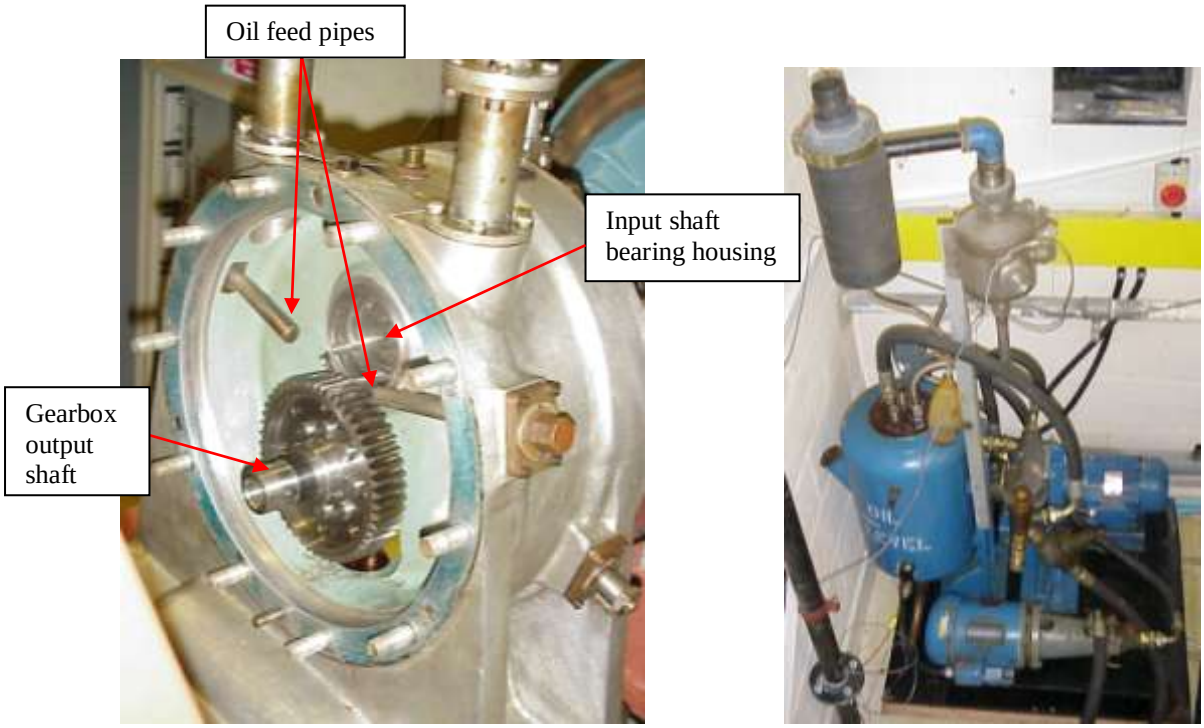

(a) **(b)**

Figure 3.2 – Pictures showing (a) Gearbox assembly during repair work, (b) Gearbox oil pump system.

3.3.3 Torquemeter

An in-line torquemeter unit transmits the gearbox output, via a flexible coupling, to the rotor, which is attached to a flange on the end of the torquemeter output shaft. The torquemeter used is a Vibro-Meter Torquemaster TM-112 which measures the torque acting on the shaft as well as the rotational speed of the disc. It transmits its signal, via an EH135 cable assembly, to an ISC 228 signal conditioning unit that contains a UAE 757 signal processing module. The signal conditioning unit then transfers the torque and speed data to a National Instruments Compact DAQ (c-DAQ) N-9205 module. This module has 16 differential (or 32 single ended) channels with a range of up to ±10 V. The data from the c-DAQ is transmitted to the visual programming data acquisition program LabVIEW 8.5, also a product of National Instruments, which controls the data acquisition process as well as displaying and storing the data.

The main components of the Torquemaster unit are the torque measuring shaft, torque transducer and built in electronics. An aluminium housing encases these components in addition to two sealed bearings which have lifelong lubrication. The unit can measure

static or dynamic torque as well as detect the direction of the torque. The transducer is defined as an inductive torque transducer. A cross section of the torquemeter unit can be seen in Figure 3.3.

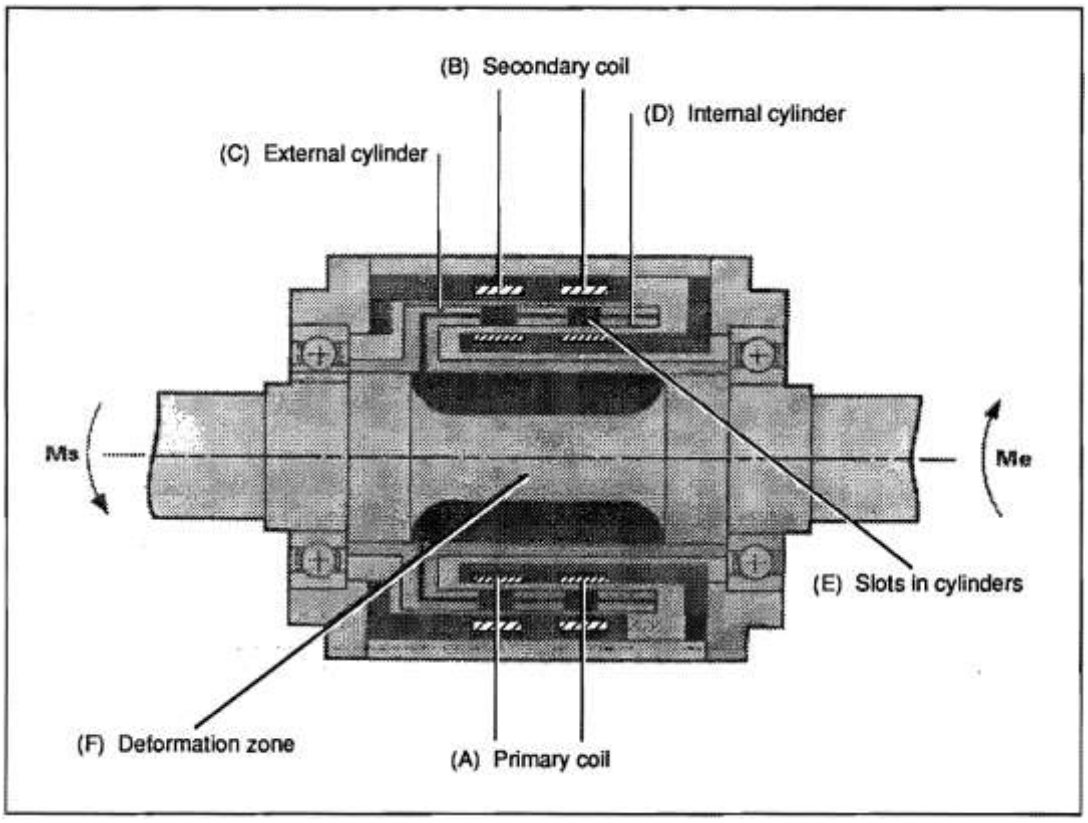

Figure 3.3 – Diagram showing Torquemaster TM 112 torquemeter unit (courtesy of Vibro-Meter).

The torquemeter operates by having the primary (A) and secondary (B) coils of a transformer divided by two concentric cylinders (C & D), one attached either side of a deformation zone (F) in the shaft. The cylinders have slots (E) positioned so that when no torque is being applied to the shaft, there is no overlap and therefore there is total screening between the primary and secondary coils. When a torque is applied, the shaft within the deformation zone undergoes angular deformation causing the slots in the cylinders to overlap. This introduces an induction between the two coils so, when the primary coil is excited by a voltage signal, the secondary coil produces a voltage relative to the amount of overlap between the two slots, which in turn is relative to the amount of torque applied.

The torquemeter has a rated output (RO) of ±5 VDC for the torque signal, relating to ±200 N m (positive or negative depending on direction of torque). However, in LabVIEW, the range for the data acquisition system is set to ±2 V as the full scale of the torquemeter is not utilized.

The Torquemaster unit also has an integrated speed transducer to provide rotational speed detection. The transducer is trained on the toothed part of a rotor and provides sixty pulses per shaft revolution. It operates on the proximity probe principle, which sets up a high frequency electric field between the transducer and its target (the toothed part of the rotor). The speed signal has a rated output of ±10 VDC and, for these tests, the signal conditioning unit is set to the 50000 rev/min range. However ,in LabVIEW, the range is set to ±3V since the highest speed required in the current range of tests is 12000 rev/min.

During the initial data acquisition phase (used only for the 9 and 18 stator bolt tests), the torque signal was acquired by a Solartron Orion 3530 data logger. This was controlled by, and transmitted data to, the data acquisition program HP-VEE 5.0, also a visual based programming package. The speed signal was taken directly from the Optidrive motor controller. This signal was also transmitted to the Solartron Orion 3530 data logger for processing.

The torquemeter was calibrated externally, by Young Calibration Ltd., up to 100 N m for the torque signal, and up to 10000 rev/min for the speed signal. The output voltage for the torque signal was plotted against the applied torque. The plot was fitted with a third order polynomial and the resulting expression, shown in Equation 3.1 where M is the adjusted torque and V is the voltage output from the torquemeter, was applied to the raw torque signal received.

$$M = 0.03V^3 - 0.11V^2 + 40.07V + 0.20 \qquad \textbf{(3.1)}$$

In a similar fashion, the output voltage for the speed signal was plotted against the frequency input and a polynomial fitted. The resulting expression, shown in Equation 3.1 where N is the adjusted speed and V is the voltage output from the torquemeter, was applied to the raw speed signal.

$$N = 1.73V^3 - 3.59V^2 + 5007.98V - 2.21 \qquad \textbf{(3.2)}$$

The speed measurements for the 9 and 18 stator bolt tests were obtained from the Optidrive motor controller. The 0 – 10 V output signal was calibrated, in-house, up to 13000 rev/min, details of which can be found in **Coren (2007)**. The correlation shown in Equation 3.3 was found where, again, N is the adjusted speed and V is the voltage output from the torquemeter.

$$N = 4.00V^2 + 1426.10V - 9.81 \qquad \textbf{(3.3)}$$

The torquemeter was re-calibrated at the end of the test program to check for drift, this time only to 50 N m. The two sets of calibration data are plotted in Figure 3.4, which shows the variation of applied torque with the voltage output of the torquemeter. It can be seen that there is generally good agreement, to within 4%, between the two calibrations.

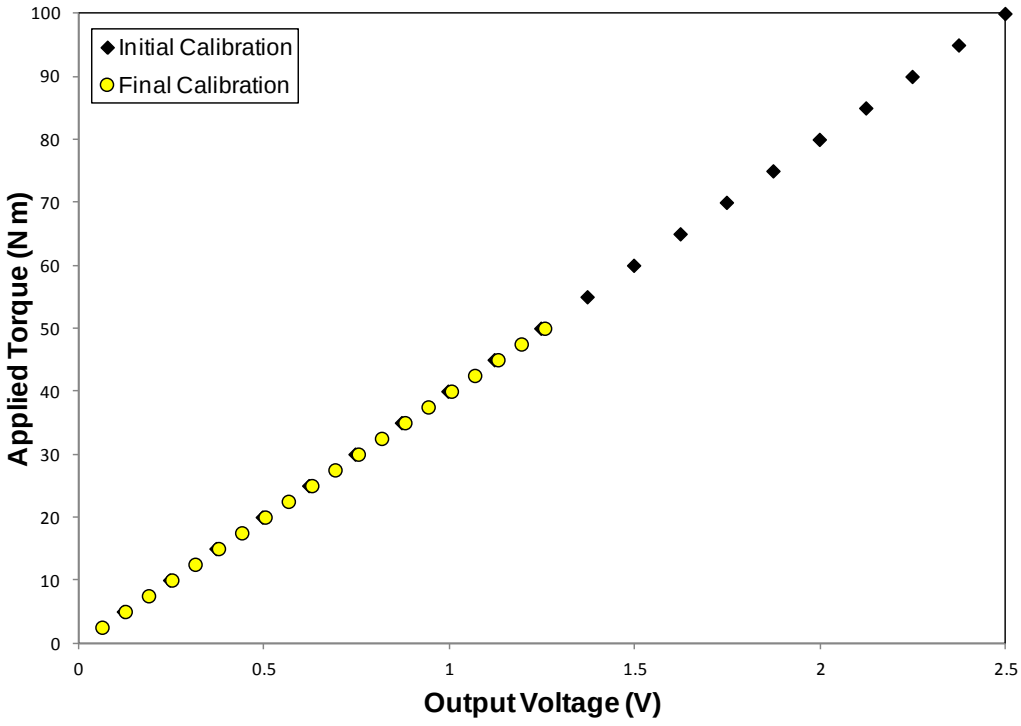

Figure 3.4 – Graph showing the variation of applied torque with voltage output for the two separate calibrations of the torquemeter.

3.4 Pressurised Casing

The rotor sits inside a sealed casing which comprises the main part of the test rig assembly. A section of the assembly is shown in Figure 3.5. Drawings of the main components of the test rig assembly can be found in Appendix B. For further details the reader is referred to **Coren (2007)**.

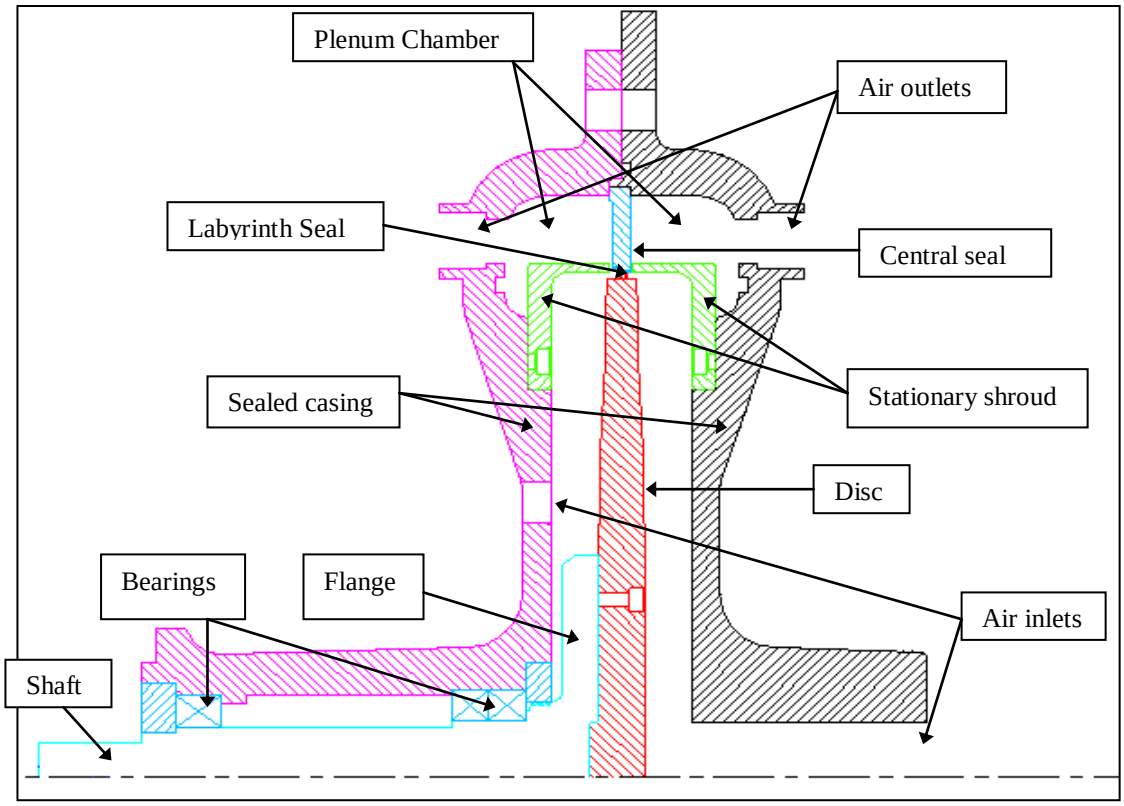

Figure 3.5 – Diagram showing half section of inside the pressurised casing

The driveshaft is supported by a pair of thrust bearings close to the rotating disc, to absorb any axial thrust that may occur due to unbalanced flow conditions, and also by a single bearing situated towards the torquemeter output shaft. The driveshaft has a flange to which the turbine disc attaches with eight countersunk 3/16” cap screws. The disc is made from a titanium alloy consisting of titanium with 4% vanadium and 6% aluminium. It is tapered in cross section but in stages so that there are two flat sections at radii r = 0.135 m and 0.2 m, which are 20.75 mm wide in the radial direction. Figure 3.6 shows a cross section of the disc highlighting the two flat sections.

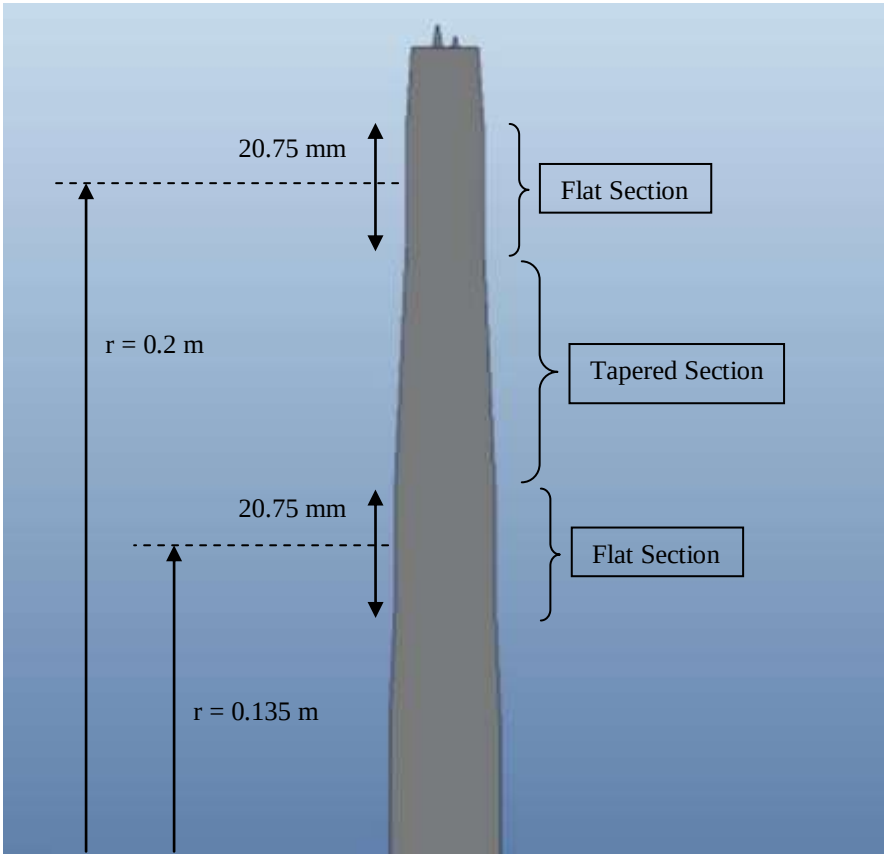

Figure 3.6 – Diagram showing cross section of the disc.

At a radius of 0.2 m, there are eighteen M14 tapped holes to allow the attachment of bolts or surface cavities required for the current test program. The flat section at r = 0.135 m is residual from a previous testing phase. There are nine M14 tapped holes in this section for attachment of protrusions, but for the current experimental work these are not used and as such were filled with plaster of paris, and sanded to give a smooth surface. Machined around the periphery of the disc is a labyrinth seal to provide a controlled exit route for the air flowing through the cavity.

Surrounding the disc is a two piece, cast steel casing which provides a sealed housing around the disc. The casing is fixed to the main structure of the test rig. This structure has an integrated crane to enable one side of the casing to be removed, allowing changes to the internal configuration to be made. Figure 3.7 shows the open casing.

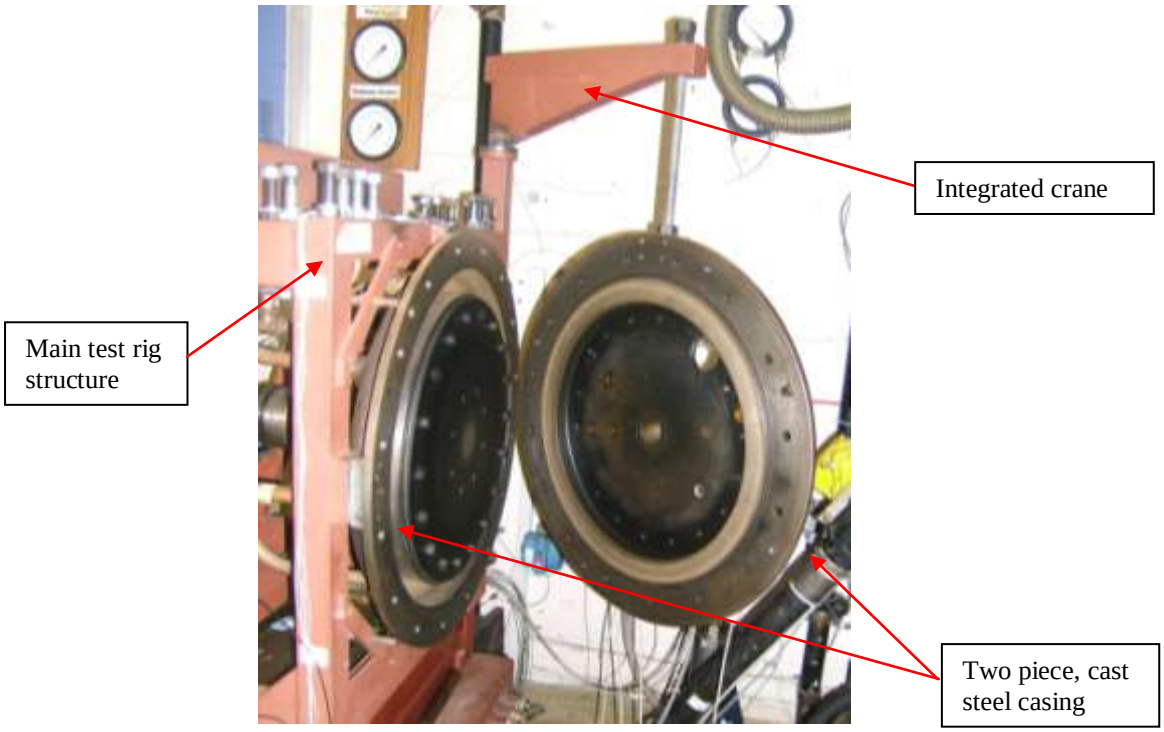

Figure 3.7 – Picture showing casing structure

As was seen previously in Figure 3.5, 'L' shaped seals are fixed to both sides of the casing. A picture of the seal on the balance side of the casing can be seen in Figure 3.8. These seals create a cylindrical shroud encasing the cavities on each side of the rotor. A central seal is also employed to aid the labyrinth seal in controlling the flow of exiting air. This has an 'Apticote 800/38' abraidable coating applied to it which is designed to wear away in the event of contact so as not to damage the labyrinth seal.

Figure 3.8 – Picture showing the 'L' shaped seal creating a cylindrical shrouding on balance side of casing.

The compressed air is supplied to the test rig on both sides of the rotor to reduce any axial loading on the shaft bearings. This also reduces any heat transfer across the rotor resulting from imbalanced test conditions. On the right side of the casing assembly, as seen in Figure 3.5, the air is supplied centrally along the axis of rotation. This side of the casing is called the test side as it has the majority of the temperature and pressure instrumentation. The left side is referred to as the balance side. On the balance side of the casing there is less instrumentation and, due to the centrally positioned shaft, the air is introduced through four equidistant pipes located around the driveshaft. Upon exiting the cavity the air is exhausted through eight ports around the circumference via a plenum chamber, one on either side of the central seal. The plenum chambers can be seen clearly in Figure 3.5, and Figure 3.9 shows the eight exhaust ports on the test side of the rig.

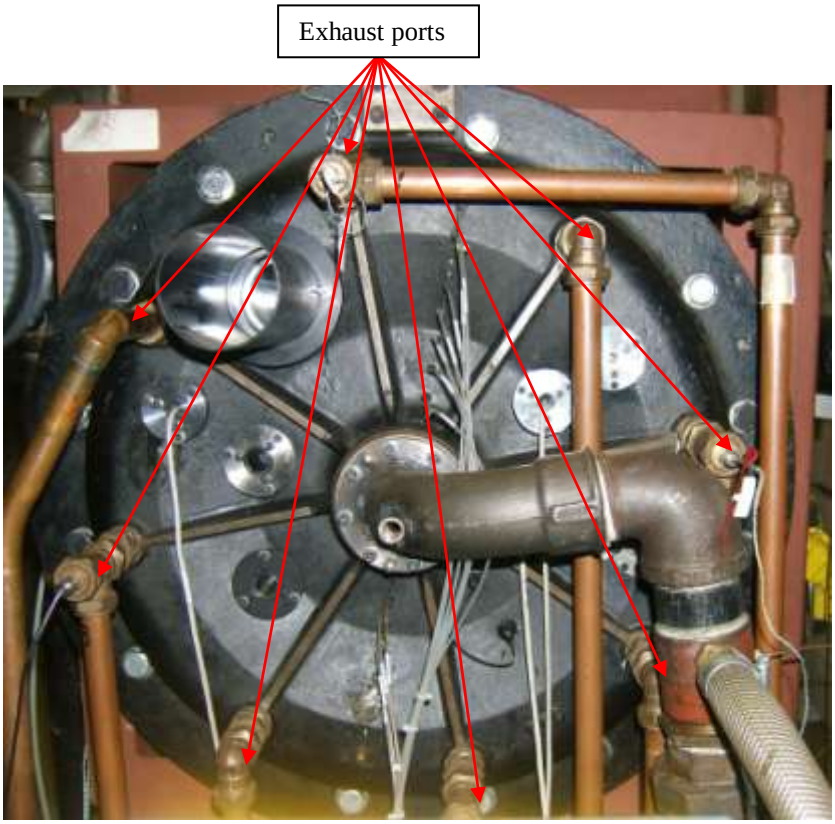

Figure 3.9 – Picture showing the eight exhaust ports on the test side of the rig.

The supply of air is controlled with motorised valves, upstream and downstream of both the test and balance side of the rig. The mass flow of air entering and exiting the rig is measured using orifice plates that are positioned upstream of the inlet valves and downstream of the outlet valves. The mass flows are shown in real time within

LabVIEW so the valves can be adjusted to achieve the required mass flow of air as well as obtain a uniform flow on both sides of the disc. Further details on the measurement of the mass flow through the orifice plates can be found in Section 4.2.3.

In the previous instrumentation and data acquisition phase, the valves were not motorised and real time mass flows were not available. Pressure measurements were acquired with a QBasic program entirely separate to the HP-VEE program used to obtain the rest of the test data. The valves were adjusted manually and the mass flow was found by taking periodic pressure and temperature measurements and entering these into an excel spreadsheet to perform the mass flow calculation. This proved to be a slow, laborious process and was a contributory factor in the decision to upgrade the instrumentation and data acquisition systems.

3.5 Temperature Measurement

3.5.1 Thermocouples

Thermocouples are a cheap and effective way of temperature measurement and come in many forms. For the purposes of this research, k type thermocouples were used to determine the air temperature at various positions around the test rig. These have a sensitivity of 41 μV/°C. There are eleven in total: one at each of the four orifice plates measuring the upstream temperature, one measuring the temperature of each of the three bearings, three measuring the outlet air temperature on the test side of the casing and one measuring the outlet air temperature on the balance side of the casing.

The thermocouples were calibrated in house following their use in a previous test phase. The assumption was made that thermocouples made from the same batch of thermocouple wire will change in a similar way, if at all, if they have been exposed to similar working conditions. Therefore, if two of the thermocouples on the test rig are calibrated, and there is no significant change from the previous calibration, or variation between the two, it can be assumed that the whole batch will require the same calibration adjustments.

With this in mind, two thermocouples were selected at random for calibration. The reference instrument used in the calibration was a standard platinum resistance thermometer (SPRT) along with an Isotech TTI 2 temperature indicating device. The SPRT can be traced to the international temperature scale from 1990, which is the current agreed approximation to the thermodynamic temperature scale. The Isotech TTI 2 has a measurement resolution of ±0.25 mK, with an uncertainty in linearization of < ±1 mK and an uncertainty in the measurement of < ±1 mK (not including the uncertainty in the SPRT which has a measurement uncertainty of ±5 mK).

The calibration process involves attaching the measuring junction of the thermocouples to the end of an SPRT, using copper tape to ensure the thermocouples and the SPRT are measuring exactly the same temperature. They are then placed into a 915 ISOTECH parallel tube liquid bath. The liquid used in this case is oil, the temperature of which can be varied from room temperature up to 600 °C. The reference junction of the thermocouple is attached to a c-DAQ 9211 data acquisition module. The c-DAQ 9211 module is designed specifically for reading thermocouple signals. It has a range of ±80 mV and incorporates a thermistor to detect the temperature at this junction.

The thermistor was calibrated separately to ensure it was within the specified limits of uncertainty. This was done by mounting the SPRT very close to the module, care being taken to ensure that the air in close proximity to the thermistor and SPRT was still and at constant temperature. A 6 ½ digit, digital voltmeter (DVM) was connected to the thermistor output pins. Using Equations 3.4 to 3.6 the measured voltage was converted to a temperature which was then compared to the SPRT temperature.

$$x = \frac{2.5 - V}{5000} \qquad \textbf{(3.4)}$$

$$y = \ln\left(\frac{V}{x}\right) \qquad \textbf{(3.5)}$$

$$T = \left(\frac{1}{1.30e^{-3} + y\left[2.34e^{-4} + 1.02e^{-7}y^{2}\right]}\right) - 273.15 \qquad \textbf{(3.6)}$$

In these equations, V is the measured voltage and T is the thermistor temperature in °C. From this calibration, carried out on three separate occasions, the thermistor was found to be within the limits of uncertainty (±0.6 °C) specified by the manufacturer.

The 915 ISOTECH parallel tube liquid bath is controlled through the program CalNotePad06. The program also logs both the temperature and resistance of the SPRT via the TTI 2 temperature indicating device. It was programmed to vary the temperature of the bath from 25 °C to 80 °C in 5 °C intervals. The bath was left at each temperature set point for forty minutes to ensure enough time for the SPRT temperature to stabilise. The temperatures at each set point are logged for each thermocouple through LabVIEW, which calculates the thermocouple temperatures using the standard relationship for a k type thermocouple of 41 μK/°C. The calibration results for each thermocouple were compared to the other, as well as the calibration data acquired from the previous calibration, during the last test phase. The data was considered similar enough to assume all the thermocouples on the test rig can use the same calibration data. An average of the two current calibration data sets was taken and a plot made of the variation of the SPRT temperature with thermocouple temperature. A third order polynomial curve was fitted, the result of which is shown in Equation 3.7 where T is the adjusted temperature and T_{tc} is the thermocouple temperature measurement. This expression was applied to the signal within LabVIEW.

$$T = 1.48\times10^{-6}T_{tc}^{3} + 2.13\times10^{-4}T_{tc}^{2} + 0.98T_{tc} + 0.39 \qquad \textbf{(3.7)}$$

During the original instrumentation and data acquisition phase the thermocouple signals were measured using the Solartron Orion data logger and the measurements stored and displayed using HP-VEE. The reference junction temperature was measured using an LM 35CZ sensor installed inside the connector box where the thermocouple connections were made. This precision temperature sensor had its own power supplied by an ISOTECH IPS2302A power supply. It had an operating range of -40 °C to 110 °C and a sensitivity of 10 mV/°C. The thermocouples at this time were calibrated separately to the data acquisition device. An ice bath was used as the reference junction, which is accurate to ±0.01 °C, and a 6 ½ digit DVM was used to measure the resulting signal at each temperature set point. The same SPRT was used, along with the

TTI 2 temperature indicating device and the 915 ISOTECH parallel tube liquid bath, to acquire the temperature set points. The calibration process was the same as described previously. The SPRT temperature was plotted against the DVM voltage and the relationship shown in Equation 3.8 was found from plotting a second order polynomial, where T is the adjusted temperature and V is the thermocouple signal voltage. This expression was then applied to the signal within HP-VEE.

$$T = -8.30x10^{4}V^{2} + 2.47x10^{4}V + 0.19 \qquad \textbf{(3.8)}$$

3.5.2 Platinum Resistance Thermometers

Some air temperatures in the rig were also measured using platinum resistance thermometers (PRT). There are four of these devices, one at the inlet and outlet of the test and balance side of the rig. This was to enable a more accurate calculation of the enthalpy rise, and therefore the windage heating, occurring within the cavity (the reader is referred to Section 4.2.2 for further details). The specific type of PRT used is referred to as a PT100 device, and is connected using a four wire configuration. These have a resistance of 100 Ω at 0 °C and 138.5 Ω at 100 °C, giving a sensitivity of 0.385 Ω/°C or 2.597 °C/Ω. The sensors, which are mounted in a stainless steel probe, have an operating temperature range of -50 °C $\leq T \leq$ 250 °C. The PRT signals are measured using a National Instruments SCXI-1121 data acquisition module, which is specifically designed to read PRT signals. It applies an excitation current of 0.45 mA to each channel and measures the resulting voltage signal. The data is then transferred to LabVIEW via a PCI-6034E data acquisition card at the computer terminal. In LabVIEW the voltage signal is converted back into a resistance measurement, from which a temperature can be calculated.

The calibration process for the PRTs was similar to the thermocouple calibration procedure, although all four of them were individually calibrated to ensure a high degree of accuracy. The sensing end of the PRT was placed in the calibration bath along with the SPRT, and the other end was connected to the SCXI-1121 data acquisition module. The temperature, controlled by CalNotePad06, was increased from 25 °C to 80 °C in 5 °C intervals, leaving the temperature constant for forty minutes at each set point to allow the SPRT to stabilise. The PRT resistance and SPRT

temperatures were logged and plotted for each sensor. A third order polynomial was fitted to each plot of the variation of SPRT temperature with PRT resistance and an equation obtained, one for each sensor. The four equations are shown in Equations 3.9 to 3.12. In each case *T* is the adjusted temperature and *R* is the PRT resistance. These equations were applied to the respective output signals in LabVIEW.

Test side, inlet: $T = 5.31\times10^{-5}R^3 - 1.80\times10^{-2}R^2 + 4.60R - 335.68$ ***(3.9)***

Test side, outlet: $T = 2.57\times10^{-5}R^3 - 8.04\times10^{-3}R^2 + 3.41R - 287.79$ ***(3.10)***

Balance side, inlet: $T = 4.58\times10^{-5}R^3 - 1.52\times10^{-2}R^2 + 4.26R - 321.07$ ***(3.11)***

Balance side, outlet: $T = 2.61\times10^{-5}R^3 - 8.23\times10^{-3}R^2 + 3.43R - 289.00$ ***(3.12)***

In the previous data acquisition phase the PRT signals were measured using an Alpha 912 data logger used in 4-wire PT100 mode. This is also specifically designed to measure PRT signals and provides a 75 mA current to each PRT. The resulting signal was sent directly to the HP-VEE program where it was displayed and stored. The calibration method was the same as described for the current instrumentation, except that the PRTs signal was obtained by the Alpha 912, not the SCXI-1121. The liquid bath was set manually at 10 °C intervals from 25 °C to 115 °C. The PRT and SPRT temperatures were manually recorded (from HP-VEE and the TTI2 respectively) after a suitable amount of time had passed for the temperature of the SPRT to stabilise. The resulting second order polynomial equations acquired from plotting the variation of SPRT temperature with PRT temperature are shown in Equations 3.13 to 3.16.

Test side, inlet: $T = 3e^{-5}T_{PRT}^2 + T_{PRT} + 0.1470$ ***(3.13)***

Test side, outlet: $T = 1e^{-5}T_{PRT}^2 + T_{PRT} - 0.1779$ ***(3.14)***

Balance side, inlet: $T = 1e^{-5}T_{PRT}^2 + T_{PRT} - 0.1263$ ***(3.15)***

Balance side, outlet: $T = 7e^{-6}T_{PRT}^2 + T_{PRT} + 0.2163$ ***(3.16)***

In these equations T is the adjusted temperature and T_{PRT} is the measured PRT temperature. These expressions were then applied to the acquired signals within HP-VEE.

3.5.3 Infra Red Sensors

Raytek Thermalert RayMIC10LT infra red sensors were used to measure the surface temperature of the disc. There are six in total, five measuring the temperature of the test side of the disc at radii of: 0.096 m, 0.135 m, 0.154 m, 0.2 m and 0.2105 m, these correspond to: r/b = 0.427, 0.6, 0.684, 0.887 and 0.935, and one on the balance side at a radius of 0.2 m (r/b = 0.887). Their positions on the test side of the casing can be seen in Figure 3.10.

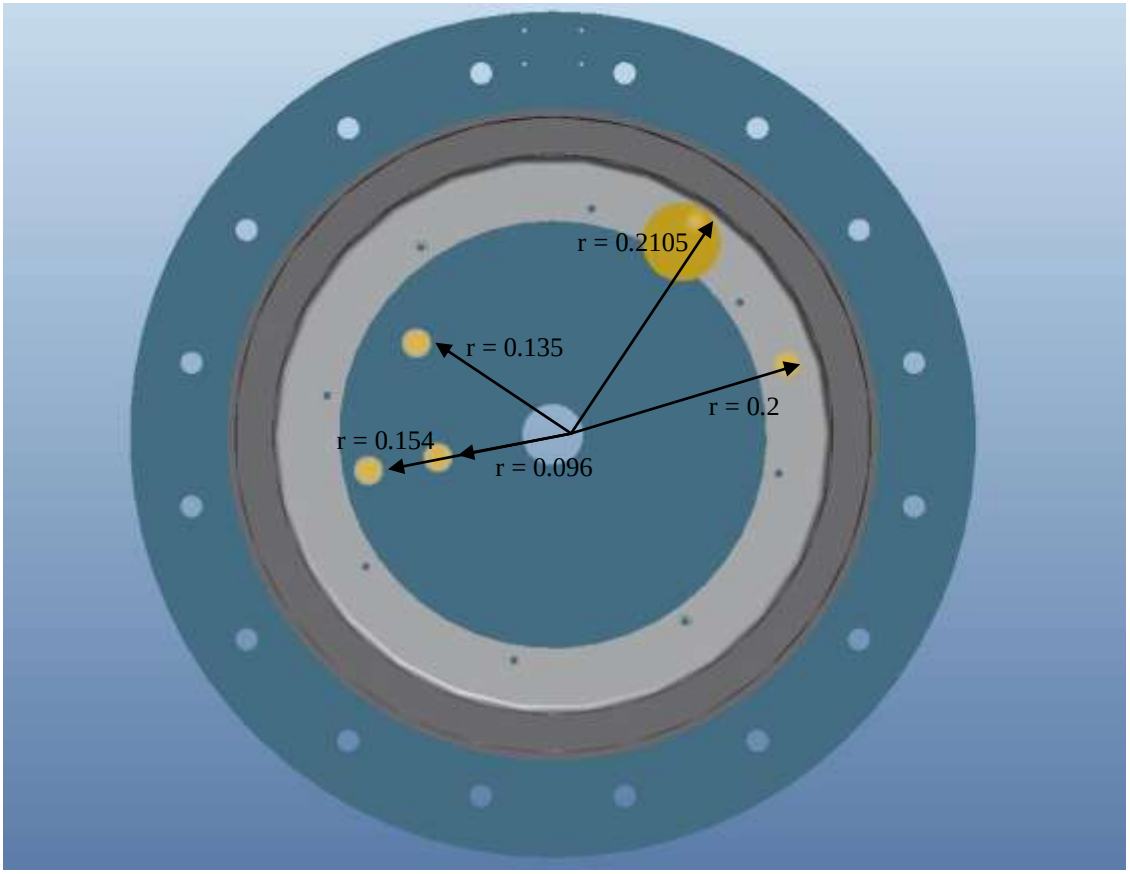

Figure 3.10 – Diagram showing the positions of the infra red sensors on the test side of the casing.

These sensors have a measurement range of 0 °C to 500 °C and a response time of 350 ms. Each sensor has an individual signal conditioner, the signal from which is transmitted to an SCXI-1100 module, which then transfers the data to LabVIEW. Previous to the data acquisition upgrade, the sensor outputs were transmitted to the Alpha 912 data logger, and then logged in HP-VEE.

The disc and the inside of the cavity are painted black using high temperature 3M black paint so that close to black body radiation could be assumed. Research by **Betts *et al.* (1985)** suggests that it is reasonable to assume that generic 3M black paint will be as good as the more expensive, specially, designed black body paint for this application.

The sensors need to be protected from the pressures and temperatures encountered during the tests and so they are housed within specially designed cartridges with a window for optical access to the disc. The windows, 20 mm diameter and 5 mm thick, are made from Zinc Selenide, which can be used in temperatures up to 250 °C. The windows have a wavelength transmission range of 0.6 μm to 21 μm but are coated on each side with a broad band anti-reflection layer, which passes light with a wavelength of 10.6 μm. This filter allows the passing of infra red light, and improves the transmissivity of the beams from 80% to 99.2%.

The cartridges were designed with ease of access in mind and can therefore be removed easily to allow cleaning of the windows. Figures 3.11 (a) and (b) show the design of the two types of cartridges used. The sensor positioned at the outermost radius, $r/b = 0.935$, made use of a larger optical access hole in the casing, remaining from the previous test phase. The cartridge for this sensor can be seen in Figure 3.11 (a). The other sensors all used the same design of cartridge, shown in Figure 3.11 (b).

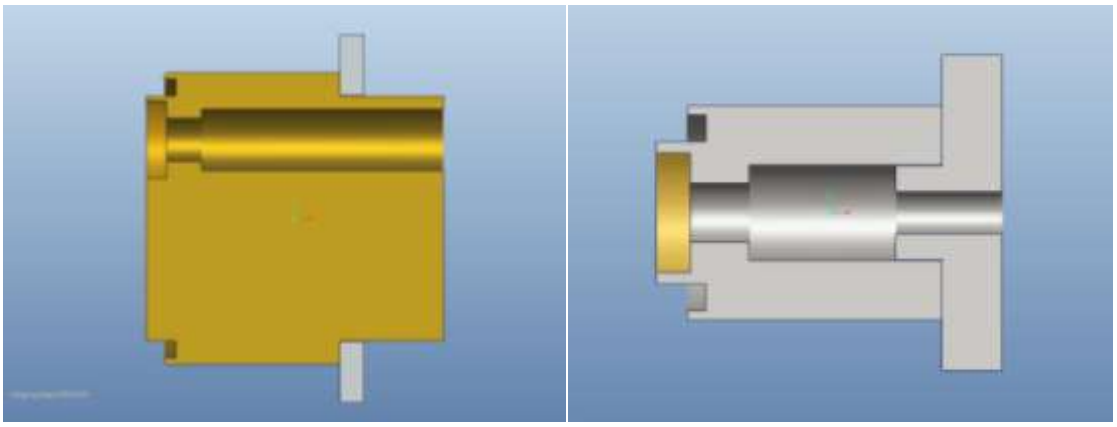

(a) **(b)**

Figure 3.11 - (a) Large infra red cartridge for the sensor at *r/b* = 0.935 (b) Cartridge design for the other sensors.

The infra red sensors were individually calibrated externally by Young Calibration Ltd. assuming an emissivity of 0.97. The data from the calibrations were plotted and a sixth order polynomial applied. Initially a third order polynomial was used, however, when analysing the uncertainty of the measurement, it was found that the application of a polynomial was the greatest contributor, by some margin. It was therefore decided to increase the order of the polynomial applied to the calibration data, thereby reducing the uncertainty. The resulting polynomials for each sensor, represented by its radial position on the rig, are shown in Equations 3.17 to 3.22, where T is the adjusted temperature, and V is the voltage output from the sensor.

***r* = 0.2 m (balance side):**

$$T = -122.05V^6 + 474.84V^5 - 680.74V^4 + 444.74V^3 - 135.71V^2 + 118.35V + 0.60 \quad \textbf{(3.17)}$$

***r* = 0.096 m:**

$$T = -201.60V^6 + 874.17V^5 - 1148.94V^4 + 1151.92V^3 - 451.93V^2 + 178.62V - 4.15 \quad \textbf{(3.18)}$$

***r* = 0.135 m:**

$$T = -101.83V^6 + 408.04V^5 - 609.34V^4 + 426.98V^3 - 149.11V^2 + 121.63V + 0.23 \quad \textbf{(3.19)}$$

***r* = 0.154 m:**

$$T = -88.68V^6 + 331.50V^5 - 442.70V^4 + 252.80V^3 - 57.78V^2 + 101.93V + 0.57 \quad \textbf{(3.20)}$$

***r* = 0.2 m:**

$$T = 55.77V^6 - 289.23V^5 + 559.15V^4 - 499.04V^3 + 206.21V^2 + 64.23V + 2.32 \qquad \textbf{(3.21)}$$

***r* = 0.210 m:**

$$T = 34.51V^6 - 196.69V^5 + 409.88V^4 - 389.61V^3 + 169.69V^2 + 67.17V + 2.76 \qquad \textbf{(3.22)}$$

3.6 Pressure Measurement

All pressure measurements made are gauge pressure, so a reading of the local atmospheric pressure was taken at the start of each test in order to calculate the absolute pressure. This was done using an ON S907 precision grade barometer that uses mercury as its working fluid. Measurements were taken of the mercury column height along with the ambient air temperature. The atmospheric air pressure was then found using the relationship shown in Equation 3.23, where ρ_{Hg} is the density of mercury, h_{Hg} is the mercury column height reading, and the value of gravity is taken to be g = 9.80665 m/s^2.

$$P_{atm} = \rho_{Hg} g h_{Hg} \qquad \textbf{(3.23)}$$

The value of mercury density was corrected for local temperature using the relationship shown in Equation 3.24, sourced from **Coren (2007)**, where T is the local ambient temperature in K.

$$\rho_{Hg} = -2.4T + 14250 \qquad \textbf{(3.24)}$$

3.6.1 Rosemount pressure transmitters

In order to calculate accurate mass flows, differential pressure measurements were obtained at each orifice plate using Rosemount 1151 pressure transmitters. These have a 4 – 20 mA output signal and are connected to a National Instruments SCXI-1100 data acquisition module with high quality 250 Ω resistors across each connection. This allowed a voltage reading to be taken, which could then be converted to resistance

within LabVIEW. The Rosemount units used at the two inlet orifice plates have a specified range of 200 mbar. However, they were required to measure differential pressures of up to 350 mbar. It was made clear by the suppliers that the units were capable of handling this pressure, though they would need calibrating to this higher value. Young Calibration Ltd. were employed to carry out the calibration up to 370 mbar. The data from the calibrations were plotted and a polynomial fitted. The resulting equations were applied to the output signals in LabVIEW. These polynomials are shown in Equations 3.25 and 3.26, where Δp is the adjusted differential pressure and V is the output voltage from the pressure transmitters.

Test inlet: $\Delta p = 0.008V^2 + 92.45V - 92.46$ ***(3.25)***

Balance inlet: $\Delta p = -0.001V^2 + 92.50V - 92.51$ ***(3.26)***

The two units at the outlet orifice plates have a range of 1865 mbar, which is sufficient for their intended use and so the supplied calibration data was used, following verification of the accuracy of the data using a dead weight tester. The calibration data was plotted and a polynomial fitted. The resulting equations were again applied to the signals in LabVIEW. These are shown in Equations 3.27 and 3.28.

Test outlet: $\Delta p = -0.017V^2 + 466.52V - 466.91$ ***(3.27)***

Balance outlet: $\Delta p = 0.008V^2 + 466.38V - 466.68$ ***(3.28)***

3.6.2 Scanivalve digital pressure transducer

Pressure measurements were obtained at a variety of positions on the test rig. Throughout the casing itself the pressure tappings are positioned on the test side at radii of r = 0.076 m, 0.1 m, 0.125 m, 0.148m, 0.168m, 0.210m and 0.232m (the pressure tapping at r = 0.232 is measuring the pressure in the plenum chamber) and again at r = 0.076 m, 0.1 m, 0.125 m and 0.148 m in the opposing half of the casing, as shown below in Figure 3.12.

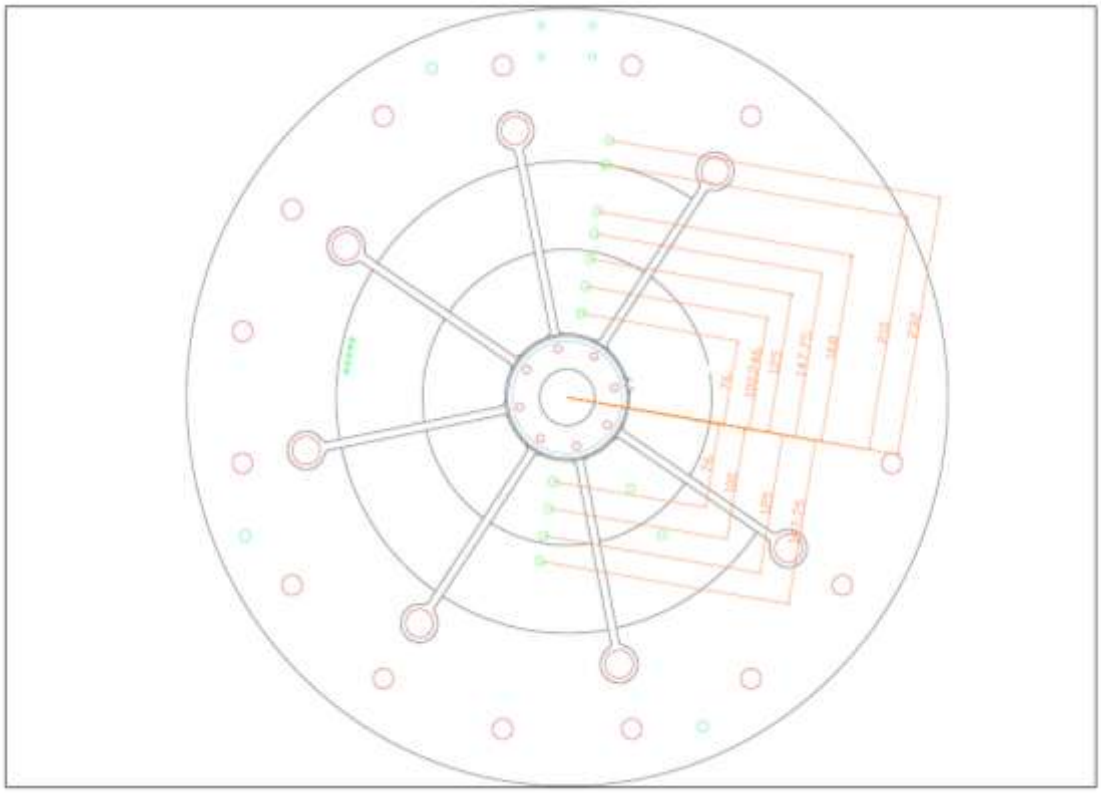

Figure 3.12 – Diagram showing pressure tap locations on test side of the casing (dimensions in mm).

On the balance side there are just two pressure taps situated at radii r = 0.076 m and r = 0.148 m. There is also a pressure tapping at the air inlet on the test side of the casing and one upstream of each orifice plate. The pressure is transmitted to a Scanivalve digital pressure transducer, a DSA3217 digital sensor array, by way of 1.59 mm outside diameter tubulations. There are two of these Scanivalve units: one sixteen channel module (DSA 5174) and one eight channel module (DSA 5176), both of which have a range of 6.89 bar. Each channel has its own temperature compensated piezoresistive pressure sensor. The unit contains a 16 bit A/D converter as well as a microprocessor, and it communicates data to LabVIEW via Ethernet connection. The sixteen channel unit acquires data from the main casing pressure taps (fourteen of them in total) and the eight channel unit acquires the four upstream orifice plate pressures. The eight channel unit also obtains a pressure reading from the main Atlas Copco compressor supply air. This ensures the maximum pressure (7.5 bar) is not reached whilst making flow adjustments to the rig during a test.

The Scanivalve units were acquired brand new and as such came equipped with a full set of calibration data for each individual channel. Before applying this calibration data, a selection of points were checked using a dead weight tester. The calibration data for each channel was plotted. A second order polynomial was fitted to each set of data to acquire an expression that was applied to each signal. The equations were of the form shown in Equation 3.29, where P_{adj} is the adjusted pressure and P_m is the measured pressure.

$$P_{adj} = AP_m^2 + P_m + B \qquad \textbf{(3.29)}$$

Table 3.1 shows the coefficients A and B for each channel of the sixteen channel unit (DSA 5174), of which the first 14 are used, and Table 3.2 shows the coefficients for each channel of the eight channel unit (DSA 5176), of which the first 5 are used. Appendix A shows the position on the rig that each channel measures.

Channel Number	A	B
1	3×10^{-5}	9×10^{-5}
2	2×10^{-5}	2×10^{-4}
3	5×10^{-5}	-6×10^{-7}
4	2×10^{-5}	9×10^{-5}
5	4×10^{-5}	1×10^{-4}
6	2×10^{-5}	4×10^{-4}
7	3×10^{-5}	-2×10^{-4}
8	2×10^{-5}	2×10^{-4}
9	3×10^{-5}	4×10^{-5}
10	4×10^{-5}	-9×10^{-5}
11	1×10^{-5}	8×10^{-5}
12	3×10^{-5}	-1×10^{-4}
13	2×10^{-5}	8×10^{-5}
14	2×10^{-5}	-2×10^{-4}
15	1×10^{-5}	5×10^{-5}
16	3×10^{-5}	2×10^{-4}

Table 3.1 – Table showing coefficients of calibration equations for each channel of DSA 5174

Channel Number	A	B
1	-2×10^{-10}	-35.18
2	3×10^{-10}	19.84
3	-4×10^{-11}	-48.66
4	1×10^{-10}	-17.86
5	1×10^{-10}	9.45
6	5×10^{-11}	-18.98
7	2×10^{-10}	0.09
8	3×10^{-10}	8.51

Table 3.2 - Table showing coefficients of calibration equations for each channel of DSA 5176

3.7 Data Acquisition

The majority of the measurements were obtained through National Instruments hardware and were manipulated using National Instruments' graphical programming software, LabVIEW. The hardware consists of two types of modular data acquisition systems. Firstly there is an SCXI-1001 data acquisition chassis that houses both an SCXI-1100 and SCXI-1121 module. The SCXI-1121 module has four channels that can read signals from two, three or four wire PRTs. It applies an excitation current of 0.45 mA to each channel and measures the resulting voltage signal. The SCXI-1100 has 32 input channels able to read a voltage signal of up to ±10 V. The SCXI-1001 chassis transfers the data to a PCI-6034E data acquisition card installed in the computer, where the data is displayed and logged using LabVIEW.

The second type of modular data acquisition system is the CompactDAQ (c-DAQ) data acquisition chassis that houses three N-9211 modules and one N-9205 module. The N-9211 modules are specifically designed to read thermocouple signals. There are four thermocouple channels and an internal cold junction compensation channel in each module. The voltage measurement range is ±80 mV and they have a 24 bit resolution. The N-9205 module has 16 differential input channels, with a programmable input range of ±200 mV to ±10 V, and a 16 bit resolution. The c-DAQ uses a USB

connection to transfer the signals directly to the computer where they are displayed and logged using LabVEW.

The only measurements not acquired using the National Instruments hardware are the casing and orifice plate pressure measurements. These are acquired using digital scanivalve units (as described in Section 3.6.2). These relay their signal directly to the computer via Ethernet connection. The data is then also displayed and logged using LabVIEW.

Figure 3.13 shows the flow of data for all measurements from the instrumentation through to their display in LabVEW. Figure 3.14 shows the front screen in LabVEW which is used to show the relevant information during testing.

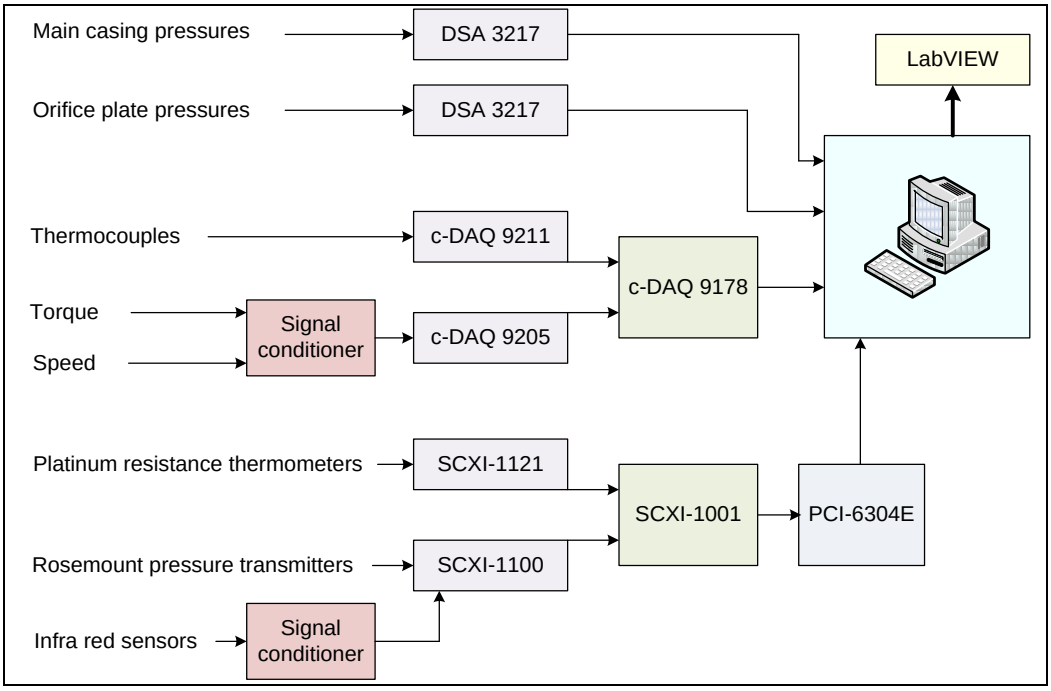

Figure 3.13 – Diagram showing flow of information from measurement devices to data acquisition program.

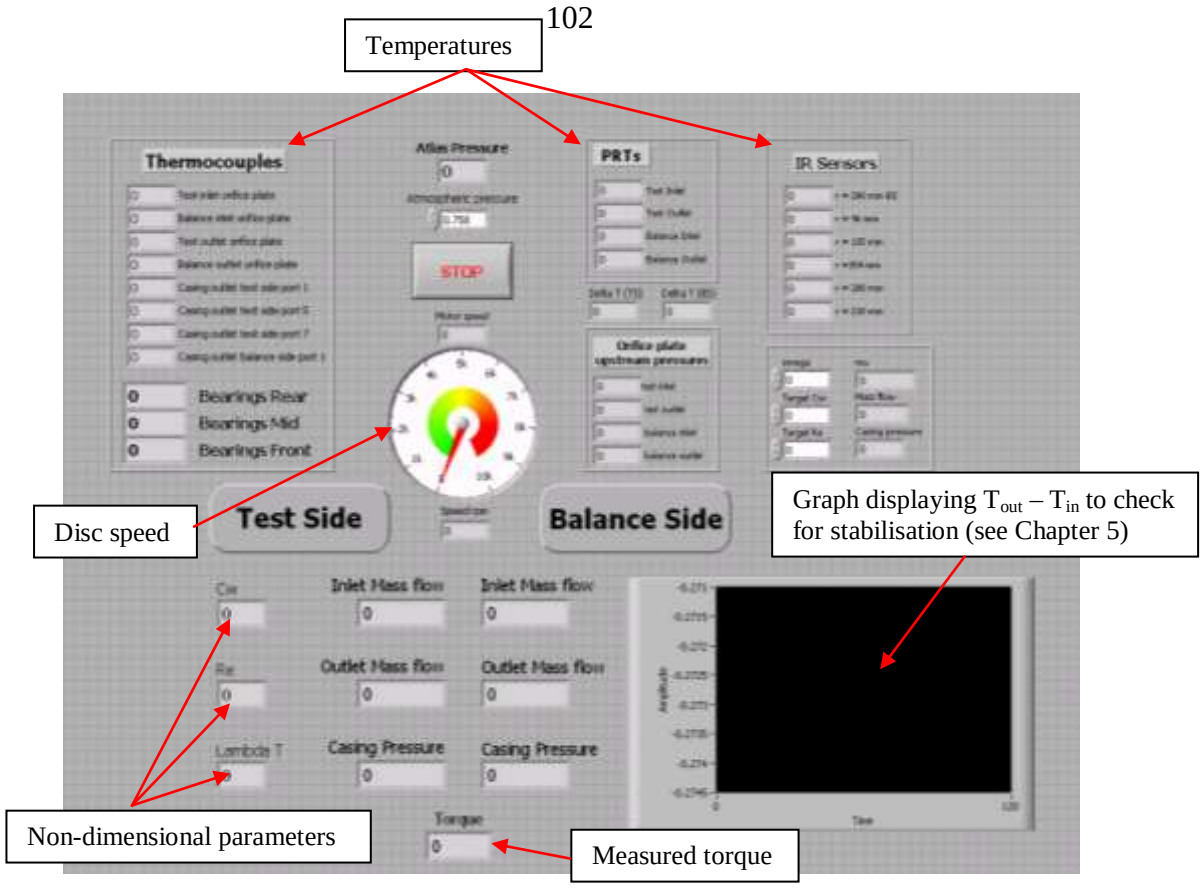

Figure 3.14 - Screen shot of LabVIEW front screen used to display test measurements.

3.8 Particle Image Velocimetry (PIV)

Particle Image Velocimetry (PIV) was used to measure the tangential velocity of the air flow within the test rig. PIV is a measurement technique for obtaining instantaneous velocities for a whole flow field. The principle is to measure the distance travelled by particles added to the flow, known as seeding, in a given time interval. These parameters are then used to calculate the velocity of the particles and hence the air flow. In order to detect the movement of the particles in the flow, a light sheet is generated by a laser. The light-sheet is not continuous but pulsed to produce a stroboscopic effect which essentially freezes the position of the seeding particles. To detect the position of the seeding particles a charged coupled device (CCD) camera is positioned perpendicular to the light-sheet. The camera is synchronised to the pulsing of the laser. Seeding particle positions appear as light specks on a dark background on each frame captured. The distance travelled by the particles between two frames is analysed and since the time between pulses is a specified quantity, the velocity of each particle can be calculated. From these calculations a vector map can be produced for the entire field of

view of the camera. In order to be able to measure the actual distances travelled it is necessary to know the scaling factor between the image and the object(s) of interest.

To calculate the scale factor a ruler, or an object of known length, would usually be placed in the path of the light sheet and from the resulting image the relationship between the specified distance (i.e. 1 mm on the ruler) and number of pixels can be calculated. Since placing a ruler within the rotor-stator cavity at the correct position would not be possible, a range of images were taken of a ruler at distances between 230 mm and 350 mm away from the camera. This distance is measured from the object to the position in the camera where the CCD device operates (represented with a green line on the side of the camera). From the resulting scale factors from each image it was possible to create a relationship between scale factor and distance. This relationship is shown in Equation 3.30 where x is the distance between the camera and the light sheet, and S is the resulting scale factor. Once the camera and laser were located in their required positions, the distance from the camera to the light sheet was measured to be 345 mm. Using Equation 3.30 the scale factor was then calculated to be 3.67.

$$S = -6.68\times10^{-5}x^2 + 5.80\times10^{-2}x - 8.39 \qquad \textbf{(3.30)}$$

The laser used is a Solo PIV 120 mJ, supplied by Dantec Dynamics. The laser is fixed to a 3-axis traverse system to enable positioning of the laser to 0.1 mm in any direction. An endoscope is attached to the laser and passed through a hole in the inlet pipework at the centre of the casing, as shown in Figure 3.15.

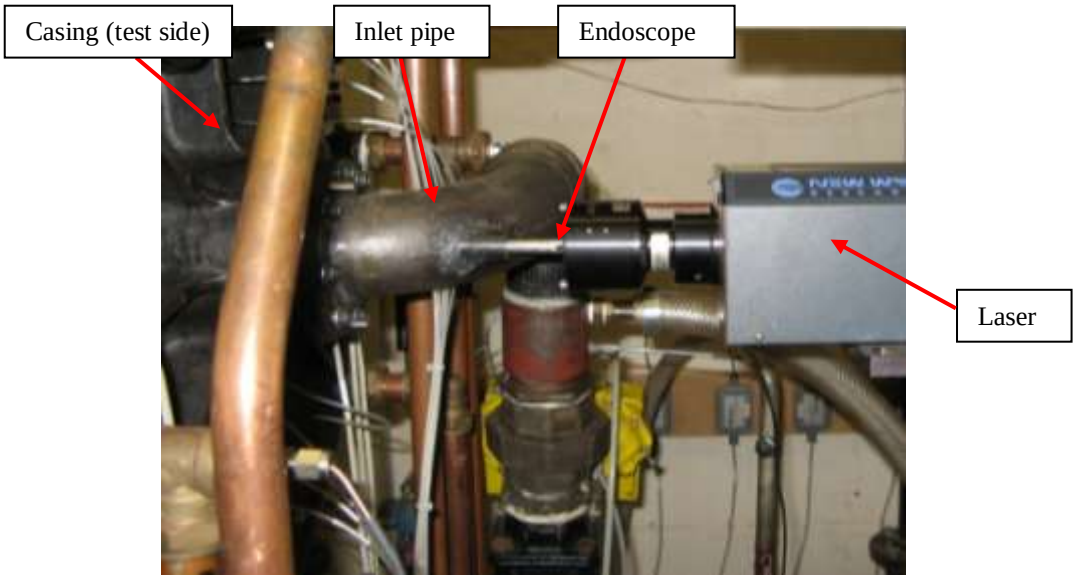

Figure 3.15 – Picture showing laser endoscope in position

The light sheet is emitted perpendicular to the endoscope and diverges, giving a larger lit area further away from the source. The light sheet travels radially outward through the cavity, parallel to the rotor and stator surfaces, as shown in Figure 3.16.

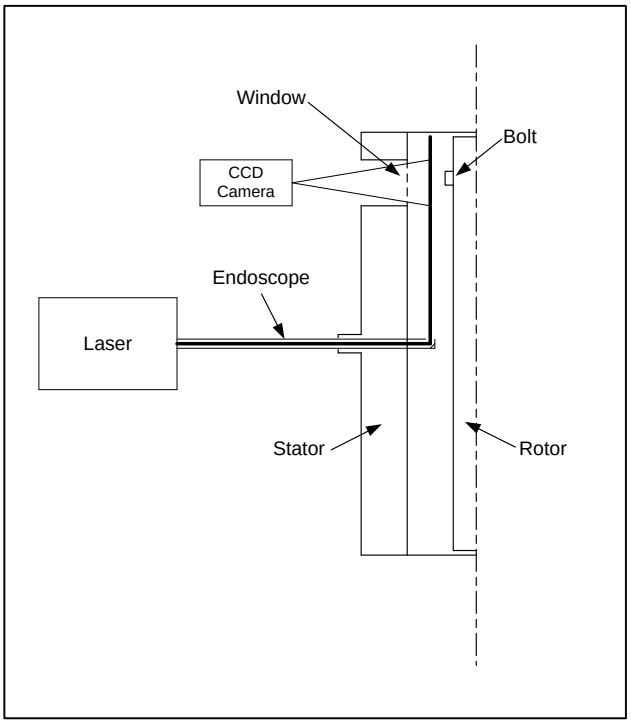

Figure 3.16 – Diagram showing light sheet in rotor-stator cavity.

Seeding is introduced into the cavity using an air pressurised jet atomiser seen in Figure 3.17 (a). This feeds very fine olive oil particles, of the order of 1 μm, into the airflow slightly upstream of the inlet to the rotor-stator cavity, as shown in Figure 3.17 (b).

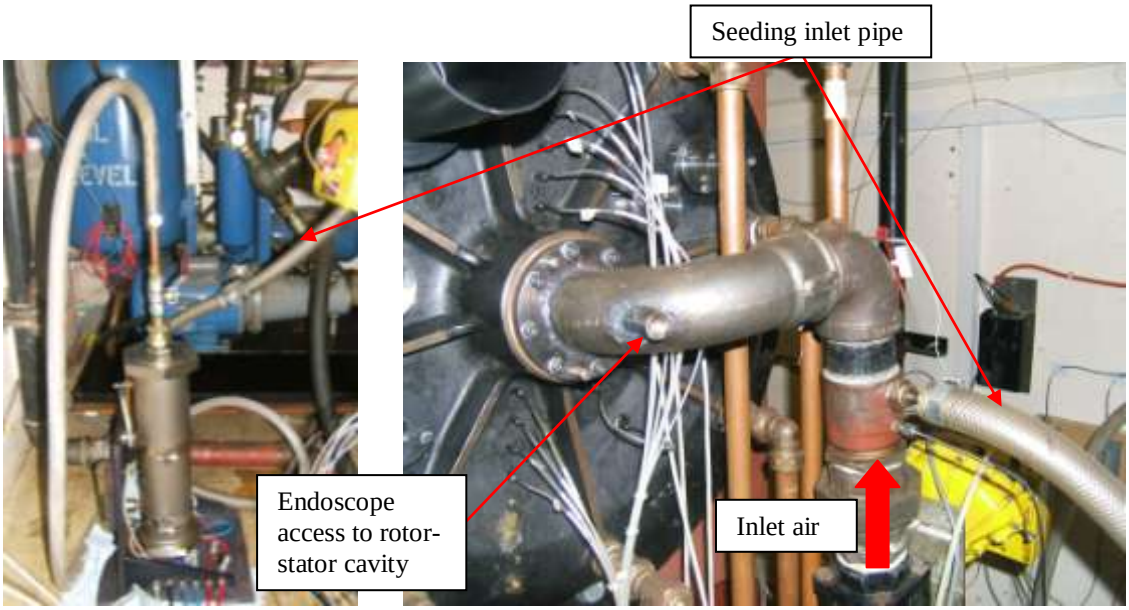

Figure 3.17 – Pictures showing (a) Air pressurised jet atomiser, (b) Seeding inlet.

A FlowSense 2 mega pixel CCD camera was used with a 60 mm telephoto lens. The aperture size and focal length were chosen to give a very narrow depth of field to ensure the camera is focused solely on the laser light sheet, avoiding interference from the rotating disc. A stand was made to attach the camera to the traverse alongside the laser so as to avoid any vibrations from the rig during testing. This can be seen in Figure 3.18. It also allowed the light sheet and the camera to move synchronously, avoiding unnecessary re-focusing of the camera when the light sheet was moved to a different axial position within the cavity. The camera stand was made so that the horizontal plane of the camera's field of view exactly matched the tangential direction of the rotor at the centre of the optical access window. The stand is adjustable in the horizontal and vertical direction to aide correct positioning of the camera.

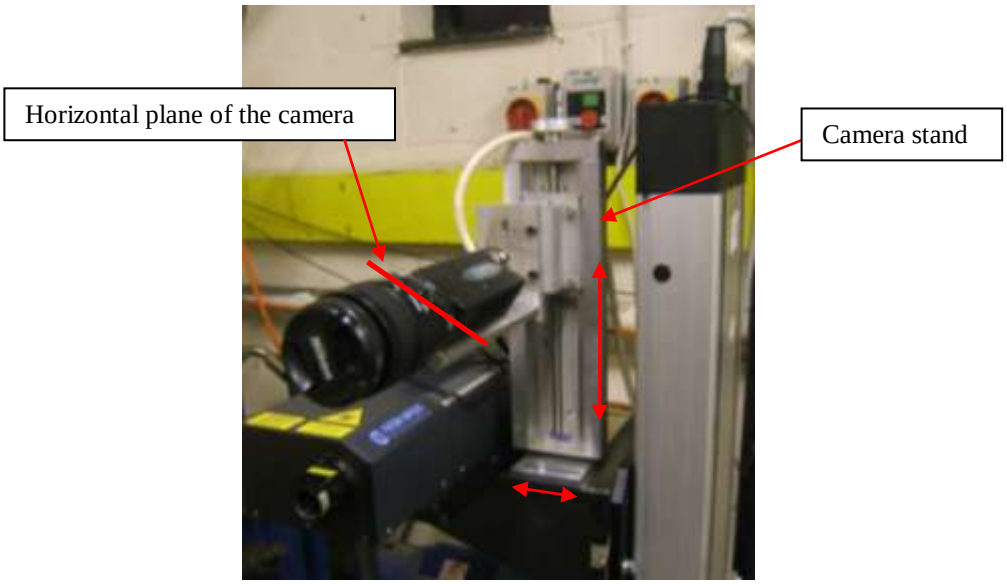

Figure 3.18 – Picture showing the camera stand

The window that is currently used for the outermost infra red sensor was utilised to allow optical access to the cavity. A new cartridge, shown in Figure 3.19 (a), was designed to allow the camera to photograph as large an area as possible. A tube was attached to the window cartridge, covering the gap between the cartridge and the end of the camera in order to protect the images from light pollution, which could lead to poor image quality. This can be seen in Figure 3.19 (b).

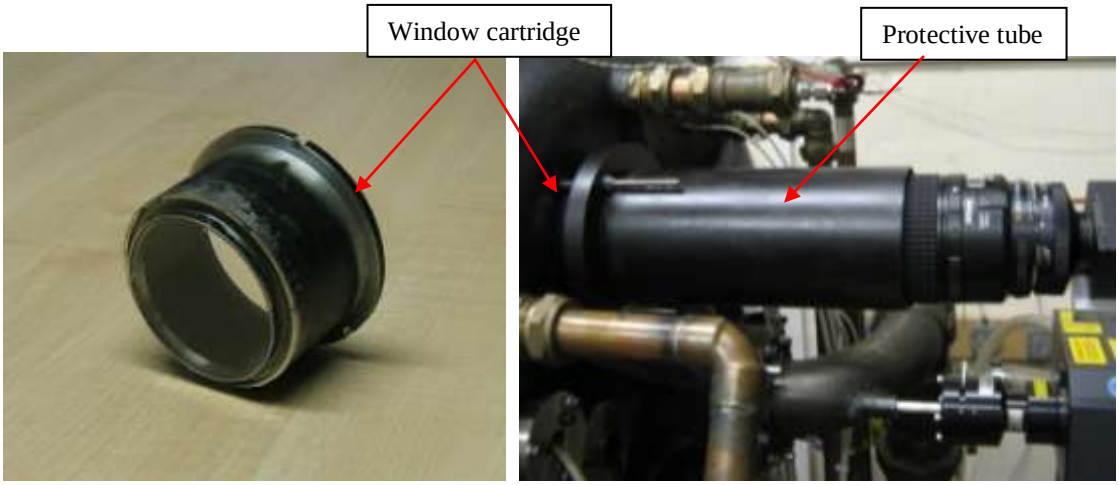

(a) **(b)**

Figure 3.19 – Pictures showing (a) New window cartridge. (b) Protective tube

A datum for the laser traverse had to be established, representing the point where the tip of the laser endoscope is just brushing the surface of the disc at the centre. To achieve this, the rig casing was opened and the laser was moved carefully into position. The

program used to control the traverse was then reset so this point represented 0,0,0, thus providing a datum for all tests.

It was then necessary to align the endoscope very carefully with the axis of the driveshaft. If the endoscope and driveshaft are out of alignment this would affect the positioning of the light sheet, relative to the required measurement plane. In order to check the alignment of the endoscope a piece of black card was held against, and perpendicular to, the disc so that the edge of the light sheet was visible. This is shown in Figure 9.4 (a). Figure 9.4 (b) illustrates the two ways that the endoscope could be misaligned. If the endoscope were misaligned in the horizontal plane, the edge of the light sheet would look like either of the red broken lines on the black card in Figure 9.4 (b). If the endoscope were misaligned in the vertical plane, the edge of the light sheet would look like either of the blue lines.

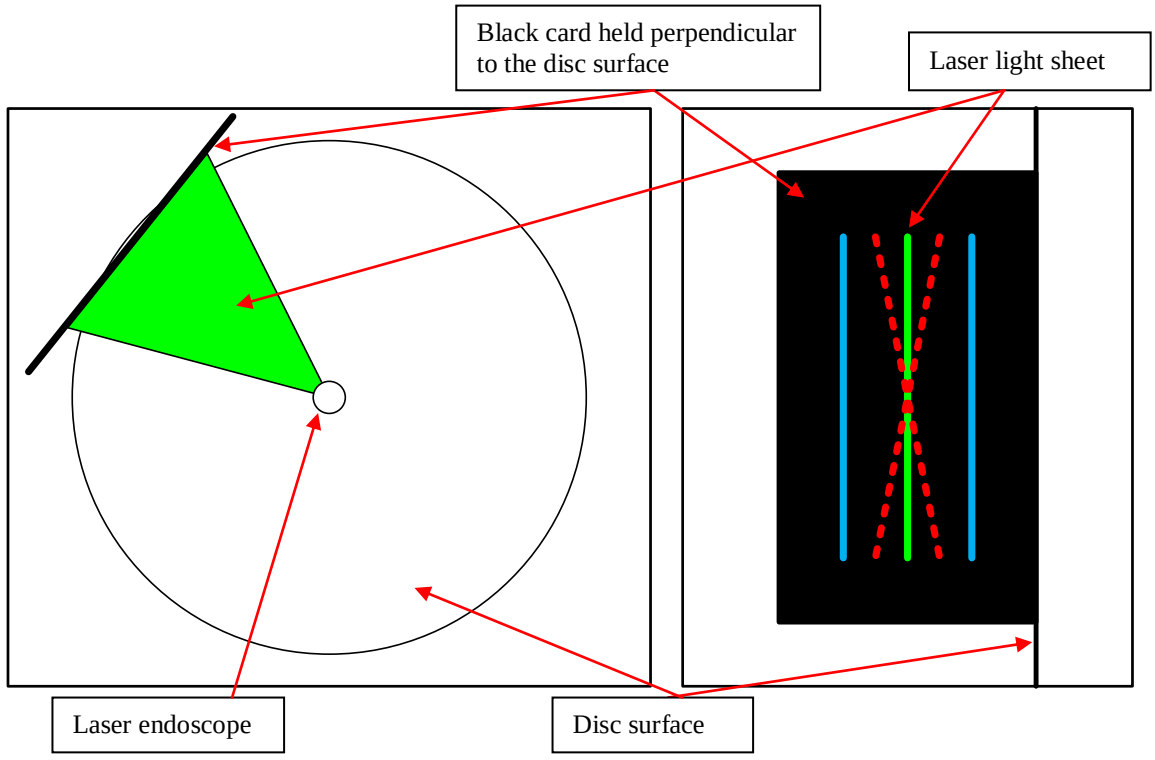

Figure 3.20 – (a) Diagram showing positioning of card for alignment checks. (b) Diagram showing the two type of misalignment of the laser sheet, horizontal (red broken lines) and with driveshaft axis (blue lines).

The light sheet emerges 3 mm from the tip of the endoscope. With the tapering of the disc (see Section 3.4) this means that, when the endoscope is in the datum position 0,0,0, the light sheet will be 8.5 mm away from the disc surface at the radius of the bolt, r = 0.2 m. In order to check the alignment in the vertical plane, the piece of card was held perpendicular to the disc surface at the bolt radius and the distance between the laser sheet and the disc surface was measured to ensure it was 8.5 mm. To check the alignment in the horizontal plane, a plumb bob was used to ensure the edge of the light sheet, as viewed on the card, was vertical.

Once the laser endoscope was in the correct position it was necessary to ensure that it could be freely inserted and withdrawn from the cavity during a series of subsequent measurement cycles. The existing point of entry was much larger than the diameter of the endoscope, which would create problems sealing the cavity so a cap was made. To allow the endoscope to enter freely and without interference, the cap had a slightly larger diameter hole than the endoscope shaft and was placed over the endoscope before insertion into the cavity. Once the endoscope was in place, the cap could then be screwed into the existing hole in the inlet pipe. An o ring, also placed around the endoscope shaft before insertion, was pressed up against the cap to seal the gap. Since the pressures within the cavity for the PIV tests were very low (up to a maximum of p = 1.27 bar), this provided adequate sealing.

For the tests with bolts it was necessary to set up a trigger on the drive shaft so that the camera and laser could be synchronised to a specified position on the disc. This meant that the bolt would be in the same positions for each pair of images. An encoder was positioned adjacent to a suitable section of the driveshaft, as shown in Figure 3.21. The encoder is an HOA709 reflective sensor, which uses and infra red emitting diode alongside a phototransistor. The phototransistor responds to the infra red radiation only when a reflective object passes. A matt black marker was placed on the driveshaft flange as a pick up, as seen in Figure 3.21, and the signal from the encoder was used to trigger the laser and camera. Once the trigger had been set up, the resulting images were inspected and a time offset was applied, within the PIV software. This delayed the triggering of the laser and camera, so that the bolt was in a suitable position in the image.

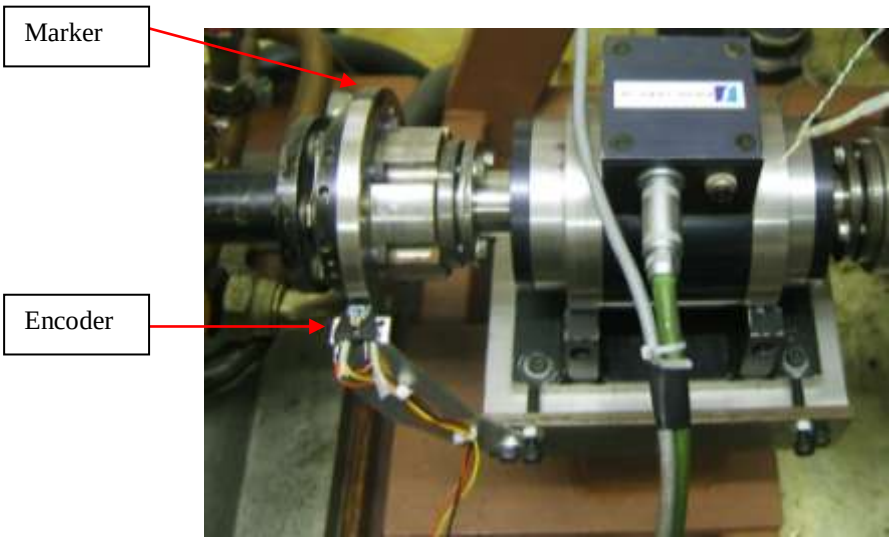

Figure 3.21 – Picture showing encoder for laser and camera triggering

Chapter 4. Method of Results Analysis and Uncertainty Analysis

4.1 Introduction

This chapter explains the methods used in analysing the experimental data. Section 4.2 includes a description of the main governing flow parameters used, followed by details of the torque, mass flow and infra red temperature measurements and how the data is manipulated for ease of further analysis. The analysis methods described within this chapter are common to all test results. For the particular case where Particle Image Velocimetry measurements are obtained, the analysis method is described in Chapter 9. Section 4.3 goes on to describe the uncertainty calculations for both individual measurements and for the relevant combined parameters. Examples are presented for each individual and combined parameter, at typical test conditions.

4.2 Procedure for Results Analysis

4.2.1 Governing flow parameters

Rotating flows in rotor-stator cavities are generally characterised by two main non-dimensional parameters: the rotational Reynolds number, Re_ϕ and the throughflow Reynolds number, C_w. The rotational Reynolds number is defined in Equation 4.1, where ρ is the density of the fluid (calculated using the average maximum radius pressure and exhaust temperature), ω is the rotational speed of the rotor, b is the outer radius of the rotor and μ is the dynamic viscosity of the fluid (calculated using average exhaust temperature).

$$\mathrm{Re}_\phi = \frac{\rho \omega b^2}{\mu} \qquad \textbf{(4.1)}$$

As discussed in Chapter 2, rotation of the disc will induce a radial outflow of fluid within the boundary layer, this necessarily has to be replaced and this process is referred to as entrainment. The governing non-dimensional parameter for radial flow, whether the flow is induced by the rotation only or purposely superimposed into the cavity, is the throughflow Reynolds number, defined in Equation 4.2, where $\dot{m}$ is the mass flow of fluid.

$$C_w = \frac{\dot{m}}{\mu b} \tag{4.2}$$

Also noted in Chapter 2 was von Kármán's expression for the flow entrained by a free disc in turbulent flow (Equation 2.8) $C_{w,ent} = 0.219\mathrm{Re}_\phi^{0.8}$. **Owen and Rogers (1989)** used this expression to develop the turbulent flow parameter, defined in Equation 4.3, to describe the flow within a rotor stator cavity.

$$\lambda_T = \frac{C_w}{\mathrm{Re}_\phi^{0.8}} \tag{4.3}$$

For $\lambda_T < 0.219$ the flow is said to be rotationally dominant and for $\lambda_T > 0.219$ the flow is said to be radially dominant.

It is these three non-dimensional parameters; C_w, Re_ϕ and λ_T that were referenced when deciding on the conditions to be tested (see **Coren (2007)** for details of how test conditions were decided upon), as well as, where necessary, to match current conditions to the tests carried out previously by Coren.

4.2.2 Torque Measurements

Shaft torque measurements are gathered during every test using an inline torquemeter, described in Section 3.3.3, which measures the windage within the rotor-stator cavity. For tests where protrusions are present, the measured windage will necessarily include the contributions from viscous friction, form drag and pumping losses. Where there are no protrusions present, the windage is simply due to the viscous friction resulting from the surfaces within the cavity.

This measured torque, M (which is the torque present on both sides of the rotor), is used in Equation 4.4 to calculate the moment coefficient, C_m. The moment coefficient is the parameter used to compare the windage for different test conditions.

$$C_m = \frac{M}{\frac{1}{2}\rho\omega^2 b^5} \qquad \textbf{(4.4)}$$

As well as the direct torque measurements, as a matter of course the rate of enthalpy difference in the rotor-stator system was also calculated using the relationship shown in Equation 4.5.

$$\Delta H = \dot{m}(C_{p,out}T_{0,out} - C_{p,in}T_{0,in}) \qquad \textbf{(4.5)}$$

In this relationship ΔH is the rate of change of enthalpy within the system. The specific heat at constant pressure, and the total temperature at the casing inlet are $C_{p,in}$ and $T_{0,in}$ respectively. The specific heat at constant pressure, and the total temperature at the casing outlet are $C_{p,out}$ and $T_{0,out}$, and $\dot{m}$ is the mass flow of throughflow air. The rate of change of enthalpy is calculated for the cavities on both sides of the disc and the two added together. The rate of change of enthalpy is a measure of the work done by the system on the fluid, therefore dividing through by the rotational speed of the rotor gives the frictional torque resulting from windage.

Due to the lack of insulation around the casing, as well as influences from the main bearings, which sit very close to the balance side cavity, there are larger uncertainties associated with the enthalpy method of calculating torque. Consequently, all the torque results included in this thesis are from the torquemeter only. The enthalpy change calculations allow a secondary measurement of the torque in order to corroborate the measurement from the torquemeter.

Another parameter, that was introduced in Chapter 2 as von Kármán's expression for the moment coefficient for a free disc with turbulent flow (Equation 2.5) $C_m = 0.146\ \mathrm{Re}_\phi^{-0.2}$, is used in the results analysis. This parameter was used in the form $C_m\mathrm{Re}_\phi^{0.2}$ for analysis, which for a free disc in turbulent flow is constant, at a value of 0.146. Using

the parameter $C_m \mathrm{Re}_\phi^{0.2}$ allows the increased windage over and above that of the free disc to be readily observed.

4.2.3 Mass Flow Rate Measurements

The mass flow rate is measured using an orifice plate which is designed in accordance with the guidelines in the **British Standards Institution** document, Measurement of Flow in Closed Conduits BS 1042 (1992). Figure 4.1 shows the D/2 type orifice plates used, which are designed to comply with the same standard.

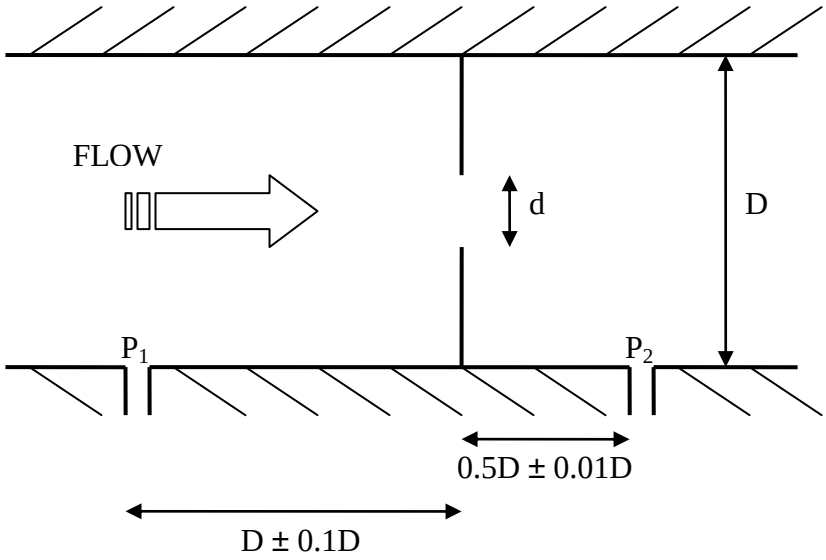

Figure 4.1 – Diagram showing D/2 type orifice plates used for mass flow calculations

The mass flow calculation, obtained from Equation 4.6, is done so by iteration since the discharge coefficient, *C*, and the expansibility factor, ε, are initially unknown quantities. The starting values for these quantities, used in the iteration, are 0.607 and 0.995 respectively. A form of this equation is found in the **International Organisation for Standardisation** document ISO 5167 (2003).

$$\dot{m} = C\varepsilon \frac{\pi d^2}{4}\left(1-\left(\frac{d}{D}\right)^4\right)^{-0.5}\left(2(p_1 - p_2)\left(\frac{p_1}{RT}\right)\right)^{0.5} \qquad \textbf{(4.6)}$$

In this equation, d is the orifice plate throat diameter and D is the inside pipe diameter. The orifice plates used for the current test rig have measurements of d = 0.035 m and D = 0.05 m. In Equation 4.6, p_1 is the upstream pressure, p_2 is the downstream pressure, T is the downstream temperature and R was calculated from Equation 4.7, and is found to be 287.01 J/kgK for air.

$$R = \frac{\Re}{m_{m_{Air}}} \qquad \textbf{(4.7)}$$

$\Re$ is the universal gas constant, which is quoted by the National Institute of Standards and Technology to be 8314.471 J/molK. The molar mass of air, m_{mAir}, is calculated from the molar masses for the three major components of air, taken as quoted by **Rogers and Mayhew (1995)**: Nitrogen = 28.013 kg/kmol, Oxygen = 31.999 kg/kmol and Argon = 39.948 kg/kmol. It is assumed (again as quoted by **Rogers and Mayhew (1995)**) that the composition of air, by volume, is N_2 = 78%, O_2 = 21% and Ar = 1%. So the molar mass of each component is multiplied by the relevant fraction to give m_{mAir} = 28.969 kg/kmol.

4.2.4 Infra Red Temperature Measurements

Disc temperature measurements are taken at five radial locations on the test side of the disc at radii of: 0.096 m, 0.135 m, 0.154 m, 0.2 m and 0.2105 m, these correspond to: r/b = 0.427, 0.6, 0.684, 0.887 and 0.935. A measurement is also taken at a single location on the balance side at r = 0.2 m (r/b = 0.887) to verify that the conditions are balanced on both sides of the disc. For further information on the layout of the instrumentation and definition of ‘test’ and ‘balance’ side the reader is referred to Section 3.4.

During analysis of the infra red data the preferred quantity used is the differential temperature between the disc and the inlet air, since there are variations in inlet air temperature from one test to another. Some of the data in this thesis is therefore presented in terms of T-T_{in}. However, in order to make effective comparison between different test conditions it is necessary to refer to the average disc temperature. This is an area average calculated using Equation 4.8.

$$T_{av} = \frac{1}{A}\int_{r=r_1}^{r=r_5} T\,2\pi r\,dr \qquad \textbf{(4.8)}$$

In this equation r_1 and r_5 are respectively the inner and outer radial locations of the innermost and outermost infra red sensors, giving r_1 = 0.096 m and r_5 = 0.2105 m. The temperature, T, is the differential temperature (T-T_{in}) of the disc relative to the inlet air at each location, and r is the radial location. The integral in Equation 4.8 is approximated using Simpson's rule, shown in Equation 4.9, where n is the number of segments over which the integration occurs.

$$\int_{r_1}^{r_5} f(x)dx \approx \frac{(r_5 - r_1)}{3n}\left[f(x_0) + 4f(x_1) + 2f(x_2) + 4f(x_3) + ... + f(x_n)\right] \qquad \textbf{(4.9)}$$

The infrared sensors are not evenly spaced over the radius of the disc, consequently a second order polynomial was fitted to the data taken from the five sensors on the test side of the rig, and the disc temperature obtained at five equidistant points ranging from between radii r_1 = 0.096 m to r_5 = 0.2105 m. These five equidistant disc temperatures were then used in Equation 4.9 to find the area average disc temperature.

4.3 Uncertainty Analysis

This section introduces the method used to calculate the uncertainties for each individual measurement, as well as for the combined parameters described in Section 4.2.

It is necessary when specifying the result of a measurement to also make a statement of the associated uncertainty within that measurement to a specified level of confidence. The uncertainties in a measurement can be divided into two categories; Type A and Type B. Type A are those that can be evaluated by statistical methods, Type B are those that are evaluated by other means. In this thesis Type A uncertainties will be referred to as precision uncertainties, and Type B as bias uncertainties.

All the results shown throughout this thesis are an average of 121 readings, so the precision uncertainty of each measurement is calculated using Equation 4.10.

$$w_{pr} = \frac{s}{\sqrt{121}} \qquad \textbf{(4.10)}$$

In this equation w_{pr} is the precision uncertainty of the measurement and s is the sample standard deviation of the 121 readings.

The bias uncertainties for the instrumentation are obtained from the manufacturer's technical specification for each individual piece of equipment. Each uncertainty value acquired must be divided by a number associated with its assumed probability distribution. Unless otherwise stated these bias uncertainties are assumed to have a normal distribution and therefore have a divisor of 1. The SCXI-1100, SCXI-1121, cDAQ - 9211 and the cDAQ - 9205 data acquisition systems were checked for an offset, as well as for drift over the course of six months. Drift in all cases was negligible and any offsets found were accounted for in the results. As a result these contributions to the bias uncertainty were ignored for the purposes of the uncertainty calculations in this thesis.

The total uncertainty for a single measurement is obtained by taking the square root of the sum of the squares (RSS) of each individual, independent source of uncertainty.

When specifying the uncertainty in a measurement it is usual to express the expanded uncertainty, which includes a specified level of confidence. In this thesis a coverage factor of 1.98 is applied to the total uncertainty of each parameter to give a confidence level of 95%. This multiplier is applied only to the total uncertainty. It has been assumed for the purpose of these calculations that the bias uncertainties obtained from manufacturer's specifications do not already include a coverage factor. Therefore any precision or bias uncertainties quoted in this chapter have not had any coverage factor applied.

To calculate the uncertainties in the combined parameters, which in this thesis are all functions of independent parameters, the Taylor series uncertainty propagation analysis,

shown in Equation 4.11, is used. This equation in specified in the **International Organisation for Standardisation** document, Guide to the expression of uncertainty in measurement.

$$w_F = \sqrt{\left(\frac{\partial F}{\partial x_1} w_1\right)^2 + \left(\frac{\partial F}{\partial x_2} w_2\right)^2 + ... + \left(\frac{\partial F}{\partial x_n} w_n\right)^2} \qquad \textbf{(4.11)}$$

In this equation w_F is the absolute uncertainty in the combined parameter F, F is a function of the variables x_1, x_2, ..., x_n, and w_1, w_2, ..., w_n are the total uncertainties of each variable.

4.3.1 Uncertainties for individual measurements

For each individual parameter described in this section the uncertainties will be calculated using two example test cases representing different flow conditions. These conditions are shown in Table 4.1, where p is the casing pressure measured at r/b = 0.53, N is the rotational speed of the rotor and C_w, Re_ϕ and M are as described previously in this chapter.

Example 1 – Three bi-hexagonal bolts	**Example 2 – Eighteen 10 mm bolts**
$C_w = 0.3 \times 10^5$	$C_w = 10^5$
$Re_\phi = 0.272 \times 10^7$	$Re_\phi = 1.341 \times 10^7$
M = 2.32 N m	M = 27.1 N m
p = 2.02 bar (absolute)	p = 5.01 bar (absolute)
N = 3940 rev/min	N = 8793 rev/min

Table 4.1 – Test conditions for the two examples used for calculating uncertainty throughout section 4.3.

TORQUE

The torquemeter signal is acquired using a National Instruments c-DAQ 9205 data acquisition module. Since the measured value of M has to be corrected to account for the driveline friction (the reader is referred to Chapter 5 for details of the driveline friction measurement), the uncertainties of both the measurement of M, and the

measurement of the driveline friction have to be included. So the total torque, *M*, is as shown in Equation 4.12:

$$M = M_{measured} - M_{driveline} \qquad \textbf{(4.12)}$$

To calculate the uncertainty in *M*, the Taylor series uncertainty propagation analysis (Equation 4.11) must be used. The partial derivatives, of Equation 4.12, describing the sensitivity of each parameter are calculated as shown in Equations 4.13 and 4.14.

$$\frac{\partial M}{\partial M_{measured}} = 1 \qquad \textbf{(4.13)}$$

$$\frac{\partial M}{\partial M_{driveline}} = -1 \qquad \textbf{(4.14)}$$

So, the absolute uncertainty for the measurement *M* can be found using Equation 4.15.

$$w_M = \sqrt{\left(w_{M_{measured}}\right)^2 + \left(-w_{M_{driveline}}\right)^2} \qquad \textbf{(4.15)}$$

Firstly, w_M will be calculated using the values from the first example test case (shown in Table 4.1), where C_w = 0.3 x 10^5, p = 2.02 bar (absolute), N = 3940 rev/min and M = 2.32 N m.

The uncertainty due to the torquemeter for the driveline friction measurement is calculated using the root sum squared (RSS) method from the following components:

- The calibration uncertainty, based on a standard uncertainty (in accordance with ISO 17025).
- The uncertainty due to the application of a polynomial correlation to the torquemeter output signal.
- The long term stability effect on the zero value.
- The long term stability effect on the rated output (RO).
- The precision uncertainty of the measurement (calculated using Equation 4.10).

The values of these uncertainty components are shown in Table 4.2.

Calibration uncertainty (from calibration certificate)	±0.019 N m
Interpolation uncertainty from polynomial correlation	±0.01 N m
Long term stability on zero (< 0.05% of RO/year)	±0.01 N m
Long term stability on rated output (< 0.05% of RO/year)	±0.01 N m
Precision error of the measurements	±0.02 N m
Total (calculated using RSS method)	**±0.033 N m**

Table 4.2 – Uncertainty components due to the torquemeter, for the driveline friction measurements in example test case one.

The uncertainty in the data acquisition device, the c-DAQ 9205, also needs to be included. This was calculated using the RSS method from the following components, taken from the manufacturer's technical specification based on a ±2 V range:

- Absolute accuracy.
- Random noise.
- Zero order uncertainty, which is the half interval of the resolution of the device, this has a rectangular distribution therefore a divisor of √3 is applied.

The values of these uncertainty components are shown in Table 4.3.

Absolute accuracy:	±3230 μV
Random noise:	±116 μV
Zero order uncertainty:	±8.8 μV
Total (calculated using RSS method)	**±3232.2 μV**

Table 4.3 – Uncertainty due to c-DAQ 9205 for torque measurements

For the torque measurements 1 V = 40 N m, therefore ±3232.2 μV = ±0.129 N m. Incorporating the c-DAQ 9205 uncertainty with the torquemeter uncertainty, using the RSS method, gives a total uncertainty for the driveline friction measurement, $w_{driveline}$ = ±0.133 N m.

The uncertainty due to the torquemeter for the measured torque values is calculated from the same components as for the driveline friction measurements. The values of uncertainty are shown in Table 4.4:

Calibration uncertainty (from calibration certificate)	±0.019 N m
Interpolation uncertainty from polynomial correlation	±0.01 N m
Long term stability on zero (< 0.05% of RO/year)	±0.025 N m
Long term stability on rated output (< 0.05% of RO/year)	±0.025 N m
Precision error of the measurements	±0.015 N m
Total (calculated using RSS method)	**±0.044 N m**

Table 4.4 – Uncertainty components due to the torquemeter for the measured torque in example test case one.

Incorporating the uncertainty of the c-DAQ 9205, calculated as ±0.129 N m, the total uncertainty for the measured torque is $w_{measured}$ = ±0.137 N m.

Using Equation 4.15 this gives a total uncertainty in the corrected torque measurement, M, of w_M = ±0.19 N m. A coverage factor of 1.98 is applied to give a 95% confidence interval, giving an expanded uncertainty of ±0.378 N m (95%). This is 16.3% of the total measured torque (M = 2.32 N m) in this example.

Now w_M is calculated for the second example test case (as shown in Table 4.1), where $C_w = 10^5$, p = 5.01 bar, N = 8793 rev/min and M = 27.1 N m.

The uncertainty due to the torquemeter for the driveline friction measurements is calculated from the components shown below in Table 4.5:

Calibration uncertainty (from calibration certificate)	±0.019 N m
Interpolation uncertainty from polynomial correlation	±0.01 N m
Long term stability on zero (< 0.05% of RO/year)	±0.01 N m
Long term stability on rated output (< 0.05% of RO/year)	±0.01 N m
Precision error of the measurements	±0.04 N m
Total (calculated using RSS method)	**±0.048 N m**

Table 4.5 – Uncertainty components due to torquemeter, for the driveline friction measurements in example test case two.

The inclusion of the instrumentation uncertainty for the c-DAQ 9205, calculated to be ±0.129 N m, gives a total uncertainty in the driveline torque measurements of $w_{driveline}$ = ±0.138 N m.

The uncertainty due to the torquemeter for the measured torque is calculated from the components in Table 4.6:

Calibration uncertainty (from calibration certificate)	±0.019 N m
Interpolation uncertainty from polynomial correlation	±0.01 N m
Long term stability on zero (< 0.05% of RO/year)	±0.025 N m
Long term stability on rated output (< 0.05% of RO/year)	±0.025 N m
Precision error of the measurements	±0.08 N m
Total (calculated using RSS method)	**±0.09 N m**

Table 4.6 – Uncertainty components due to torquemeter, for measured torque values in example test case two.

Including the instrumentation uncertainty of ±0.129 N m, this gives an uncertainty of $w_{measured}$ = ±0.158 N m. So using Equation 4.15, the total uncertainty for the corrected torque measurement is w_M = ±0.209 N m. Applying a coverage factor of 1.98 gives an expanded uncertainty, with a 95% confidence interval, of ±0.415 N m (95%). Given a measured value of M = 27.1 N m, this gives a relative uncertainty of just ±1.5%.

It can be seen from these two examples that although the absolute uncertainty increases for the test with higher measured torque values, the relative uncertainty reduces dramatically from 16% to just 1.5%.

For the original data acquisition system, used to collect data for the nine and eighteen stator bolts, the torquemeter signal was obtained via a Solartron Orion 3530 data logging system. The uncertainty due to the Orion data logger is made up of two components (taken from the manufacturer's specification at a measurement speed of 40 readings/s):

- Absolute accuracy, which is calculated as ±0.5% of the reading plus ±0.5% of the range.
- Zero order uncertainty, which is the half interval of the resolution of the device and has a rectangular distribution therefore a divisor of $\sqrt{3}$.

The components of uncertainty and their values are shown in Table 4.7 for a nine bolt test where C_w = 0.3 x 10^5, p = 2.97 bar (absolute), N = 8592 rev/min and M = 1.69 N m.

Absolute accuracy:	±61.2 mV
Zero order uncertainty:	±50 μV
Total (calculated using RSS method)	**±61.2 mV**

Table 4.7 – Uncertainty due to Solartron Orion 3530 for torque measurements

The sensitivity of the torquemeter is 1 V = 40 N m, therefore the uncertainty due to the Orion is ±0.4 N m. The uncertainty due to the torquemeter for the driveline torque measurement is ±0.048 N m as calculated previously from the components shown in Table 4.5. So the total uncertainty for driveline measurement, calculated using the RSS method is ±0.403 N m.

The uncertainty due to the torquemeter for the measured torque in this example is calculated from the components shown in Table 4.8, giving a total uncertainty of ±0.046 N m. Therefore the total uncertainty for measured torque, including the uncertainty of the Orion (±0.4 N m), is ±0.403 N m.

Calibration uncertainty (from calibration certificate)	±0.019 N m
Interpolation uncertainty from polynomial correlation	±0.01 N m
Long term stability on zero (< 0.05% of RO/year)	±0.02 N m
Long term stability on rated output (< 0.05% of RO/year)	±0.02 N m
Precision error of the measurements	±0.03 N m
Total (calculated using RSS method)	**±0.046 N m**

Table 4.8 – Uncertainty components due to the torquemeter for the measured torque.

It is clear that the uncertainty due to Orion data logger is dominant, therefore the uncertainties in both the driveline friction and the measured torque, for nine and eighteen stator bolts will be taken as ±0.4 N m. So the total uncertainty for the adjusted torque measurement, calculated from the RSS method, will be ±0.57 N m. With a 95% confidence interval this gives an expanded uncertainty of ±1.12 N m (95%).

SPEED

The speed signal is acquired from the torquemeter using National Instruments' c-DAQ 9205 data acquisition device. The bias uncertainty in the data acquisition device was calculated using the RSS method from the following components, taken from the manufacturer's technical specification based on a ±3 V range:

- Absolute accuracy.
- Random noise.
- Zero order uncertainty, which is the half interval of the resolution and has a divisor of √3.

The values of these uncertainty components are shown in Table 4.9.

Absolute accuracy:	±3230 μV
Random noise:	±116 μV
Zero order uncertainty:	±13.2 μV
Total (calculated using RSS method)	**±3232.1 μV**

Table 4.9 – Uncertainty components due to c-DAQ 9205 for the speed measurements.

For the speed signal 1 V = 5000 rev/min, therefore ±3232.1 μV = ±16.16 rev/min. The speed signal has a maximum uncertainty resulting from its calibration of ±2.1 rev/min and a maximum uncertainty due to the polynomial correlation applied to the signal output of ±2 rev/min. The precision uncertainty is not included in the calculations since it is two orders of magnitude smaller than the smallest bias uncertainty. This gives a total uncertainty in the speed measurement, calculated using the RSS method, of ±16.41 rev/min. This gives an expanded uncertainty of ±32.5 rev/min (95%).

Since the maximum values were taken for the uncertainty in the polynomial correlation and the calibration uncertainty, and the uncertainty due to the c-DAQ 9205 is the same over the range of conditions, this value of uncertainty, ±32.5 rev/min (95%), will be used for the complete range of conditions tested.

The relative uncertainty for the two example test cases described in Table 4.1, changes from 0.83% at N = 3940 rev/min, to 0.37% at N = 8793 rev/min. This is a very small level of uncertainty, even at the lower measured speeds.

The measurement uncertainty for the nine and eighteen stator bolt tests, where the speed measurement was acquired from the Optidrive motor controller, was calculated by **Coren (2007)** to be ±10 rev/min, giving an expanded uncertainty of ±19.8 rev/min.

TEMPERATURE (PRT)

The primary air temperature measurements, which are used in the calculation of C_m, are obtained using PRTs. The measurements are obtained using a National Instruments SCXI-1121 data acquisition module. The uncertainty in the PRT temperature measurements is dominated, to the extent of an order of magnitude, by the uncertainty due to the polynomial correlation applied to the calibration data. Therefore the contributions to the uncertainty from the other sources are not considered in this calculation. The maximum uncertainty from the correlation is ±0.1 °C, which gives ±0.198 °C (95%). As with the speed measurements, this is a very small amount of measurement uncertainty.

Using the original data acquisition equipment the PRT signal was acquired using the Alpha 912. This has an accuracy of ±0.2 °C in PT100 mode, so including the

uncertainty due to the polynomial applied to the signal of ±0.1 °C, the total uncertainty is ±0.22 °C, which gives ±0.44 °C (95%). This applies only to the data acquired for the nine and eighteen stator bolt tests. Although this is a larger measurement uncertainty than for the newer data acquisition system, it is still reasonably low.

TEMPERATURE (THERMOCOUPLE)

Air temperature measurements are also obtained using k type thermocouples, which are used in the calculation of μ. The data acquisition device used for thermocouple measurements is a National Instruments c-DAQ 9211 module. The bias uncertainty is found from the components shown in Table 4.10 taken from the manufacturer's specification. The zero order uncertainty has a rectangular distribution and therefore a divisor of √3 has been applied.

Input noise:	±1 μV_{rms}
Gain error:	±2.4 μV
Zero order uncertainty:	±1.37 x 10^{-3} μV
Total (calculated using RSS method)	**±2.6 μV**

Table 4.10 – Uncertainty components due to c-DAQ 9211 for thermocouple temperature measurements.

For k type thermocouple temperature measurements 1°C = 41.44 μV, therefore ±2.6 μV = ±0.063 °C. The typical cold junction compensation uncertainty is ±0.6 °C. Other uncertainties relating to the calibration and application of a polynomial as well as the precision uncertainty are all at least one order of magnitude smaller than the bias uncertainty due to the c-DAQ 9211, therefore they are not included in this calculation. The total uncertainty, calculated using the RSS method, is ±0.6 °C, therefore the expanded uncertainty is ±1.2 °C (95%). This is much larger than the uncertainty calculated for the PRT measurements and highlights the reason for using PRTs at the inlet and outlet to the test rig for calculating windage from an enthalpy change (see Section 4.2.2).

For the nine and eighteen stator bolt tests the thermocouple temperature measurements are acquired by the Orion data logger with a separate device for measuring the cold

junction temperature (the reader is referred to Section 3.5.1 for details). The uncertainty due to the Orion data logger was calculated previously from the absolute accuracy and the zero order uncertainty (taken from the manufacturer's specification at a measurement speed of 40 readings/s). A typical temperature measured by the thermocouples is 50 °C. The instrument uncertainty calculated for a temperature measurement of 50 °C is shown in Table 4.11.

Absolute accuracy:	±60.4 μV
Zero order uncertainty:	±0.5 μV
Total (calculated using RSS method)	**±60.4 μV**

Table 4.11 – Uncertainty due to Solartron Orion 3530 for a thermocouple temperature measurement of 50 °C.

With a sensitivity of 1 °C = 41.44 μV this instrument uncertainty relates to ±1.45 °C. Other contributions to the uncertainty are the uncertainty in the cold junction temperature measuring device (LM 35CZ), calculated by **Coren (2007)** to be ±0.2 °C. The repeatability of the calibration, which was found to be less than ±0.1 °C, and the uncertainty due to the application of a polynomial to the output signal, found to be no more than ±0.15 °C. The precision error was found to be negligible in comparison and so is not included in the uncertainty calculation. Therefore the total uncertainty in a thermocouple temperature measurement of 50 °C, calculated using the RSS method is ±1.47 °C, giving an expanded uncertainty of ±2.91 °C (95%).

At a measured temperature of 20 °C the uncertainty due to the instrumentation is shown in Table 4.12, calculated as described previously.

Absolute accuracy:	±54.1 μV
Zero order uncertainty:	±0.5 μV
Total (calculated using RSS method)	**±54.1 μV**

Table 4.12 – Uncertainty due to the Solartron Orion 3530 for a thermocouple temperature measurement of 20 °C.

Using the same sensitivity 1 °C = 41.44 μV, the instrument uncertainty is ± 1.31 °C. The other components of uncertainty are the same as calculated previously since they are not dependant on measured temperature. Therefore the total uncertainty is ±1.33 °C, giving an expanded uncertainty of ±2.64 °C (95%). It can be seen that the uncertainty in the thermocouple temperature measurement is very large. This is mainly due to the uncertainty of the Orion data logger.

TEMPERATURE (INFRA RED)

The signals from the infra red temperature sensors, which are used to measure the disc surface temperature, are acquired by a National Instruments SCXI-1100 module which transfers the data via a PCI-6034E data acquisition card at the computer terminal. From the manufacturer's technical specifications it was clear that the uncertainty of the PCI-6034E was the dominant factor, since the main contributor to the uncertainty of the SCXI-1100 is the offset, which was accounted for in the results. Therefore the uncertainty in the SCXI-1100 module is discounted for the purposes of this calculation. The uncertainty components for the PCI-6034E and their values are shown in Table 4.13.

Absolute accuracy:	±1.79 mV
Zero order uncertainty:	±0.022 mV
Total (calculated using RSS method)	**±1.79 mV**

Table 4.13 – Components and values of uncertainty due to the PCI-6034E data acquisition card

With the sensitivity of the infra red sensors being 10 mV/°C this means that ±1.79 mV = ±0.179 °C. All six sensors were individually calibrated, so for the purposes of this example, the uncertainty will be calculated for the sensor placed at r = 0.96 m. The uncertainty due to the calibration is ±0.05 °C, and the maximum uncertainty due to the application of a polynomial to the signal output is ±0.23 °C. The precision uncertainty is negligible in comparison to the bias uncertainties, so is not included in the calculation. The total instrument uncertainty is therefore calculated as ±0.296 °C, giving an expanded uncertainty of ±0.59 °C (95%).

The calibration uncertainties for the other sensors are of the same order of magnitude as this sensor. Since this is an order of magnitude smaller than the instrument and polynomial uncertainty components, the small variations between them have a negligible effect on the total uncertainty. The instrument uncertainty does not change, and the uncertainty in the application of a polynomial, ±0.23 °C, is the maximum for all sensors. Therefore the uncertainty ±0.59 °C (95%), is used for all temperatures measured using the infra red sensors.

For the nine and eighteen stator bolt tests, the signals from the infra red sensors were acquired by an Alpha 912 data logger. The uncertainty due to the Alpha 912 is made up of two components taken from the manufacturer's specification (using the ±5 V range):

- Absolutes accuracy, which is calculated as ±0.015% of the reading plus ±1 mV.
- Zero order uncertainty, which is the half interval of the resolution of the device and has a rectangular distribution therefore a divisor of √3.

For a typical test with nine bolts on the stator, C_w = 0.3 x 10^5, p = 2.97 bar (absolute) and N = 8592 rev/min, the outermost infra red sensor measured a surface temperature of 54.16 °C. At this temperature the bias uncertainty is as shown in Table 4.14 and has been calculated using a sensitivity of 10 mV/°C.

Absolute accuracy:	±0.108 °C
Zero order uncertainty:	±0.004 °C
Total (calculated using RSS method)	**±0.108 °C**

Table 4.14 - Components and values of uncertainty due to the Alpha 912 data logger

Including the calibration and polynomial uncertainties of ±0.05 °C and ±0.23 °C respectively, the total comes to ±0.259 °C. The precision uncertainty in the measurement is again negligible and does not need to be included. Applying the coverage factor of 1.98, gives an expanded uncertainty of ±0.51 °C (95%). This value of uncertainty is used for all infra red sensors, at all test conditions. This is acceptable since the polynomial uncertainty was the maximum value across all the sensors, and the variation in absolute accuracy with measured temperature would have a negligible effect on the total uncertainty across the range of temperatures measured.

PRESSURE (SCANIVALVE)

Pressure measurements are obtained at a variety of positions around the test rig (see Section 3.6.2 for details). The total pressure, p, is the addition of the gauge pressure, p_g, measured using a digital Scanivalve pressure transducer, and the atmospheric pressure, p_{atm}, measured using a barometer, as shown in Equation 4.16.

$$p = p_g + p_{atm} \tag{4.16}$$

To calculate the uncertainty the taylor series propogation analysis (Equation 4.11) is used. The partial derivatives of Equation 4.16, describing the sensitivity of each parameter are calculated as shown in Equation 4.17 and 4.18.

$$\frac{\partial p}{\partial p_g} = 1 \tag{4.17}$$

$$\frac{\partial p}{\partial p_{atm}} = 1 \tag{4.18}$$

So the absolute uncertainty for the measurement p can be found using Equation 4.19:

$$w_p = \sqrt{\left(w_{p_g}\right)^2 + \left(w_{p_{atm}}\right)^2} \tag{4.19}$$

The uncertainty in the measurement of atmospheric pressure using the barometer was found by **Coren (2007)** to be ±7.6 N/m^2.

The uncertainty of the Scanivalve pressure measurements, taken from the calibration certificates supplied with the Scanivalve units, is calculated as 0.012% of full scale (full scale = 6.9 bar). This equates to ±82.74 N/m^2. The uncertainty due to the application of a polynomial to the calibration data is a maximum of ±40 N/m^2. The precision uncertainty associated with the measurement for the first example test case (Table 4.1), where p_g = 1.02 bar, is ±7.5 N/m^2. Therefore the total uncertainty for the Scanivalve measurement, calculated using the RSS method, is ±92.2 N/m^2. Using this value in Equation 4.19, and ±7.6 N/m^2 as the uncertainty in the atmospheric pressure measurement, the total uncertainty is ±92.5 N/m^2, giving an expanded uncertainty of ±183.2 N/m^2 (95%). Given that for the first example p = 2.02 x 10^5 N/m^2 (absolute), the relative uncertainty is ±0.091%.

For the second example (Table 4.1) the uncertainties from the calibration and polynomial application remain the same at 82.74 N/m^2 and ±40 N/m^2 respectively, but the precision uncertainty is this time ±17.4 N/m^2. This gives a total Scanivalve measurement uncertainty of ±93.53 N/m^2. Using Equation 4.19, the uncertainty in the total pressure measurement is calculated as ±93.84 N/m^2. Giving and expanded uncertainty of ±185.8 N/m^2 (95%), which is 0.037% of the total pressure reading, p = 5.01 x 10^5 N/m^2 (absolute).

The uncertainties in both cases are very small and change little with a large change in measured pressure.

PRESSURE (ROSEMOUNT)

Four Rosemount differential pressure transmitters are used, one at each of the four orifice plates on the test rig (two inlet and two outlet). The signals are acquired through a National Instruments SCXI-1100 module which is read by the PCI-6034E data acquisition card at the computer terminal. As mentioned previously, the uncertainty in the SCXI-1100 module is negligible and is not included in the calculation. The uncertainty for the PCI-6034E data acquisition card is ±1.79 mV as calculated previously (Table 4.13). For the two inlet transmitters, the range of differential pressure measured is 0 bar $\leq \Delta p \leq$ 0.37 bar, and the two outlet pressure transmitters have a differential pressure measurement range of 0 bar $\leq \Delta p \leq$ 1.865 bar. The uncertainty components and their values for both the inlet and outlet transmitters are shown in Table 4.15.

	Inlet Transmitters	**Outlet Transmitters**
Calibration uncertainty	±50 N/m^2	±58.4 N/m^2
Polynomial application uncertainty	±2 N/m^2	±50 N/m^2
PCI-6034E uncertainty	±13.2 N/m^2 (1 V = 0.074 bar)	±66.7 N/m^2 (1 V = 0.373 bar)
Total (calculated using RSS method)	**±51.8 N/m^2**	**±101.8 N/m^2**

Table 4.15 – Uncertainty components and values for inlet and outlet Rosemount pressure transmitters.

For the inlet transmitters the total uncertainty is ±51.8 N/m^2, therefore the expanded uncertainty is ±102.6 N/m^2 (95%). The inclusion of barometric pressure here is not necessary due to the measurement being differential. In the first example test case, the differential pressure measurement at the inlet was 4.8 x 10^3 N/m^2, therefore the relative uncertainty is 2.1%. For the second example test case the differential pressure measurement at the inlet was 25 x 10^3 N/m^2, so the relative uncertainty is just 0.4%.

For the outlet transmitters the total uncertainty is ±101.8 N/m^2, and an expanded uncertainty of ±201.6 N/m^2 (95%). In the first example test case the differential pressure measurement at the outlet was 11.8 x 10^3 N/m^2 and so the relative uncertainty is 1.7%. For the second example test case the differential pressure measurement at the inlet was 119 x 10^3 N/m^2, so the relative uncertainty is just 0.17%.

For both inlet and outlet transmitters these relative uncertainties are very small, particularly where the measured pressure differential is large.

4.3.2 Uncertainties for combined parameters

For each of the combined parameters the uncertainty calculations are presented using the two examples used throughout Section 4.3.1, the conditions of which can be found in Table 4.1.

DIFFERENTIAL TEMPERATURE, T-T_{in}

For clarity, the differential temperature T-T_{in} will be referred to in this chapter as ΔT, expressed as shown in Equation 20.

$$\Delta T = T - T_{in} \qquad \textbf{(4.20)}$$

The partial derivatives describing the sensitivity of each parameter are shown in Equations 4.21 and 4.22.

$$\frac{\partial \Delta T}{\partial T} = 1 \qquad \textbf{(4.21)} \qquad \frac{\partial \Delta T}{\partial T_{in}} = -1 \qquad \textbf{(4.22)}$$

These partial derivatives are used in Equation 4.11 to evaluate the total uncertainty using the values w_T = 0.59 °C and w_{Tin} = 0.198 °C, calculated previously for the infra red sensors and PRT respectively. The resulting total uncertainty is ΔT = ±0.62 °C (95%).

MOMENT COEFFICIENT, C_m

The moment coefficient is defined in Equation 4.4, but substituting the ideal gas equation ($\rho = p/RT$) for the density, C_m can be expressed as shown in Equation 4.23.

$$C_m = \frac{MRT}{1/2\, p\omega^2 b^5} \qquad \textbf{(4.23)}$$

The partial derivatives of Equation 4.23 describing the sensitivity of each parameter are shown in Equations 4.24 to 4.29.

$$\frac{\partial C_m}{\partial M} = \frac{2RT}{p\omega^2 b^5} \qquad \textbf{(4.24)} \qquad \frac{\partial C_m}{\partial p} = \frac{2MRT}{p^2\omega^2 b^5} \qquad \textbf{(4.25)}$$

$$\frac{\partial C_m}{\partial T} = \frac{2MR}{p\omega^2 b^5} \qquad \textbf{(4.26)} \qquad \frac{\partial C_m}{\partial \omega} = \frac{-4MRT}{p\omega^3 b^5} \qquad \textbf{(4.27)}$$

$$\frac{\partial C_m}{\partial R} = \frac{2MT}{p\omega^2 b^5} \qquad \textbf{(4.28)} \qquad \frac{\partial C_m}{\partial b} = \frac{-10MRT}{p\omega^3 b^6} \qquad \textbf{(4.29)}$$

These partial derivatives can be used in Equation 4.11 to calculate the absolute uncertainty in C_m. It is more convenient, however, to calculate the relative uncertainty by substituting Equations 4.23 to 4.29 into Equation 4.11 and then dividing through by Equation 4.23. The resulting relative uncertainty for the moment coefficient is shown in Equation 4.30.

$$\frac{w_{C_m}}{C_m} = \sqrt{\left(\frac{w_M}{M}\right)^2 + \left(\frac{w_T}{T}\right)^2 + \left(\frac{w_p}{p}\right)^2 + \left(\frac{-2w_\omega}{\omega}\right)^2 + \left(\frac{w_R}{R}\right)^2 + \left(\frac{-5w_b}{b}\right)^2} \qquad \textbf{(4.30)}$$

The uncertainties in M, T, p and ω have been calculated in the previous section. The uncertainties in the measurement of b and R do not need to be included in the calculation for the majority of the results shown in this thesis. This is due to the fact that they are constant throughout the range of experiments and so are inconsequential to any trends found within the data set. However, for the particular case where a universal correlation is introduced, the uncertainties will necessarily include b and R, therefore their uncertainties are discussed here.

The measurement of b was performed using equipment with a resolution of 0.01 mm, the uncertainty is the half interval of the resolution. Assuming a rectangular distribution, and including a 95% confidence interval, this gives an uncertainty of $\pm 5.716 \times 10^{-3}$ m (±95%). The gas constant for air, R, is calculated using Equation 4.7, where $\Re$ is the universal gas constant and is quoted by the National Institute of Standards and Technology as 8.31447 J/molK with an uncertainty of ±0.000014 J/molK. The molar mass of air, $m_{m,Air}$ is calculated from the molar masses of the individual components of air multiplied by the fraction of air they represent (as discussed in Section 4.2.3), this is shown in Equation 4.31. The molar masses of each component of air and their respective uncertainties are shown in Table 4.16

$$m_{m,Air} = 0.78m_{m,N} + 0.21m_{m,O} + 0.01m_{m,Ar} \qquad \textbf{(4.31)}$$

	m_m	w_{mm}
Nitrogen	28.0134g/mol	±0.0002 g/mol
Oxygen	31.9988 g/mol	± 0.0003 g/mol
Argon	39.948 g/mol	±0.001 g/mol

Table 4.16 – Table showing the molar masses and their uncertainties for the three major components of air

The partial derivatives representing the sensitivity of each parameter in Equation 4.31 are shown in Equations 4.32 to 4.34. These are then used in Equation 4.11 with the uncertainty of each component as shown in Table 4.16, giving the total uncertainty in $m_{m,Air}$ of ±168.537 x 10^{-9} kg/mol.

$$\frac{\partial m_{m,Air}}{\partial m_{m,N}} = 0.78 \qquad \textbf{(4.32)} \qquad \frac{\partial m_{m,Air}}{\partial m_{m,O}} = 0.21 \qquad \textbf{(4.33)} \qquad \frac{\partial m_{m,Air}}{\partial m_{m,Ar}} = 0.01 \qquad \textbf{(4.34)}$$

The combined uncertainty in the gas constant for air, R, is calculated by using the partial derivatives shown in Equation 4.35 and 4.36 in Equation 4.11, along with the uncertainties of both $\Re$ and $m_{m,Air}$ to give a total uncertainty in R of ±3.44 x 10^{-3}J/kgK (95%)

$$\frac{\partial R}{\partial \Re} = \frac{1}{m_{m,Air}} \qquad \textbf{(4.35)} \qquad \frac{\partial R}{\partial m_{m,Air}} = \frac{-\Re}{m_{m,Air}^{\ 2}} \qquad \textbf{(4.36)}$$

Substituting into Equation 4.30 the measurements and measurement uncertainties of R and b as well as the other parameters, previously calculated for example test case one (Table 4.1), gives a relative uncertainty of ±16.4%. Each parameter and their respective uncertainties, all of which have a coverage factor of 1.98 included, are shown in Table 4.17. The value of C_m in this example is 0.02, therefore the absolute uncertainty is w_{Cm} = 3.28 x 10^{-3} (95%).

Measurement	Uncertainty
M = 2.32 N m	w_M = ±0.378 N m
T = 22.75 °C	w_T = ±0.198 °C
p = 2.02 bar (absolute)	w_p = ±1.832 x 10^{-3} bar
N = 3940 rev/min	w_N = ±32.5 rev/min
R = 287.01 J/kgK	w_R = ±3.44 x 10^{-3} J/kgK
b = 0.225 m	w_b = ±5.716 x 10^{-6} m

Table 4.17 – Measurement and uncertainty values for parameters in example test case one.

The main contributor to this uncertainty value is clearly the uncertainty of the torque measurement, as this was calculated to be 16.3%. Even the factor of two applied to the speed measurement uncertainty in Equation 4.30, does not have a significant effect on the overall uncertainty in C_m, since the relative uncertainty in the speed measurement is an order of magnitude smaller than that of the torque measurement.

The same calculation, but using the values from example test case two (Table 4.1), gives a relative uncertainty of just ±1.75%. The measurements and their respective uncertainties are shown in Table 4.18

Measurement	Uncertainty
M = 27.1 N m	w_M = ±0.415 N m
T = 46.05 °C	w_T = ±0.198 °C
p = 5.01 bar (absolute)	w_p = ±1.858 x 10^{-3} bar
N = 8793 rev/min	w_N = ±32.5 rev/min
R = 287.01 J/kgK	w_R = ±3.44 x 10^{-3} J/kgK
b = 0.225 m	w_b = ±5.716 x 10^{-6} m

Table 4.18 - Measurement and uncertainty values for parameters in example test case two.

With the measured value of C_m being again 0.02, the absolute uncertainty is w_{Cm} = ±3.51 x 10^{-4}. The uncertainty of the torquemeter is again shown to be the dominant factor in the uncertainty of C_m, as for this example it was calculated to be 1.5%.

However, the uncertainty in the speed measurement does have a small influence at these conditions.

Since the two examples shown here are very different test conditions representing the extents of the complete data set, it is reasonable to assume that the measurement uncertainties for temperature, pressure, radius and the gas constant for air, are negligible compared with torque in all cases. Therefore all uncertainty bars for C_m shown within the results sections of this thesis are based solely on the uncertainty due to the torque and speed measurements.

ROTATIONAL REYNOLDS NUMBER, $\mathbf{Re_\phi}$

The rotational Reynolds number, Re_ϕ, is defined in Equation 4.1 and μ is defined using Sutherland's law, which is shown in Equation 4.37.

$$\mu = \frac{1.458\times10^{-6}\,T_{tc}^{\,1.5}}{110+T_{tc}} \qquad \textbf{(4.37)}$$

In this equation, T_{tc} is the temperature used in the calculation of μ and is measured using a thermocouple, not a PRT like the temperature used in calculating the moment coefficient. Substituting Equation 4.37 and the ideal gas equation into Equation 4.1 gives the expression for Re_ϕ shown in Equation 4.38.

$$\mathrm{Re}_\phi = \frac{p\omega b^2\left(110+T_{tc}\right)}{1.458\times10^{-6}T_{tc}^{1.5}RT} \qquad \textbf{(4.38)}$$

Equations 4.39 to 4.42 show the partial derivatives representing the sensitivity of each parameter in Equation 4.38.

$$\frac{\partial \mathrm{Re}_\phi}{\partial p} = \frac{110\omega b^2}{1.458\times10^{-6}T_{tc}^{1.5}RT} + \frac{\omega b^2}{1.458\times10^{-6}T_{tc}^{0.5}RT} \qquad \textbf{(4.39)}$$

$$\frac{\partial \mathrm{Re}_\phi}{\partial \omega} = \frac{110\,pb^2}{1.458\times10^{-6}T_{tc}^{1.5}RT} + \frac{pb^2}{1.458\times10^{-6}T_{tc}^{0.5}RT} \qquad \textbf{(4.40)}$$

$$\frac{\partial \mathrm{Re}_{\phi}}{\partial T_{tc}} = \frac{-165 p \omega b^2}{1.458 \times 10^{-6} T_{tc}^{2.5} RT} - \frac{0.5 p \omega b^2}{1.458 \times 10^{-6} T_{tc}^{1.5} RT} \qquad \textbf{(4.41)}$$

$$\frac{\partial \mathrm{Re}_{\phi}}{\partial T} = \frac{-110 P \omega b^2}{1.458 \times 10^{-6} T_{tc}^{1.5} RT^2} - \frac{P \omega b^2}{1.458 \times 10^{-6} T_{tc}^{0.5} RT^2} \qquad \textbf{(4.42)}$$

The uncertainties in *b* and *R* are not included because the parameter Re_{ϕ} is only discussed in this thesis, with respect to other data obtained using the current test rig. The values of *b* and *R* are constant throughout the test phase, therefore their uncertainties are considered inconsequential to any trends found within the data set and so are excluded from the current calculation. By substituting the sensitivity equations (Equations 4.39 to 4.42) into Equation 4.11 and dividing through by Equation 4.38, the relative uncertainty in Re_{ϕ} can be calculated as shown in Equation 4.43

$$\frac{w_{\mathrm{Re}_{\phi}}}{\mathrm{Re}_{\phi}} = \sqrt{\left(\frac{w_p}{p}\right)^2 + \left(\frac{w_{\omega}}{\omega}\right)^2 + \left(\left[\frac{-165 T_{tc}^{-2.5} - 0.5 T_{tc}^{-1.5}}{110 T_{tc}^{-1.5} + T_{tc}^{-0.5}}\right] w_{T_{tc}}\right) + \left(\frac{-w_T}{T}\right)^2} \qquad \textbf{(4.43)}$$

For the first example test case shown in Table 4.1, the measurements of each parameter and their relative uncertainties, again including a coverage factor of 1.98, are shown in Table 4.19.

Measurement	Uncertainty
p = 2.02 bar (absolute)	w_p = ±1.832 x 10^{-3} bar
N = 3940 rev/min	w_N = ±32.5 rev/min
T_{tc} = 23.32 °C	w_{Ttc} = ±1.2 °C
T = 22.75 °C	w_T = ±0.198 °C

Table 4.19 – Measurement and uncertainty values for parameters in example test case one.

Using the values shown in Table 4.19 in Equation 4.43, gives the relative uncertainty in Re_{ϕ} as 6.92%. This leads to an absolute uncertainty of ±0.0188 x 10^7 (95%), given that for this example Re_{ϕ} = 0.272 x 10^7.

Using the values for example test case two, shown in Table 4.20, the relative uncertainty is 3.5%. In this example, $\mathrm{Re}_\phi = 1.341 \times 10^7$, therefore the absolute uncertainty, $\pm 0.0469 \times 10^7$ (95%).

Measurement	Uncertainty
p = 5.01 bar (absolute)	$w_p = \pm 1.858 \times 10^{-3}$ bar
N = 8793 rev/min	$w_N = \pm 32.5$ rev/min
T_{tc} = 42.44 °C	$w_{Ttc} = \pm 1.2$ °C
T = 46.05 °C	$w_T = \pm 0.198$ °C

Table 4.20 – Measurement and uncertainty values for parameters in example test case two.

Due to the sensitivity of the thermocouple measurement uncertainty (in Equation 4.38), if the total uncertainty for Re_ϕ was calculated using solely the thermocouple uncertainty, the relative uncertainty for example test case one would be 6.82%, and for example test case two would be 3.45%. It is deemed reasonable to assume then, that the uncertainties in the other parameters measured are negligible, therefore they are not included in the calculation of the uncertainty in Re_ϕ for the results presented in this thesis.

$C_m\mathrm{Re}_\phi^{0.2}$

Having calculated the uncertainty in both C_m and Re_ϕ separately, the uncertainty in the parameter $C_m\mathrm{Re}_\phi^{0.2}$ can also be determined. For clarity this parameter will be referred to in this chapter as Γ, as shown below in Equation 4.44.

$$\Gamma = C_m \mathrm{Re}_\phi^{0.2} \qquad \textbf{\textit{(4.44)}}$$

The partial derivatives describing the sensitivity of each parameter in Equation 4.44 are shown in Equations 4.45 and 4.46

$$\frac{\partial \Gamma}{\partial C_m} = \mathrm{Re}_\phi^{0.2} \qquad \textbf{\textit{(4.45)}}$$

$$\frac{\partial \Gamma}{\partial \mathrm{Re}_\phi} = 0.2 C_m \mathrm{Re}_\phi^{-0.8} \qquad \textbf{\textit{(4.46)}}$$

Using these in Equation 4.11 and dividing through by Γ, leads to the equation for the relative uncertainty shown in Equation 4.47:

$$\frac{w_\Gamma}{\Gamma} = \sqrt{\left(\frac{w_{C_m}}{C_m}\right)^2 + \left(\frac{0.2 w_{\mathrm{Re}_\phi}}{\mathrm{Re}_\phi}\right)^2} \qquad \textit{(4.47)}$$

For the example test case one, where the parameter values and uncertainties are as shown in Table 4.21, the relative uncertainty in Γ is ±16.5% so with the value Γ = 0.385, the absolute uncertainty is ±0.063 (95%).

Parameter	Uncertainty
$C_m = 0.02$	$w_{Cm} = \pm 3.28 \times 10^{-3}$
$\mathrm{Re}_\phi = 0.272 \times 10^7$	$w_{\mathrm{Re}_\phi} = \pm 0.0188 \times 10^7$

Table 4.21 – Measurement and uncertainty values for combined parameters in example test case one.

For example test case two, where the combined parameter values and uncertainties are as shown in Table 4.22, the relative uncertainty in Γ is ±1.89% so with the value Γ = 0.54, the absolute uncertainty is ±0.01 (95%).

Parameter	Uncertainty
$C_m = 0.02$	$w_{Cm} = \pm 3.51 \times 10^{-4}$
$\mathrm{Re}_\phi = 1.341 \times 10^7$	$w_{\mathrm{Re}_\phi} = \pm 0.047 \times 10^7$

Table 4.22 – Measurement and uncertainty values for combined parameters in example test case two.

It can be seen that these relative uncertainties are highly dependent on the relative uncertainty of C_m, which were 16.4% and 1.75% for example test cases one and two respectively.

MASS FLOW RATE, $\dot{m}$

The equation used to calculate the mass flow through the orifice plate is shown in Equation 4.6. In this instance the pressure difference between upstream and downstream of the throat is measured using a differential pressure transducer, therefore $p_1 - p_2$ can be replaced with Δp. Substituting, this along with the parameter β into Equation 4.6, where $\beta = d/D$, gives the expression shown in Equation 4.48

$$\dot{m} = C\varepsilon \frac{\pi}{4} d^2 \left(1-\beta^4\right)^{-0.5} \sqrt{2\Delta p \frac{p_1}{RT}} \qquad \textbf{(4.48)}$$

The partial derivatives describing the sensitivity of each parameter are shown in Equations 4.49 to 4.56

$$\frac{\partial \dot{m}}{\partial C} = \varepsilon \frac{\pi}{4} d^2 \left(1-\beta^4\right)^{-0.5} \sqrt{2\Delta p \frac{p_1}{RT}} \qquad \textbf{(4.49)}$$

$$\frac{\partial \dot{m}}{\partial \varepsilon} = C \frac{\pi}{4} d^2 \left(1-\beta^4\right)^{-0.5} \sqrt{2\Delta p \frac{p_1}{RT}} \qquad \textbf{(4.50)}$$

$$\frac{\partial \dot{m}}{\partial d} = C\varepsilon \frac{\pi}{2} d \left(1-\beta^4\right)^{-0.5} \sqrt{2\Delta p \frac{p_1}{RT}} \qquad \textbf{(4.51)}$$

$$\frac{\partial \dot{m}}{\partial \beta} = C\varepsilon \frac{\pi}{2} d^2 \beta \sqrt{2\Delta p \frac{p_1}{RT}} \qquad \textbf{(4.52)}$$

$$\frac{\partial \dot{m}}{\partial \Delta p} = C\varepsilon \frac{\pi}{8} d^2 \left(1-\beta^4\right)^{-0.5} \sqrt{\frac{2p_1}{\Delta p RT}} \qquad \textbf{(4.53)}$$

$$\frac{\partial \dot{m}}{\partial p_1} = C\varepsilon \frac{\pi}{8} d^2 \left(1-\beta^4\right)^{-0.5} \sqrt{\frac{2\Delta p}{p_1 RT}} \qquad \textbf{(4.54)}$$

$$\frac{\partial \dot{m}}{\partial R} = -C\varepsilon \frac{\pi}{8} d^2 \left(1-\beta^4\right)^{-0.5} \sqrt{2\Delta p \frac{p_1}{R^3 T}} \qquad \textbf{(4.55)}$$

$$\frac{\partial \dot{m}}{\partial T} = -C\varepsilon \frac{\pi}{8} d^2 \left(1-\beta^4\right)^{-0.5} \sqrt{2\Delta p \frac{p_1}{RT^3}} \qquad \textbf{(4.56)}$$

Using these partial derivatives in Equation 4.11 and then dividing through by Equation 4.48 gives the relative uncertainty in $\dot{m}$ as shown in Equation 4.57

$$\frac{w_{\dot{m}}}{\dot{m}} = \sqrt{\left(\frac{w_C}{C}\right)^2 + \left(\frac{w_\varepsilon}{\varepsilon}\right)^2 + \left(\frac{2w_d}{d}\right)^2 + \left(\frac{2\beta w_\beta}{1-\beta^{-2}}\right)^2 + \left(\frac{w_{\Delta P}}{2\Delta p}\right)^2 + \left(\frac{w_{p_1}}{2p_1}\right)^2 + \left(\frac{-w_R}{2R}\right)^2 + \left(\frac{-w_T}{2T}\right)} \qquad \textbf{(4.57)}$$

The uncertainties for the parameters, Δp, p_1, R and T have been calculated previously. The value of uncertainty for the discharge coefficient is taken from **Coren (2007)** since all relevant measurements and relationships are the same for both studies. The value of uncertainty given by Coren, including a 1.98 coverage factor, is ±9.04 x 10^{-4} (95%) or ±0.129%. The uncertainties in d, β, and ε are calculated as follows:

The parameter β is shown in Equation 4.58

$$\beta = \frac{d}{D} \qquad \textbf{(4.58)}$$

The uncertainty is calculated by substituting the partial derivatives shown in Equation 4.59 and 4.60 into Equation 4.11 along with the measurement uncertainties.

$$\frac{\partial \beta}{\partial d} = \frac{1}{D} \qquad \textbf{(4.59)} \qquad\qquad \frac{\partial \beta}{\partial D} = -\frac{d}{D^2} \qquad \textbf{(4.60)}$$

The uncertainties in the measurement of both d and D are calculated as the half interval of the resolution. With the assumption of a rectangular distribution, and the inclusion of a 1.98 coverage factor, this comes to ±5.716 x 10^{-6}m (95%) for each parameter. Therefore the total uncertainty in β is ±1.396 x 10^{-4} m (95%).

The expansibility factor, ε, is given in Equation 4.61

$$\varepsilon = 1 - \left(0.41 + 0.35\beta^4\right)\left(\frac{\Delta p}{\gamma p_1}\right) \qquad \textbf{(4.61)}$$

The partial derivatives expressing the sensitivity of each parameter in Equation 4.61 are shown in Equations 4.62 to 4.65.

$$\frac{\partial \varepsilon}{\partial \Delta p} = \frac{0.41 + 0.35\beta^4}{\gamma p_1} \qquad \textbf{(4.62)}$$

$$\frac{\partial \varepsilon}{\partial \gamma} = -\frac{\left(0.41 + 0.35\beta^4\right)\Delta p}{\gamma^2 p_1} \qquad \textbf{(4.63)}$$

$$\frac{\partial \varepsilon}{\partial p_1} = -\frac{\left(0.41 + 0.35\beta^4\right)\Delta p}{\gamma p_1^2} \qquad \textbf{(4.64)}$$

$$\frac{\partial \varepsilon}{\partial \beta} = \frac{1.4\beta^3 \Delta p}{\gamma p_1} \qquad \textbf{(4.65)}$$

In order to calculate the uncertainty in the expansibility factor a value for the uncertainty in the ratio of specific heats, γ, must be found. This is taken to be the same as was calculated by **Coren (2007)** since the same method of calculation was used. The uncertainty in γ was found by Coren to be $\pm 4.323 \times 10^{-5}$ (95%) or $\pm 3.09 \times 10^{-3}$%. The measurement uncertainties in Δp, β and p_1 are as stated previously in this chapter. The partial derivatives shown in Equations 4.62 to 4.65 are used, along with the respective measurement uncertainties in Equation 4.11 to find the uncertainty in ε.

Using the same two example test points (Table 4.1), the relevant parameters for calculating the uncertainty in the mass flow rate are shown in Table 4.23 along with the associated measurement uncertainties for each parameter. These values are taken for the orifice plate measuring the mass flow at the inlet to the test side of the test rig.

	Example 1		Example 2	
Parameter	**Value**	**Uncertainty**	**Value**	**Uncertainty**
C	0.657	8.47×10^{-4}	0.627	8.09×10^{-4}
ε	0.9934	6.705×10^{-6}	0.9849	1.525×10^{-5}
d (m)	0.035	5.716×10^{-6}	0.035	5.716×10^{-6}
β	0.7	1.396×10^{-4}	0.7	1.396×10^{-4}
Δp (N/m^2)	4871	102.6	25545	102.6
p_1 (N/m^2)	258652.3	258.65	596312.8	596.3
R (J/kgK)	287.01	3.44×10^{-3}	287.01	3.44×10^{-3}
T (°C)	19.05	1.2	16.05	1.2
γ	1.401	4.329×10^{-5}	1.401	4.329×10^{-5}

Table 4.23 - Measurement values and uncertainty for the parameters used to calculate $\dot{m}$

Putting these values into Equation 4.57 gives a relative uncertainty in the mass flow of 3.32% for Example 1 and 3.75% for Example 2. Given that for Example 1 the mass flow rate is measured at 0.125 kg/s, the absolute uncertainty in the mass flow measurement is $\pm 4.15 \times 10^{-3}$ kg/s (95%). For Example 2, where the measured mass flow rate is 0.413 kg/s, the absolute measurement uncertainty is ±0.0155 kg/s (95%). It can be seen that the relative uncertainty is fairly small and does not change much throughout the range of mass flow rates measured. This is due to the fact that the largest contributor to the uncertainty of $\dot{m}$ is the uncertainty in the temperature measurement, which does not vary greatly over the extent of the tests.

THROUGHFLOW REYNOLDS NUMBER, C_w

The throughflow Reynolds number, C_w, is shown in Equation 4.2. Substituting into this the relationship shown in Equation 4.37 for μ, we get the expression shown in Equation 4.66.

$$C_w = \frac{\dot{m}(110 + T_{tc})}{1.458 \times 10^{-6} T_{tc}^{1.5} b} \qquad \textbf{(4.66)}$$

For the purposes of the results presented in this thesis, the uncertainty in the measurement of *b* is not included since this is constant throughout the experiments and therefore has no bearing on any trends seen for C_w. The partial derivatives for $\dot{m}$ and T_{tc} are shown in Equations 4.67 and 4.68.

$$\frac{\partial C_w}{\partial \dot{m}} = \frac{110 + T_{tc}}{1.458 \times 10^{-6} T_{tc}^{1.5} b} \qquad \textbf{(4.67)}$$

$$\frac{\partial C_w}{\partial T_{tc}} = \left(-\frac{165}{T_{tc}^{2.5}} - \frac{0.5}{T_{tc}^{1.5}} \right) \left(\frac{\dot{m}}{1.458 \times 10^{-6} b} \right) \qquad \textbf{(4.68)}$$

Using these partial derivatives in Equation 4.11 and dividing through by Equation 4.66 gives the relative uncertainty in the measurement shown in Equation 4.69.

$$\frac{w_{C_w}}{C_w} = \sqrt{\left(\frac{w_{\dot{m}}}{\dot{m}} \right)^2 + \left[\left(\frac{-165 T_{tc}^{-2.5} - 0.5 T_{tc}^{-1.5}}{110 T_{tc}^{-1.5} + T_{tc}^{-0.5}} \right) w_{T_{tc}} \right]^2} \qquad \textbf{(4.69)}$$

Using the same two example test points as before, the values and respective uncertainties for $\dot{m}$ and T_{tc} are shown in Table 4.24.

	Example 1		**Example 2**	
Parameter	**Value**	**Uncertainty**	**Value**	**Uncertainty**
$\dot{m}$ (kg/s)	0.125	4.15 x 10^{-3}	0.413	0.0155
T_{tc} (°C)	23.32	1.2	42.44	1.2

Table 4.24 - Measurement and uncertainty values for the combined parameters used in calculating C_w.

Using these values, the relative uncertainties for Example 1 and Example 2 are 7.58% and 5.1% respectively. For Example 1 C_w = 0.3 x 10^5 giving a total uncertainty of ±2.27 x 10^3 (95%). For Example 2, C_w = 0.97 x 10^5 therefore the total uncertainty is ±4.93 x 10^3 (95%).

TURBULENT FLOW PARAMETER, λ_T

The turbulent flow parameter, λ_T, is calculated as shown previously in Equation 4.3. The partial derivatives of this equation are shown in Equations 4.70 and 4.71.

$$\frac{\partial \lambda_T}{\partial C_w} = \mathrm{Re}_\phi^{-0.8} \qquad \textbf{(4.70)}$$

$$\frac{\partial \lambda_T}{\partial \mathrm{Re}_\phi} = -0.8 C_w \mathrm{Re}_\phi^{-1.8} \qquad \textbf{(4.71)}$$

Substituting these into Equation 4.11 gives the total uncertainty in the measurement of λ_T as shown in Equation 4.72.

$$w_{\lambda_T} = \sqrt{\left(\mathrm{Re}_\phi^{-0.8}\, w_{C_w}\right)^2 + \left(\left(-0.8 C_w \mathrm{Re}_\phi^{-1.8}\right) w_{\mathrm{Re}_\phi}\right)^2} \qquad \textbf{(4.72)}$$

Again using the same two example test points (Table 4.1), the values and respective uncertainties are given in Table 4.25 for Re_ϕ and C_w.

	Example 1		**Example 2**	
Parameter	**Value**	**Uncertainty**	**Value**	**Uncertainty**
Re_ϕ	0.272×10^7	1.88×10^5	1.341×10^7	4.69×10^5
C_w	0.3×10^5	2.27×10^3	0.97×10^5	4.93×10^3

Table 4.25 – Measurement and uncertainty values for the combined parameters used in calculating λ_T.

For Example 1, the total uncertainty in the measurement is ±0.02 (95%), which gives a relative uncertainty of ±9.35% since $\lambda_T = 0.214$. For Example 2, where $\lambda_T = 0.192$, the total uncertainty is ±0.011 (95%) giving a relative uncertainty of ±5.73%. These uncertainties are fairly large which is not entirely surprising since the value of λ_T is calculated from two combined parameters. Each combined parameter is made up of a variety of measured values, each with an uncertainty associated to its measurement. The uncertainty in λ_T is therefore compound and it is expected that it would be large.

Chapter 5. Plain Disc Tests

5.1 Introduction

This chapter discusses the testing method and results obtained for the driveline friction tests and also the plain disc tests.

The driveline friction tests were necessary to determine the mechanical friction in the bearings and gearbox, as well as aerodynamic friction due to the rotation of the driveshaft. The driveline friction is subtracted from the measured torque. The resulting net torque is due to windage from the rotation of the disc, with or without features on the rotor or stator surface. Driveline friction tests were carried out between 2000 rev/min $\leq N \leq$ 12000 rev/min.

The plain disc tests create a baseline to which all further measurements can be compared. This allows the evaluation of windage arising solely due to the features on either the rotor or stator surface. The plain disc tests were carried out over the range of dimensionless conditions: $0.17 \times 10^7 \leq \mathrm{Re}_\phi \leq 1.61 \times 10^7$, $0.29 \times 10^5 \leq C_w \leq 1.03 \times 10^5$ and $0.063 \leq \lambda_T \leq 0.601$.

5.2 Driveline friction test procedure

To measure the friction in the driveline a low windage disc was fitted. The low windage disc has the same mass as the normal test disc, but has a smaller radius, r = 0.025 m instead of r = 0.225 m. Since windage is proportional to b^5 and the low windage disc is roughly $1/10^{th}$ of the size of the normal test disc, the windage will be 10^5 times smaller than that of the normal test disc. It can therefore be assumed that disc windage will be negligible, and the measured torque can be taken as a measurement of

friction within the driveline itself (i.e. bearings and aerodynamic drag on the driveshaft). Figure 5.1 shows the low windage disc fitted to the rig.

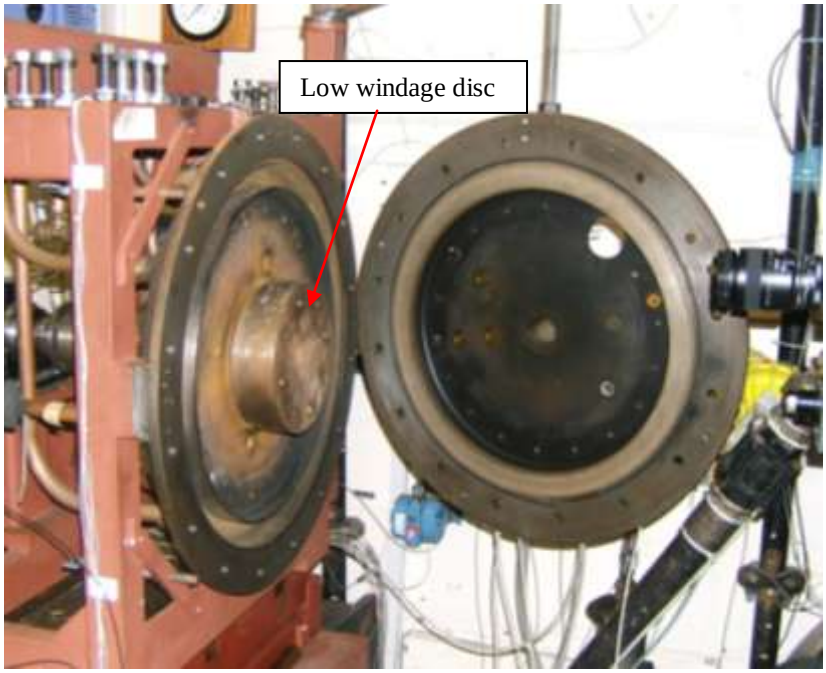

Figure 5.1 – Picture of low windage disc attached to the test rig.

During the tests the casing is left open and unpressurised as seen in Figure 5.1. Tests were carried out for the range of speeds 2000 rev/min $\leq N \leq$ 12000 rev/min, at intervals of 2000 rev/min. The test rig was held at each speed for five minutes in order to settle and to enable a reliable average to be calculated. The torque data was averaged over the final two minutes at each speed. The process was carried out on four separate occasions, over two days, to check for repeatability. The separate tests are referred to as Test 1, Test 2, Test 3, and Test 4.

5.3 Driveline friction test results

This section discusses the results obtained from the driveline friction tests and compares them to those formerly obtained by **Coren (2007)** for the same test rig.

Figure 5.2 shows the variation of measured torque with speed for the four separate tests. The mean torque at each speed was calculated and the variation of this with rotational speed is represented by a third order polynomial. The equation for the third order polynomial fitted to the driveline torque data is shown in Equation 5.1. It is valid for any speed between 2000 rev/min $\leq N \leq$ 12000 rev/min. In this equation, N is the rotational speed in rev/min, and M is the corresponding driveline frictional torque in N m.

$$M = 2.53\times10^{-12}N^3 - 4.27\times10^{-8}N^2 + 2.07\times10^{-4}N + 0.55 \qquad \textbf{(5.1)}$$

The uncertainty bars shown in Figure 5.2 are calculated using the method described in Section 4.3.1.

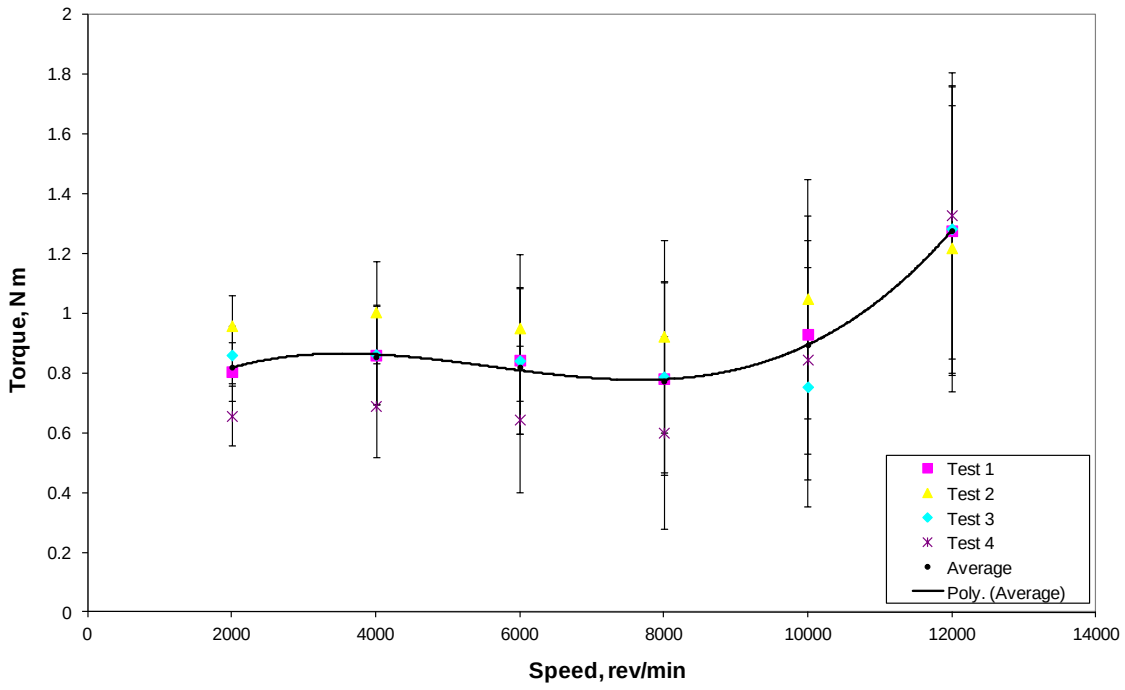

Figure 5.2 - Variation of driveline torque with rotational speed for four separate tests.

Figure 5.3 shows the variation of driveline frictional torque with rotational speed for both the current data as well as that obtained by **Coren (2007)**. It can be seen here that there is a significant difference between the two sets of data, exceeding the relatively large uncertainties in the measurement. At 4000 rev/min the variation in torque between the current driveline friction results and the results obtained by Coren is about 0.6 N m. Typically, with the normal test disc as well as superimposed throughflow at 4000 rev/min, the measured torque can be between 1.5 N m and 10 N m, depending on the flow conditions and the presence, or not, of features. At 10 N m of measured torque, this variation in driveline frictional torque between the two sets of results is just 6% of the measurement. However, when measuring torque values of just 1.5 N m, this difference is 40% of the measurement. For the plain disc tests discussed later in this chapter a third of the measured toque values are between 1 N m and 2 N m. Therefore the difference between the current and previous results is significant.

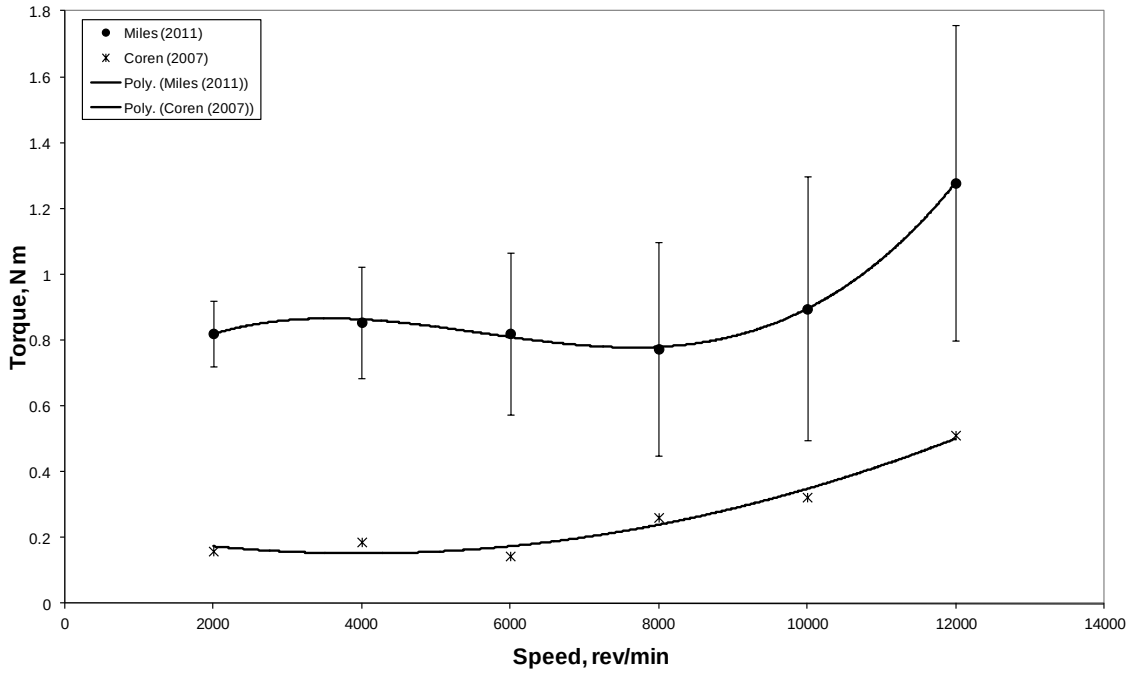

Figure 5.3 – Variation of driveline torque with rotational speed for the average current and previous driveline friction test results.

The cause of this change in driveline characteristic was given lengthy consideration. The main shaft bearings were replaced and a number of inspections were carried out to check the circularity of the bearings and the alignment of the driveline. However, no reason for the difference in driveline characteristic between the current results and those

obtained by Coren could be found. It is worthwhile to note that in between the current and previous driveline tests the driveline was dismantled on two occasions, once to rebuild the gearbox during the previous test phase, and once to recalibrate the torquemeter when the disagreement between the two sets of results was first noted. Many tests were carried out during this period of inspections, and the results were found to be very repeatable. Consequently the current results obtained for the driveline friction are deemed reliable and are used throughout this thesis. See Appendix E for TFMRC internal report by **Miles (2008)** which gives details on the tests carried out, the results obtained and the methods used for investigating the change in driveline characteristic.

For all results shown in this thesis, the windage torque presented has had the corresponding driveline friction torque subtracted from it.

5.4 Plain disc test procedure

The procedure for carrying out plain disc tests is explained in this section. This procedure, described here for the plain disc tests, was also applied to tests with rotor and stator protrusions and surface cavities.

The plain disc tests were carried out for the range of conditions shown in Table 5.1. No protrusions or pockets were fitted to either the disc surface or the stationary casing. In carrying out these tests a baseline is set to which all further test results can be compared, thereby allowing the increased windage due to the protrusions or pockets to be found.

The test matrix for the plain disc tests was designed to account for different values of the turbulent flow parameter, λ_T ($\lambda_T = C_w/Re_\phi^{0.8}$), with two different mass flows of superimposed air, $\dot{m}$ = 0.12 kg/s and 0.4 kg/s. Conditions were chosen to match the planned stator bolt, rotor bolt and pocket tests. A complete set of the test conditions can be found in Appendix C. Table 5.1 shows the ranges of rotational Reynolds number, Re_ϕ ($Re_\phi = \rho\omega b^2/\mu$), throughflow Reynolds number, C_w ($C_w = \dot{m}/\mu b$) , turbulent flow parameter, λ_T, pressure, p, mass flow, $\dot{m}$, and rotational speed, N.

Re_ϕ	$0.17 \times 10^7 \leq Re_\phi \leq 1.61 \times 10^7$
C_w	$0.29 \times 10^5 \leq C_w \leq 1.03 \times 10^5$
λ_T	$0.063 \leq \lambda_T \leq 0.601$
p (absolute, bar)	$2 \leq p \leq 5$
$\dot{m}$ (kg/s)	$0.12 \leq \dot{m} \leq 0.4$
N (rev/min)	$2000 \leq N \leq 10100$

Table 5.1 – Test conditions for the plain disc tests.

For each test, once the correct flow conditions had been achieved, the casing inlet and outlet air temperatures were monitored using platinum resistance thermometers (PRTs). Once the difference between the inlet and outlet air temperature changed by no more than 0.05 °C over a period of 120 seconds, the rig was considered to have stabilised. Only this last 120 s of data is then used in the results analysis. Figure 5.4 shows the casing inlet and outlet PRT temperatures for the duration of a plain disc test with the conditions $C_w = 0.28 \times 10^5$, $Re_\phi = 0.8 \times 10^7$, $\lambda_T = 0.09$.

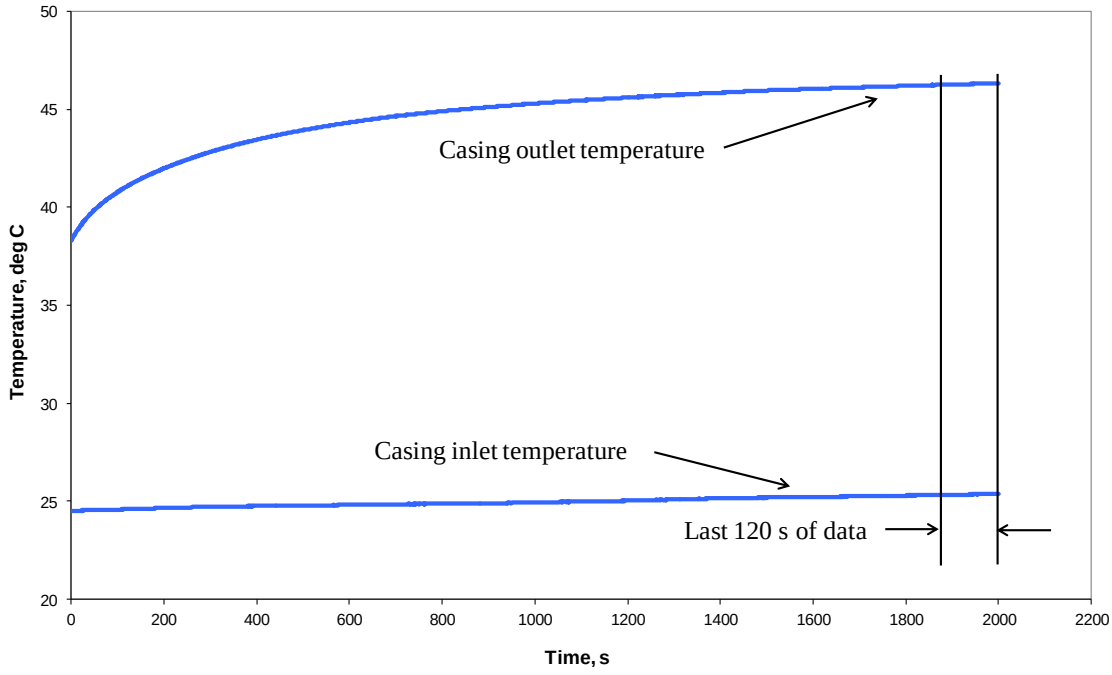

Figure 5.4 – Variation of inlet and outlet air temperatures with time for a plain disc test, $C_w = 0.28 \times 10^5$, $Re_\phi = 0.8 \times 10^7$ and $\lambda_T = 0.09$.

Torque measurements were acquired at 1 Hz throughout the duration of each test. Figure 5.5 shows a plot of the variation of torque with time for a plain disc test with the same conditions as in Figure 5.4, C_w = 0.28 x 10^5, Re_ϕ = 0.8 x 10^7 and λ_T = 0.09.

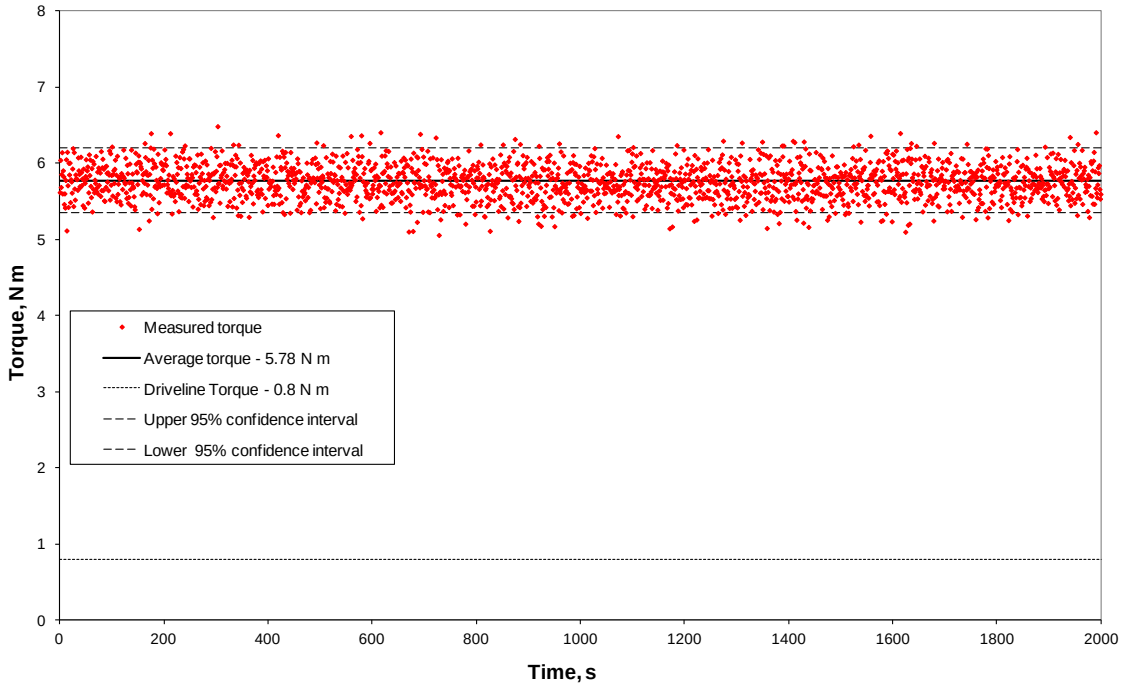

Figure 5.5 – Variation of torque with time for a plain disc, C_w = 0.28 x 10^5, Re_ϕ = 0.8 x 10^7 and λ_T = 0.09.

The average torque shown in Figure 5.5 is calculated from the last 120 seconds of data from the test. The driveline friction torque, calculated for this particular speed (8700 rev/min) from Equation 5.1, is shown as are the upper and lower 95% confidence intervals. The moment coefficient, C_m, is obtained from Equation 5.2, where M is the average net measured torque (after subtracting the driveline torque), ρ is calculated from the average pressure measurement at r/b = 0.53 and outlet air temperature (averaged from the two PRT outlet air temperature measurements, see Section 3.5.2), ω is the rotational speed and the disc radius, b = 0.225 m. All the data used in Equation 5.2 has been averaged over the last 120 s of data obtained from the test.

$$C_m = \frac{M}{\frac{1}{2}\rho\omega^2 b^5} \qquad \textbf{(5.2)}$$

Disc surface temperature measurements are also made throughout each test using infra red sensors. These sensors are positioned at five radial locations on the test side of the disc (the test side being the side of the test rig where the majority of the measurements are made): 0.096 m, 0.135 m, 0.154 m, 0.2 m and 0.2105 m (r/b = 0.427, 0.6, 0.684, 0.887 and 0.935). Measurements are also taken on the balance side at r = 0.2 m (r/b = 0.889), to check that flow conditions are equal on both sides of the disc. Figure 5.6 shows the variation of the disc surface temperature with time (for clarity only 1 in 20 data points are shown here) for each sensor, for the duration of a plain disc test with the conditions $C_w = 0.28 \times 10^5$, $\mathrm{Re}_\phi = 0.8 \times 10^7$ and $\lambda_T = 0.09$. The last 120 seconds of data, indicated in Figure 5.6, is then used to find an average temperature reading for each sensor.

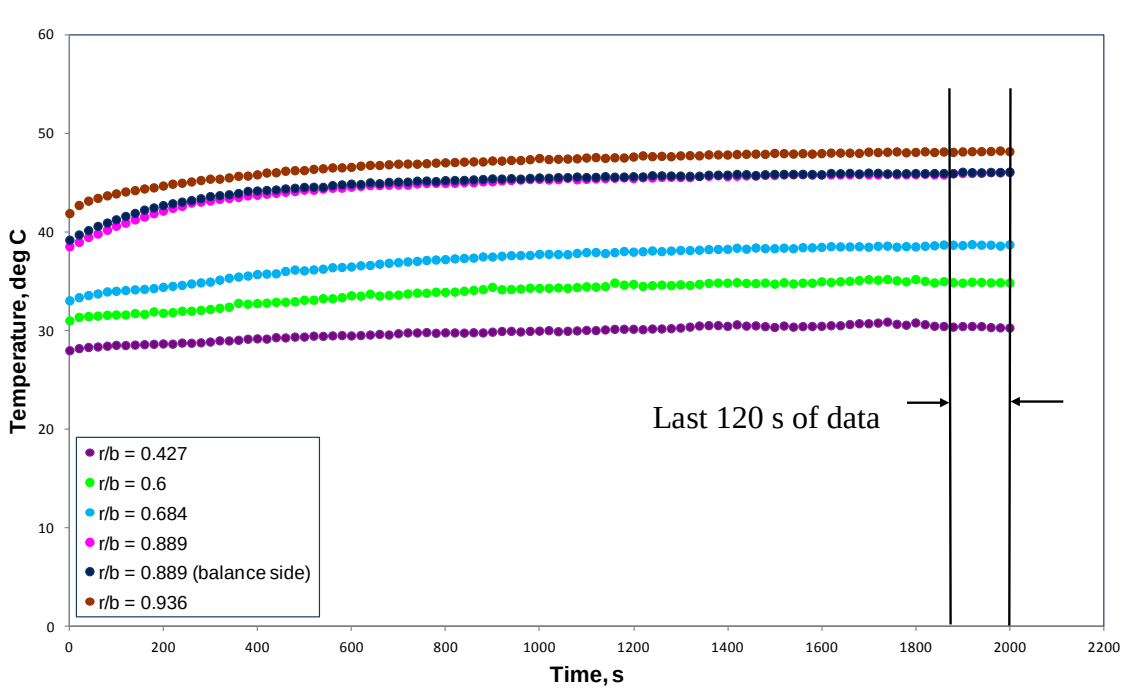

Figure 5.6 - Variation of disc surface temperature with time for a plain disc, $C_w = 0.28 \times 10^5$, $\mathrm{Re}_\phi = 0.8 \times 10^7$ and $\lambda_T = 0.09$.

The torque and disc surface temperature measurements were entered into a Microsoft Excel spreadsheet along with all other measurements made during the test including casing pressures, air temperatures and speed measurements; all of which are averaged over the final 120 seconds of data. The spreadsheet brings together the complete set of data and presents all the required information for each test: Pressures, temperatures, mass flows, rotational speed, torque measurements and non-dimensional parameters.

An example of the main page of the spreadsheet used to present this information is shown in Figure 5.7.

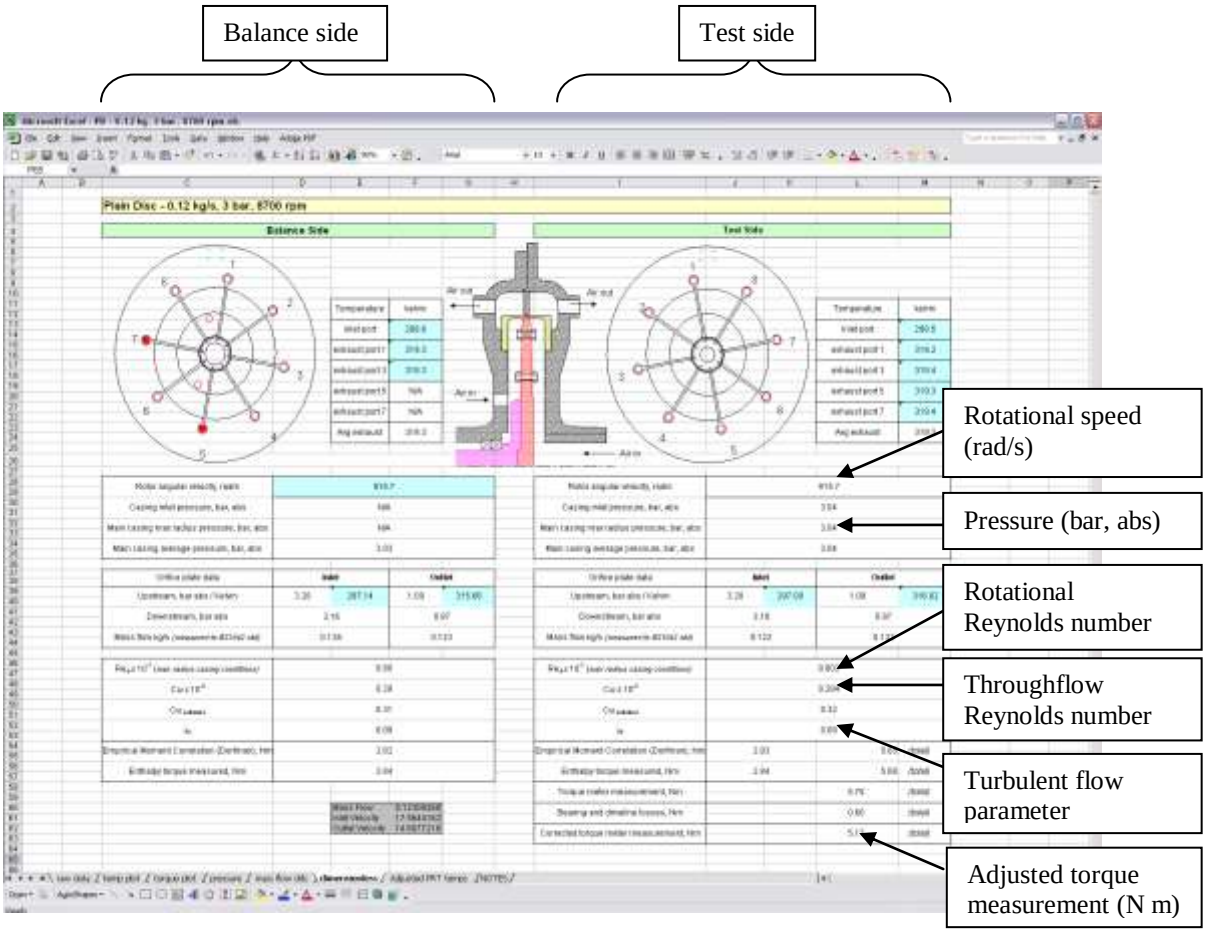

Figure 5.7 – Screen shot of the main page of a Microsoft Excel spreadsheet used to calculate the required data from the measurements obtained in each test.

5.5 Plain disc windage results

This section describes the windage results for the plain disc tests. Initially the windage measurements will be discussed and compared to the data previously obtained by **Coren (2007)** using the same test rig. Following this, the data will be compared to correlations and existing data for the free disc as well as similar rotor-stator systems.

5.5.1 Comparison with Coren (2007)

Figure 5.8 shows the variation of moment coefficient, C_m, with rotational Reynolds number, Re_ϕ, for the current plain disc test results along with those previously obtained on the same test rig by **Coren (2007)**.

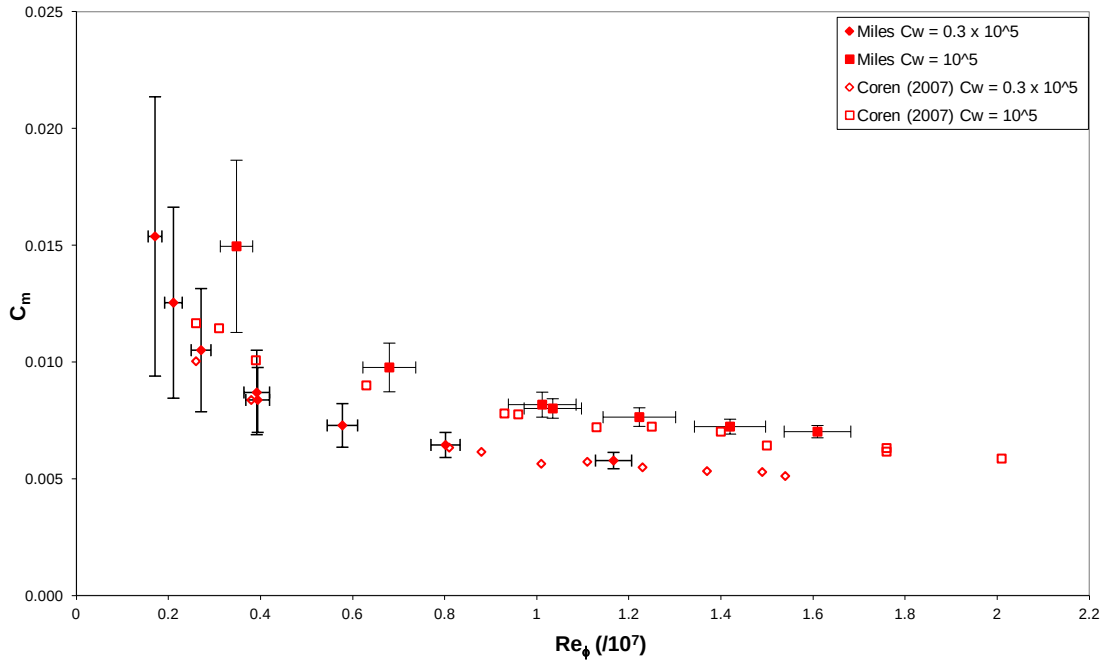

Figure 5.8 – Variation of C_m with Re_ϕ for current and previous plain disc test results, $0.05 \leq \lambda_T \leq 0.601$.

It can be seen from Figure 5.8 that there is generally good agreement between the two sets of data. Coren's measurements are within 4% of the current measurements where $C_w = 0.3 \times 10^5$. The variation between the results is slightly larger for $C_w = 10^5$, although still generally within 8%. The exception is where $C_w = 10^5$ and $Re_\phi = 0.35 \times 10^7$, the variation is as much as 23%. However, the relative uncertainty of the current measurement at this condition is 24%, and is likely to be similar for the measurement by Coren, therefore, although the variation between the measurements seems large, it is still within the limits of uncertainty.

A number of repeat tests were carried out and Figure 5.9 shows the results of a set of tests carried out on three separate occasions (referred to as Test 1, Test 2 and Test 3). The tests were undertaken at the conditions $C_w = 10^5$ and $Re_\phi = 0.68 \times 10^7$, 10^7 and $1.4 \times$

10^7. It can be seen that the results are consistent with one another to within the limits of uncertainty.

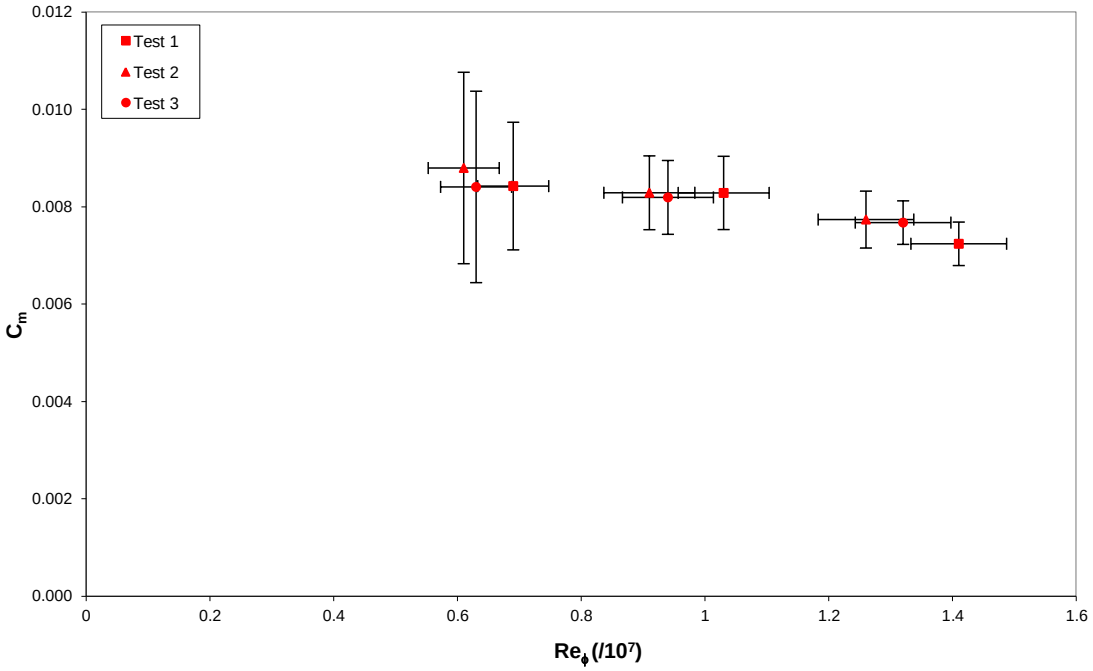

Figure 5.9 – Variation of C_m with Re_ϕ for plain disc repeatability tests carried out on three separate occasions, $C_w = 10^5$ and $0.158 \leq \lambda_T \leq 0.313$.

Selected plain disc tests were also carried out in the middle and at the end of the test programme. The results were found to agree to a similar extent as the repeatability tests shown in Figure 5.9.

It is possible that some pre-swirl could be introduced to the inlet air flow due to the configuration of the inlet air pipework. If swirl exists in the test rig, the windage and temperature measurements would be higher in one direction than the other. In order to detect if it is present, two plain disc tests with the same flow conditions were carried out, but with the disc rotating in different directions. The results from the two tests however, produced both torque and outlet air temperature measurements that were within 7% of each other. This is within the limits of measurement uncertainty, which at the flow condition tested is ±10%.

The consistency of the results between the current test program and the tests carried out by **Coren (2007)**, as well as the good repeatability shown within the current test program, leads to a high level of confidence in the data presented in this thesis.

5.5.2 Comparison with the free disc

Figure 5.10 shows the variation of moment coefficient, C_m, with rotational Reynolds number, Re_ϕ, for the current plain disc tests. Also shown are the theoretical free disc values obtained from the relationships given by **von Kármán (1921)** in Equation 5.3**, Dorfman (1958)** in Equation 5.4 and **Bayley and Owen (1969)** in Equation 5.5.

$$C_m = 0.146\,\mathrm{Re}_\phi^{-0.2} \qquad \textbf{(5.3)}$$

$$C_m = 0.982(\log_{10}\mathrm{Re}_\phi)^{-2.58} \qquad \textbf{(5.4)}$$

$$C_m = 0.131\mathrm{Re}_\phi^{-0.186} \qquad \textbf{(5.5)}$$

It can be seen that the relationships of Dorfman and Bayley and Owen have very similar values of C_m for a given value of Re_ϕ, although the two diverge slightly where $\mathrm{Re}_\phi < 0.6 \times 10^7$. They both have higher predicted values of C_m than the relationship produced by von Kármán throughout the range of rotational Reynolds numbers. This is due to differences in the assumptions made about the velocity profile within the boundary layer. Whereas von Kármán has assumed a $1/7^{th}$ power law, Dorfman and Bayley and Owen have used a logarithmic profile. The $1/7^{th}$ power law is generally thought to be a good approximation of the boundary layer velocity profile for $\mathrm{Re}_\phi < 10^6$. The logarithmic boundary layer velocity profile however, is thought to give a better approximation of real fluid conditions over a wider range of rotational Reynolds numbers, except in the region immediately adjacent to the disc. This is supported by the results shown in Figure 5.10, where the correlations of Dorfman and Bayley and Owen are closer to the current test results.

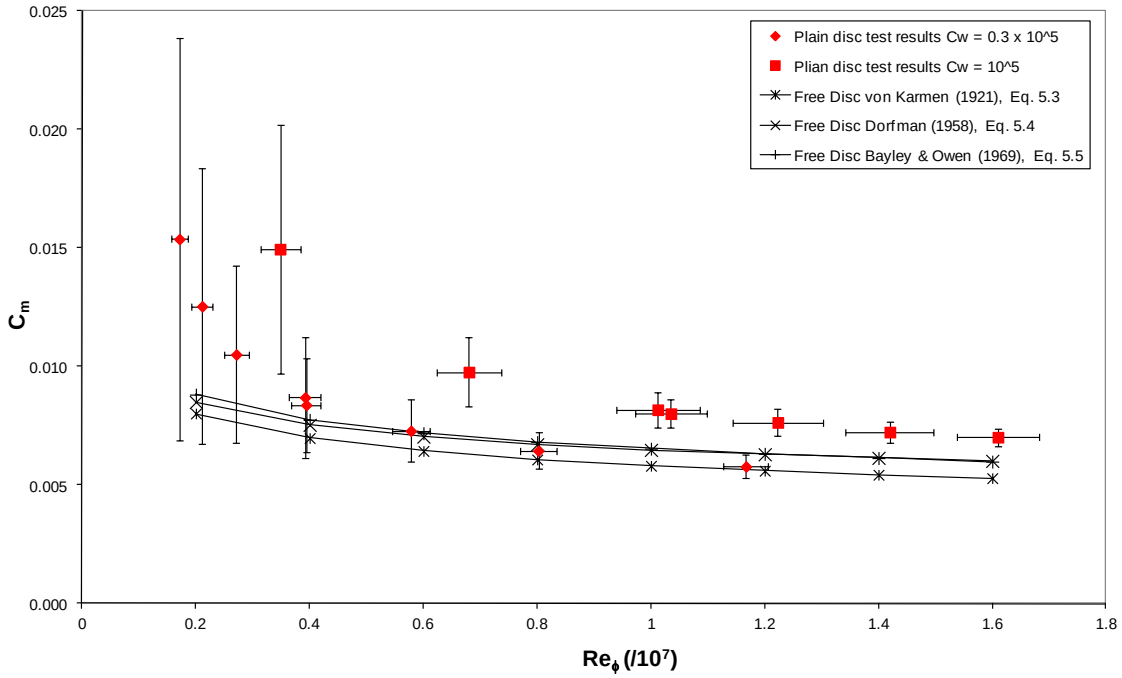

Figure 5.10 – Variation of C_m with Re_ϕ for plain disc test results, as well as existing correlations for a free disc, $0.063 \leq \lambda_T \leq 0.601$.

Figure 5.10 shows the moment coefficients obtained from the rotor-stator test facility for $C_w = 10^5$ to be higher than those obtained from the theoretical relationships given for a free disc. In principle a free disc should have higher frictional torque than a rotor-stator system. This is because for a free disc, the air away from the disc is stationary. In a rotor-stator system there is the central core of air rotating at a fraction of the disc speed, resulting in a smaller relative velocity between the disc and the core. However, the physical features of this test rig along with assumptions, that necessarily have to be made when dealing with turbulent flows, mean that this is not always the case.

One explanation for the higher than free disc moment coefficients obtained for the current test results could be the assumptions made about the velocity profile in the boundary layer. The boundary layer in the test rig may well be better modelled at these high values of rotational Reynolds number, using an alternative method to the logarithmic or $1/7^{th}$ power law profiles. The power law, which is generally used in the $1/7^{th}$ form for rotating flows, can also be used with indices other than $1/7^{th}$. It is generally accepted (**Schlichting (1955)**) that as the rotational Reynolds number increases, so does the denominator in the index, *n*. The expression developed by **Owen**

and Rogers (1989), shown in Equation 5.6, is used in Figure 5.11 to plot the variation of moment coefficient with rotational Reynolds number for the range $7 \leq n \leq 10$.

$$C_m = \varepsilon_m \, \mathrm{Re}_\phi^{-\frac{2}{n+3}} \qquad \textbf{(5.6)}$$

In Equation 5.6, ε_m is dependent on the value of n. Table 5.2 shows the values for ε_m, taken from Owen and Rogers, which account for only one side of the disc.

n	ε_m
7	0.0729
8	0.0561
9	0.0448
10	0.0365

Table 5.2 – Values of ε_m for varying power law index, n.

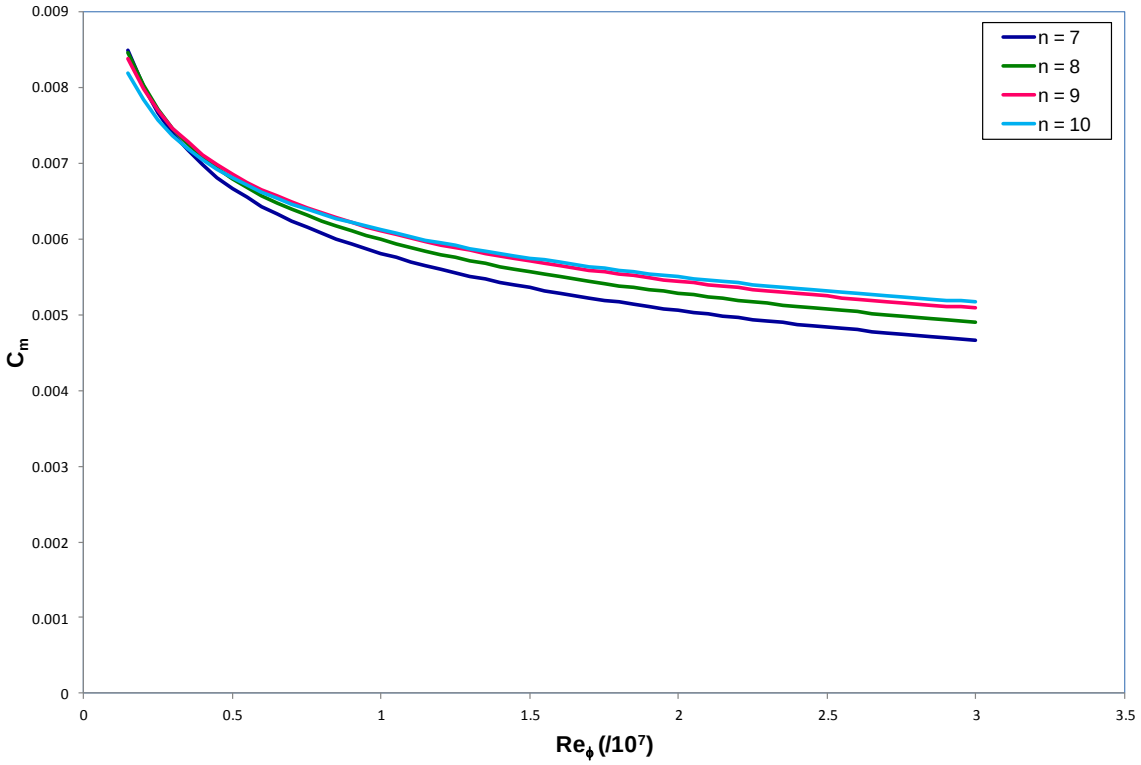

Figure 5.11 – Variation of C_m with Re_ϕ for Equation 5.6.

It can be seen from Figure 5.11 that for $Re_\phi > 0.5 \times 10^7$, as the value of n increases, the moment coefficient for a given value of Re_ϕ also increases. However, this increase in moment coefficient is small in comparison to the difference between the plain disc test results and the free disc correlation of von Kármán. This is illustrated in Figure 5.12, which shows the variation of moment coefficient with rotational Reynolds number for the plain disc test results as well as Equation 5.6 with $n = 7$ (von Kármán's solution) and $n = 10$.

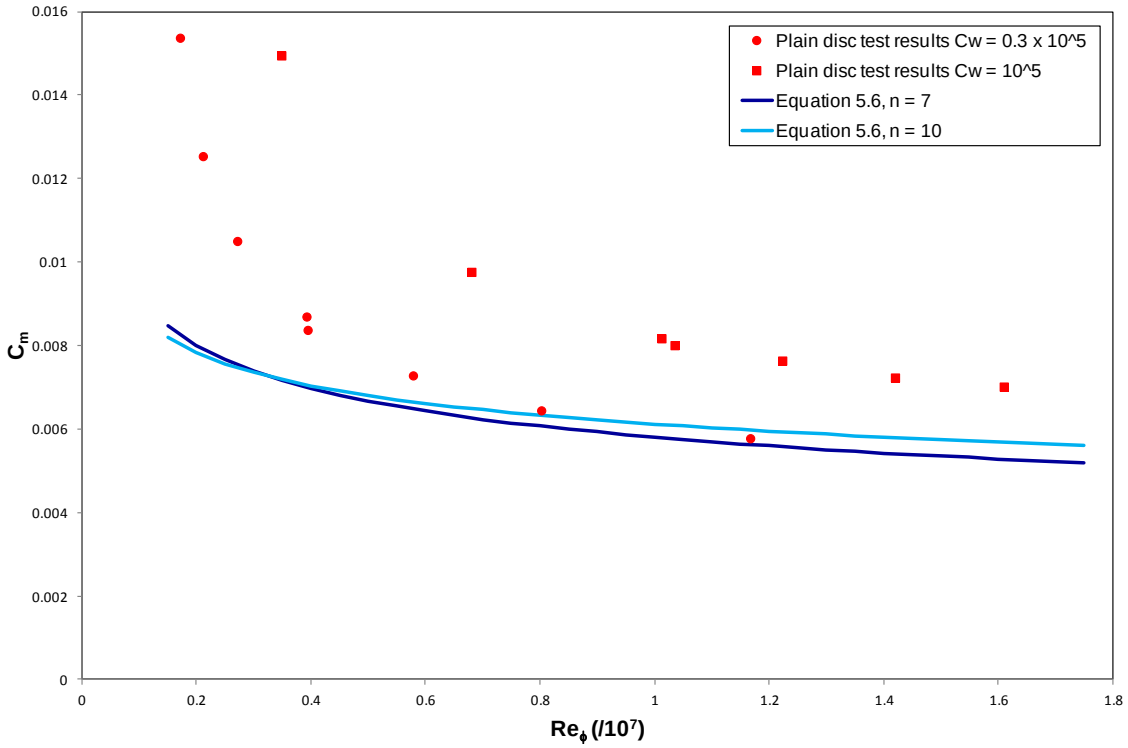

Figure 5.12 – Variation of C_m with Re_ϕ for Equation 5.6 and plain disc test results, $0.063 \leq \lambda_T \leq 0.601$.

It is more likely that the higher than free disc moment coefficients measured in the current test program, can be attributed to the design of the test rig rather than differences in the boundary layer velocity profile. The labyrinth seal around the perimeter of the disc is expected to generate a significant contribution to the measured torque. **Millward and Edwards (1994)** investigated the effects of labyrinth type seals on windage in rotor-stator systems. Details of which can be found in Section 2.8. They developed a correlation to predict the seal windage heating, Equation 2.57. This can be expressed as a torque, M_L, as shown in Equation 5.7, where L is the length of the seal surface (for the current test rig $L = 21.2$ mm) and ρ was calculated using the outlet air temperature

(taken as an average of the two PRT outlet air temperature measurements) and air pressure at r/b = 0.53.

$$M_L = C_{m,seal}\pi L\rho\omega^2 b^4 \qquad \textbf{(5.7)}$$

The parameter $C_{m,seal}$ is the seal moment coefficient which is calculated using Equation 5.8, where n_f is the number of fins (for the current test rig, n_f = 2)

$$C_{m,seal} = 0.06\left(\frac{C_w}{\mathrm{Re}_\phi}\right)^{0.55} n_f^{-0.65} \qquad \textbf{(5.8)}$$

The stated uncertainty by Millward and Edwards of Equation 5.7 is that it estimates the windage due to a labyrinth seal to within ±25%. Figure 5.13 shows the details of the labyrinth seal on the test disc.

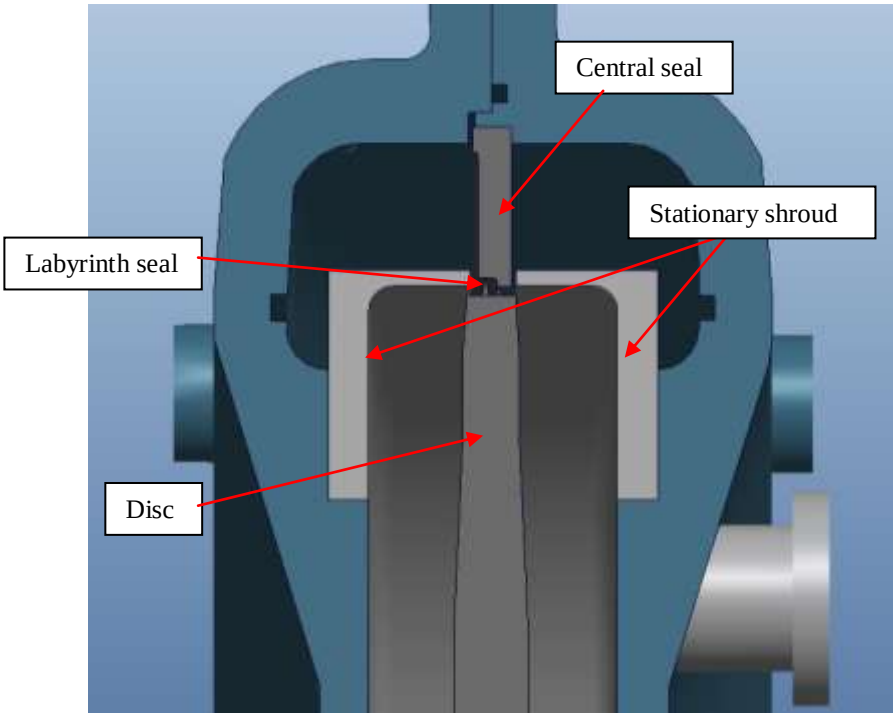

Figure 5.13 – Diagram showing detail of seal and shroud.

Using Equation 5.7 it is possible to modify the measured torque to allow for the windage due to the labyrinth seal. The data can then more readily be compared to the free disc data. It was found that the labyrinth seal in the current test rig contributes

between 16% and 23% of the total measured torque, depending on the flow conditions. Figure 5.14 shows the same data as Figure 5.10 but with the torque contribution from the labyrinth seal subtracted.

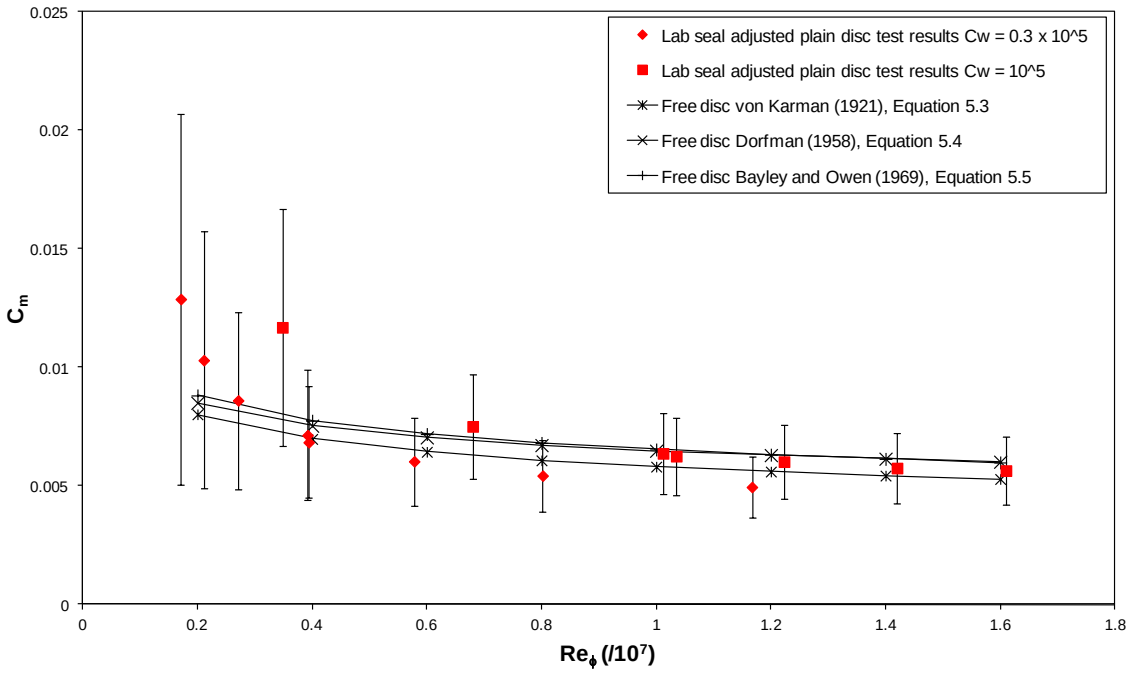

Figure 5.14 – Variation of C_m with Re_ϕ for a plain disc, with labyrinth seal windage adjustment, as well as existing correlations for a free disc, $0.063 \leq \lambda_T \leq 0.601$.

It can be seen that from Figure 5.14 that deducting the labyrinth seal windage from the current test data reduces the values of moment coefficient to similar to that of the free disc. Only where $\mathrm{Re}_\phi < 0.4 \times 10^7$, which is where the rotational speed drops below 3900 rev/min, does the test data diverge significantly from the free disc correlations. It is at these conditions that the uncertainties in the measurement are relatively high. The uncertainty bars in Figure 5.14 include the stated uncertainty in the labyrinth seal torque of ± 25%.

It is thought that the moment coefficient will also increase in a shrouded rotor-stator system with increasing gap ratio, G ($G = s/b$, where s is the axial spacing between the rotor and the stator, and b is the radius of the disc). This is due to the increasing surface area of the shroud causing increased frictional resistance. However, **Haynes and Owen (1975)** showed, both analytically and experimentally, that for $0.06 \leq G \leq 0.18$ the effect of G on the moment coefficient is weak. The current experimental set up has a

gap ratio G = 0.102. Consequently, adjustments to account for the shroud windage are not deemed necessary.

5.5.3 Comparison with rotor-stator systems

Owen (1987) and **Gartner (1997)** have both produced analytical predictions for windage in a rotor-stator system with superimposed throughflow. These are discussed in more detail in Section 2.4. In their calculations they both distinguish between rotationally dominant flow ($\lambda_T < 0.219$) and radially dominant flow ($\lambda_T > 0.219$).

For the rotationally dominant flow condition, both Owen and Gartner's models identify two separate regions of flow: the source region near the axis of the rotating disc, and the core rotation region located radially outwards of the source region. Equations 5.9 and 5.10 show Owen's relationships for calculating the moment coefficient in the source region and the core rotation region respectively.

$$C_{m1} = 0.0729\,\mathrm{Re}_\phi^{-\frac{1}{5}}\, x_c^{\frac{23}{5}} \qquad \textbf{(5.9)}$$

$$C_{m2} = 0.0398\,\mathrm{Re}_\phi^{-\frac{1}{5}}\left[\left(1 - x_c^{\frac{23}{5}}\right) + 14.7\lambda_T\left(1 - x_c^2\right) + 90.4\lambda_T^2\left(1 - x_c^{-\frac{3}{5}}\right)\right] \qquad \textbf{(5.10)}$$

The parameter, x_c, is defined as the radial location where the source region ends and core rotation begins and is dependent on λ_T. The equation for calculating x_c is shown in Equation 5.11.

$$x_c = 1.79\lambda_T^{\frac{9}{13}} \qquad \textbf{(5.11)}$$

The results for the two regions are then combined to give the total moment coefficient for the whole disc, shown in Equation 5.12.

$$C_m = C_{m1} + C_{m2} \qquad \textbf{(5.12)}$$

Gartner's model adds to Owen's model a component of windage resulting from the circumferential shroud, which is proportional to the gap ratio, *G*. Gartner's model can be seen in Equation 5.13.

$$C_m = C_{m1} + C_{m2} + C_{m3} \qquad \textbf{(5.13)}$$

C_{m1} and C_{m2} are given in Equations 5.9 and 5.10. The third component, C_{m3}, is calculated using Equation 5.14 where β is the core rotation factor, and γ is a number derived directly from β. The methods for calculating β and γ are in Section 2.4, Equations 2.33 to 2.35.

$$C_{m3} = 0.18\frac{s}{b}\gamma^{-\frac{1}{4}}\beta^{\frac{7}{4}}(1-\beta)^{-\frac{3}{20}}\mathrm{Re}_{\phi}^{-\frac{1}{5}} \qquad \textbf{(5.14)}$$

Figure 5.15 shows the variation of C_m with Re_ϕ for $\lambda_T < 0.219$, where the flow is expected to be rotationally dominant. The plot shows the current test results along with the analytical predictions produced by Owen and Gartner. It can be seen from Figure 5.15, the additional term in Gartner's model makes little difference to the total moment coefficient predicted by Owen's model for the current values of $G = 0.102$ and $0.28 \times 10^5 \leq C_w \leq 1.01 \times 10^5$.

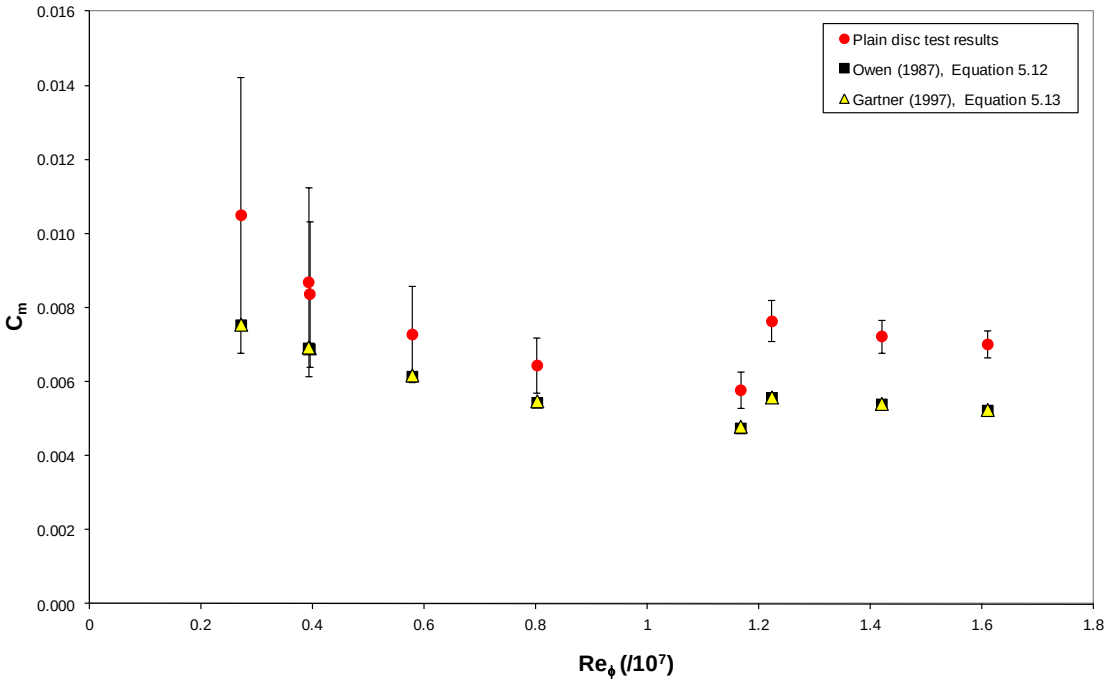

Figure 5.15 – Variation of C_m with Re_ϕ for a plain disc, as well as analytical predictions for a rotor-stator cavity with throughflow, $\lambda_T < 0.219$ and $0.28 \times 10^5 \leq C_w \leq 1.01 \times 10^5$.

The measured test results show higher values of moment coefficient than both Owen and Gartner's analytical models. However neither of these models account for the windage resulting from air exiting the cavity through a labyrinth seal. When the labyrinth seal windage, calculated using Equation 5.7, is subtracted from the test data both models give a very good prediction of the windage in the test rig. This can be seen in Figure 5.16 which shows the same data as in Figure 5.15, but with the windage adjustment applied to the test data.

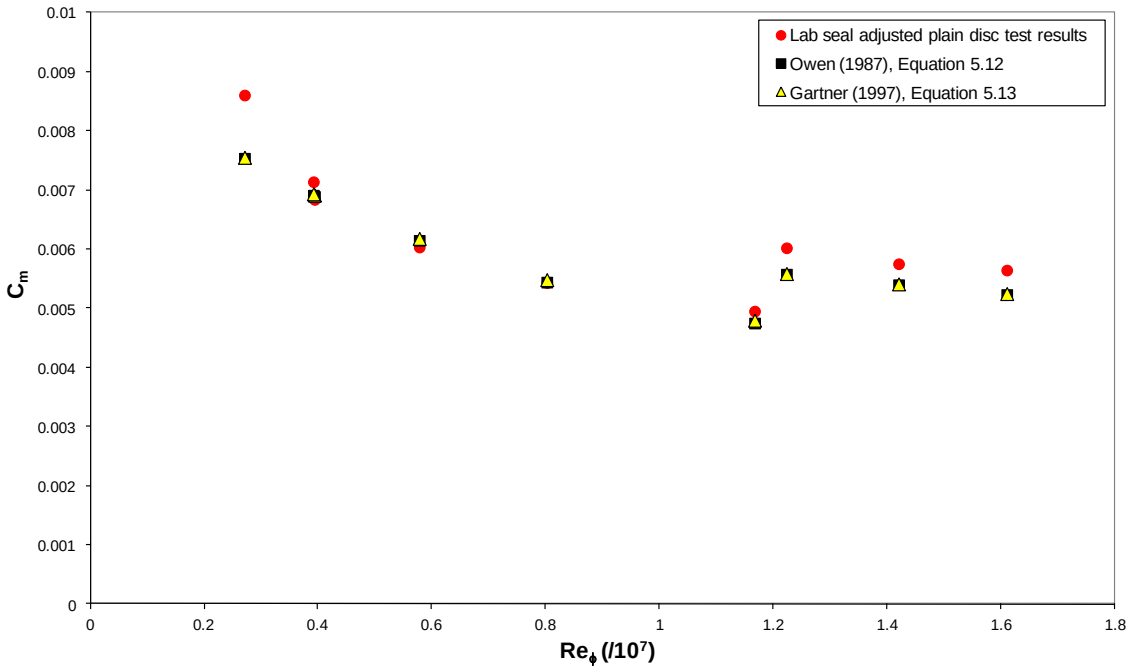

Figure 5.16 – Variation of C_m with Re_ϕ for a plain disc, with labyrinth seal windage adjustment, as well as analytical predictions for a rotor-stator cavity with throughflow, $\lambda_T < 0.219$ and $0.28 \times 10^5 \leq C_w \leq 1.01 \times 10^5$.

In Figures 5.15 and 5.16 there appears to be a sudden increase in C_m when $Re_\phi > 1.2 \times 10^7$. This is explained by the fact that where $Re_\phi > 1.2 \times 10^7$ the tests are carried out with a high superimposed throughflow, $C_w = 10^5$. Where $Re_\phi < 1.2 \times 10^7$ the tests are carried out with low superimposed throughflow, $C_w = 0.3 \times 10^5$.

For the radially dominant flow condition, $\lambda_T > 0.219$, Owen assumes a wall jet solution to be valid, whereby the superimposed flow is forced into the boundary layer on the disc. Under this assumption he derived the expression for the moment coefficient shown in Equation 5.15.

$$C_m = 0.333\lambda_T \, Re_\phi^{-\frac{1}{5}} \qquad \textbf{(5.15)}$$

To gain this solution, Owen solved the momentum integral equation and the conservation of mass to gain a solution for the boundary layer thickness. However, the boundary layer thickness in his solution can become larger than the axial distance between the rotor and stator. So Gartner made the assumption that the boundary layer

thickness is constant and equal thickness to the axial gap between rotor and stator. Using this assumption Gartner derived the expression for the moment coefficient shown in Equation 5.16.

$$C_m = 0.2827\,\mathrm{Re}_\phi^{-\frac{1}{4}}\left(\frac{s}{b}\right)^{-\frac{1}{4}}\int_0^b\left(\frac{r}{b}\right)^{\frac{15}{4}}\left[1+\frac{0.02533\lambda_T^2\,\mathrm{Re}_\phi^{-0.08}\left(s/b\right)^{1.14}}{\left(0.0017+0.0162\lambda_T\right)^2}\left(\frac{r}{b}\right)^{-4}\right]^{\frac{3}{8}}\frac{1}{b}\,dr \qquad \textbf{(5.16)}$$

Figure 5.17 shows the variation of C_m with Re_ϕ for $\lambda_T > 0.219$ and $0.3 \times 10^5 \leq C_w \leq 1.03 \times 10^5$. The plot shows the measured test data along with Owen and Gartner's models. It can be seen that Owen's model tends to under predict the test results, whereas Gartner's tends to over predict them.

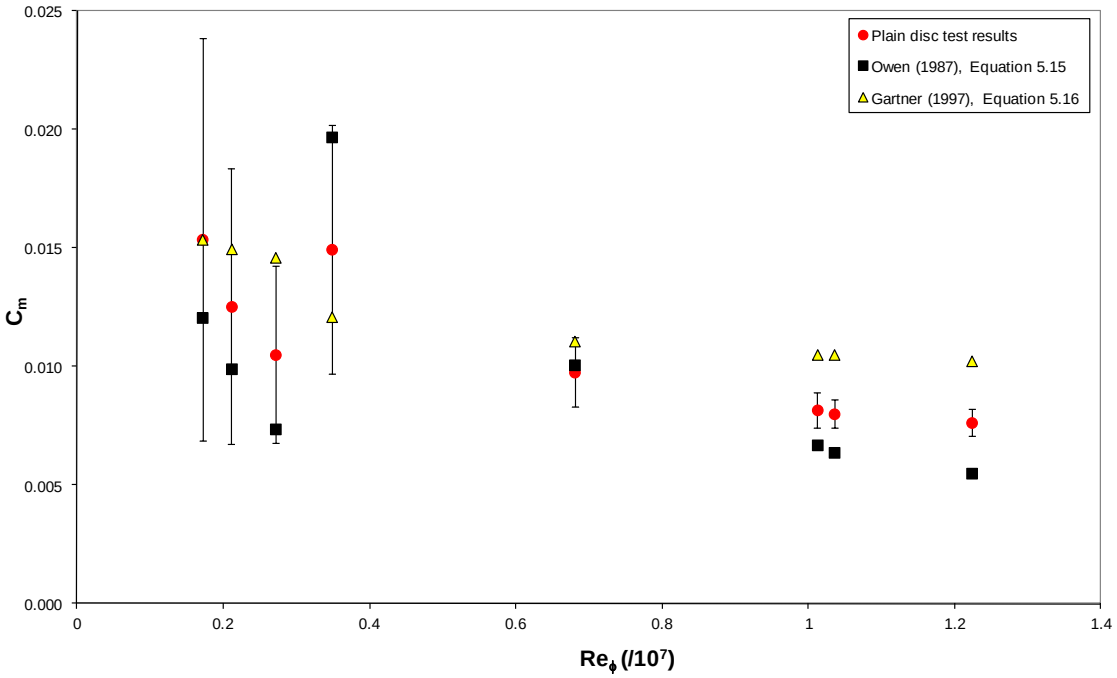

Figure 5.17 - Variation of C_m with Re_ϕ for a plain disc, as well as analytical predictions for a rotor-stator cavity with throughflow, $\lambda_T > 0.219$ and $0.3 \times 10^5 \leq C_w \leq 1.03 \times 10^5$.

Figure 5.18 shows the same data as in Figure 5.17, but with the drag associated with the labyrinth seal (calculated using Equation 5.7) subtracted. It can be seen that Owen's model gives much better agreement with the data than Gartner's model.

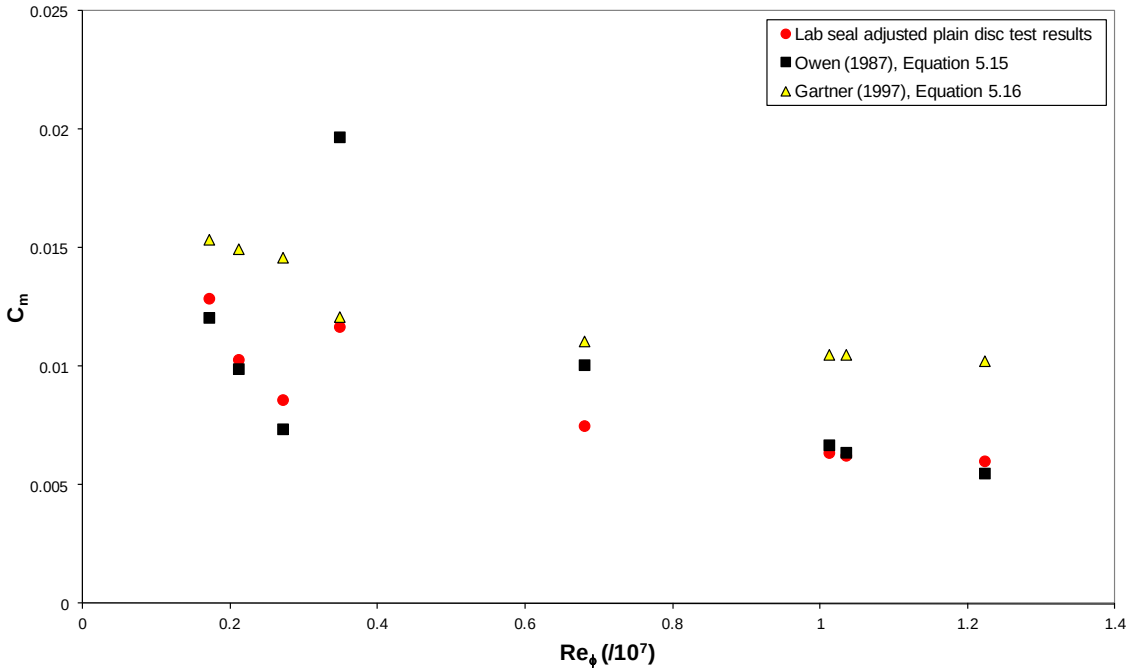

Figure 5.18 - Variation of C_m with Re_ϕ for a plain disc, with labyrinth seal windage adjustment, as well as analytical predictions for a rotor-stator cavity with throughflow, $\lambda_T > 0.219$ and $0.3 \times 10^5 \leq C_w \leq 1.03 \times 10^5$.

A comparison was made of the current test results with both analytical and empirical correlations (Equations 5.17 and 5.18 respectively) obtained by **Daily *et al.* (1964)**. Their experiments were carried out on a test facility similar to that of the current test rig, details of the test rig and testing method they used can be found in Section 2.4.

$$C_m = \left[\frac{0.663}{b^{\frac{23}{5}} \mathrm{Re}_\phi^{0.2}} \right] \int_0^b r^{\frac{18}{5}} (1-\beta)^{\frac{5}{4}} \left[1 + \left(\frac{0.162}{1-\beta} \right)^2 \right]^{\frac{3}{8}} dr \qquad \textbf{(5.17)}$$

$$\frac{C_m - C_{m,o}}{C_{m,o}} = 13.9 \beta^* \frac{\lambda_T}{\left(s/b \right)^{0.125}} \qquad \textbf{(5.18)}$$

In Equation 5.17, β represents the core velocity when superimposed throughflow is present in the cavity. It can be calculated from Equation 5.19, using the theoretical maximum core velocity with no throughflow, β^*. For $G = 0.102$, $\beta^* = 0.43$ as specified

by **Daily and Nece (1960)**. In Equation 5.19, C is a constant chosen to be 12.74 by Daily et al. to match experimental data at r/b = 0.648.

$$\beta = \beta^* \left[1 + \frac{C\lambda_T}{\left(r/b\right)^{2.6}} \right]^{-1} \qquad \textbf{(5.19)}$$

In Equation 5.18 the left hand side of the equation represents the fractional increase in moment coefficient as compared with the no throughflow case found by Daily and Nece using the same test rig, but without the ability to superimpose fluid into the cavity. The parameter $C_{m,0}$ represents the moment coefficient with no superimposed throughflow. The work by Daily and Nece is discussed in Section 2.3. For turbulent flow with separate boundary layers, as is the case with the current test facility, Daily and Nece found the moment coefficient with no throughflow to be as shown in Equation 5.20.

$$C_{m,0} = 0.102\left(\frac{s}{b}\right)^{0.1} \mathrm{Re}_\phi^{-0.2} \qquad \textbf{(5.20)}$$

Figure 5.19 shows the variation of C_m with Re_ϕ for the current test results as well as the theoretical and empirical correlations of Daily *et al.*. The no throughflow case of Daily and Nece is also shown. By showing their correlation (Equation 5.20) in Figure 5.19, the extent that the windage is increased due to the superimposed fluid is illustrated.

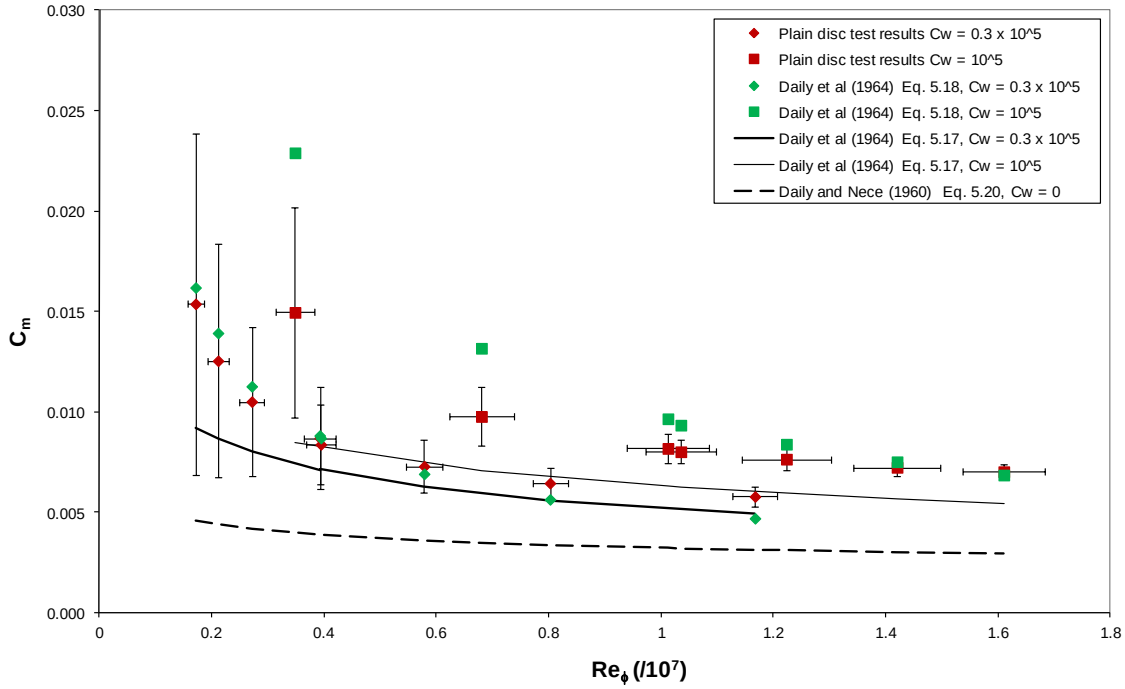

Figure 5.19 – Variation of C_m with Re_ϕ for a plain disc, as well as the analytical and empirical correlations for an enclosed rotor-stator system with throughflow, $0.063 \leq \lambda_T \leq 0.601$.

It can be seen that the Daily *et al.* empirical correlation (Equation 5.18) for $C_w = 0.3 \times 10^5$ shows very good agreement with the current measured test data. For the analytical prediction (Equation 5.17), although still within the limits of uncertainty, the agreement with test data is not quite as good. For $C_w = 10^5$, Equation 5.18 corresponds well to the current test data when $\mathrm{Re}_\phi > 10^7$. However below this the results diverge, with the current test results showing lower moment coefficients than the correlation. The analytical prediction, Equation 5.17, for $C_w = 10^5$ significantly under predicts the moment coefficients obtained from the current experiments.

The current experimental data was not adjusted to account for losses due to the labyrinth seal when comparing it to the empirical correlation of Daily *et al.*. The reason being that although there is no labyrinth seal present on the test facility used by Daily *et al.*, there will inevitably be losses due to the fluid exiting from the rotor-stator cavity. As it is not possible to put a value on the losses present in the Daily *et al.* test facility, it is more appropriate to compare the data without any adjustments. It is possible that the difference between the losses from the two experimental test rigs may account for the differences seen between the two sets of data where $\mathrm{Re}_\phi < 10^7$.

The analytical correlation produced by Daily *et al.* was shown in Figure 5.19 to under predict the test results quite substantially where $C_w = 10^5$. This correlation does not take into account any losses arising from the air leaving the enclosed rotor-stator cavity. When the current test results are adjusted to remove the labyrinth seal windage, as seen in Figure 5.20, the agreement with the analytical predictions of Daily *et al.* is very good, except where $Re_\phi < 0.4 \times 10^7$, a region in which the experimental uncertainties become relatively large.

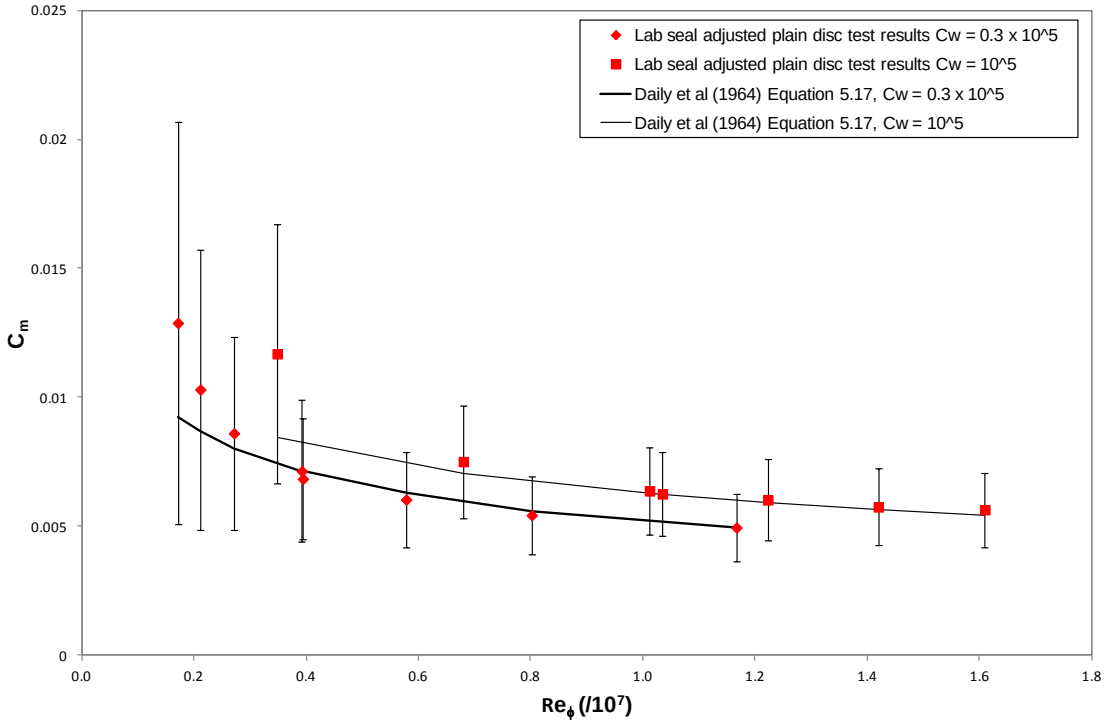

Figure 5.20 – Variation of C_m with Re_ϕ for a plain disc, as well as the analytical correlation of Daily *et al.* for an enclosed rotor-stator system with throughflow, $0.063 \leq \lambda_T \leq 0.601$.

The limits of the experimental work carried out by Daily *et al.* are $0 < \lambda_T < 0.083$. Consequently, their correlation is only valid for rotationally dominant flow. This can be seen clearly in Figure 5.21 which shows the variation of C_m with λ_T, for the current test data along with the analytical and empirical correlations from Daily *et al.* (Equations 5.17 and 5.18 respectively). Where $\lambda_T < 0.219$, the current test results and Equation 5.18 are in good agreement. At higher values of λ_T, Equation 5.18 does not account for the case of radially dominated flow where C_m becomes less sensitive to changes in λ_T, therefore Equation 5.18 gives much larger moment coefficients for a given value of λ_T

than the current test results. The analytical prediction by Daily *et al.* (Equation 5.17), however, does account for the case of radially dominated flow. This can be seen in Figure 5.21, more noticeably where $C_w = 0.3 \times 10^5$, by the reducing gradient of the curve at higher values of λ_T.

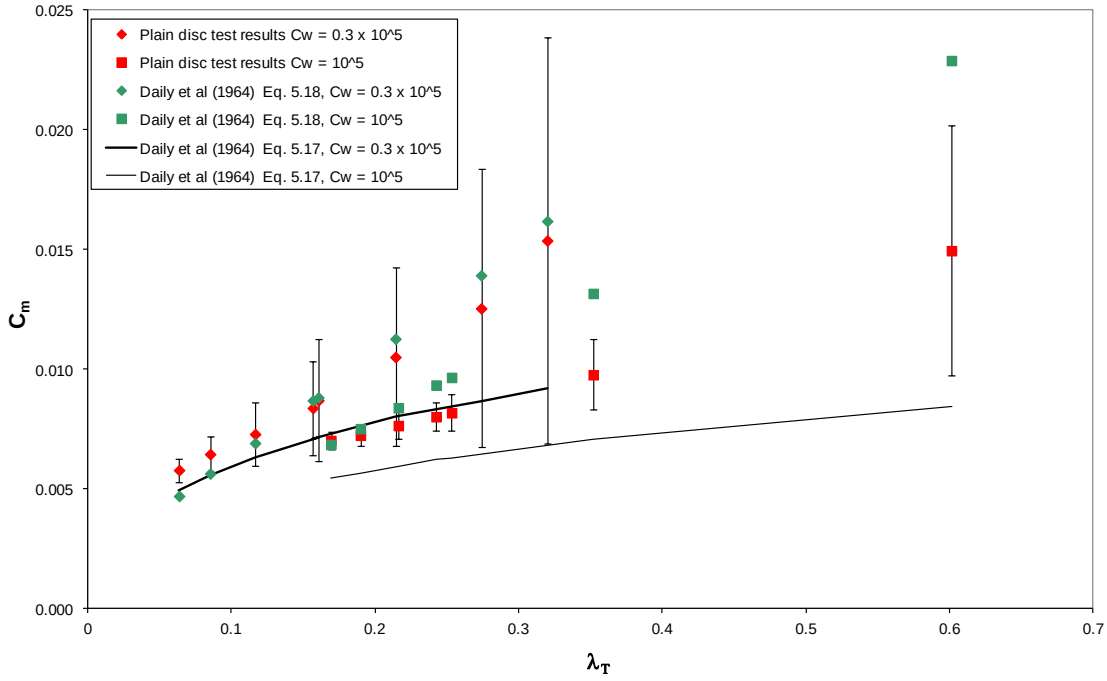

Figure 5.21 – Variation of C_m with λ_T for a plain disc, as well as the analytical and empirical correlations for an enclosed rotor-stator system with throughflow, $0.17 \times 10^7 \leq \mathrm{Re}_\phi \leq 1.6 \times 10^7$.

Figure 5.22 shows the variation of C_m with Re_ϕ but this time compared to the results obtained by **Zimmermann *et al.* (1986)**. The correlation given by Zimmermann *et al.* for the moment coefficient, of an enclosed rotor-stator system with superimposed throughflow, is given by Equation 5.21. The correlation consists of an empirical correction factor added to von Kármán's free disc relationship (Equation 5.3) between moment coefficient and rotational Reynolds number. This term is included in the square brackets. The original value of leading constant (= 0.073) in Zimmermann *et al.*'s correlation has been multiplied by a factor of two in Equation 5.21 to account for both sides of the disc, enabling a direct comparison with the current test data.

$$C_m = 0.146\,\mathrm{Re}_\phi^{-0.2}\left[1+10^{-4}C_w\left(4.1\mathrm{Re}_\phi^{-0.16}-0.32\right)\right] \qquad \textbf{(5.21)}$$

It can be seen in Figure 5.22 that for $C_w = 0.3 \times 10^5$ there is reasonable agreement between the two sets of results, but for $C_w = 10^5$ the current plain disc test results show higher values of moment coefficient then those predicted by Zimmermann *et al.*.

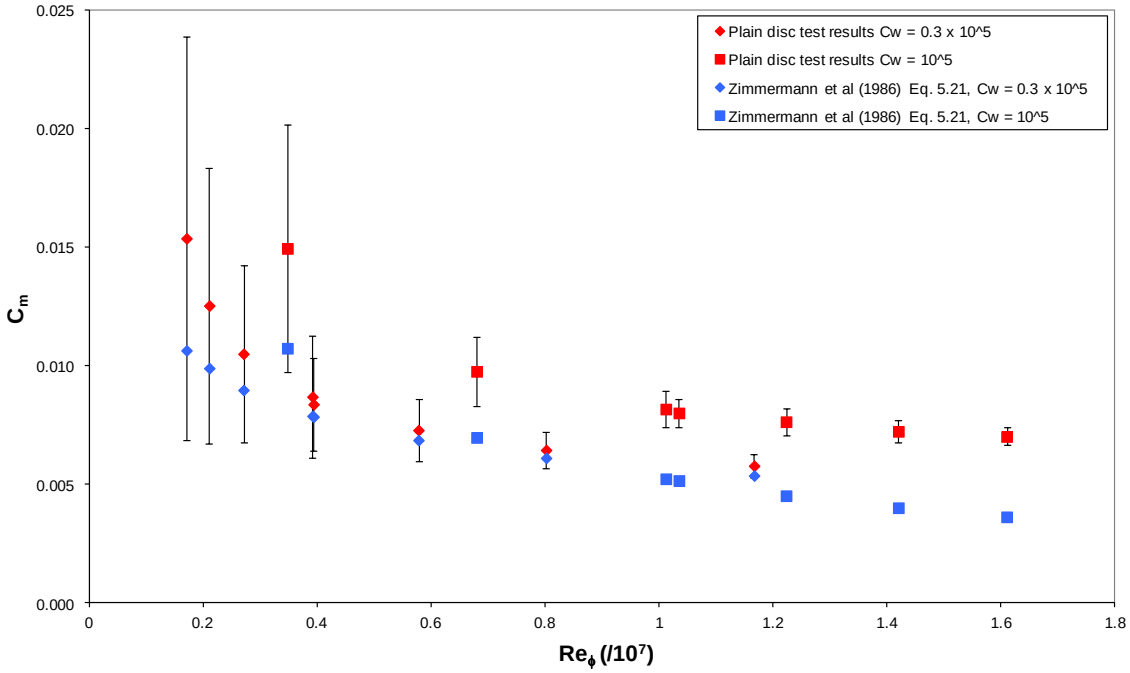

Figure 5.22 – Variation of C_m with Re_ϕ for a plain disc, as well as the correlation of Zimmermann *et al.* (1986) for an enclosed rotor-stator system with throughflow, $0.063 \leq \lambda_T \leq 0.601$.

One possibility for this is again to do with the increased torque due to the labyrinth seal in the current test facility (the results in Figure 5.22 have not been adjusted). But, again, although Zimmermann *et al.*'s test facility does not have a labyrinth seal, there would almost certainly be some losses due to the air exiting the cavity. The difference in the losses between the two test facilities could possibly account for the large difference in moment coefficient seen at the higher values of C_w. A more likely cause however is that the results of Zimmermann *et al.* were obtained using a low superimposed throughflow of $C_w = 0.26 \times 10^5$ and a maximum rotational Reynolds number of $\mathrm{Re}_\phi = 0.7 \times 10^7$. Looking at Figure 5.22, it can be seen that it is at similar conditions to these ($C_w = 0.3 \times 10^5$, $\mathrm{Re}_\phi < 0.7 \times 10^7$) that there is good agreement between the two sets of data. It would therefore be reasonable to assume that the correlation produced by Zimmermann *et al.* does not apply very well outside the range of his experimental data.

Figures 5.23 and 5.24 show the variation of C_m with Re_ϕ for all the correlations for rotor-stator systems introduced within this section, along with the current test results, for $C_w = 0.3 \times 10^5$ and $C_w = 10^5$ respectively. Throughout Section 5.5 the current test results have been compared to each individual correlation separately, and not all show very close agreement. However, it can be seen in Figures 5.23 and 5.24 that although there are slight variations between the current test data and each individual correlation, there are larger variations between the correlations themselves. Figures 5.23 and 5.24 both show that the current test results, without any adjustments applied, sit comfortably within the range of the various correlations.

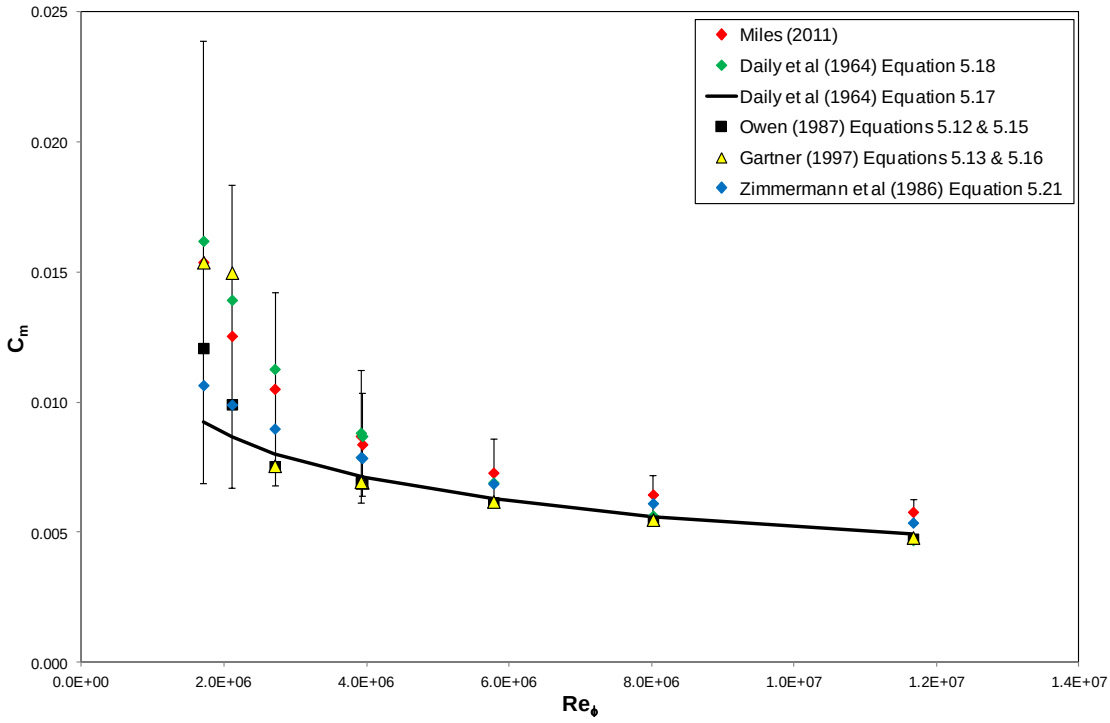

Figure 5.23 – Variation of C_m with Re_ϕ for current test results and all correlations for an enclosed rotor-stator system with throughflow, $C_w = 0.3 \times 10^5$ and $0.06 \leq \lambda_T \leq 0.32$.

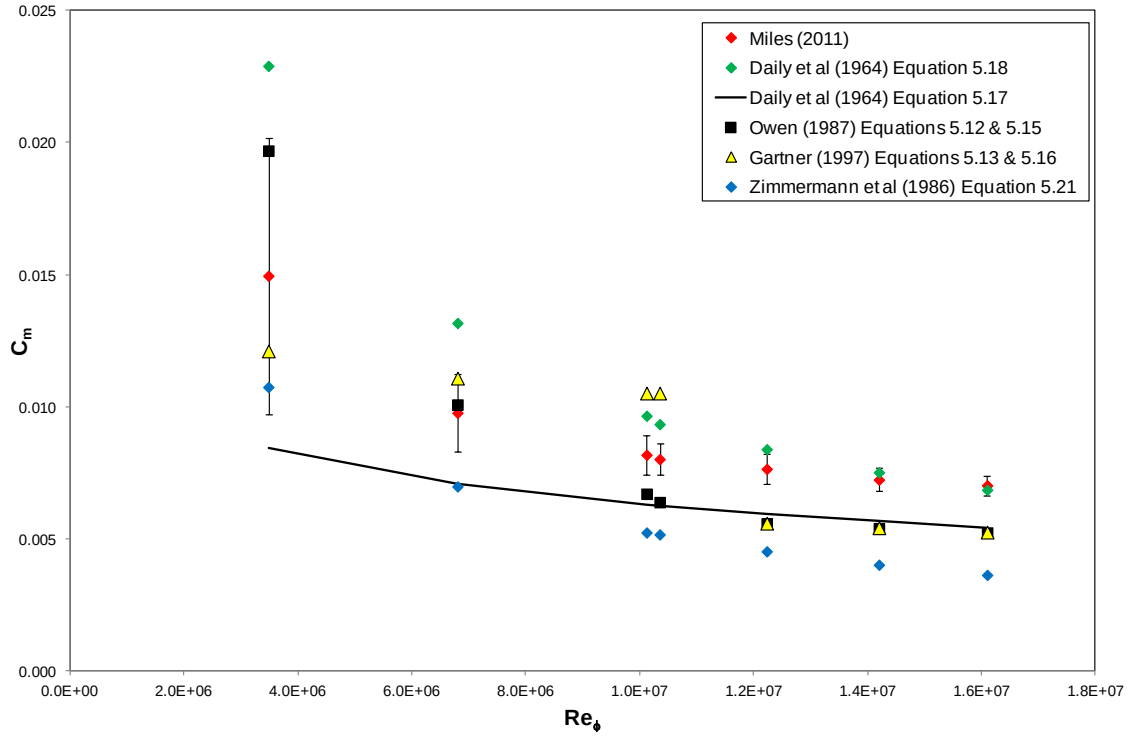

Figure 5.24 – Variation of C_m with Re_ϕ for current test results and all correlations for an enclosed rotor-stator system with throughflow, $C_w = 10^5$ and $0.17 \leq \lambda_T \leq 0.6$.

5.6 Plain disc surface temperature results

This section discusses the disc surface temperature results acquired using the infra red sensors. The results are compared to the theoretical adiabatic disc temperature for a free disc from **Owen and Rogers (1989)**, as well as the results obtained by **Coren (2007)** in the previous test phase.

5.6.1 Comparison to the free disc case

As mentioned earlier in this chapter, the disc surface temperature measurements are taken at five radii on the test side (r/b = 0.427, 0.6, 0.684, 0.887 and 0.935) as well as at one radius on the balance side (r/b = 0.887). The last 120 seconds of data, from each sensor for each test, is averaged to get a temperature measurement for each position on the disc. Since there are variations in inlet temperature from one test to another, the data is presented in terms of the disc-surface-to-inlet-air temperature difference. Figure 5.25 shows a plot of the variation of disc-surface-to-inlet-air temperature difference

with non-dimensional radius for a test with the conditions C_w = 0.28 x 10^5, Re_ϕ = 0.8 x 10^7 and λ_T = 0.09. The uncertainty bars shown are calculated using the method described in Section 4.3.2.

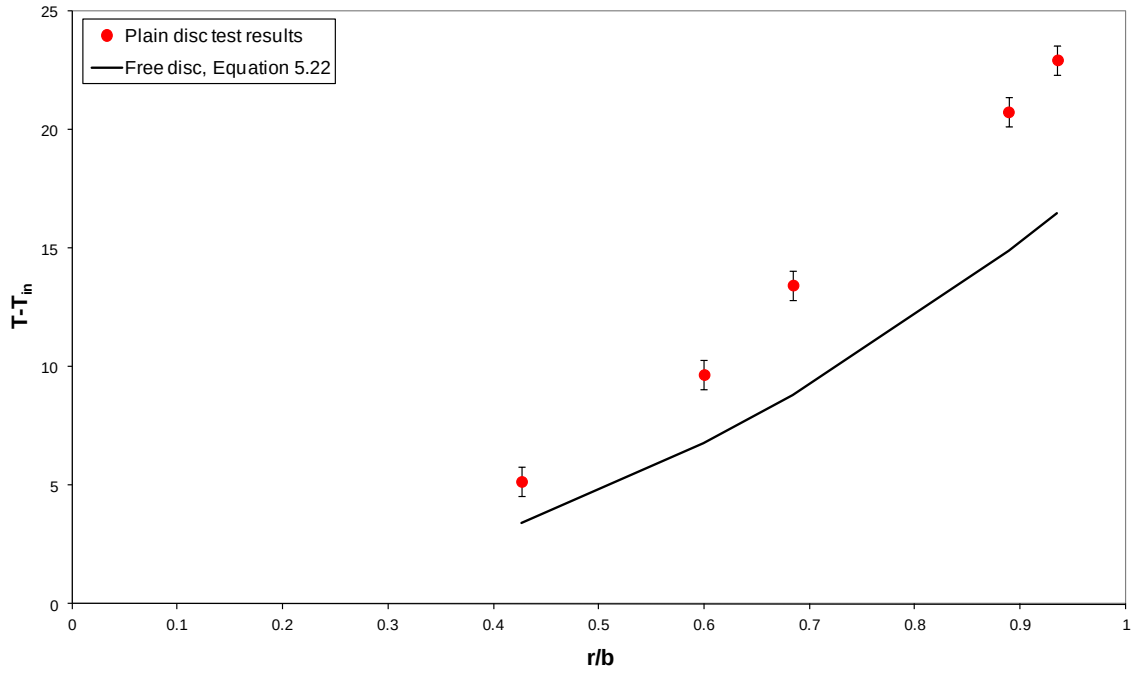

Figure 5.25 – Variation of disc-surface-to-inlet-air temperature rise with non-dimensional radius for a plain disc, as well as the theoretical values for a free disc, C_w = 0.28 x 10^5, Re_ϕ = 0.8 x 10^7 and λ_T = 0.09.

Also shown in Figure 5.25 is the theoretical adiabatic disc-surface-to-inlet-air temperature difference for a free disc calculated using Equation 5.22 from **Owen and Rogers (1989)**:

$$T_{0,ad} - T_\infty = R\frac{\omega^2 r^2}{2C_p} \qquad \textbf{(5.22)}$$

Where $T_{0,ad}$ is the adiabatic disc temperature and T_∞ is the temperature of the air far away from the disc, taken here as the static temperature measured at the inlet to the rotor-stator cavity. C_p is the specific heat of the air at constant pressure, calculated using T_∞. The recovery factor R was taken to be 0.9 from the approximation that R =

$Pr^{1/3}$. Pr is the Prandtl number, evaluated from Equation 5.23 where k is the thermal conductivity and μ is the dynamic viscosity of the air.

$$\mathrm{Pr} = \frac{\mu Cp}{k} \qquad \textbf{(5.23)}$$

It can be seen in Figure 5.25 that the increase in temperature for the plain disc is higher than that expected of a free disc. The moment coefficient results presented earlier in this chapter, showed that at this particular condition the plain disc moment coefficient is very similar to the free disc correlations. One possible reason why the measured disc surface temperature is higher than that predicted for a free disc when the measured torque is similar, is that heat generated by the labyrinth seal could be conducting through the disc. This theory is supported by the fact that the difference between the measured disc temperature and the theoretical free disc temperature increases with radius. Another possible reason is that at the condition shown in Figure 5.25, where λ_T = 0.09, there is only a very small amount of throughflow air flowing over the disc. The throughflow air has a large cooling effect. A free disc of the same size, rotating at the same speed would have a much higher mass flow of air pumped over the disc surface, therefore the disc surface temperature would be lower.

In order to make a comparison with the free disc across the range of conditions tested, the area average disc-surface-to-inlet-air temperature was calculated for each test condition, as described in Section 4.2.4, using Equation 5.24, where r_1 = 0.096 m, r_5 = 0.2105 m and T is the temperature at each radial location, r.

$$T_{av} = \frac{2}{r_5^{\,2} - r_1^{\,2}} \int_{r_1}^{r_5} Tr\,dr \qquad \textbf{(5.24)}$$

The integral in Equation 5.24 is approximated using Simpson's rule, described in Section 4.2.4.

The average adiabatic disc-surface-to-inlet-air temperature difference was calculated using Equation 5.25, between the same inner and outer radial locations as used in Equation 5.24.

$$\Delta T_{ad,av} = \frac{\omega^2}{Cp(r_5^2 - r_1^2)} \int_{r_1}^{r_5} r^3 dr = \frac{\omega^2 (r_5^2 + r_1^2)}{4Cp} \qquad \textbf{(5.25)}$$

Figure 5.26 shows the variation of the average disc-surface-to-inlet-air temperature, normalised by the average adiabatic disc-surface-to-inlet-air temperature, with λ_T.

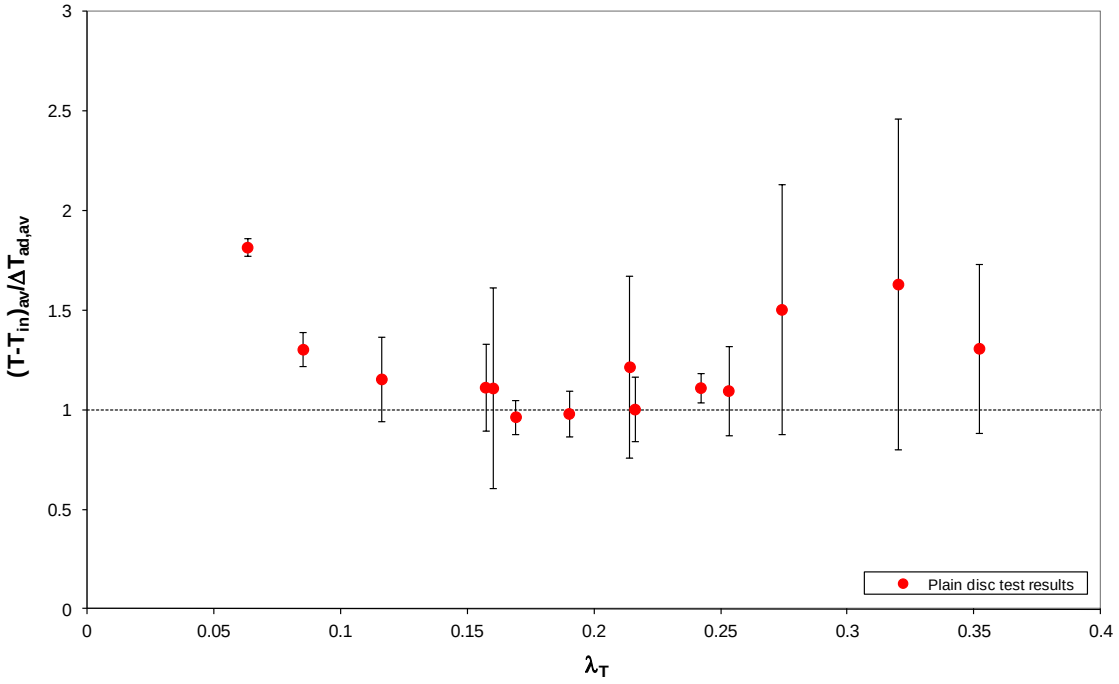

Figure 5.26 – Variation of average disc-surface-to-inlet-air temperature, normalised by the adiabatic average disc-surface-to-inlet-air temperature, with λ_T for a plain disc, $0.17 \times 10^7 \leq \mathrm{Re}_\phi \leq 1.6 \times 10^7$ and $0.29 \times 10^5 \leq C_w \leq 1.03 \times 10^5$.

It can be seen that the average disc surface temperature can be over 50% higher than the free disc at very low values of λ_T. However, at most conditions the average disc temperature is predicted fairly well by the adiabatic free disc case. Particularly where $\lambda_T \sim 0.2$ and the flow is most like that of a free disc.

5.6.2 Comparison to Coren (2007)

The complete data set is not compared to **Coren (2007)**, as the ability to make disc surface temperature measurements was only introduced toward the end of the previous test phase. As a result, temperature data for the plain disc in the previous test phase is

only available for the repeat tests that were carried out at the end. However, two test conditions are picked out to compare to the current results.

Figures 5.27 and 5.28 show the variation of disc-surface-to-inlet-air temperature difference with non-dimensional radius, for the current and previous test data. The test conditions are C_w = 0.3 x 10^5, Re_ϕ = 0.4 x 10^7 and λ_T = 0.16, and C_w = 0.3 x 10^5, Re_ϕ = 0.8 x 10^7 and λ_T = 0.09 respectively.

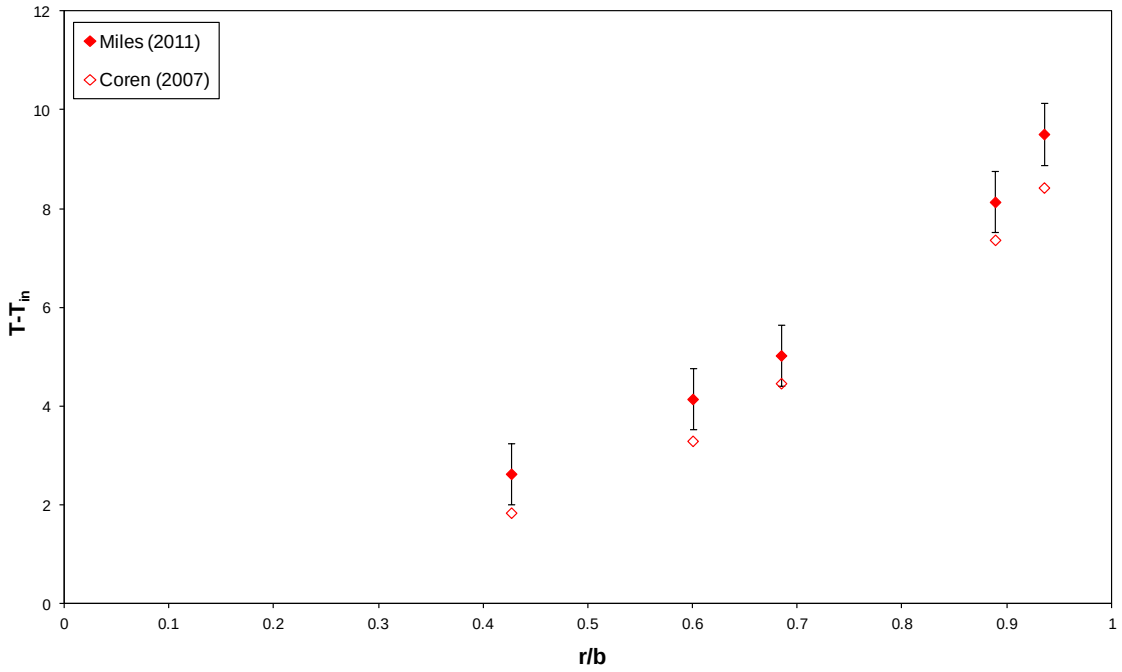

Figure 5.27 - Variation of disc-surface-to-inlet-air temperature difference with non-dimensional radius for current and previous plain disc test results, C_w = 0.3 x 10^5, Re_ϕ = 0.4 x 10^7 and λ_T = 0.16.

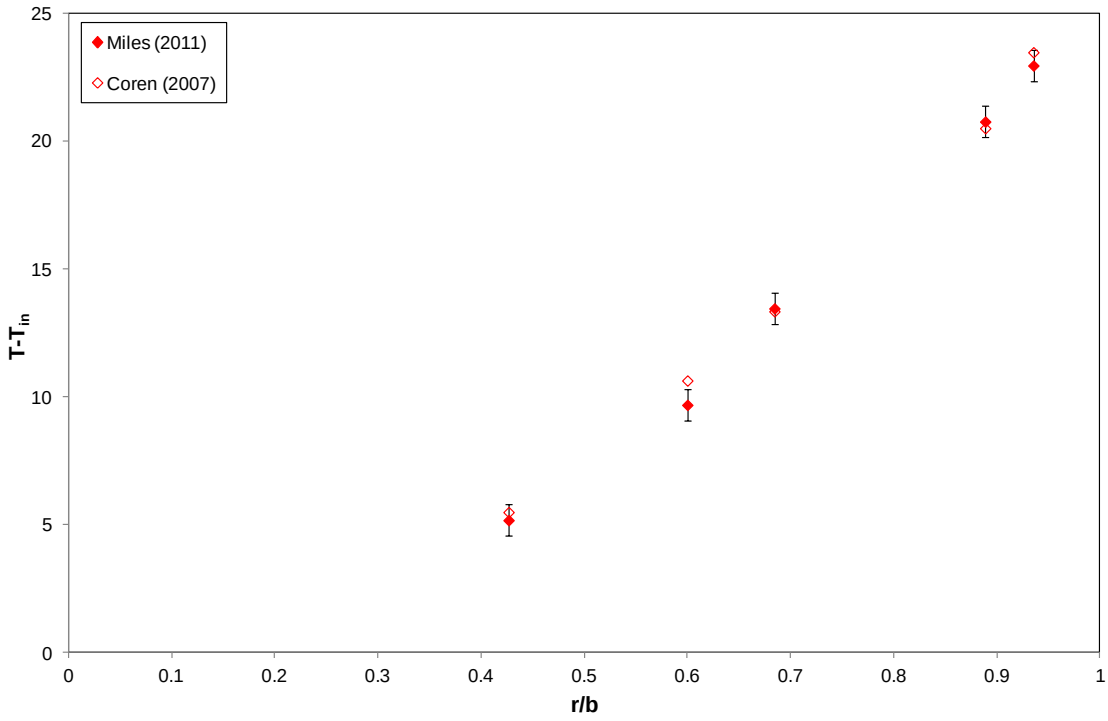

Figure 5.28 - Variation of disc-surface-to-inlet-air temperature rise with non-dimensional radius for current and previous plain disc test results, C_w = 0.3 x 10^5, Re_ϕ = 0.8 x 10^7 and λ_T = 0.09.

It can be seen in Figure 5.28 that the two set of data agree well, to within 5%, with any variation being within the limits of uncertainty, except where r/b = 0.6. In Figure 5.27, the agreement does not at first seem as good. The variation between the two data sets is more like 10% to 20%. Coren did not use the ordinate T-T_{in} in his evaluation, and therefore did not calculate the uncertainty associated with it. However, it is fair to assume an uncertainty similar to that applied to the current experimental data is valid, since the measurements were obtained using the same hardware. Therefore the agreement between the two data sets, for both flow conditions, is assumed to be within the limits of uncertainty.

5.7 Summary

The plain disc test results showed a high level of repeatability along with good agreement between the current and previous sets of plain disc data. The results were also compared with free disc results from open literature as well as existing analytical and empirical correlations for rotor-stator systems. In most cases there was good agreement found, once any assumptions or variation in the test facilities had been accounted for. It has also been shown that the variation between the current test results and any one correlation is smaller than the variation between the correlations themselves. These factors led to confidence in the results obtained as well as the future results in the remainder of the test program.

Chapter 6. Stator Bolts Tests

6.1 Introduction

This chapter discusses the test procedure and results obtained from the tests with hexagonal bolts attached to the stationary casing of the test rig. The tests covered the range of non-dimensional conditions: $0.17 \times 10^7 \leq Re_\phi \leq 1.6 \times 10^7$; $0.25 \times 10^5 \leq C_w \leq 10^5$; and $0.06 \leq \lambda_T \leq 0.6$. The test conditions were designed to match the rotor bolt tests carried out by **Coren (2007)**, using the same facility. The data from the stator and rotor bolt tests were then compared to each other as well as the plain disc results, in order to analyse the effects of stator bolts on both the moment coefficient and rotor surface temperature.

Stator bolt tests were previously carried out by **Coren (2007)** using the same test rig. However, at that time the equipment to acquire rotor surface temperature measurements was not available. Work by **Kurokawa *et al.* (1978)** showed that with roughness on the stator surface, the central core of fluid between the rotor and stator is slower than when the surface is smooth. This slowing of the core would be expected to increase the viscous friction between the rotor and the core which may result in an increase in the rotor surface temperature. The tests discussed in this chapter, which include rotor surface temperature measurements, aim to demonstrate whether this slowing of the core also occurs when discrete protrusions, such as stator bolts, are present.

In the interests of reducing build time between test phases, the tests carried out by Coren had protrusions attached to one side of the stationary casing only. The test results were then adjusted to account for windage due to protrusions on both sides of the casing, enabling the data to be directly compared to the plain disc data. In the current test programme, the test rig was modified to accommodate stator bolts on both sides of the casing. This was essential to get accurate rotor surface temperature measurements. A

non-symmetrical geometry could introduce conduction across the rotor, which would result in a biased data set with significant measurement uncertainties.

6.2 Stator bolt test procedure

Testing involved varying the number of bolts as well as the flow conditions in order to fully analyse the effect of stator bolts on the moment coefficient and rotor surface temperature. The number of bolts, n, was varied so that three, nine and eighteen bolts were tested to match the equivalent rotor bolt measurements obtained by **Coren (2007)**. The bolts were attached to both sides of the stationary casing at a radius of $r = 0.2$ m, representing a non-dimensional radius $r/b = 0.889$ (where r is the local radius and b is the disc radius).

Hexagonal bolt heads were made for the tests and an M6 cap screw was used to attach them to the casing. The bolt head and cap screw can be seen in Figure 6.1(a). The bolt heads measure 16 mm across the flat sides and 11 mm deep. The dimensions of the bolt head can be seen in Figure 6.1(b). There is a 6.5 mm recess in the front surface, into which the M6 cap screw is placed. There is also a 2.1 mm recess in the rear surface of the bolt head, which is utilized only when the bolts are placed on the rotor, details can be found in Section 7.2.

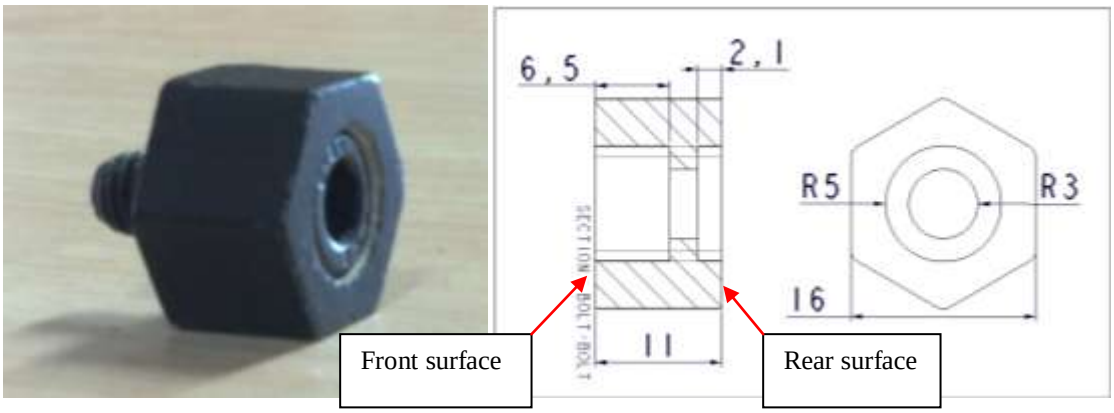

Figure 6.1 – (a) Hexagonal bolt head with M6 cap screw. (b) Bolt head dimensions (mm).

It was necessary throughout the range of tests that the bolts were always placed on the stator in the same orientation with respect to the direction of the core flow rotation. The direction for this set of tests can be seen in Figure 6.2, where $\beta\omega r_b$ is the velocity of the core relative to the stator.

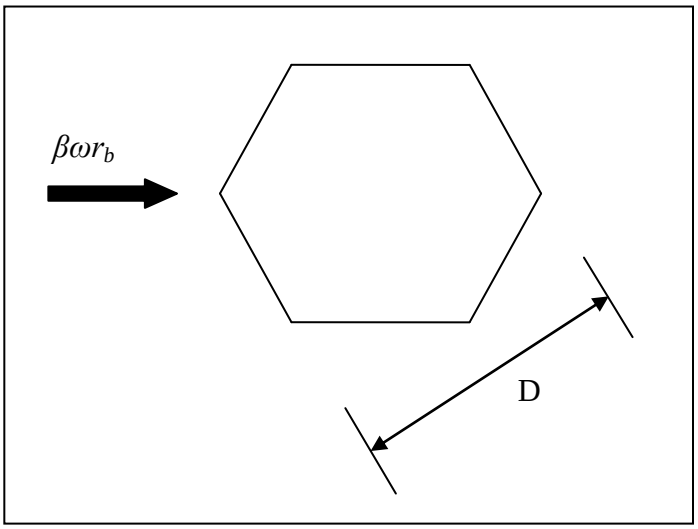

Figure 6.2 – Bolt orientation with respect to direction of rotation.

To achieve this, a tool was made so that the hexagonal bolt head can be secured in the required direction whilst the cap screw is tightened with an Allen key. The tool is shown in Figure 6.3.

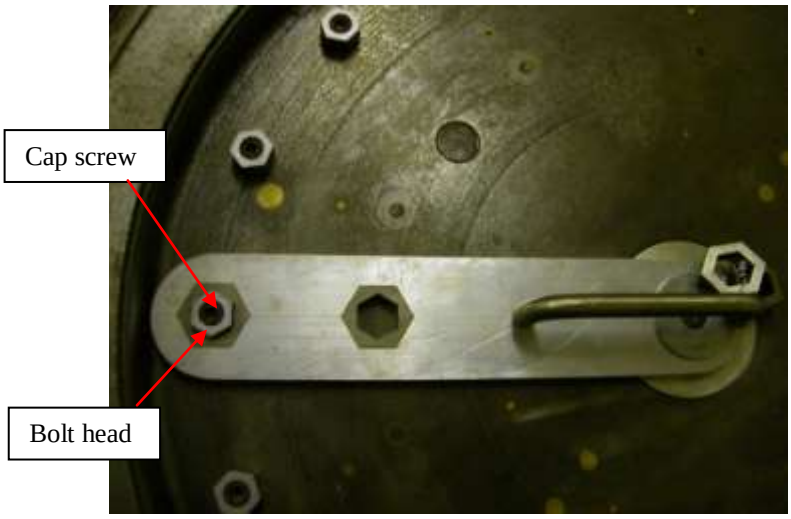

Figure 6.3 – Picture of bolt orientation tool in use.

The test conditions included a range of turbulent flow parameter, λ_T ($\lambda_T = C_w/\mathrm{Re}_\phi^{0.8}$, where $C_w = \dot{m}/\mu b$ and $\mathrm{Re}_\phi = \rho\omega b^2/\mu$), for two different values of superimposed throughflow, $C_w = 0.3 \times 10^5$ and 10^5. Test conditions were chosen to match rotor bolt tests carried out by **Coren (2007)** so that a direct comparison of the effects of stator and rotor bolts, on both the moment coefficient and the rotor surface temperature, could be made. Table 6.1 shows the range of test conditions. The complete set of test conditions is shown in Appendix C.

Re_ϕ	$0.17 \times 10^7 \leq \mathrm{Re}_\phi \leq 1.6 \times 10^7$
C_w	$0.25 \times 10^5 \leq C_w \leq 10^5$
λ_T	$0.06 \leq \lambda_T \leq 0.6$
p (absolute, bar)	$2 \leq p \leq 5$
$\dot{m}$ (kg/s)	$0.12 \leq \dot{m} \leq 0.4$
N (rev/min)	$2000 \leq N \leq 10100$

Table 6.1 – Test conditions for stator bolt tests.

For each test, once the correct flow conditions had been achieved the test rig was allowed to stabilise before any measurements were taken. The stabilisation conditions used for the current test program are discussed in Section 5.4. This process took approximately half an hour.

6.3. Stator bolt rotor surface temperature results

Rotor surface temperature measurements were obtained at five radii on the test side (r/b = 0.427, 0.6, 0.684, 0.887 and 0.935) as well as at one radius on the balance side (r/b = 0.887). The last 120 seconds of data from each sensor for each test is averaged to get a temperature measurement for each position on the rotor. More details on the data acquisition method can be found in Section 5.4 with reference to the plain disc tests. Since there are variations in inlet temperature from one test to another, the data is presented in terms of the rotor-surface-to-inlet-air temperature difference.

Figure 6.4, shows the variation of rotor-surface-to-inlet-air temperature difference with non-dimensional radius for three bolts where $C_w = 10^5$, $Re_\phi = 1.4 \times 10^7$ and $\lambda_T = 0.18$. The uncertainty bars are calculated using the method described in Section 4.3.2. Also shown are the equivalent rotor bolt and plain disc results (rotor bolt measurements obtained by **Coren (2007)**).

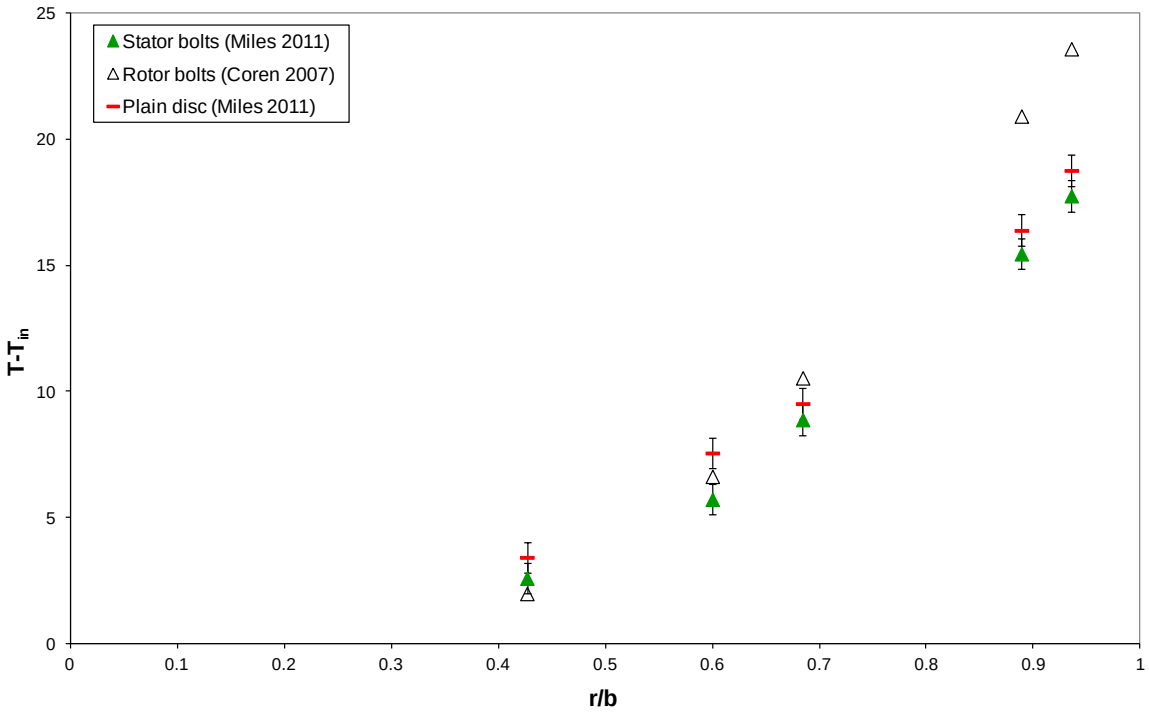

Figure 6.4 – Variation of rotor-surface-to-inlet-air temperature difference with non-dimensional radius, n = 3, $C_w = 10^5$, $Re_\phi = 1.4 \times 10^7$ and $\lambda_T = 0.18$.

It can be seen from Figure 6.4 that there is no measureable difference in rotor surface temperature when three stator bolts are present compared to the plain disc. Conversely the rotor bolt results show a large increase in rotor surface temperature over the plain disc, towards the outer radius of the rotor.

In a rotor-stator system, there is a core of fluid between the rotating and stationary surface rotating at a fraction of disc speed. This core fluid to rotor tangential velocity ratio is given by the term β, as shown in Equation 6.1, where V_ϕ is the tangential velocity of the fluid, ω the rotational speed of the rotor and r, radial location.

$$\beta = \frac{V_\phi}{\omega r} \qquad \textbf{(6.1)}$$

Work by **Kurokawa *et al.* (1978)** and **Coren (2007)** showed that the tangential velocity of the core is not only affected by the flow conditions, but also whether features, such as discrete protrusions (Coren) or general surface roughness (Kurokawa *et al.*), are present. The effect of these features on the velocity ratio between the fluid and the disc, depends whether they are present on the rotating or the stationary surfaces. Coren used Laser Doppler Anemometry (LDA) to obtain measurements of the core velocity both with and without bolts present on the rotor. His results showed that for rotationally dominant flow conditions, where $\lambda_T < 0.219$, the core rotation increased from $\beta = 0.25$ for the plain disc to $\beta = 0.8$ with bolts present. For radially dominant flow, where $\lambda_T > 0.219$, the increase was from $\beta = 0.1$ to $\beta = 0.3$. Kurokawa *et al.*, using pitot tubes for velocity measurements, found the core rotation to increase from $\beta = 0.42$ for the smooth disc up to $\beta = 0.55$, where $r/b > 0.9$, with roughness on the rotor surface. The measurements were obtained with no superimposed throughflow. The work done by rotor bolts in increasing the tangential velocity of the fluid, is the dominant factor causing the temperature rise observed in Figure 6.4.

Kurokawa *et al.* also showed that converse to roughness on the rotor surface, roughness on the stator surface led to a decrease in core rotation from $\beta = 0.42$ to $\beta = 0.39$. This is a much smaller velocity change than that observed with roughness on the rotor surface. It is assumed then, that a reduction in tangential velocity would also be observed with stator bolts present. If the reduction in tangential velocity relative to the increase in

tangential velocity when rotor bolts are present is also roughly the same as seen by Kurokawa *et al.*, then the work done by the stator bolts in slowing the core and the resulting temperature rise will be much less than for the rotor bolts. The resulting temperature rise is also acting on fluid far away from the rotor, and it would be expected that not all of this would necessarily be transferred to the rotor, leading to much lower rotor surface temperatures than for the rotor bolts. A decrease in core rotation, however, would increase the relative velocity between the core and the rotor, leading to an increase in viscous friction in the rotor boundary layer. This could result in an increase in rotor surface temperature, however this is clearly not a measureable effect for the conditions shown in Figure 6.4.

By combining the data from tests with similar flow conditions but a different number of bolts, it is possible to observe the effect of increasing the number of bolts on rotor surface temperature. Figure 6.5, shows the variation of rotor-surface-to-inlet-air temperature difference with non-dimensional radius for n = 3, 9 and 18, C_w = 0.3 x 10^5, Re_ϕ = 0.8 x 10^7 and λ_T = 0.08. Again, the equivalent rotor bolt and plain disc results are also shown.

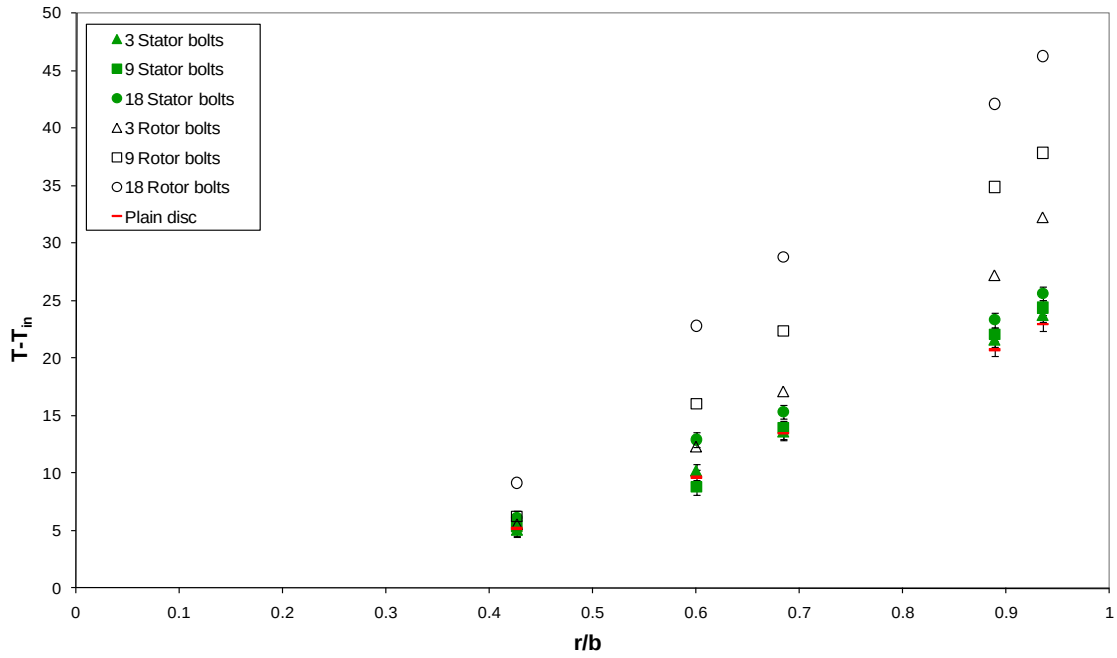

Figure 6.5 - Variation of rotor-surface-to-inlet-air temperature difference with non-dimensional radius, n = 3, 9 and 18, C_w = 0.3 x 10^5, Re_ϕ = 0.8 x 10^7 and λ_T = 0.08.

Figure 6.5 shows that where $r/b > 0.8$ there is a 2 °C (~10%) increase in rotor surface temperature with eighteen stator bolts compared with three. So at this flow condition it seems the core flow is increasingly retarded by the increasing number of bolts and the resulting increase in viscous friction is measureable as an increase in rotor surface temperature. Once again, the rotor bolts show a large increase in rotor surface temperature and a very clear trend between the number of bolts and the surface temperature.

The area average rotor-surface-to-inlet-air temperature difference allows a comparison of the stator bolt, rotor bolt and plain disc test results to be made over the complete range of conditions tested. This is calculated using Equation 6.2, where $r_1 = 0.096$ m, $r_5 = 0.2105$ m and T is the disc-surface-to-inlet-air temperature difference, at each radial location, r.

$$T_{average} = \frac{2}{r_5^2 - r_1^2} \int_{r_1}^{r_5} Tr\,dr \qquad \textbf{(6.2)}$$

The integral on the right hand side of Equation 6.2 is approximated using Simpson's rule, the method is discussed in Section 4.2.4. Figure 6.6 shows the variation of the area average disc-surface-to-inlet-air temperature difference with λ_T for stator bolts, $n = 3$, 9 and 18, as well as the plain disc.

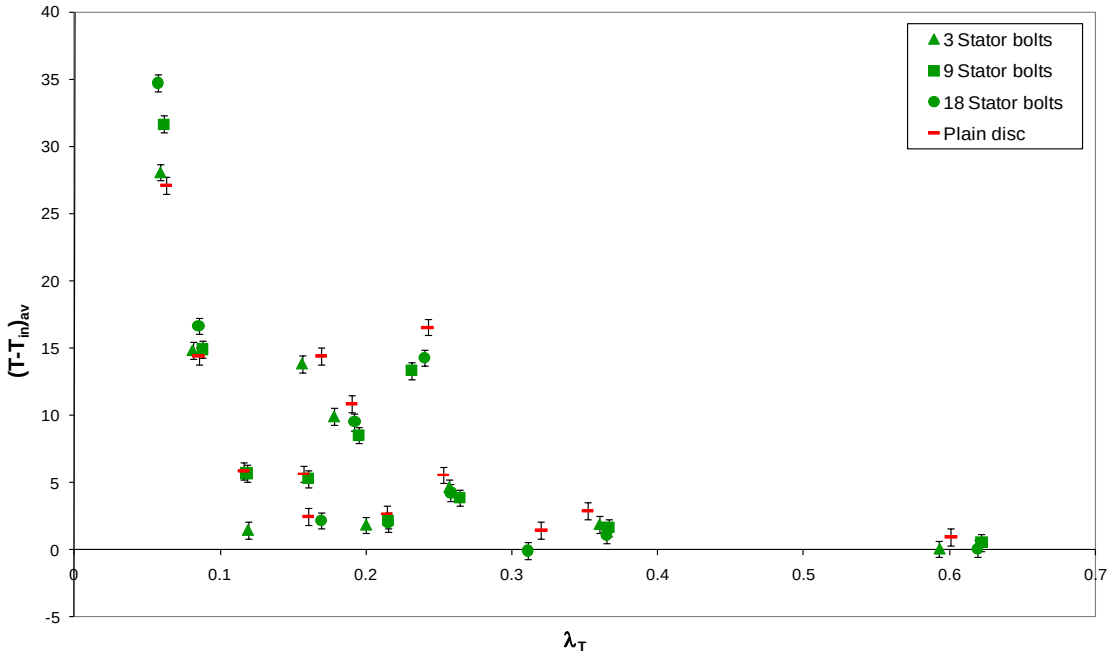

Figure 6.6 – Variation of area average disc-surface-to-inlet-air temperature difference with λ_T, n = 3, 9 and 18, 0.3 x $10^5 \leq C_w \leq 10^5$ and 0.17 x $10^7 \leq Re_\phi \leq 1.6$ x 10^7.

It can be seen in Figure 6.6 that when $\lambda_T < 0.1$, there is an increase in disc surface temperature with stator bolts, over that of the plain disc and also with increasing number of bolts. For the condition $\lambda_T = 0.06$, there is a 4.5 °C increase with nine stator bolts and 8 °C increase with eighteen bolts, relating to a 17% and 28% increase respectively. This condition is closest to that of a typical gas turbine engine, where an 8 °C increase in disc surface temperature could lead to a significant reduction in the life of a turbine disc. For other conditions though, where $\lambda_T > 0.1$, the stator bolts have no measureable effect on the disc surface temperature.

In order to investigate further the increase in viscous friction due to stator bolts, plots such as Figure 6.7 were produced for different values of λ_T. Figure 6.7 shows the variation of disc-surface-to-inlet-air temperature difference, relative to the outlet-to-inlet air temperature difference, with non-dimensional radius for $\lambda_T = 0.08$, $C_w = 0.3$ x 10^5 and $Re_\phi = 0.8$ x 10^7. The plot shows the results for n = 3, 9 and 18 stator and rotor bolts, as well as the plain disc.

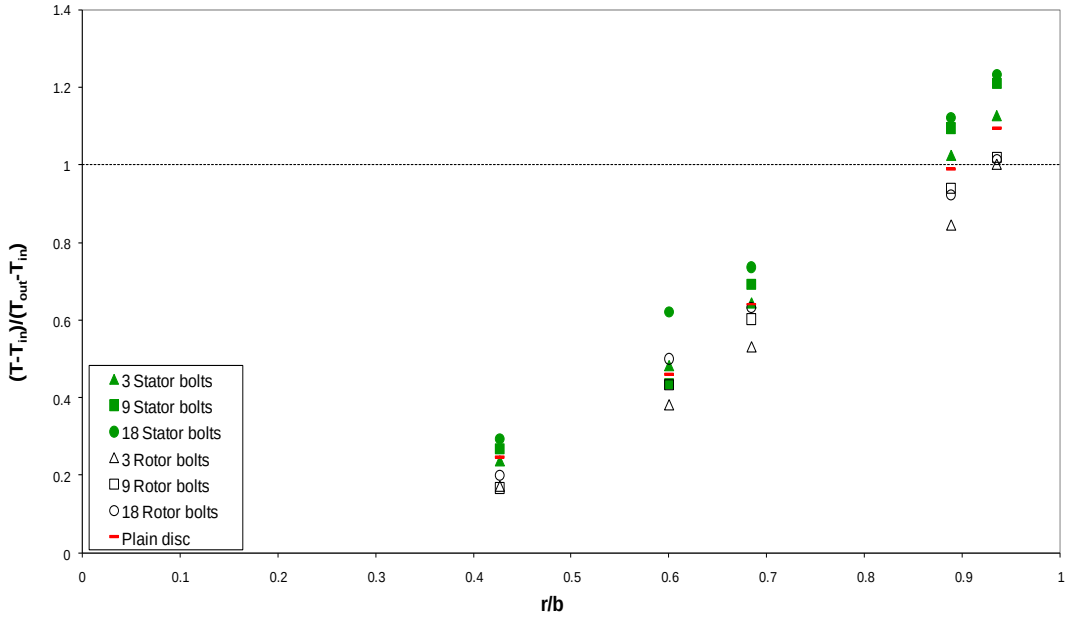

Figure 6.7 - Variation of disc-surface-to-inlet-air temperature difference, relative to the outlet-to-inlet air temperature difference, with non-dimensional radius, n = 3, 9 and 18, $\lambda_T = 0.08$, $C_w = 0.3 \times 10^5$ and $\mathrm{Re}_\phi = 0.8 \times 10^7$.

It can be seen from Figure 6.7 that at this particular condition the disc surface temperature for the plain disc, and to a larger extent the stator bolts, is above the outlet air temperature at the outer radii. This would suggest localised heating close to the rotor surface, possibly resulting from viscous friction. It can also be seen from Figure 6.7 that the relative disc surface temperature increases with a larger number of stator bolts, suggesting an additional retardation of the core flow. A similar result is observed at λ_T = 0.06, but at higher values of λ_T this is not the case.

Figure 6.8 shows the same as Figure 6.7 but for the conditions: $\lambda_T = 0.35$, $C_w = 10^5$ and $\mathrm{Re}_\phi = 0.65 \times 10^7$. Here the plain disc and stator bolt results are shown to be roughly the same. It looks as though the stator bolts actually reduce the relative disc surface temperature compared to the plain disc, however this is likely to be a result of the measurement uncertainty and not a real effect. At this test condition, the disc-surface-to-inlet-air temperature difference is of the same order of magnitude as the uncertainty in the infra red temperature measurements.

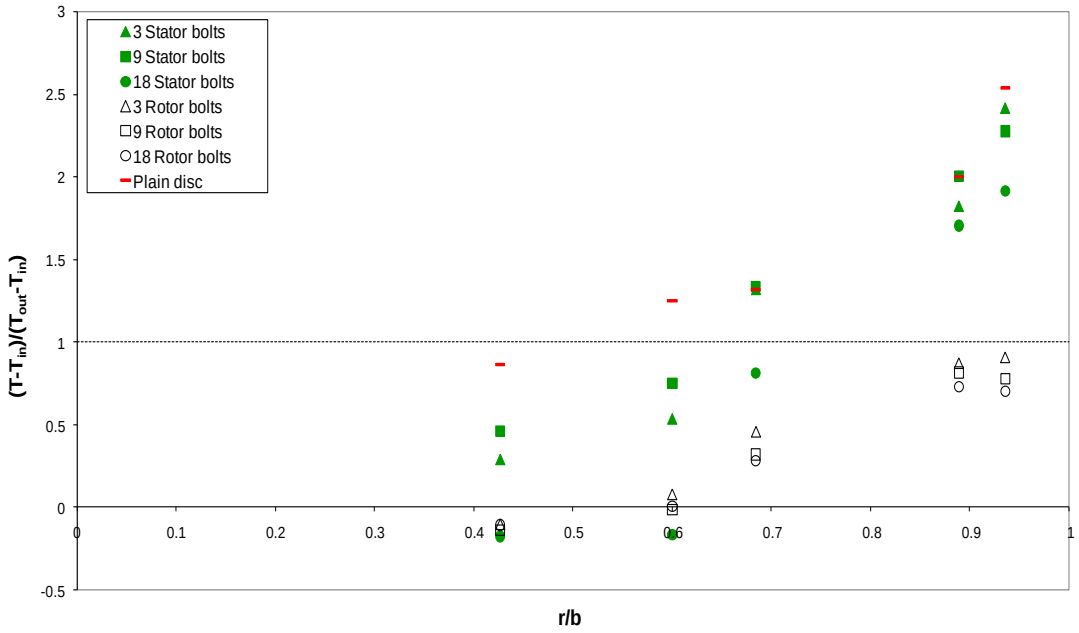

Figure 6.8 - Variation of disc-surface-to-inlet-air temperature difference, relative to the outlet-to-inlet air temperature difference, with non-dimensional radius, n = 3, 9 and 18, $\lambda_T = 0.35$, $C_w = 10^5$ and $\mathrm{Re}_\phi = 0.65 \times 10^7$.

So where $\lambda_T < 0.1$, it has been shown that the stator bolts slow the rotating core sufficiently to create a measureable increase in the disc surface temperature. It is probable that this is mainly due to the increase in viscous friction between the core and the disc. Where $\lambda_T > 0.1$, however, this is not the case. Any increase in disc temperature due to slowing of the core, is not measurable with the current instrumentation, therefore no variation from the plain disc results was found.

Contrary to this, with rotor bolts present the disc surface temperature (where $r/b > 0.8$) is always below or equal to the outlet air temperature, unlike the plain disc which is always higher. This would suggest that the increased core rotation due to the rotor bolts, reduces viscous friction compared with the plain disc.

6.4. Stator bolt windage results

Torque measurements were acquired at 1 Hz throughout each test, using an in-line torquemeter positioned between the gearbox and the rotor shaft. The last 120 s of data

was then averaged to give a torque measurement for each test point. Further details on the data acquisition method can be found in Section 5.4 with reference to the plain disc tests. The torque measurement, M, was then converted to a moment coefficient C_m ($C_m = 2M/\rho\omega^2 b^5$) which is used to compare windage for different test conditions.

Figures 6.9 and 6.10 are two examples of plots that were produced for all test conditions, showing the variation of moment coefficient, C_m, with rotational Reynolds number, Re_ϕ. Figure 6.9 shows the results for three stator bolts where $C_w = 0.3 \times 10^5$ and $0.06 \leq \lambda_T \leq 0.2$. Figure 6.10 shows the results for eighteen stator bolts at the conditions, $C_w = 10^5$ and $0.19 \leq \lambda_T \leq 0.62$. Both plots also show the equivalent rotor bolt and plain disc results.

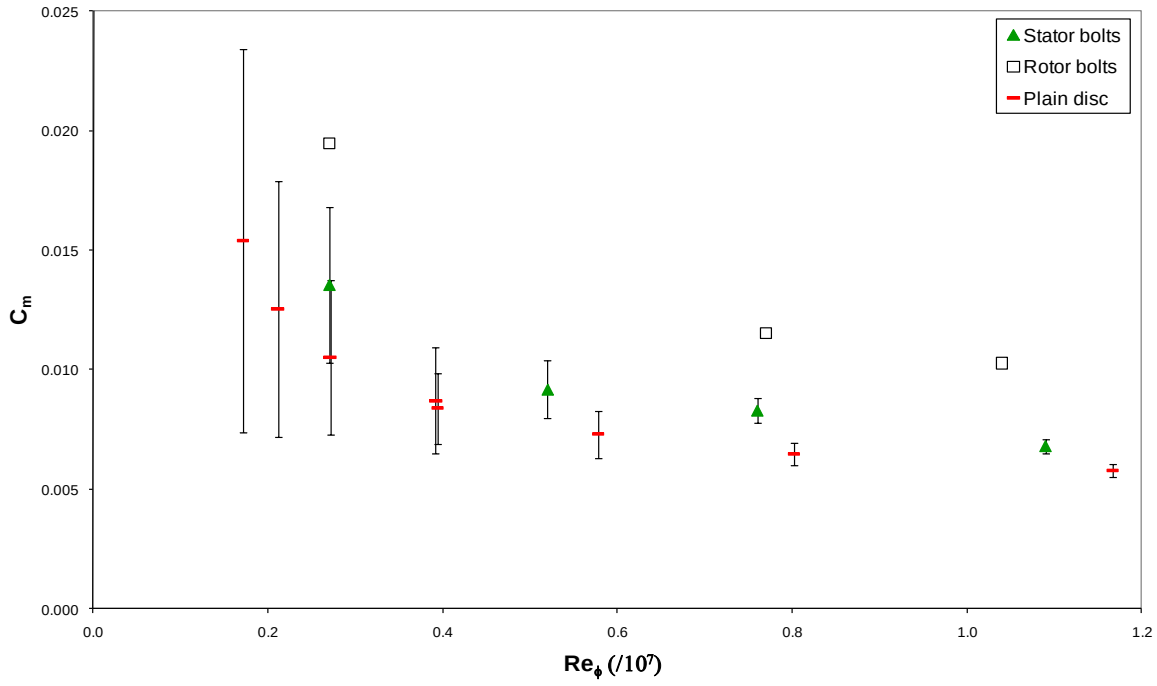

Figure 6.9 – Variation of C_m with Re_ϕ, $n = 3$, $C_w = 0.3 \times 10^5$ and $0.06 \leq \lambda_T \leq 0.2$.

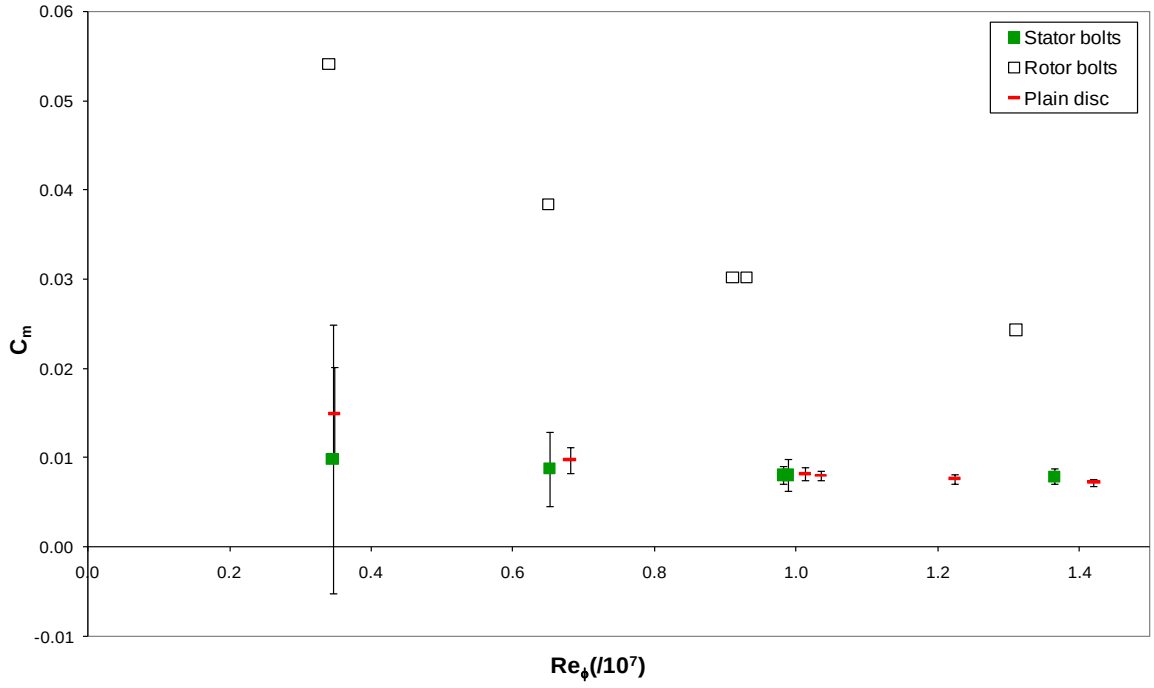

Figure 6.10 – Variation of C_m with Re_ϕ, n = 18, $C_w = 10^5$ and $0.19 \leq \lambda_T \leq 0.62$.

The results in both Figure 6.9 and 6.10 show that there is generally no measureable increase in moment coefficient with stator bolts present, over that of the plain disc. The exception is where $\lambda_T < 0.1$, represented in Figure 6.9 where $Re_\phi > 0.7 \times 10^7$. Here there is an increase in moment coefficient of 28% where $Re_\phi \approx 0.8 \times 10^7$, and 17% where $Re_\phi \approx 1.1 \times 10^7$ (corresponding to $\lambda_T \approx 0.08$ and 0.06 respectively). It is at these same conditions that an increase in disc surface temperature was observed, as discussed in the previous section. Where there are rotor bolts present, it can be seen from Figures 6.9 and 6.10 that there is a large increase in moment coefficient at all conditions. Similar results were found throughout the complete range of conditions tested.

Figure 6.11 shows the variation of $C_m Re_\phi^{0.2}$ with λ_T for the entire set of stator and rotor bolt data, n = 3, 9 and 18, $0.3 \times 10^5 \leq C_w \leq 10^5$ and $0.17 \times 10^7 \leq Re_\phi \leq 1.6 \times 10^7$, as well as the plain disc results. The ordinate $C_m Re_\phi^{0.2}$ was chosen because it represents the effect of the protrusions in terms of the increase in C_m over that of a free disc at the same conditions. The free disc, as calculated by **von Kármán (1921)** (Equation 6.3), has a constant value, indicated in Figure 6.11 by the solid line at $C_m Re_\phi^{0.2} = 0.146$.

$$C_m = 0.146\, Re_\phi^{-0.2} \qquad \textbf{(6.3)}$$

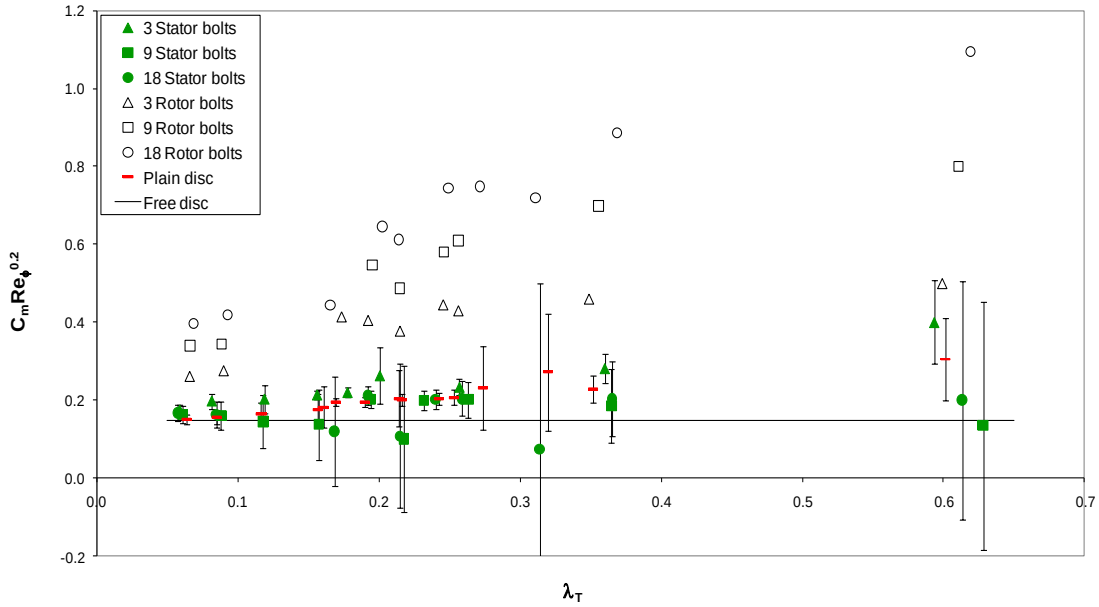

Figure 6.11 – Variation of $C_m \mathrm{Re}_\phi^{0.2}$ with λ_T, n = 3, 9 and 18, $0.3 \times 10^5 \leq C_w \leq 10^5$ and $0.17 \times 10^7 \leq \mathrm{Re}_\phi \leq 1.6 \times 10^7$.

Again, it is clear from Figure 6.11 that stator bolts do not have a measureable effect on the parameter $C_m Re_\phi^{0.2}$, even with a large number of bolts, over that of a plain disc. The rotor bolts do, however, increase $C_m Re_\phi^{0.2}$ above that of a plain disc over the complete range of conditions tested. Moreover, the increase in moment coefficient is directly linked to the number of bolts present.

Zimmermann *et al.*. (1986) state that the total moment coefficient can be separated into three main loss components, form drag, viscous friction and pumping losses. Rotor bolts create large pumping losses since the superimposed radial throughflow is constantly being pumped circumferentially by the bolts, therefore work is done in changing its angular momentum. Stator bolts on the other hand produce only small pumping losses, resulting from the tangential velocity gradient between the inner and outer edges of the bolt. As such, in the case of stator bolts, pumping losses can be neglected. Form drag occurs as a result of the separation of the fluid as it passes over the bolt. In the case of stator bolts the retarding force resulting from form drag is acting only on the stator and is not being measured, therefore the only loss component measured in the stator bolt tests is that resulting from viscous friction. From the results presented in Figures 6.9 and 6.10, it is evident that only where $\lambda_T < 0.1$ is the slowing of the core velocity large enough for the increase in viscous friction to be measurable as a

retarding torque on the rotor. When compared with the increase in moment coefficient observed when rotor bolts are present, it is clear that the viscous friction component of moment coefficient is a small compared with the form drag and pumping losses.

6.5 Summary

The stator bolt measurements show that where $\lambda_T < 0.1$, there is a measureable increase in the disc surface temperature as well as the moment coefficient. In both cases this increase is up to 28% above the plain disc values. This is attributed to an increase in viscous friction between the core and the rotor; the result of the stationary bolts decreasing the tangential velocity of the core flow. From previous data it is clear that there is a large increase in moment coefficient at all conditions when rotor bolts are present. This would suggest that the contribution to the total moment coefficient from viscous friction is small relative to the contribution from form drag and pumping losses.

Chapter 7. Rotor Bolt Tests

7.1 Introduction

This chapter discusses the testing method and results obtained from the hexagonal rotor bolt tests. The tests involved fixing hexagonal bolts to both sides of the rotor. Both the number and the size of the bolt were varied so that n = 3, 9 and 18 and D = 10 mm, 13 mm and 16 mm. Each configuration was tested at a range of flow conditions covering the non-dimensional conditions: $0.18 \times 10^7 \leq Re_\phi \leq 1.5 \times 10^7$; $0.24 \times 10^5 \leq C_w \leq 1.06 \times 10^5$; and $0.058 \leq \lambda_T \leq 0.631$.

Tests with 16 mm hexagonal bolts on the rotor were previously carried out by **Coren (2007)**. It was originally intended that the current test programme include two further sizes of hexagonal bolt and the data compared to that obtained by Coren for the 16 mm bolts. It became clear however that this would not be possible due to the application of different stabilisation criteria (see section 5.4) for the current test phase compared to the previous test phase carried out by Coren. Consequently a new set of 16 mm hexagonal rotor bolt tests were also carried out.

7.2 Hexagonal rotor bolt test procedure

Tests were performed with bolts attached to the rotor surface for varying flow conditions in order to analyse the effect of rotor bolts on the moment coefficient and rotor surface temperature. The number of bolts, n, was varied so that three, nine and eighteen bolts were tested. To extend the work done previously by **Coren (2007)**, the diameter, D, was varied so that D = 10 mm, 13 mm and 16 mm, measured across the flat sides of the bolt. The depth of the bolt was constant at 11 mm. The bolts were placed on both sides of the rotor at a radius of r_b = 0.2 m (r_b/b = 0.889, where b is the

disc radius). The bolts for the 16 mm tests are the same as those used for the stator bolt tests. The dimensions of the 16 mm bolt head can be seen in Figure 7.1(a).

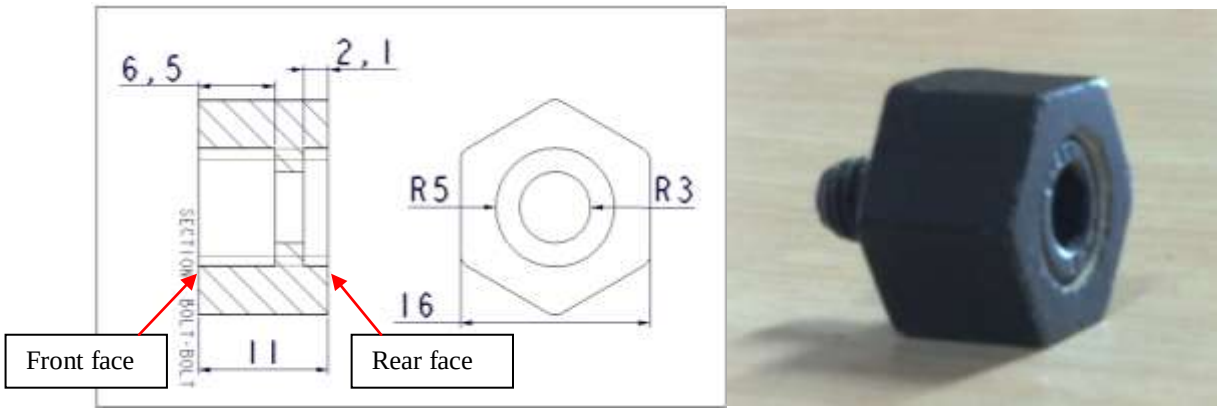

(a) **(b)**

Figure 7.1 – (a) Diagram showing 16 mm bolt head dimensions (mm). (b) Picture of bolt head with M6 cap screw.

There is a 6.5 mm recess in the front face of the bolt head, into which an M6 cap screw is placed to attach the bolt head to the rotor. The cap screw and bolt head are shown in Figure 7.1(b). There is also a 2.1 mm recess in the rear face. When the disc was made, it had been anticipated that future test programmes would include testing with surface cavities in the disc (see Sections 8.5 and 8.6). As a result, large M14 holes were machined into the disc to accommodate surface cavity inserts. In order for the bolt heads to be attached to the disc locating studs, with an M14 outside diameter and M6 hole in the centre, are inserted into the holes in the disc and the bolt heads are then attached via the M6 cap screw. The picture in figure 7.2 shows the locating studs in position on the disc.

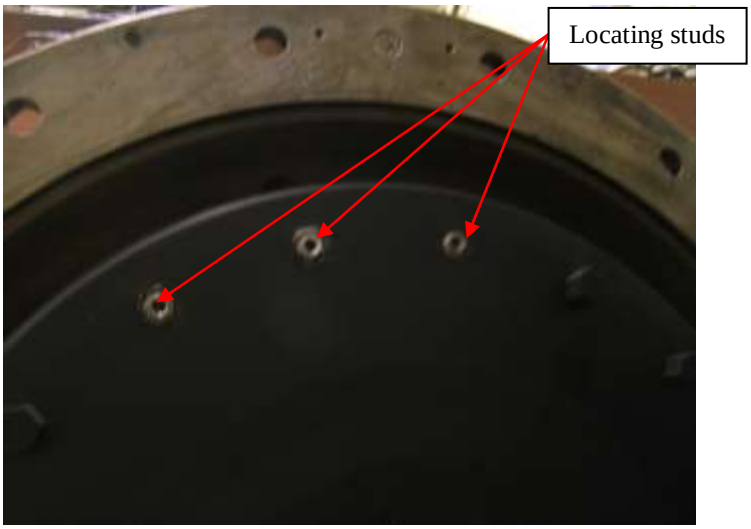

Figure 7.2 – Picture showing locating studs used for attaching bolt heads to the rotor.

These locating studs do not sit quite flush with the disc surface. So in order that the bolt heads do, they have a 2.1 mm recess (seen in Figure 7.1(a)) machined into the rear face so that they sit over the protruding locating stud and flush with the disc surface. The 13 mm bolt heads were made to the same design with smaller dimensions across the flat sides. For the 10 mm bolt heads, a set of M6 cap screws were machined to give a smaller head, 8 mm in diameter. The bolt heads were made to the same design as the 16 mm and 13 mm bolts, but measuring 10 mm across the flat sides with an 8 mm diameter recess in both the front and rear surfaces.

As with the stator bolt tests, it was necessary to ensure that all bolts had the same orientation with respect to the direction of rotation. The direction for these tests is shown in Figure 7.3, where $(1-\beta)\omega r_b$ is the velocity of the core relative to the rotor.

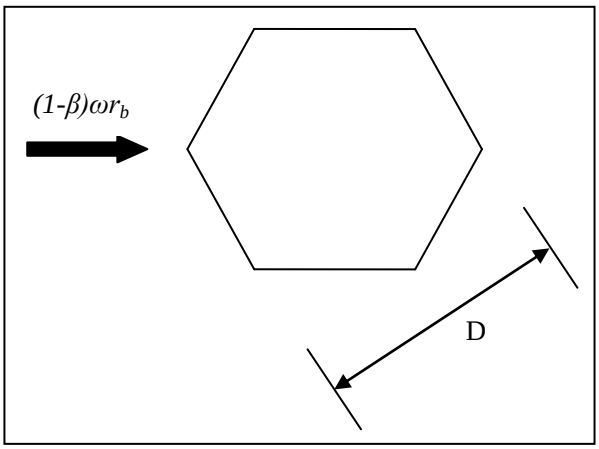

Figure 7.3 – Diagram showing bolt orientation with respect to direction of rotation.

To achieve this, the tool shown in Figure 7.4 was made. With this tool the hexagonal bolt head is secured in the required direction whilst the cap screw is tightened with an Allen key. It can be seen in Figure 7.4 that the tool has a hexagonal hole, containing an insert which sits around the bolt head. This is held in place with a grub screw. An insert was made for each size bolt head so that the same tool could be used throughout the test program. Once the bolts were attached to the rotor, the recess in each cap screw was filled with plaster of paris and the bolts and disc surface were sprayed with high temperature matt black paint, so that close to black body emissivity could be assumed (See section 3.5.3).

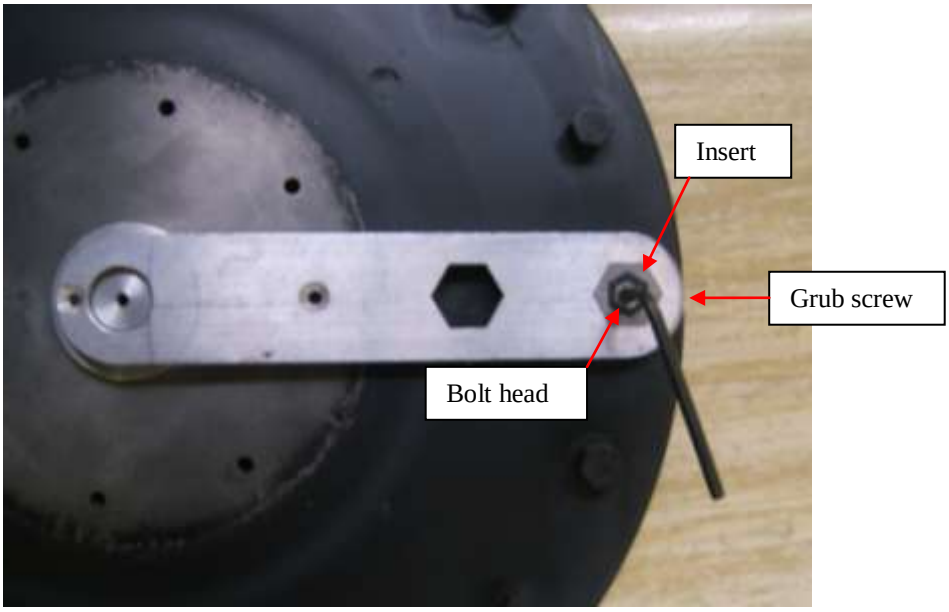

Figure 7.4 – Picture showing bolt orientation tool in use.

The test conditions included a range of values of turbulent flow parameter, λ_T ($\lambda_T = C_w/\mathrm{Re}_\phi^{0.8}$, where $C_w = \dot{m}/\mu b$ and $\mathrm{Re}_\phi = \rho\omega b^2/\mu$), for two different values of superimposed throughflow, $C_w = 0.3 \times 10^5$ and 10^5. Table 7.1 shows the range of test conditions. The complete set of test conditions is shown in Appendix C.

Re_ϕ	$0.18 \times 10^7 \leq Re_\phi \leq 1.5 \times 10^7$
C_w	$0.24 \times 10^5 \leq C_w \leq 1.06 \times 10^5$
λ_T	$0.058 \leq \lambda_T \leq 0.631$
p (absolute, bar)	$2 \leq p \leq 5$
$\dot{m}$ *(kg/s)*	$0.12 \leq \dot{m} \leq 0.4$
N (rev/min)	$2500 \leq N \leq 10100$

Table 7.1 – Range of conditions covered by all hexagonal rotor bolt tests.

For each test, once the correct flow conditions had been achieved the test rig was allowed to stabilise before any measurements were taken, this process took approximately half an hour. The stabilisation conditions used for the current test program are discussed in Section 5.4.

7.3 Hexagonal rotor bolt windage results

Torque measurements were acquired at 1 Hz throughout each test, using an in-line torquemeter positioned between the gearbox and the rotor shaft. The last 120 s of data was then averaged to give a torque measurement for each test point. Further details on the data acquisition method can be found in Section 5.4 with reference to the plain disc tests. The torque measurement, M, was then converted to a moment coefficient C_m ($C_m = 2M/\rho\omega^2 b^5$) which is used to compare windage for different test conditions.

Figure 7.5 shows the variation of moment coefficient, C_m, with rotational Reynolds number, Re_ϕ, for $n = 9$ and $D = 10$ mm covering the range of turbulent flow parameter $0.06 \leq \lambda_T \leq 0.34$. It can be seen that the moment coefficient, for a given value of Re_ϕ, is much larger when $C_w = 10^5$ compared with the lower value of $C_w = 0.3 \times 10^5$. Where $Re_\phi \approx 1 \times 10^7$, the moment coefficient is increased from $C_m = 0.011$ to $C_m = 0.019$, an increase of nearly 60%. A similar plot to Figure 7.5 was produced for all test conditions and the same trend was found in each case. The uncertainty bars shown in this, and further plots in this chapter were calculated using method described in Section 4.3.2.

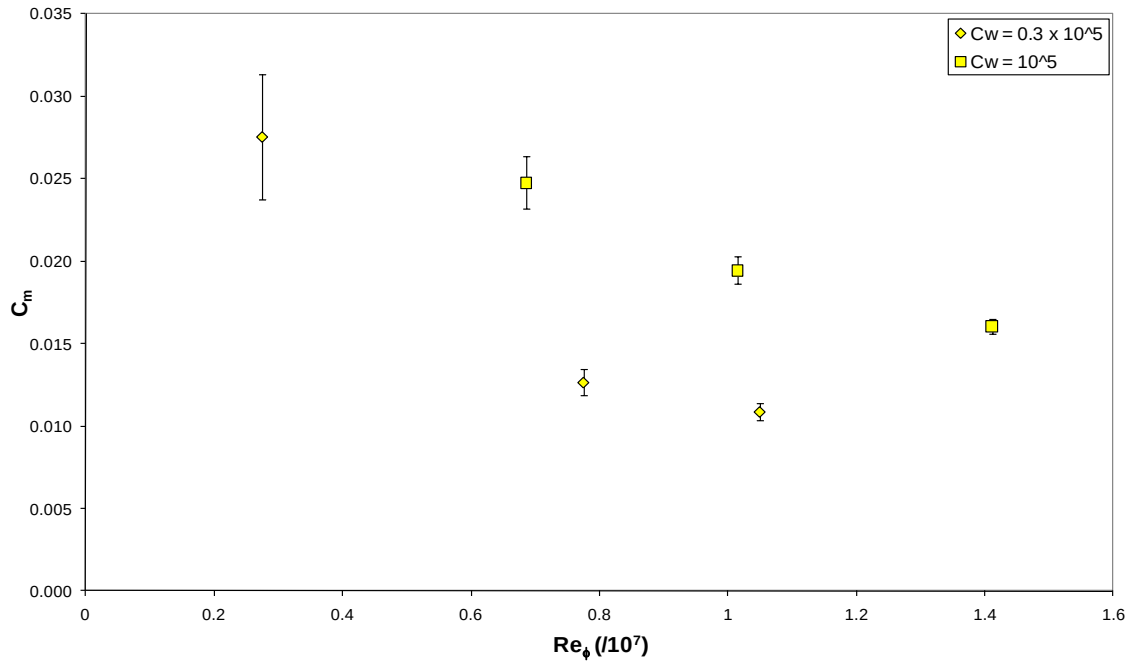

Figure 7.5 – Variation of C_m with Re_ϕ and C_w, n = 9, D = 10 mm and $0.06 \leq \lambda_T \leq 0.34$.

For comparison of the results from the different sized bolts, plots such as Figure 7.6 were produced covering the complete range of flow conditions tested. Figure 7.6 shows the variation of C_m with λ_T for n = 9, $C_w = 10^5$ and $0.68 \times 10^7 \leq \mathrm{Re}_\phi \leq 1.41 \times 10^7$. All three bolt sizes are shown as well as the plain disc results for comparison. It can be seen that the moment coefficient for the 16 mm bolts is consistently higher than the 13 mm and 10 mm bolts, up to 16% higher than the 10 mm bolts where $\lambda_T = 0.19$ (±4%). This increase however, is not generally observed between the 10 mm and 13 mm, as might be expected, except when $\lambda_T = 0.19$ the 13 mm bolts show a 7% increase in C_m over the 10 mm bolts.

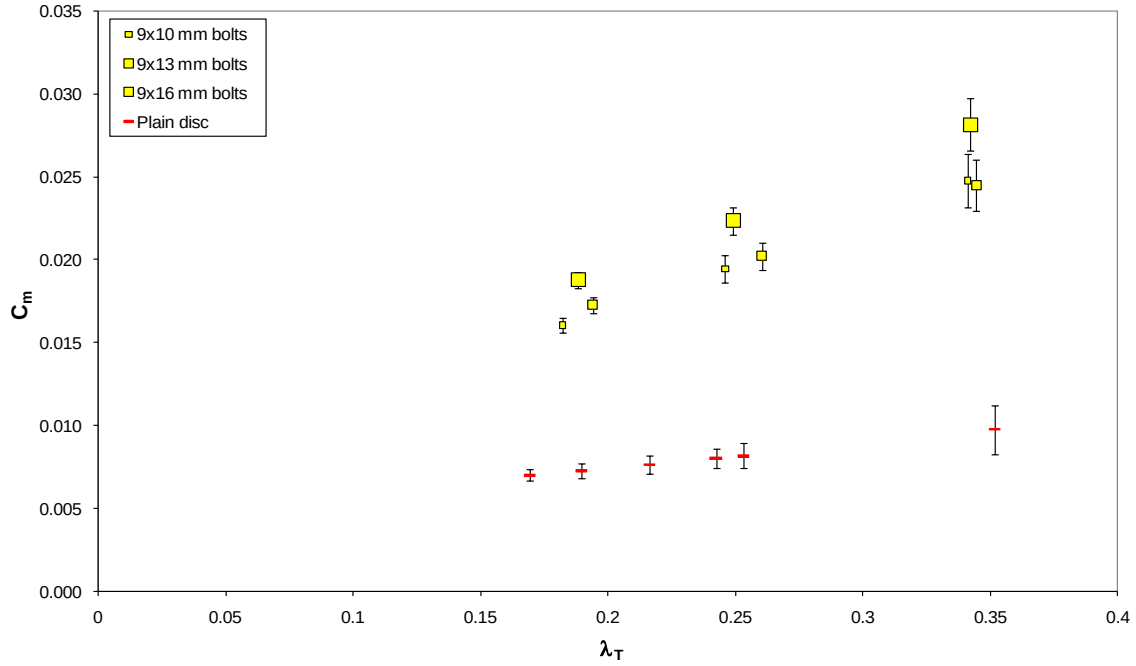

Figure 7.6 – Variation of C_m with λ_T and D, n = 9, $C_w = 10^5$ and 0.68 x $10^7 \leq$ Re$_\phi \leq$ 1.41 x 10^7.

Figure 7.7 shows the variation of C_mRe$_\phi^{0.2}$ with λ_T and bolt diameter, for n = 9 and D = 10 mm, 13 mm and 16 mm. The plain disc measurements are also shown for comparison. The ordinate C_mRe$_\phi^{0.2}$ was chosen because it represents the effect of the protrusions in terms of the increase in C_m over a free disc at the same conditions. The free disc has a constant value of C_mRe$_\phi^{0.2}$ = 0.146, using the correlation for calculating moment coefficient described by **von Kármán (1921)** where $C_m = 0.146\text{Re}_\phi^{-0.2}$. This is indicated on Figure 7.7 with a solid line.

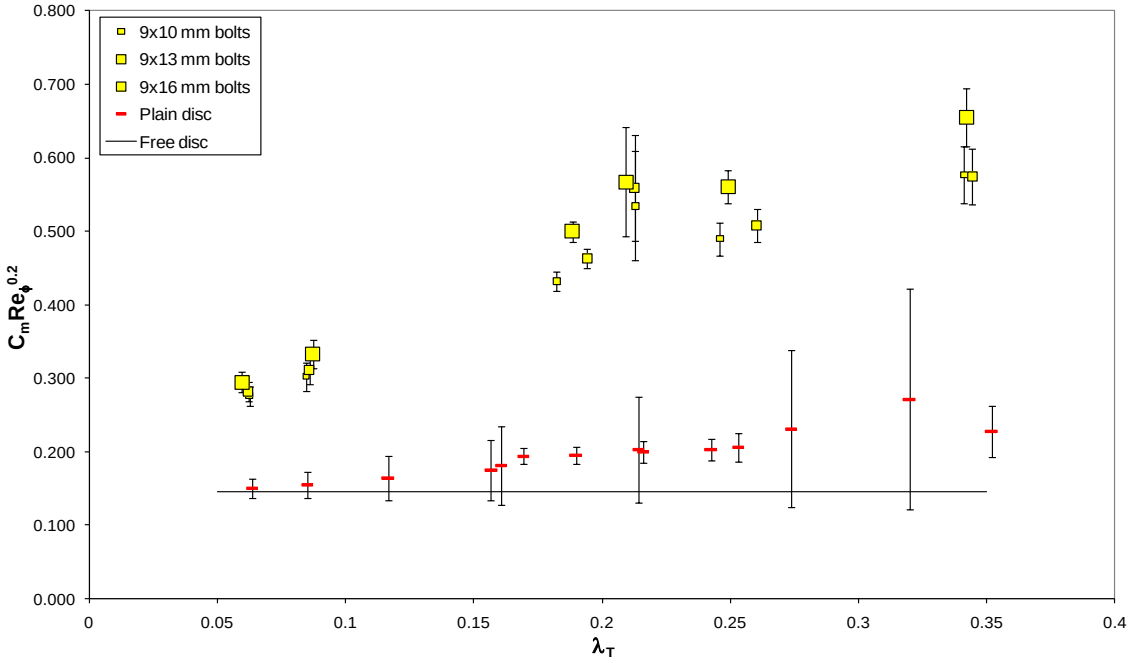

Figure 7.7 – Variation of $C_m Re_\phi^{0.2}$ with λ_T and D, n = 9, 0.24 x $10^5 \leq C_w \leq$ 1.04 x 10^5 and 0.27 x $10^7 \leq Re_\phi \leq$ 1.41 x 10^7.

Figure 7.7 shows that throughout the range of conditions tested there is an increase in moment coefficient for the 16 mm bolts over the 10 mm and 13 mm bolts. This would be expected from an increase in form drag due to the increased frontal area of the bolt. At most values of λ_T however, there is not a measureable increase in moment coefficient between the 10 mm and 13 mm bolts. In Figure 7.7 the data at λ_T = 0.21 has particularly large uncertainty bars because these results were acquired at low a rotational speed, with low superimposed throughflow. It is at these conditions that the uncertainty in the torque measurement is relatively high, since the windage torque produced is so low (~3 N m).

Figure 7.8 shows the variation of C_m, with bolt number and diameter, for three values of λ_T that are nominally constant. Plain disc values can be seen on the left hand axis at n = 0.

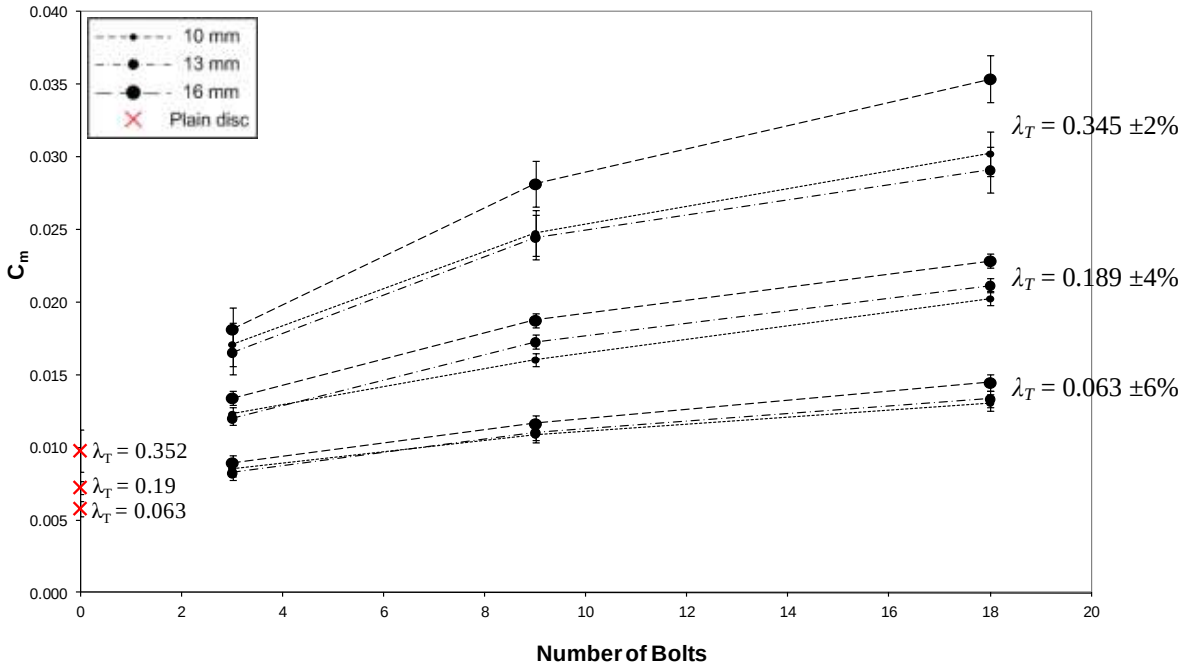

Figure 7.8 – Variation of C_m with n, D and λ_T, 0.67 x $10^7 \leq$ $Re_\phi \leq$ 1.49 x 10^7 and 0.24 x $10^5 \leq$ $C_w \leq$ 1.06 x 10^5.

The hypothesis that increasing the diameter of the bolt increases form drag, would suggest a consistent increase in moment coefficient with increasing bolt diameter. It can be seen from Figure 7.8 that this is not always the case. Where λ_T = 0.345 and 0.063, it can be seen that increasing the diameter from D = 10 mm to D = 13 mm produces very little difference in moment coefficient. Whereas increasing the diameter of the bolt to D = 16 mm produces a more definite increase.

Figure 7.9 shows the variation of moment coefficient with bolt diameter and λ_T for n = 18, 0.18 x $10^7 \leq$ $Re_\phi \leq$ 1.34 x 10^7 and 0.24 x $10^5 \leq$ $C_w \leq$ 1.06 x 10^5. It is clear to see that moment coefficient does not increase consistently with increasing bolt diameter, particularly at higher values of λ_T, where the flow is radially dominant.

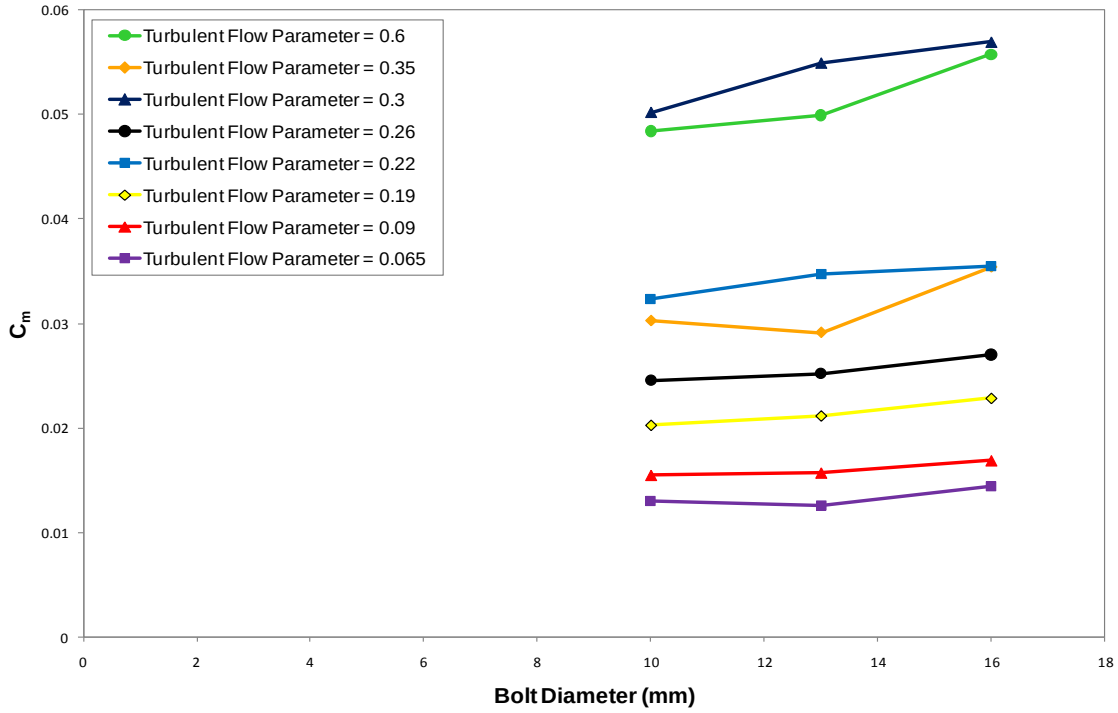

Figure 7.9 – Variation of C_m with D and λ_T, $0.18 \times 10^7 \leq Re_\phi \leq 1.34 \times 10^7$ and $0.24 \times 10^5 \leq C_w \leq 1.06 \times 10^5$.

We can estimate a Reynolds number, Re_D, based on the velocity of the central core of fluid relative to the bolt, and using bolt diameter as a length scale. This is shown in Equation 7.1, where β is the fluid to disc velocity ratio for a plain disc, which can be calculated using the empirical relationship developed by **Daily *et al.* (1964)** shown in Equation 7.2. The parameter β^* is the velocity ratio for a rotor-stator system with no superimposed throughflow and is taken here as $\beta^* = 0.431$, as specified by **Daily and Nece (1960)** for a gap ratio of $G = 0.1$ (the gap ratio of the current test facility). In Equation 7.1, C is a multiplier representing the increased core velocity resulting from having bolts attached to the rotor, which is an unknown quantity but is thought to be between $1 < C < 3$. The velocity of the fluid in the core relative to the bolt is represented by $V_{\phi,rel}$.

$$Re_D = \frac{\rho V_{\phi,rel} D}{\mu} = \left\{(1 - C\beta)\frac{r_b}{b}\frac{D}{b}\right\} Re_\phi \qquad \textbf{(7.1)}$$

$$\beta = \beta^* \left[1 + \frac{12.74\lambda_T}{\left(r_b / b \right)^{2.6}} \right]^{-1} \qquad \textbf{(7.2)}$$

For this test program, the range of bolt Reynolds number, Re_D, is $10^5 < Re_D < 8 \times 10^5$, based on the assumption that $C = 1.5$. Figure 7.10 shows that the values of drag coefficient, C_D, for a circular cylinder, as specified by **Schlichting (1979)**, can be very sensitive to changes in Re_D within this range. So, although it is not suggested that the hexagonal bolts will have the same numerical value of drag coefficient as the circular cylinder, it might be expected that the flow behave in a similar fashion and have a sensitivity of drag coefficient with Reynolds number. If this is the case then the range of Reynolds numbers tested are in the complex region between laminar and turbulent separations, with associated variations in wake, and hence form drag.

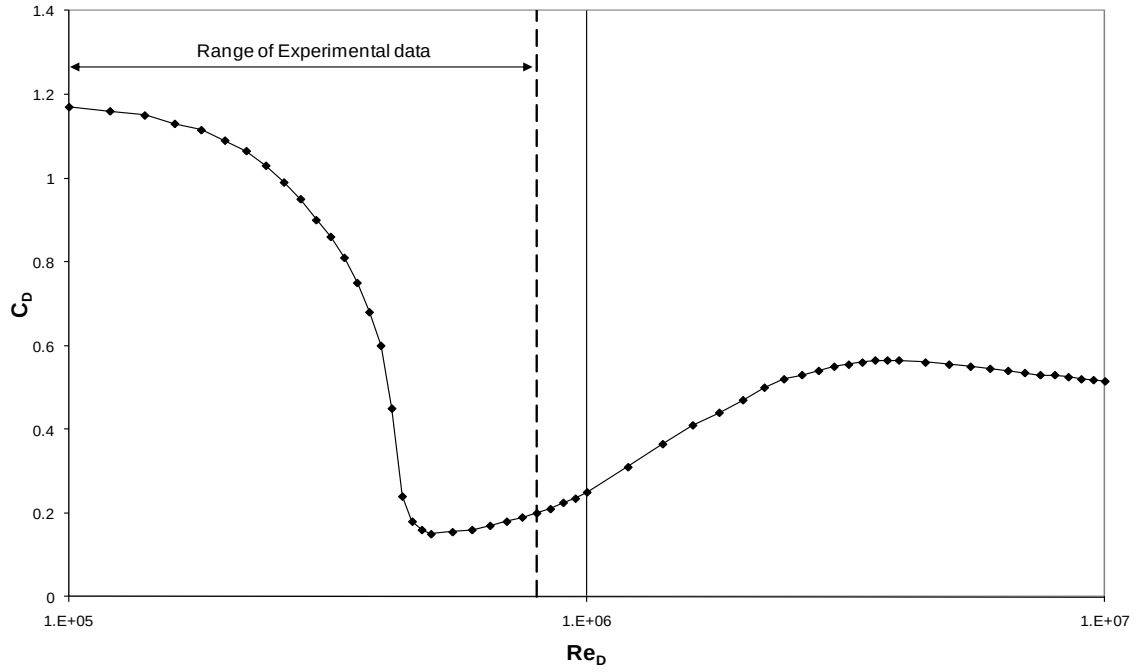

Figure 7.10 – Variation of C_D with Re_D (based on the assumption $C = 1.5$) for a circular cylinder (**Schlichting (1979)**).

Table 7.2 shows the calculated values of Re_D, again using the multiplier $C = 1.5$, along with an approximated value of C_D for an equivalent circular cylinder, found using

Figure 7.10. The values shown are for the 18 bolts case only and for the three values of λ_T presented in Figure 7.8.

	18 x 10 mm		**18 x 13 mm**		**18 x 16 mm**	
$\boldsymbol{\lambda_T}$	$\mathbf{Re_D}$	$\boldsymbol{C_D}$	$\mathbf{Re_D}$	$\boldsymbol{C_D}$	$\mathbf{Re_D}$	$\boldsymbol{C_D}$
0.345	2.42×10^5	1.03	3.15×10^5	0.86	3.84×10^5	0.60
0.189	4.51×10^5	0.13	5.83×10^5	0.16	7.12×10^5	0.18
0.063	2.60×10^5	0.99	3.43×10^5	0.75	4.09×10^5	0.55

Table 7.2 – Table showing Re_D and approximated C_D for an equivalent cylinder, for the three values of λ_T shown in Figure 7.8.

It can be seen that for the condition where $\lambda_T = 0.189$, the value of C_D is fairly consistent for all three bolt diameters. It is at this condition that a more consistent increase in moment coefficient is shown in Figure 7.8, with increasing bolt diameter. It is therefore likely to be in the stable, fully turbulent regime. At $\lambda_T = 0.063$ and 0.345, the value of C_D varies considerably, it is therefore likely that these values of Re_D are in the range of the complex transitional region (roughly $2 \times 10^5 < Re_D < 4.5 \times 10^5$). This could be the cause of the inconsistent increase in moment coefficient seen in Figure 7.8 with increasing bolt diameter.

Following the analysis of the initial data, an extra set of tests were carried out to evaluate the significance of different flow conditions involved in obtaining a particular value of λ_T. This is important since a specified value of λ_T can be reached with many different values of C_w and Re_ϕ. Measurements were focussed entirely on the 18 x 16 mm bolt configuration. The rotational Reynolds number and throughflow Reynolds number, were adjusted to cover the range of bolt Reynolds numbers, $2 \times 10^5 \leq Re_D \leq 7 \times 10^5$, whilst keeping the value of λ_T constant. This process was carried out for λ_T = 0.09, 0.18, 0.22 and 0.25. The complete set of test conditions can be found in Appendix C.

Figure 7.11 shows the variation of moment coefficient, C_m, with bolt Reynolds number, Re_D, for the four different values of λ_T with the assumption that C = 1.5.

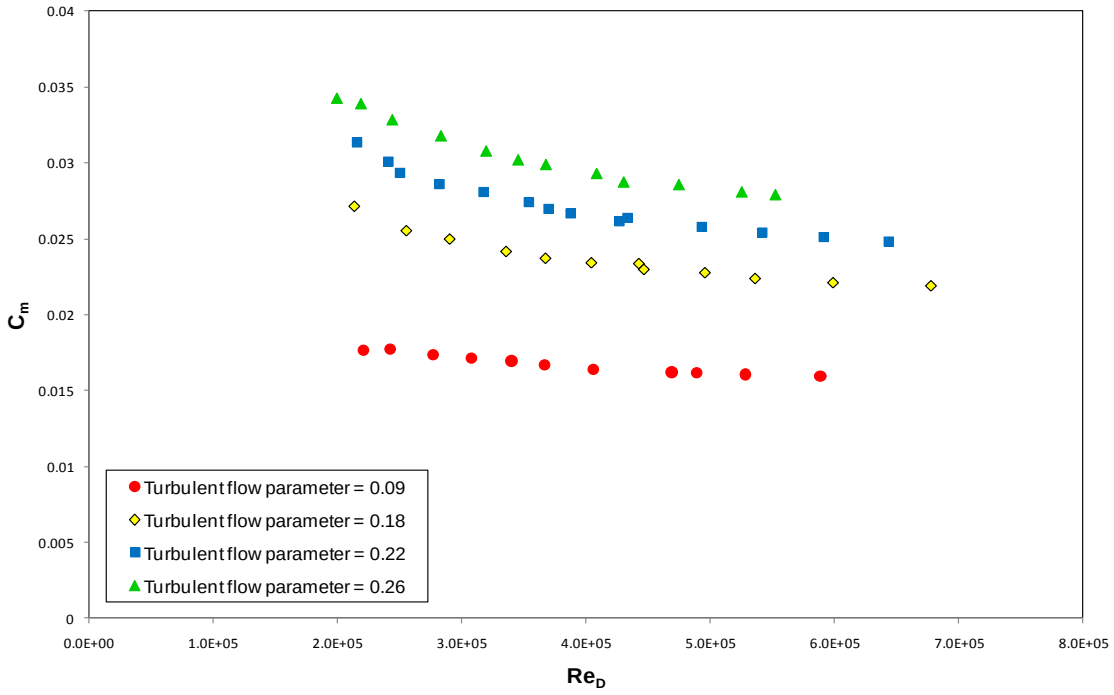

Figure 7.11 – Variation of C_m with Re_D and λ_T, C = 1.5, n = 3, 9 and 18, 0.36 x $10^7 \leq Re_\phi \leq$ 1.28 x 10^7 and 0.2 x $10^5 \leq C_w \leq 10^5$.

It can be seen that the higher values of λ_T show a clear decrease in moment coefficient with increasing bolt Reynolds number, whereas for λ_T = 0.09 the moment coefficient seems little affected by the variation of the flow conditions within the cavity. Figure 7.12 shows the same data as in Figure 7.11, with the assumption that C = 2.5. It can be seen that the variation in relative velocity between the rotor and the central core (represented by the increase in C) does not affect the value of moment coefficient for a given value of λ_T.

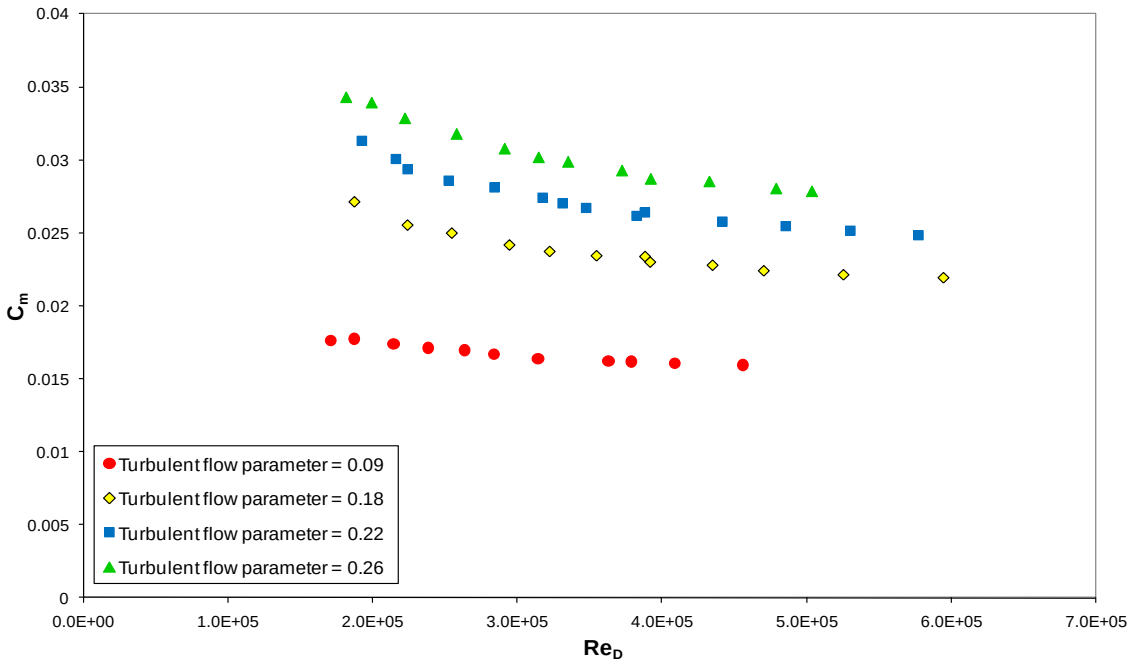

Figure 7.13 – Variation of C_m with Re_D and λ_T, C = 2.5, n = 3, 9 and 18, 0.36 x $10^7 \leq Re_\phi \leq$ 1.28 x 10^7 and 0.2 x $10^5 \leq C_w \leq 10^5$.

These results show clearly that although using λ_T for analysing the data is a useful tool, the complexity of the flow in the rotor-stator cavity is such that for a given value of λ_T, the moment coefficient may depend on the specific values of both Re_ϕ and C_w and not just λ_T.

Using the complete set of data from the hexagonal rotor bolt tests, a new correlation between the moment coefficient and the number and size of bolt was developed. This is shown in Equation 7.3, where (D/p) is the bolt diameter to pitch ratio.

$$C_m = 12.15 Re_\phi^{-0.67} C_w^{0.44} (D/p)^{0.27} \qquad \textbf{(7.3)}$$

The limits of this correlation are:

0.17 x $10^7 \leq Re_\phi \leq$ 1.5 x 10^7

0.24 x $10^5 \leq C_w \leq$ 1.06 x 10^5

$0.024 \leq (D/p) \leq 0.230$

This new correlation has significantly extended the range of D/p over which it is valid in comparison to existing correlations developed by **Millward and Robinson (1989)** and **Coren (2007)**. Millward and Robinson state the limits of bolt pitch to diameter ratio as $3 < p/D < 20$ and Coren as $4 < p/D < 26$. Converting the D/p limits of Equation 7.3 to p/D, gives a range of $4 < p/D < 42$. It can be seen, then, that the range over which Equation 7.3 can be used is considerably larger than the existing correlations.

Figure 7.13 shows a comparison between the measured values of moment coefficient and those predicted by Equation 7.3. There is good agreement, generally within 5%, between the measured and the correlated data, particularly where $C_m < 0.04$. For $C_m > 0.04$ the agreement is not quite as good. However, it is at these test points that the disc speed is lowest ($N < 3000$ rev/min). The measured torque is small in this region (between 2 N m and 4 N m) and so the measurement uncertainties are relatively large, as can be seen from the uncertainty bars shown in Figure 7.13.

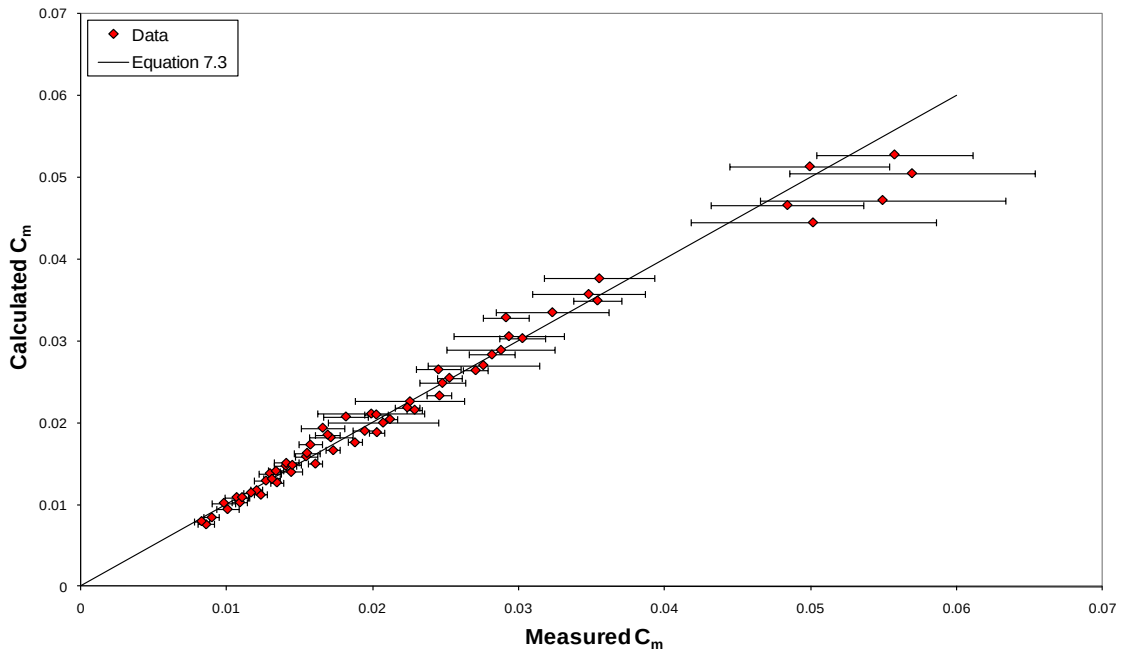

Figure 7.13 – Variation of measured C_m with C_m calculated using Equation 7.3.

This correlation can be used to predict the resulting moment coefficient, in a rotor-stator cavity with throughflow, from the number and size of bolts present. This provides turbomachinery engineers with the means to assess the windage contribution, for a much wider range of conditions than previously possible.

7.4 Hexagonal rotor bolt surface temperature results

Rotor surface temperature measurements were obtained at five radii on the test side (r/b = 0.427, 0.6, 0.684, 0.887 and 0.935) as well as at one radius on the balance side (r/b = 0.887). The last 120 seconds of data from each sensor for each test is averaged to get a temperature measurement for each position on the rotor. More details on the data acquisition method can be found in Section 5.4 with reference to the plain disc tests. Since there are variations in inlet temperature from one test to another, the data is presented in terms of the disc-surface-to-inlet-air temperature difference.

As with the plain disc results, a plot similar to Figure 7.14 was produced for every test condition. Figure 7.14 shows the variation of the disc-surface-to-inlet-air temperature difference with non-dimensional radius for n = 9, D = 13 mm, $C_w = 10^5$, $\mathrm{Re}_\phi = 1.4 \times 10^7$ and $\lambda_T = 0.194$.

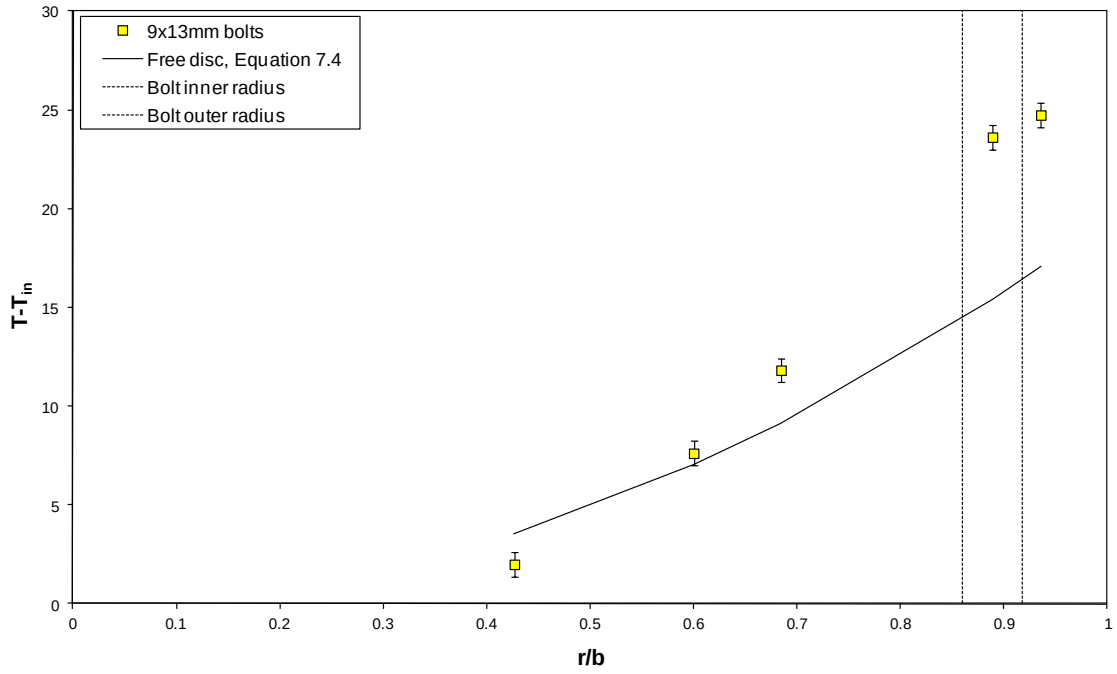

Figure 7.14 – Variation of disc-surface-to-inlet-air temperature difference with non-dimensional radius, n = 9, D = 13 mm, $C_w = 10^5$, $\mathrm{Re}_\phi = 1.4 \times 10^7$ and $\lambda_T = 0.194$.

The location of the bolt is shown by the dashed lines at r/b = 0.86 and 0.92. The adiabatic disc-surface-to-inlet-air temperature difference prediction for a free disc is also shown, as given by **Owen and Rogers (1989)** in Equation 7.4.

$$T_{0,ad} - T_{\infty} = R\frac{\omega^2 r^2}{2C_p} \qquad \textbf{(7.4)}$$

In this equation, $T_{0,ad}$ is the adiabatic disc temperature and T_{∞} is the temperature of the air away from the disc, taken here as the static temperature measured at the inlet to the cavity. The specific heat of air at constant pressure, C_p, is calculated using T_{∞}. The recovery factor R was found using the approximation $R = \mathrm{Pr}^{1/3}$. The Prandtl number, Pr, is evaluated from Equation 7.5, where k is the thermal conductivity and μ is the dynamic viscosity, evaluated at the temperature measured at the inlet to the cavity.

$$\mathrm{Pr} = \frac{\mu C_p}{k} \qquad \textbf{(7.5)}$$

The measured disc surface temperatures in Figure 7.14 show a distinct increase above the adiabatic disc temperature where $r/b > 0.6$. This is attributed to the increased windage due to the presence of the bolts, and is in agreement with the increased windage above that of the free disc, shown in Figure 7.7.

The effect of bolt diameter on disc surface temperature can be seen in Figures 7.15 and 7.16. These plots show the variation of the disc-surface-to-inlet-air temperature difference with non-dimensional radius for n = 9 and D = 10 mm, 13 mm and 16 mm. Figure 7.15 shows the results for the condition $C_w = 10^5$, $\mathrm{Re}_{\phi} = 0.7 \times 10^7$ and $\lambda_T = 0.34$, which represents radially dominated flow. Figure 7.16 shows the results for the condition $C_w = 0.3 \times 10^5$, $\mathrm{Re}_{\phi} = 10^7$ and $\lambda_T = 0.06$, representing rotationally dominant flow.

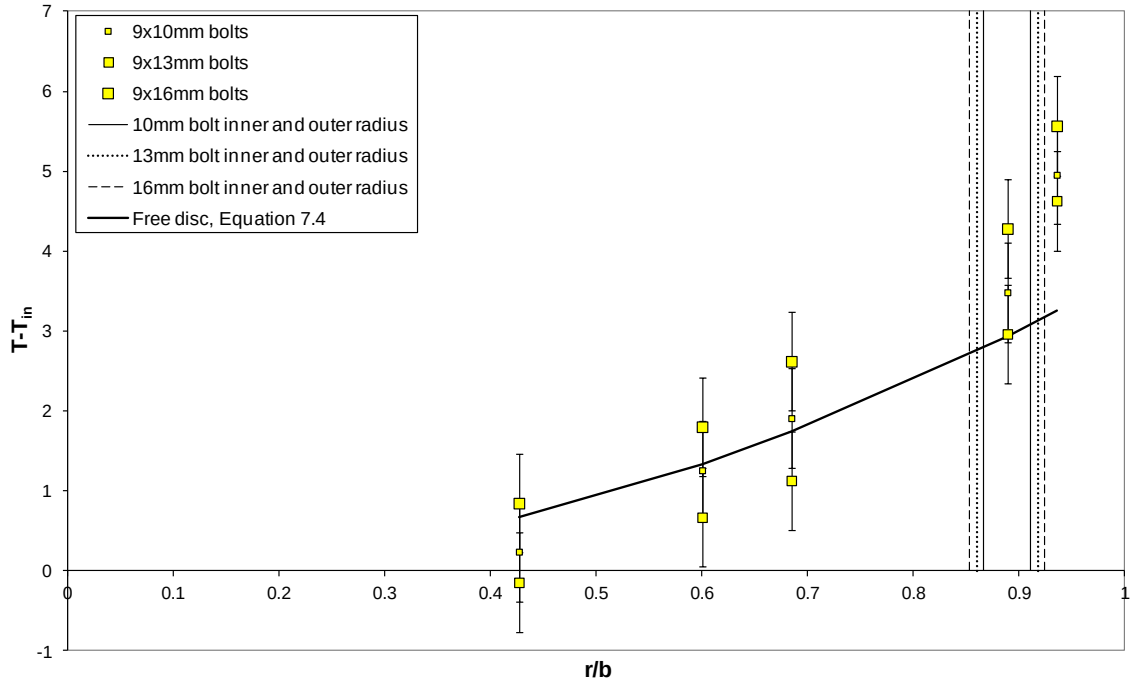

Figure 7.15 – Variation of disc-surface-to-inlet-air temperature difference with non-dimensional radius, $C_w = 10^5$, $\mathrm{Re}_\phi = 0.7 \times 10^7$ and $\lambda_T = 0.34$.

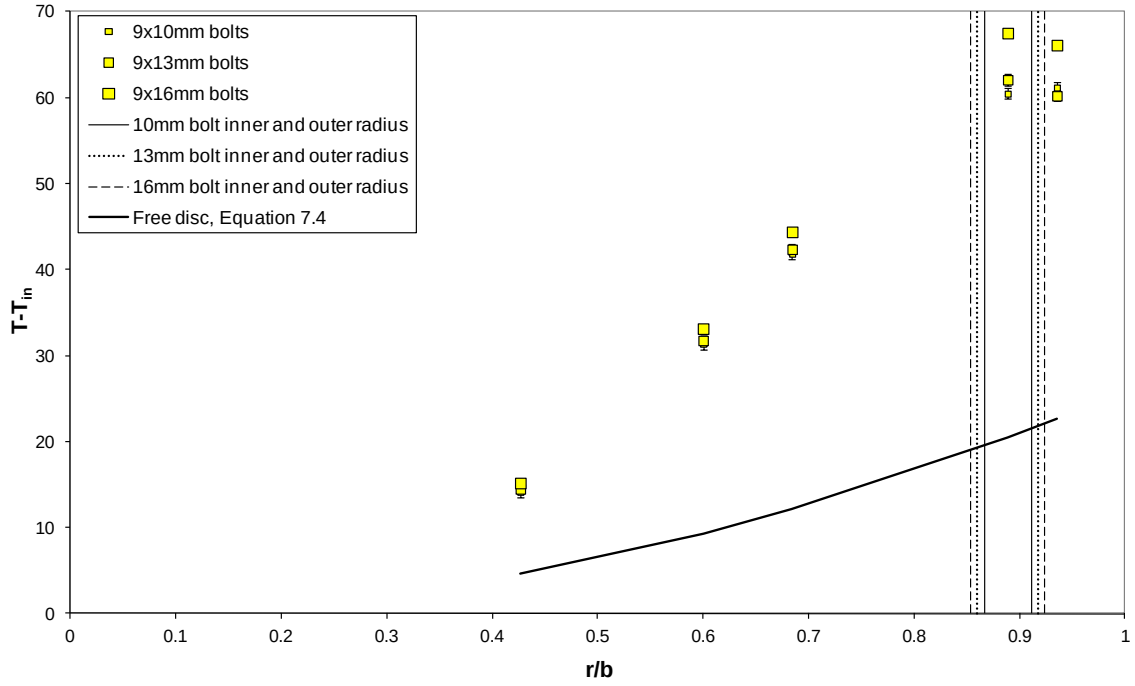

Figure 7.16 – Variation of disc-surface-to-inlet-air temperature difference with non-dimensional radius, $C_w = 0.3 \times 10^5$, $\mathrm{Re}_\phi = 10^7$ and $\lambda_T = 0.06$.

It can be seen in Figure 7.15 that a clear trend cannot be picked out due to the large relative uncertainties in the measurement. These uncertainties are large for two reasons.

Firstly, the maximum temperature difference measured at this radially dominated flow condition is just over 5 °C. Since the uncertainty in the infra red temperature measurement is ± 0.62 °C, the relative uncertainty is over 10% at this condition, and increases further with decreasing temperature difference. Secondly when referring to a differential temperature measurement, the uncertainties in each separate measurement are combined (see Chapter 4) resulting in a larger uncertainty in the differential term.

It can be seen, however, in Figure 7.16 that when $\lambda_T = 0.06$, and the flow is rotationally dominant, the disc-surface-to-inlet-air temperature difference increases with increasing bolt diameter. In the region of the bolt radius, $r/b \approx 0.9$, increasing the diameter of the bolt, from 10 mm to 16 mm, causes an increase in the disc surface temperature of 7 °C. There is also a small increase in surface temperature at this radius when increasing from 10 mm to 13 mm, although only by 2 °C. Even a small increase in disc surface temperature, however, is of great importance to turbomachinery engineers as it can considerably extended component life. As with the results presented earlier for moment coefficient, Figure 7.16 shows that the increase in temperature does not increase consistently with a consistent increase in bolt diameter.

The area average disc temperature, calculated using the method described in Section 4.2.4, is used in Figure 7.17 to compare data from the different test conditions. Figure 7.17 shows the variation of the area average disc-surface-to-inlet-air temperature difference with the number and diameter of bolts for nominally constant values of λ_T. Plain disc values are also indicated on the left hand vertical axis, at $n = 0$.

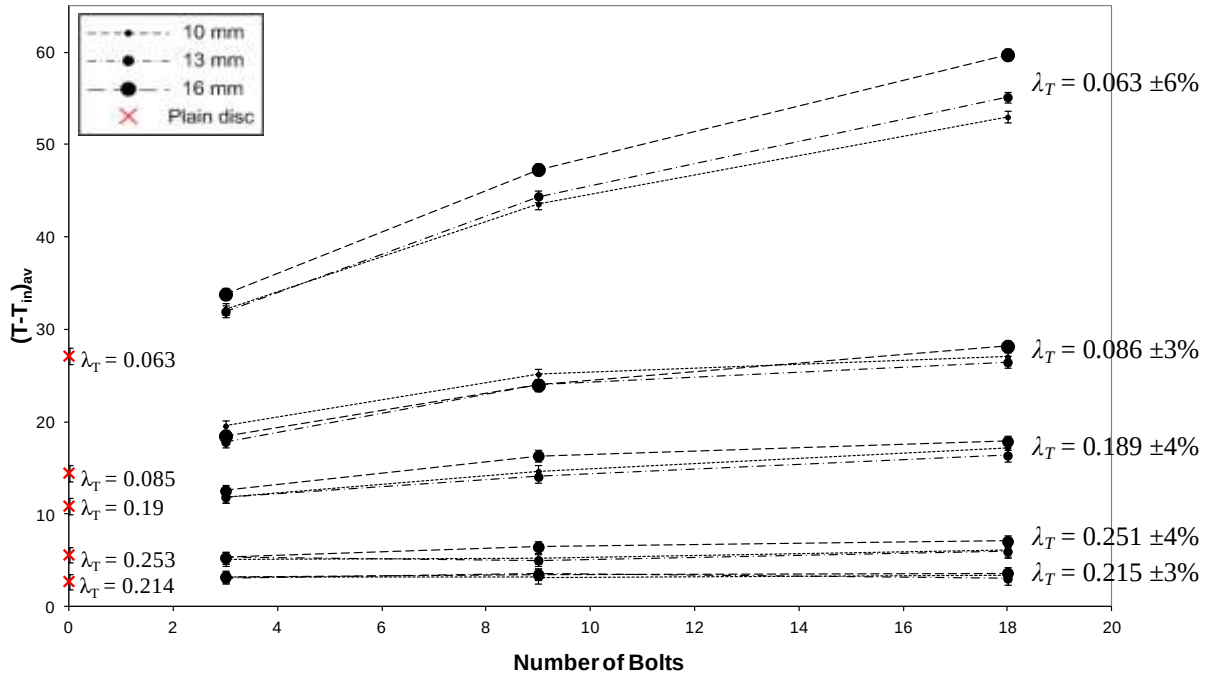

Figure 7.17 – Variation of area average disc-surface-to-inlet-air temperature difference with n, D and λ_T, $0.17 \times 10^7 \leq Re_\phi \leq 1.5 \times 10^7$.

Considering first the data for $\lambda_T = 0.06$ (± 6%), a clear trend of increasing temperature difference with bolt diameter can be seen, particularly where $n = 18$. For the higher values of λ_T, however, no clear trends can be established. This is again due to the variations in the observed temperature difference with varying bolt size, being of the order of a few Kelvin. The relative measurement uncertainties, therefore, are high. As such clear trends at these conditions cannot be expected with the current instrumentation set up.

7.5 Summary

The rotor bolt results show that windage is generally increased with increasing bolt diameter, though the increase does not appear to be consistent with a consistently increasing diameter. Relating the flow around the bolts to the flow around a circular cylinder suggests that the majority of the tests take place in the transitional region between laminar and turbulent separation. It is thought that this is the cause for the observed non-consistent increase in windage.

A correlation between the number and size of bolt and the resulting windage has been produced (Equation 7.3), which is important for turbomachinery engineers to be able to assess windage in a rotor-stator system. This new correlation can be used for a much wider range of bolt pitch to diameter ratio than the existing correlations developed by **Millward and Robinson (1989)** and **Coren (2007)**.

Chapter 8. Bi-Hexagonal Bolt and Surface Cavity Tests

8.1 Introduction

This chapter discusses the testing method and results obtained from the bi-hexagonal rotor bolt tests and the rotor surface cavity tests.

Tests were carried out with bi-hexagonal bolts because this type of bolt is commonly used within the internal structure of a gas turbine engine. The work in this thesis has so far been aimed at a theoretical investigation to provide a general understanding of the nature of the flow around a bolt. The purpose of the bi-hexagonal bolt tests is to investigate a practical application, and determine if a bi-hexagonal bolt creates the same amount of windage as an equivalent hexagonal bolt. The 13 mm bi-hexagonal bolts were fixed to both sides of the rotor. The flow conditions were designed to match the 13 mm hexagonal bolt tests so that a direct comparison could be made between the two shapes. The number of the bolts was varied so that n = 3, 9 and 18 and the tests covered the range of non-dimensional conditions: $0.27 \times 10^7 \leq \mathrm{Re}_\phi \leq 1.43 \times 10^7$; $0.26 \times 10^5 \leq C_w \leq 1.05 \times 10^5$; and $0.06 \leq \lambda_T \leq 0.62$.

The effects of cavities in the rotor surface, on windage and surface temperature were also investigated. The surface cavities aim to represent the condition sometimes found within a gas turbine engine where a large cap screw is used. The cap screws are usually countersunk into the disc surface and so the hole with which the cap screw is fastened creates a cavity. Research by **Geis *et al*. (2001)** saw increased windage effects with surface cavities and the results were considered compelling enough for further investigations. For these tests, inserts were placed into large, M14 holes in the disc, which create a cavity on either side of the disc surface. Again, the number was varied

so that n = 3, 9 and 18. The tests covered the range of non-dimensional conditions: 0.21 x $10^7 \leq$ $Re_\phi \leq$ 1.67 x 10^7; 0.26 x $10^5 \leq$ $C_w \leq$ 1.04 x 10^5; and 0.06 $\leq$ $\lambda_T \leq$ 0.52.

8.2 Bi-hexagonal bolt test procedure

Tests were performed with bi-hexagonal bolt heads attached to both side of the rotor surface, at a variety of flow conditions. The conditions were designed to match those of the 13 mm hexagonal bolt tests, so the results could be directly compared. Any variation between the two bolt shapes, in both moment coefficient and rotor surface temperature, could then be observed. The number of bolts, n, was varied so that n = 3, 9 and 18. The bolts were attached to both sides of the rotor at a radius of r = 0.2 m, representing a non-dimensional radius r/b = 0.889.

The bi-hexagonal bolt head is shown in Figure 8.1 (a). It can be seen from Figure 8.1 (b) that the bi-hexagonal bolt heads measure roughly 13 mm across and 11 mm deep, which matches the dimensions of the 13 mm hexagonal bolts.

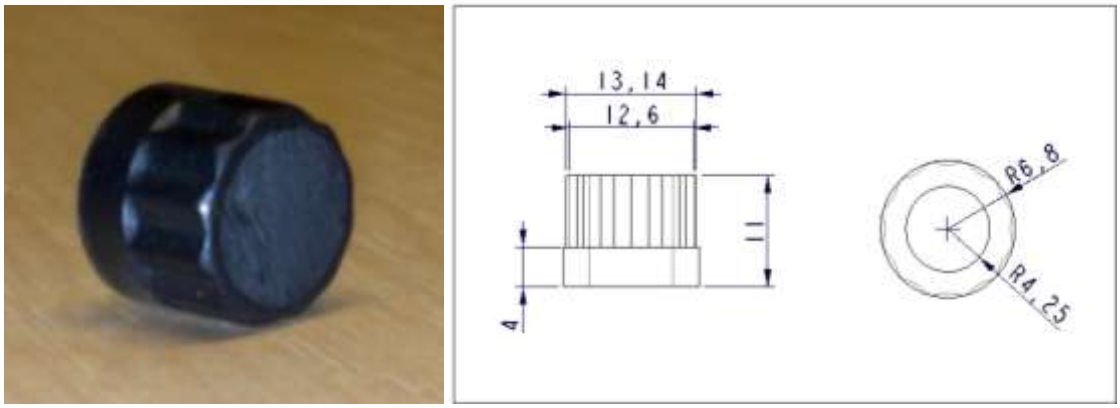

(a) **(b)**

Figure 8.1 – (a) Picture of bi-hexagonal bolt head. (b) Bolt head dimensions (mm).

In order to attach the bi-hexagonal bolt heads to the disc, inserts were made as shown in Figure 8.2 (a). These inserts fitted into the M14 holes that have been machined into the disc at a radius of r = 0.2. The bi-hexagonal bolt heads could then be screwed onto either side of the disc. The insert in the disc along with the bolt head attached to it is demonstrated in Figures 8.2 (b) and (c).

(a) **(b)** **(c)**

Figure 8.2 – (a) Picture of disc insert for bi-hexagonal bolts. (b) Insert in the disc. (c) Bi-hexagonal bolt attached.

A standard bi-hexagonal bolt was acquired, which came with a flange around the base. This was machined off for the purposes of these tests, leaving a 4 mm smooth section at the base. Any variation in windage between the two bolt shapes is expected to be due to variations in wake formation and hence form drag. It was therefore decided that smooth section at the base of the bolt was unlikely to affect the results of the tests, as this section is in the rotor boundary layer and not in the core flow where form drag is prominent.

For the hexagonal bolts, the effective diameter of the bolt with respect to the flow direction can vary by up to 2.5 mm (for the sizes of bolt tested) depending on its positioning on the disc surface, with respect to the direction of flow. Careful measures were therefore taken to ensure they were all placed in the same orientation relative to the flow (details of hexagonal bolt orientation can be found in Sections 6.2 and 7.2). Conversely, the diameter of the bi-hexagonal bolts varies little with positioning relative to flow direction. As such it was decided that the position of the bolt head relative to the flow would be inconsequential to the test results.

As with the 13 mm hexagonal bolt tests, the test conditions included a range of values of turbulent flow parameter, λ_T ($\lambda_T = C_w/\mathrm{Re}_\phi^{0.8}$, where $C_w = \dot{m}/\mu b$ and $\mathrm{Re}_\phi = \rho\omega b^2/\mu$), for two different values of superimposed throughflow, $C_w = 0.3 \times 10^5$ and 10^5. Table 8.1 shows the range of test conditions. The complete set of test conditions can be found in Appendix C.

Re_ϕ	$0.27 \times 10^7 \leq Re_\phi \leq 1.43 \times 10^7$
C_w	$0.26 \times 10^5 \leq C_w \leq 1.05 \times 10^5$
λ_T	$0.06 \leq \lambda_T \leq 0.62$
p (absolute, bar)	$2 \leq p \leq 5$
$\dot{m}$ (kg/s)	$0.12 \leq \dot{m} \leq 0.4$
N (rev/min)	$2500 \leq N \leq 10100$

Table 8.1 – Test conditions for the bi-hexagonal bolt tests.

For each test, once the correct flow conditions had been achieved the test rig was allowed to stabilise before any measurements were taken. The stabilisation conditions used for the current test program are discussed in Section 5.4. This process took approximately half an hour.

8.3 Bi-hexagonal bolt windage results

Torque measurements were acquired at 1 Hz throughout each test, using an in-line torquemeter positioned between the gearbox and the rotor shaft. The last 120 s of data was then averaged to give a torque measurement for each test point. Further details on the data acquisition method can be found in Section 5.4 with reference to the plain disc tests. The torque measurement, M, was then converted to a moment coefficient C_m ($C_m = 2M/\rho\omega^2 b^5$) which is used to compare windage for different test conditions.

Figures 8.3 and 8.4 show the variation of moment coefficient, C_m, with number of bolts, n, and turbulent flow parameter, λ_T, for bi-hexagonal and hexagonal rotor bolts where $C_w = 0.3 \times 10^5$ and 10^5 respectively. These figures show that for most values of λ_T there is a small reduction in moment coefficient, between 5% and 7%, when there are eighteen bi-hexagonal bolts present, compared to eighteen hexagonal bolts. However, the uncertainty in the measurement means that a clear trend cannot be established.

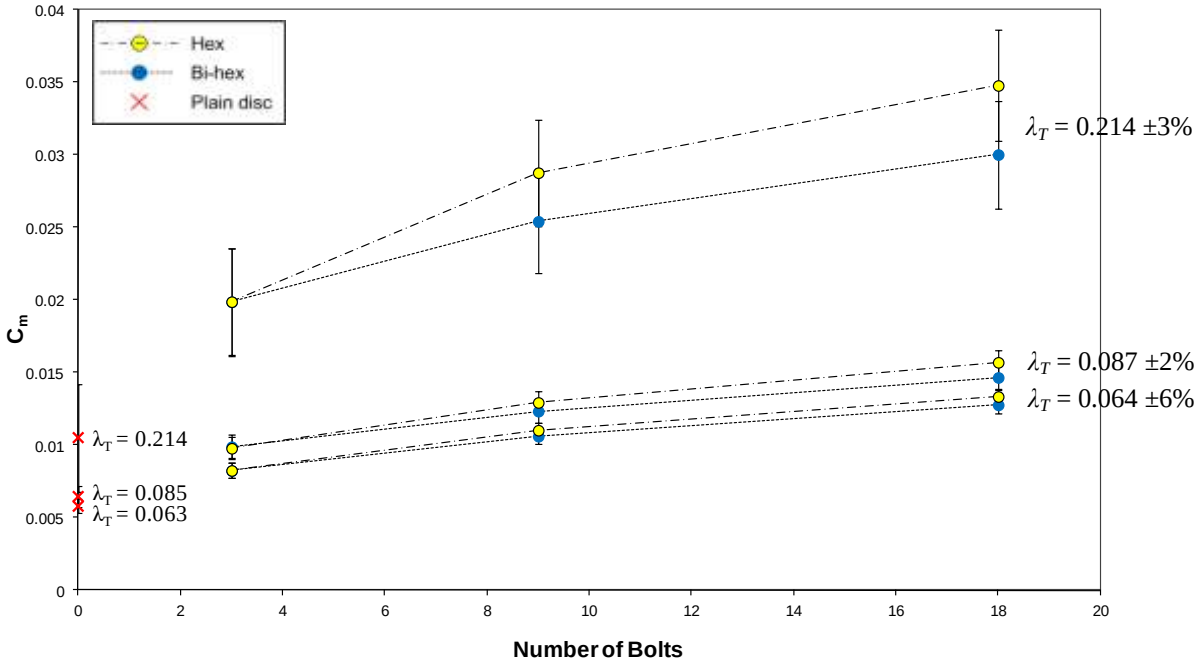

Figure 8.3 – Variation of C_m, with n and λ_T for bi-hexagonal and hexagonal bolts. C_w = 0.3 x 10^5 and 0.27 x $10^7 \leq$ $Re_\phi \leq$ 1.1 x 10^7.

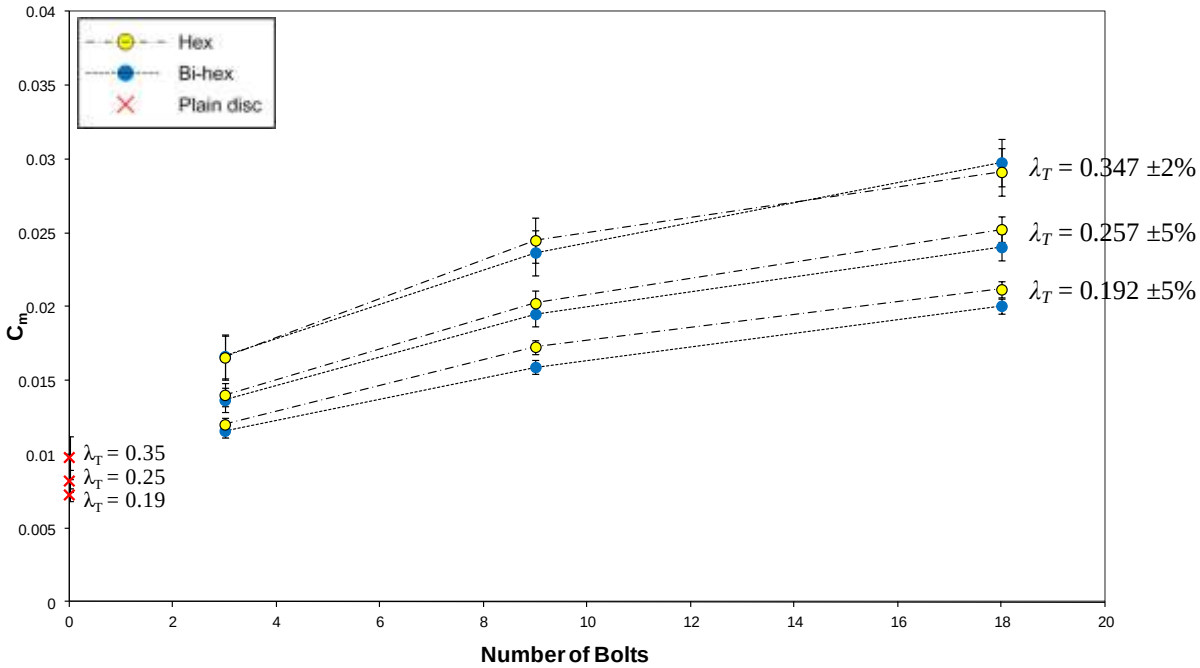

Figure 8.4 – Variation of C_m, with n and λ_T for bi-hexagonal and 13 mm hexagonal bolts. C_w = 10^5 and 0.67 x $10^7 \leq$ $Re_\phi \leq$ 1.49 x 10^7.

Figure 8.5 shows the variation of $C_m Re_\phi^{0.2}$ with λ_T for the complete set of bi-hexagonal bolt test results, along with the corresponding 13 mm hexagonal rotor bolt test results.

The ordinate $C_m \mathrm{Re}_\phi^{0.2}$ was chosen because it represents the effect of the protrusions in terms of the increase in C_m over that of a free disc at the same conditions. The free disc has a constant value, indicated in Figure 8.5 by the solid line at $C_m Re_\phi^{0.2} = 0.146$. This is taken from von Kármán's relationship for moment coefficient as shown in Equation 8.1.

$$C_m = 0.146\,\mathrm{Re}_\phi^{-0.2} \qquad \textbf{(8.1)}$$

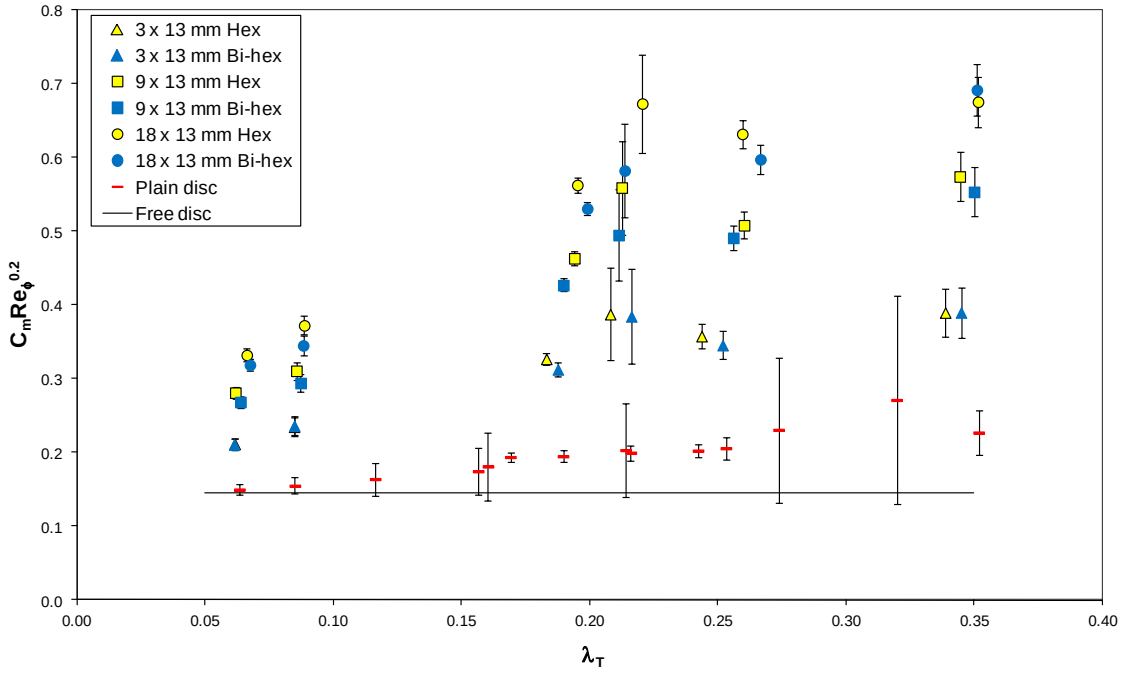

Figure 8.5 – Variation of $C_m \mathrm{Re}_\phi^{0.2}$ with λ_T for bi-hexagonal and 13 mm hexagonal bolts, $0.27 \times 10^7 \leq \mathrm{Re}_\phi \leq 1.49 \times 10^7$.

It can be seen in figure 8.5 that where $\lambda_T < 0.1$, the value of $C_m \mathrm{Re}_\phi^{0.2}$ is reduced by a small amount with 9 and 18 bi-hexagonal bolts compared with the hexagonal bolts. Again though, as with the results shown in Figures 8.3 and 8.4, this is not outside the limits of uncertainty, and therefore cannot be identified as a valid trend. Where $\lambda_T = 0.192$ (±5%), however, there is shown to be a clear reduction with 9 and 18 bi-hexagonal bolts present, by 8% and 6% respectively.

Payne (2011) used Particle Image Velocimetry (PIV) to investigate the differences in the wakes of hexagonal and bi-hexagonal bolts, and compared them with a circular cylinder. The tests were carried out in a wind tunnel and the hexagonal bolts were

tested at two angles: with the flat face toward the free stream; and with the point towards the free stream, as the bolts are positioned on the disc in the current experiments (Figure 7.3 in Chapter 7 shows the orientation of the hexagonal bolts). Payne's measurements showed that the hexagonal bolt, at both angles, always created a wider wake area than the bi-hexagonal bolt, and the wake tended to extend further downstream. The wider and longer wake results in higher form drag, which is likely to be the reason for the reduction in moment coefficients observed for the bi-hexagonal bolts at $\lambda_T = 0.192$ in Figure 8.5. The results by Payne, however, were obtained for laminar flow only. Using Equation 8.2, a Reynolds number can be estimated that is based on an approximate relative velocity between the bolt and the fluid $V_{\phi,rel}$ and the diameter of the bolt D as a length scale. For the range of conditions tested, the estimated bolt Reynolds numbers, Re_D, suggests the flow around the bolts is likely to be either transitional or fully turbulent. The wake effects, therefore, may not be the same as those observed by Payne (further details on the calculation of Re_D can be found in Section 7.3).

$$\mathrm{Re}_D = \frac{\rho V_{\phi,rel} D}{\mu} \qquad \textbf{(8.2)}$$

At the high throughflow, high rotational speed condition $\lambda_T = 0.192$ (±5%), where the larger reduction in $C_m\mathrm{Re}_\phi^{0.2}$ is observed, the measured torque is very large, nearly 70% higher than any other condition. It seems, therefore that only where the measured torque is large, does the small reduction in form drag due to the shape of the bi-hexagonal bolt, result in a measureable reduction in torque and hence a reduction in the parameter $C_m\mathrm{Re}_\phi^{0.2}$.

8.4 Bi-hexagonal bolt surface temperature results

Rotor surface temperature measurements were obtained at five radii on the test side (*r/b* = 0.427, 0.6, 0.684, 0.887 and 0.935) as well as at one radius on the balance side (*r/b* = 0.887). The last 120 seconds of data from each sensor for each test is averaged to get a temperature measurement for each position on the rotor. More details on the data acquisition method can be found in Section 5.4 with reference to the plain disc tests. Since there are variations in inlet temperature from one test to another, the data is presented in terms of the rotor-surface-to-inlet-air temperature difference.

Figures 8.6 and 8.7 show the variation of the area average disc-surface-to-inlet-air temperature difference, $(T\text{-}T_{in})_{av}$, with n and λ_T, for bi-hexagonal and hexagonal rotor bolts, where $C_w = 0.3 \times 10^5$ and 10^5 respectively. The area average disc-surface-to-inlet-air temperature difference allows a comparison of the bi-hexagonal, hexagonal and plain disc test results to be made over the complete range of conditions tested. It is calculated using Equation 8.3, where $r_1 = 0.096$ m, $r_5 = 0.2105$ m and T is the disc-surface-to-inlet-air temperature difference at each radial location, r.

$$T_{average} = \frac{2}{r_5^2 - r_1^2} \int_{r_1}^{r_5} Tr dr \qquad \textbf{(8.3)}$$

The integral on the right hand side of Equation 8.3 is approximated using Simpson's rule, as discussed in Section 4.2.4.

It can be seen in Figure 8.6 that when $\lambda_T = 0.064$ (±6%) there is a reduction in disc-surface-to-inlet-air temperature difference of 4 °C with nine and 5 °C with eighteen bi-hexagonal bolts, compared with the hexagonal bolts. There is even a 1.5 °C reduction in temperature when there are just three bolts present. This flow condition is similar to that found in a modern jet engine and this large reduction in disc surface temperature, with nine and eighteen bolts present, would significantly increase the life of a turbine disc. Even the 1.5 °C reduction observed with 3 bolts could be significant to a highly stressed turbine disc, at this high rotational engine condition. This trend, however, is not observed at other flow conditions. When λ_T increases to just 0.087 (±2%), the

reduction in disc-surface-to-inlet-air temperature difference, with 18 bi-hexagonal bolts drops to just 1.3 °C. At all other conditions, as seen in both Figure 8.6 and 8.7, there is no variation between the hexagonal and bi-hexagonal bolts outside of the uncertainty limits.

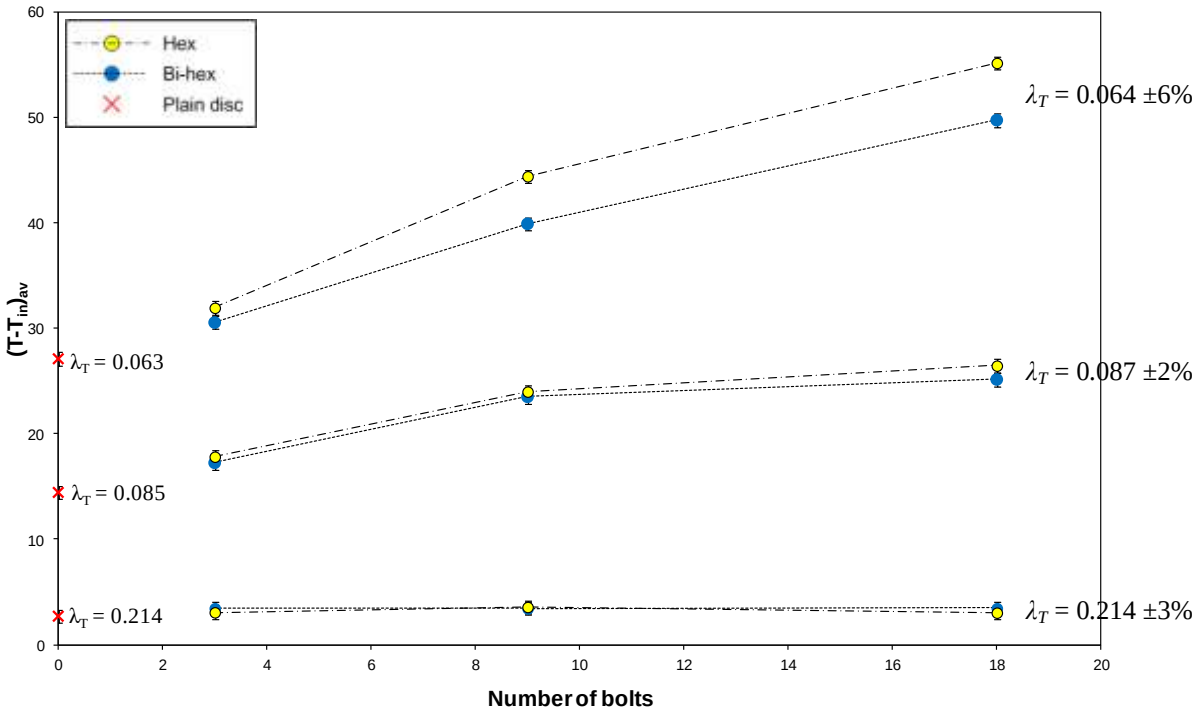

Figure 8.6 – Variation of area average disc-surface-to-inlet-air temperature difference with n and λ_T, C_w = 0.3 x 10^5 and 0.27 x $10^7 \leq$ $Re_\phi \leq$ 1.1 x 10^7.

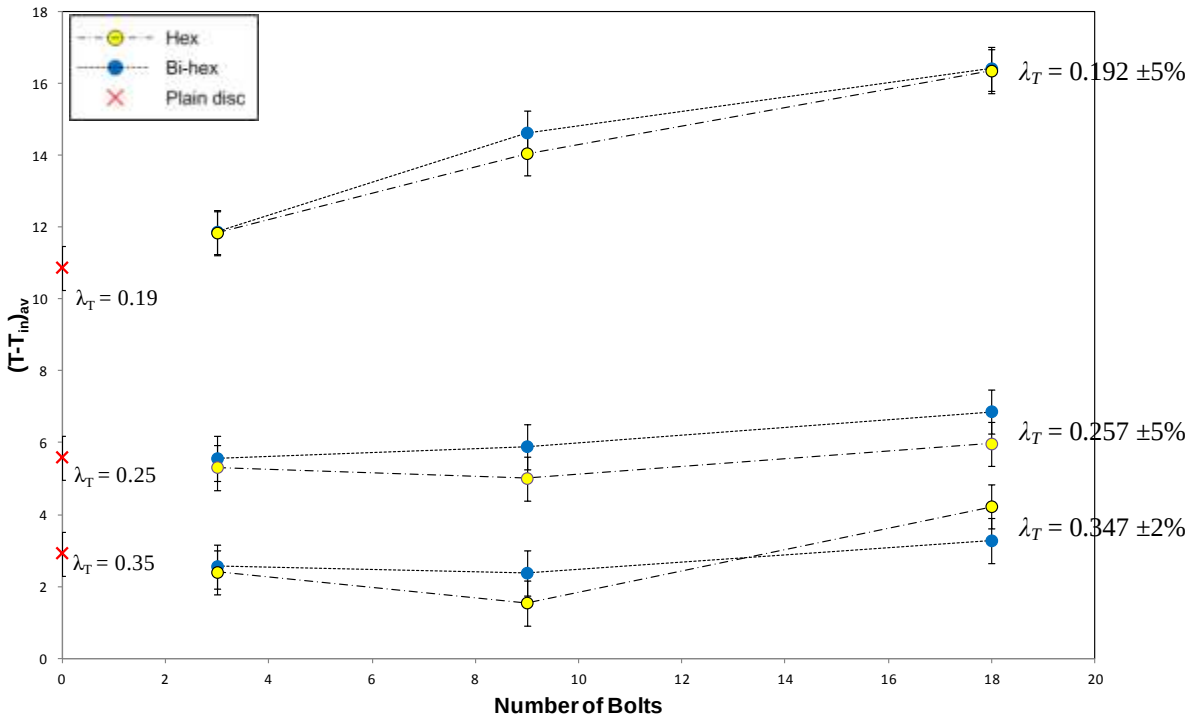

Figure 8.7 – Variation of area average disc-surface-to-inlet-air temperature difference with n and λ_T. $C_w = 10^5$ and $0.67 \times 10^7 \leq Re_\phi \leq 1.49 \times 10^7$.

It was necessary to further investigate the large reduction in disc-surface-to-inlet-air temperature difference seen for the bi-hexagonal bolts compared with the hexagonal bolts at the condition $\lambda_T = 0.064$ (±6%). Further tests were carried out with eighteen bolts and $C_w \approx 0.3 \times 10^5$ only, as the temperature difference between the hexagonal and bi-hexagonal bolts is largest at these conditions. These tests covered the range of conditions specified in Table 8.2, the full set of test conditions can be found in Appendix C.

Re_ϕ	$0.72 \times 10^7 \leq Re_\phi \leq 1.15 \times 10^7$
C_w	$0.28 \times 10^5 \leq C_w \leq 0.25 \times 10^5$
λ_T	$0.055 \leq \lambda_T \leq 0.092$
p (absolute, bar)	$3 \leq p \leq 5$
N *(rev/min)*	$7800 \leq N \leq 11400$

Table 8.2 - Test conditions for extra bi-hexagonal bolt tests.

Figure 8.8 shows the variation of the relative outlet-to-inlet air temperature difference with λ_T for these extra tests. It should be noted that it is the relative outlet-to-inlet air temperature difference used here rather than the disc-surface-to-inlet-air temperature difference that has been used previously. It is likely that the observed reduction in temperature is due to a reduction in form drag. This would most directly affect the temperature of the air, and not all of this heat energy is necessarily transferred to the disc at all conditions. Therefore the outlet air temperature relative to the inlet temperature is used for presenting these results. It can be seen that 5 °C reduction in relative outlet air temperature, seen at λ_T = 0.066 (±3%) for the bi-hexagonal bolts, only occurs at this particular flow condition. Where λ_T = 0.079 (±1%) and p = 3 bar, there is a 3 °C (3.5%) reduction observed, however, at all other conditions there is no measureable difference in relative outlet air temperature between the bi-hexagonal and hexagonal bolts.

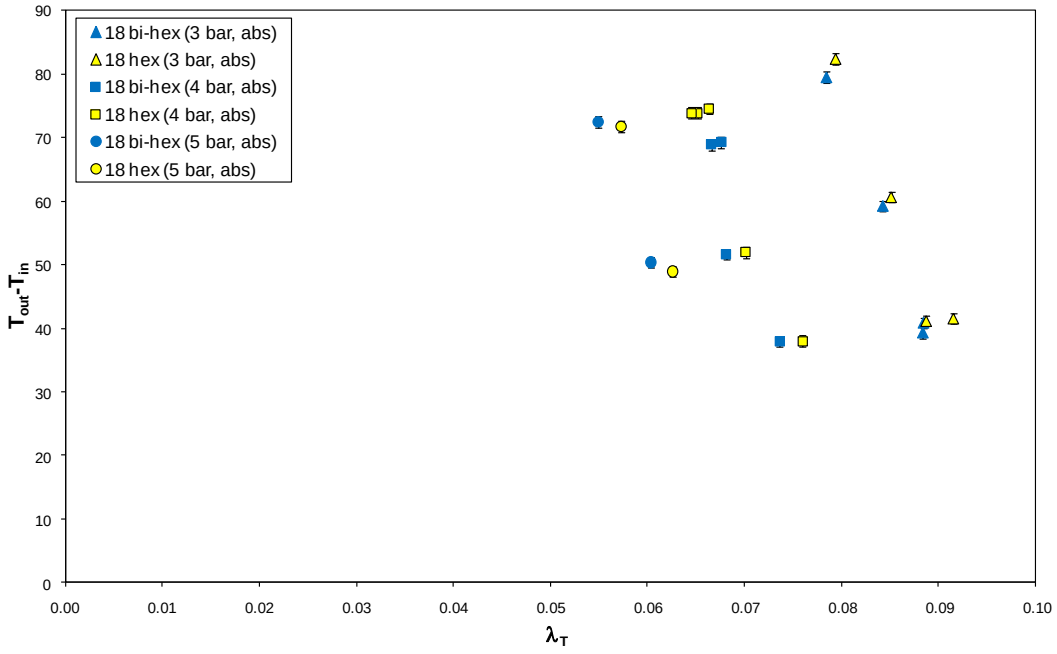

Figure 8.8 – Variation of relative outlet-to-inlet air temperature difference with λ_T and p. C_w = 0.3 x 10^5 and 0.72 x $10^7 \leq$ Re$_\phi \leq$ 1.15 x 10^7.

Figure 8.9 shows the variation of C_m with λ_T for the extra set of tests. It can be seen here that there is generally no measureable difference between the results for the bi-hexagonal and hexagonal bolts, even where λ_T = 0.066 (±6%). A small reduction, however, outside of the measurement uncertainty is observed at λ_T = 0.079 (±1%) of

6.5%. This is larger than the reduction in relative outlet temperature observed at this same condition in Figure 8.8, however the reduction in measured torque is 3.5%, the same as the temperature reduction.

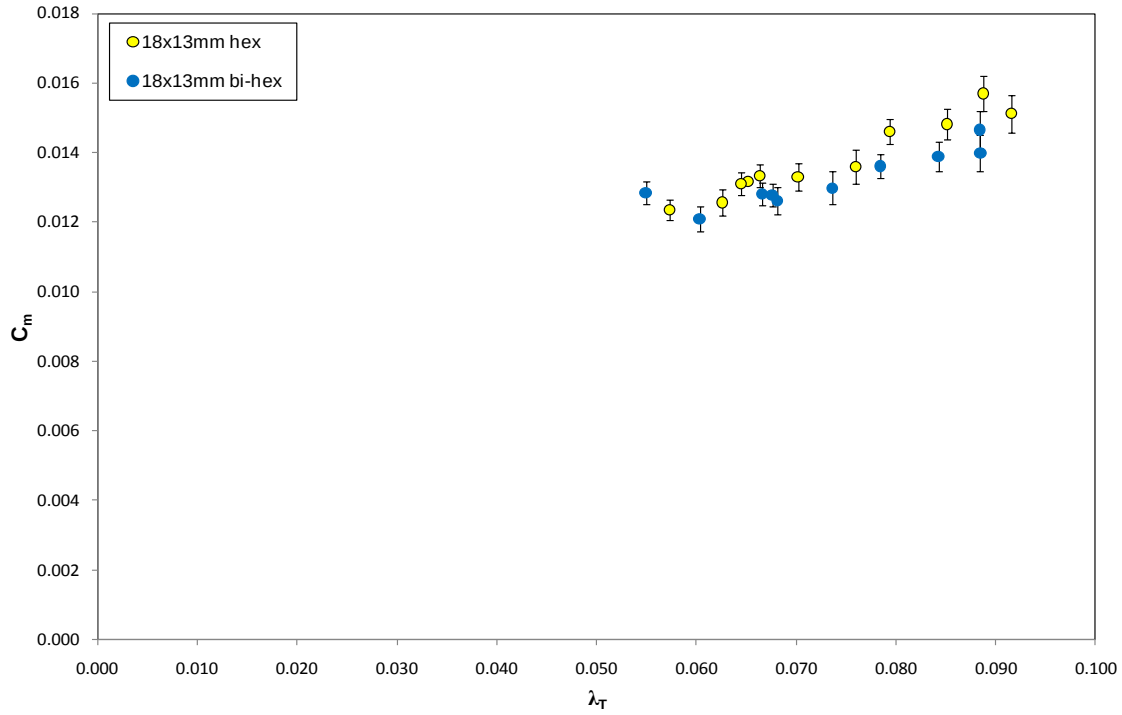

Figure 8.9 – Variation of C_m with λ_T. C_w = 0.3 x 10^5 and 0.72 x $10^7 \leq$ Re$_\phi \leq$ 1.15 x 10^7.

It seems from these tests that the temperature and moment coefficient results are conflicting. This may be due to small variations in the conditions between the hexagonal and bi-hexagonal tests. Obtaining the value of λ_T required in a test is challenging, particularly at these low throughflow rates. The use of motorised valves enabled safer testing, by removing the need to enter the test cell during a test, however, the resolution of the control was not as fine as a manual valve. Also, it was shown in Section 7.3, with reference to the hexagonal rotor bolts, that the moment coefficient is not only dependant on λ_T but also the specific values of Re$_\phi$ and C_w. This was not accounted for in the current set of tests, since the testing referred to in Section 7.3 was carried out after this set of tests. Therefore in these tests a particular value of λ_T was targeted, with a similar value of C_w and any variations in Re$_\phi$ between tests were not thought to be of great consequence.

Further testing is required to fully investigate this large reduction in surface temperature (shown in Figure 8.6 and 8.8) which is seemingly limited to one or two flow conditions within the cavity. This testing should investigate the same range of λ_T, or perhaps extend the range to lower values of λ_T, but with varying values of Re_ϕ and C_w for each value of λ_T tested. Achieving $\lambda_T = 0.066$ with a variety of Re_ϕ and C_w could produce data to help explain the cause of the large reduction in disc surface temperature observed. This further testing was not carried out in this test programme due to time constraints.

8.5 Surface cavity test procedure

To measure the effect of surface cavities on windage and disc surface temperature, tests were carried out with inserts fitted into the M14 holes in the disc at a radius of 0.2 m ($r/b = 0.889$). Figure 8.10 shows one side of the disc with a surface cavity insert, however each insert creats an equivalent cavity on both surfaces of the disc.

Figure 8.10 – Picture showing surface cavity inserts in disc.

Inserts were produced to replicate three different sized cavities: 10 mm diameter and 6 mm deep; 10 mm diameter and 3 mm deep; and 5 mm diameter and 6 mm deep. The 10 mm diameter, 6 mm deep insert can be seen in Figure 8.11 (a) and the dimensions are shown in Figure 8.11 (b).

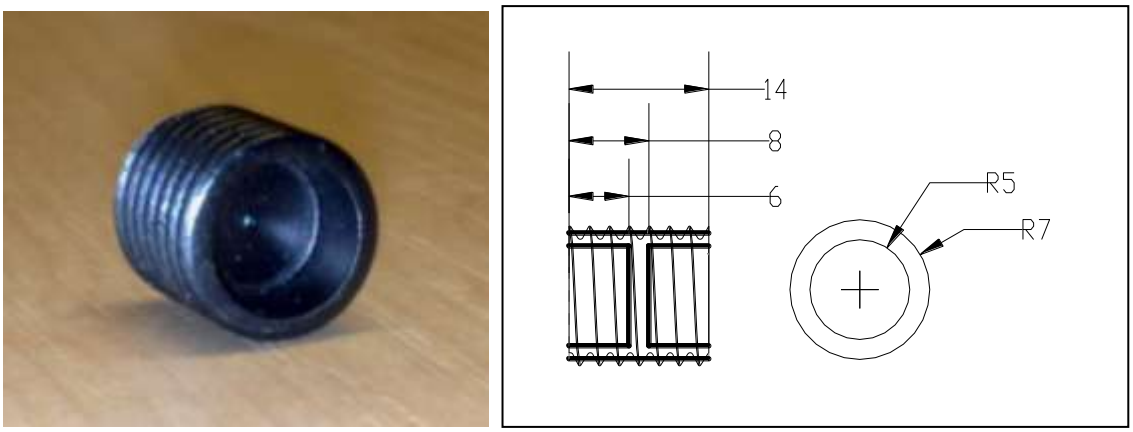

(a) **(b)**

Figure 8.11 – (a) Picture of surface cavity insert. (b) Surface cavity dimensions (mm).

The number of cavities, *n*, was varied so that three, nine and eighteen cavities were tested. The test conditions included a range of values of turbulent flow parameter, λ_T, for two different values of superimposed throughflow, $C_w = 0.3 \times 10^5$ and 10^5. Table 8.3 shows the range of test conditions used. The complete set of test conditions can be found in Appendix C. As with the other tests, once the correct flow conditions had been achieved the test rig was allowed to stabilise before any measurements were taken. This process took approximately half an hour and the stabilisation conditions can be found in Section 5.4.

Re_ϕ	$0.21 \times 10^7 \leq Re_\phi \leq 1.67 \times 10^7$
C_w	$0.26 \times 10^5 \leq C_w \leq 1.04 \times 10^5$
λ_T	$0.06 \leq \lambda_T \leq 0.52$
p (absolute, bar)	$2 \leq p \leq 5$
$\dot{m}$ *(kg/s)*	$0.12 \leq \dot{m} \leq 0.4$
N (rev/min)	$3000 \leq N \leq 10100$

Table 8.3 – Test conditions for surface cavity tests.

In order to place the inserts into the holes in the disc, the tool shown in Figure 8.12 (a) was made. The tool was placed into the cavity, as seen in Figure 8.12 (b), and whilst ensuring the two top nuts are locked tightly together, the bottom nut can be tightened to pull the screw head at the bottom of the tool, up a small amount. This had the effect of

expanding the end of the cylindrical casing slightly, as there are slots cut into the side, tightening the fit within the cavity. This gave enough grip to be able to screw the cavity into the disc. Once the insert was in place, the bottom nut was released and the fit inside the cavity loosened allowing the tool to be removed.

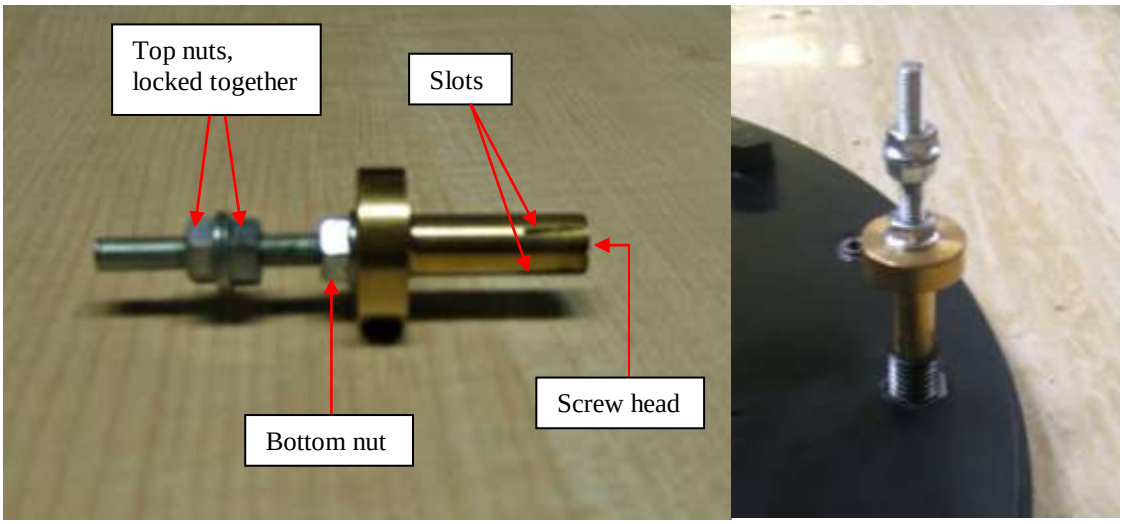

(a) **(b)**

Figure 8.12 – Pictures showing (a) Tool for inserting the surface cavity insert into the disc, (b) Tool positioning the insert into the disc.

Once the cavity inserts were in place the slight surface unevenness around the cavity due to the thread was filled with plaster of paris and the whole surface was sprayed with 3M high temperature matt black paint to ensure accurate infra red temperature measurements. For the tests with three and nine cavity inserts, the remaining holes in the disc were also filled with plaster of paris, sanded to make a smooth surface and then sprayed with the matt black paint.

8.6 Surface cavity test results

The windage and rotor surface temperature measurements for the rotor surface cavity tests, were obtained using the same method as for the bi-hexagonal bolt tests, described in the Sections 8.3 and 8.4.

Testing began with the largest of the three sizes of surface cavity produced, 10 mm in diameter and 6 mm deep (as seen in Figure 8.11). Figure 8.13 shows the variation of $C_m\mathrm{Re}_\phi^{0.2}$ with λ_T for the surface cavity measurements as well as the plain disc results for comparison. It can be seen that there is generally no measureable difference in the moment coefficient between the plain disc and any number of surface cavities. The only exception is where $\lambda_T = 0.168$ (±3%). At this condition there is a 7%, 15% and 20% increase in $C_m\mathrm{Re}_\phi^{0.2}$ for 3, 9 and 18 surface cavities respectively, compared with the plain disc. The uncertainty in the measurement is relatively small at this condition compared with the other conditions tested, since the measured torque is 70% higher than any other condition.

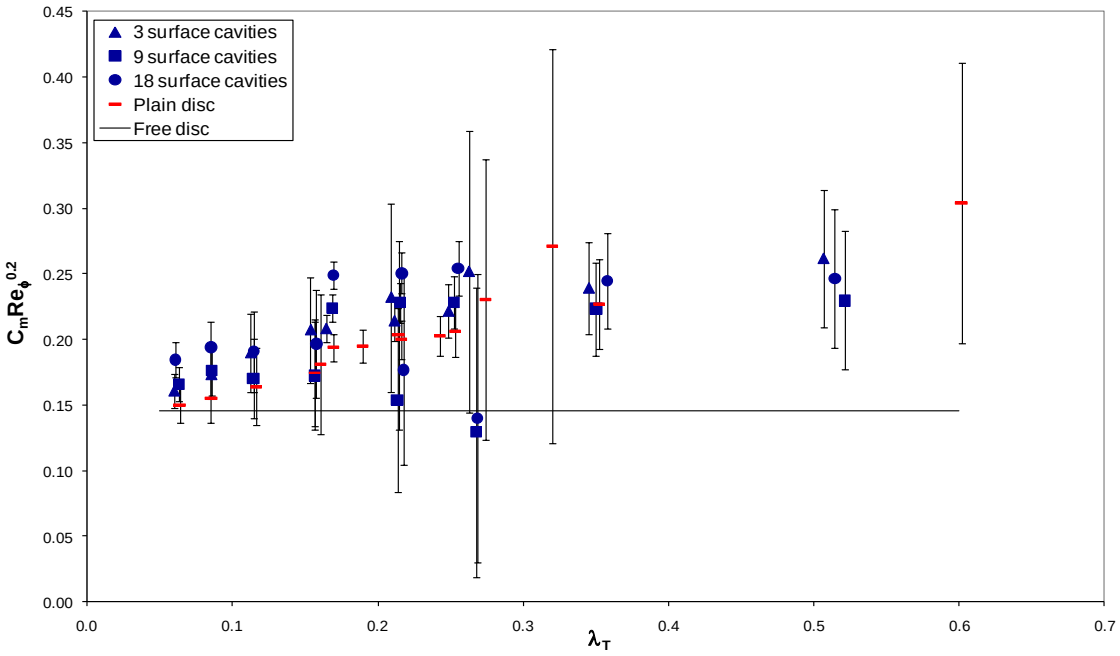

Figure 8.13 - Variation of $C_m\mathrm{Re}_\phi^{0.2}$ with λ_T for surface cavities, n = 3, 9 and 18, 0.3 x $10^5 \leq C_w \leq 10^5$ and 0.21 x $10^7 \leq \mathrm{Re}_\phi \leq$ 1.67 x 10^7.

Figure 8.14 shows the variation of λ_T with the area average disc-surface-to-inlet-air temperature difference, calculated using Equation 8.2, for 3, 9 and 18 surface cavities as well as the plain disc for comparison. It can be seen from Figure 8.14 that where λ_T = 0.062 (±3%) and 0.084 (±2%), there is a 2 °C temperature rise, relating to a 7% and 14% increase respectively, for 18 surface cavities over that of the plain disc. There is also a 1.5 °C (10%) increase for 9 surface cavities at $\lambda_T = 0.084$. These two conditions are most similar to that of the high pressure turbine stage of a modern gas turbine engine

and even these small increases in temperature could have a significant effect on component life. At all other conditions, however, there is generally no measureable difference between the results for the surface cavities and the plain disc, nor is there any increase in rotor temperature with increasing number of surface cavities.

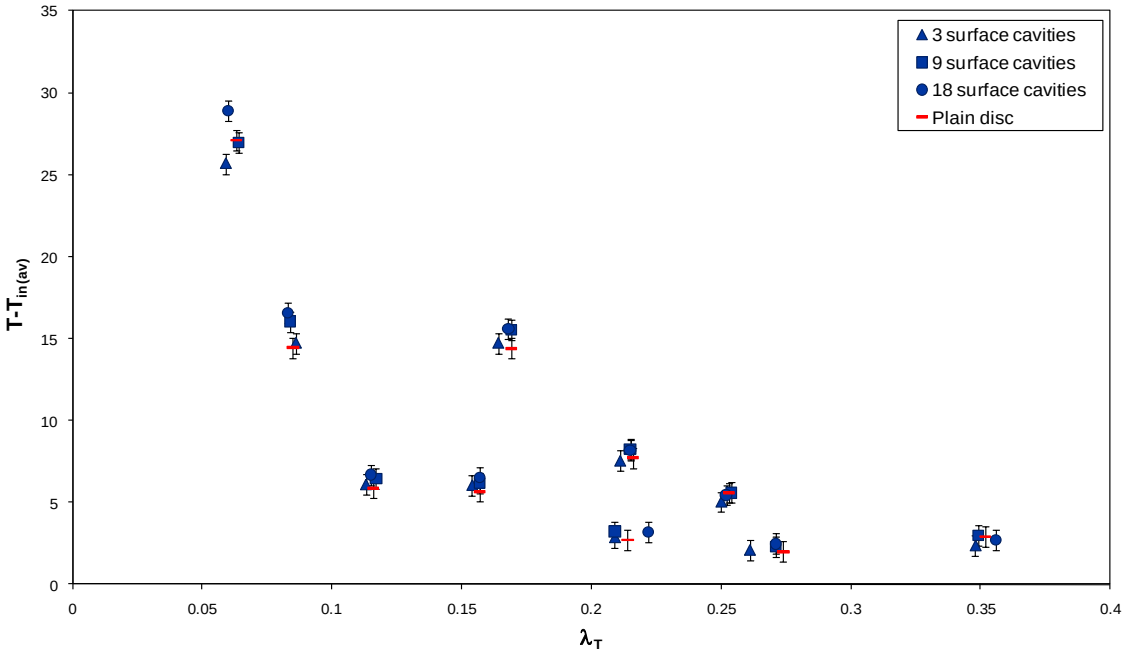

Figure 8.14 - Variation of area average rotor-surface-to-inlet-air temperature difference with λ_T. n = 3, 9 and 18, 0.3 x $10^5 \leq C_w \leq 10^5$ and 0.21 x $10^7 \leq Re_\phi \leq 1.67$ x 10^7.

It is clear from both the windage and surface temperature measurements that with the current instrumentation set up, most of the variation from the plain disc results for the 10 mm by 6 mm surface cavities, is lost in the uncertainty of the measurement. This meant that continuing with the further tests including the smaller, 10 mm by 3 mm and 5 mm by 6 mm surface cavities would be futile since they would no doubt result in even smaller variations. Therefore no further testing was carried out.

8.7 Summary

A reduction in windage for the bi-hexagonal bolts was only observed where λ_T = 0.192 (±5%) and the measured torque was very large. Similarly, a significant drop in rotor surface temperature was observed at a condition where λ_T = 0.064 (±6%) and the measured temperature was large. At most test conditions however, any reduction there may be in either windage or disc surface temperature was not a measureable effect.

Testing with rotor surface cavities showed that the moment coefficient or rotor surface temperature can be increased with cavities present, at certain conditions. As with the bi-hexagonal bolts however, at most flow conditions any increase there may be in moment coefficient or temperature due to the surface cavities was not a measureable effect.

Chapter 9. Particle Image Velocimetry

9.1 Introduction

This chapter describes the testing and analysis method, and the results for Particle Image Velocimetry (PIV) measurements obtained for the plain disc as well as with eighteen, 13 mm hexagonal bolts attached to the disc surface. Both geometries were tested at a variety of flow conditions. Firstly, with varying rotor speed 1000 rev/min $\leq N \leq$ 5000 rev/min, but with no superimposed throughflow, then with throughflow introduced and a range of both constant speed and constant throughflow conditions where $0.053 \times 10^7 \leq \mathrm{Re}_\phi \leq 0.172 \times 10^7$, $0.033 \times 10^5 \leq C_w \leq 0.31 \times 10^5$ and $0.041 \leq \lambda_T \leq 0.324$.

The PIV tests allowed the velocity of the air in the rotor-stator cavity to be measured and analysed. The initial aim was to measure the tangential velocity of the core for the plain disc and also with both rotor and stator bolts. This was to show the increase in core velocity with rotor bolts present, and also the decrease when stator bolts are present. That the core slows down with stator bolts present has not yet been demonstrated. Work by **Kurokawa *et al.* (1978)**, however, showed that this was the case when surface roughness was applied to the stator. Since there have been compelling similarities between roughness work and discrete protrusions, it is reasonable to assume that the core might slow down with stator bolts also. The infra red temperature measurements, discussed in Section 6.3, were designed to show if the core does in fact slow down, by measuring the resulting increase in viscous friction as an increase in rotor surface temperature. However, an increase in disc surface temperature was only measured at very low values of λ_T. Therefore PIV measurements of the flow with stator bolts, is a key piece of work that could quantify the retardation of the core flow for a range of λ_T. Unfortunately due to failure of the PIV system the stator bolt work was not carried out. The rotor bolt measurements however, which were carried

out before the system failure, were obtained with reference to bolt position. This was achieved by way of an encoder set up to trigger the laser and camera when a bolt was in the required position within the captured image. The results therefore give some interesting insight into the complexity of the flow around the bolt, as well as measuring the increase in core tangential velocity.

9.2 PIV set up and test procedure

The PIV software uses the distance travelled by seeding particles, over a set time period, between two images captured using a charged coupled device (CCD) camera. The seeding particles are illuminated using a laser with an endoscope creating a sheet of light perpendicular to the camera. A detailed description of the equipment used can be found in Section 3.8. In order to be able to measure the actual distances travelled it is necessary to know the scaling factor between the image and the flow being measured.

To calculate the scale factor a ruler, or an object of known length, would usually be placed in the path of the light sheet and from the resulting image the relationship between the specified distance (i.e. 1 mm on the ruler) and number of pixels can be calculated. Since placing a ruler within the rotor-stator cavity at the correct position would not be possible, a range of images were taken of a ruler at distances between 230 mm and 350 mm away from the camera. This distance is measured from the object to the position in the camera where the CCD device operates (represented with a green line on the side of the camera). From the resulting scale factors calculated from each image, it was possible to create a relationship between scale factor and distance. This relationship is shown in Equation 9.1 where x is the distance between the camera and the light sheet, and S is the resulting scale factor. Once the camera and laser were located in their required positions, the distance from the camera to the light sheet was measured to be 345 mm. Using Equation 9.1 the scale factor was then calculated to be 3.67. Using this scale factor the field of view represented by the image was calculated as 42.58 mm by 31.29 mm.

$$S = -6.6837\times10^{-5}x^{2} + 5.8024\times10^{-2}x - 8.3888 \qquad \textbf{(9.1)}$$

The test rig casing already had a large optical access hole, suitable for use by the CCD camera with its 60 mm telephoto lens, remaining from the previous test phase to accommodate a window for LDA measurement. For the current phase of testing this has been used as a window for infra red measurements (see Section 3.5.3). For the purposes of the PIV measurements, a new window cartridge was made to enable access for the camera whilst sealing against the air flow within the cavity. The window can be seen in Figure 9.1.

Figure 9.1 – Picture of the new window cartridge.

A stand to hold the camera in position was made and fixed to the same traverse that carries the laser. Being separate from the rig avoids any unnecessary vibrations that would occur if the camera were attached to the frame of the test rig. It also meant the camera did not have to be refocused when the laser was moved, making it easy to carry out measurements at varying axial locations within the cavity.

The camera stand was designed so that the camera is positioned at an angle corresponding to the tangential velocity of the flow at the centre of the window, therefore the tangential velocity is measured across the longer side of the rectangular images. This ensures maximum velocity resolution in the tangential direction, which is the quantity under observation. The stand is adjustable in the horizontal and vertical direction to aide correct positioning of the camera relative to the window. Figure 9.2 shows the camera stand on the laser traverse.

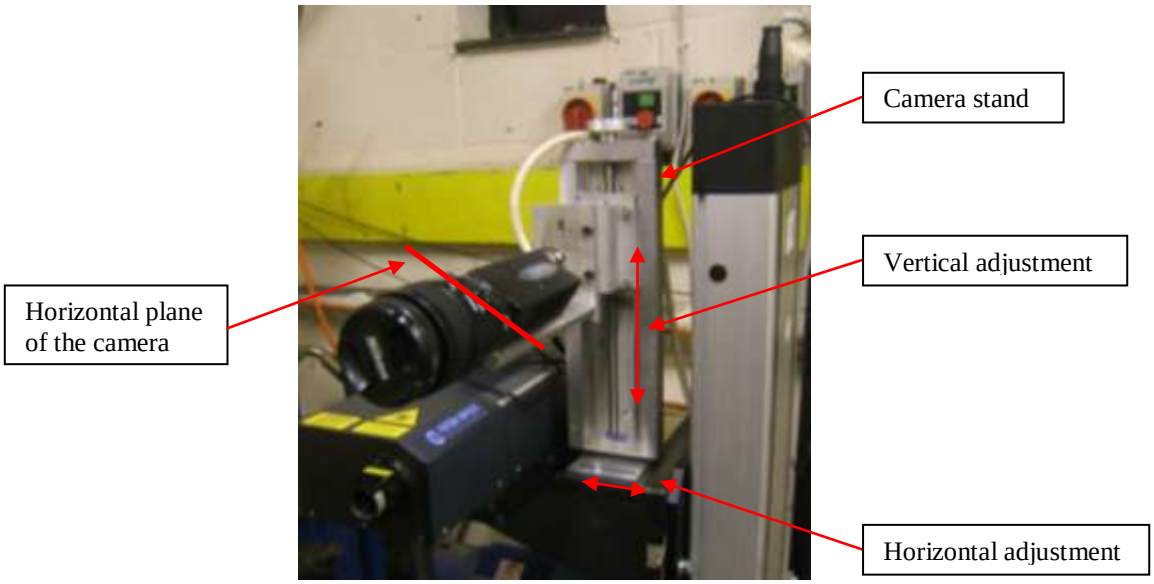

Figure 9.2 – Picture showing camera stand on the laser traverse

In order to prevent light pollution degrading the quality of the PIV images a tube was attached to the window cartridge, covering the gap between the cartridge and the end of the camera lens. This is shown in Figure 9.3.

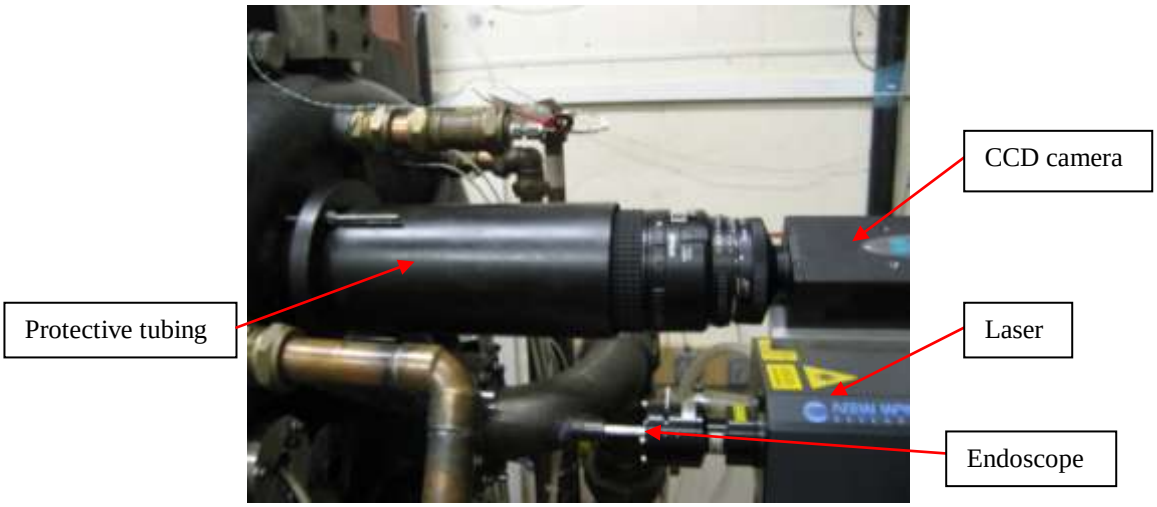

Figure 9.3 – Picture showing protective tube preventing light pollution in the PIV images.

A datum for the laser traverse had to be established, representing the point where the tip of the laser endoscope is just brushing the surface of the disc at the centre. To achieve this, the rig casing was opened and the laser was moved carefully into position. The program used to control the traverse was then reset so this point represented 0,0,0, thus providing a datum for all tests.

It was then necessary to align the endoscope very carefully with the axis of the driveshaft. If the endoscope and driveshaft are out of alignment this would affect the positioning of the light sheet, relative to the required measurement plane. In order to check the alignment of the endoscope a piece of black card was held against, and perpendicular to, the disc so that the edge of the light sheet was visible. This is shown in Figure 9.4 (a). Figure 9.4 (b) illustrates the two ways that the endoscope could be misaligned. If the endoscope were misaligned in the horizontal plane, the edge of the light sheet would look like either of the red broken lines on the black card in Figure 9.4 (b). If the endoscope were misaligned in the vertical plane, the edge of the light sheet would look like either of the blue lines.

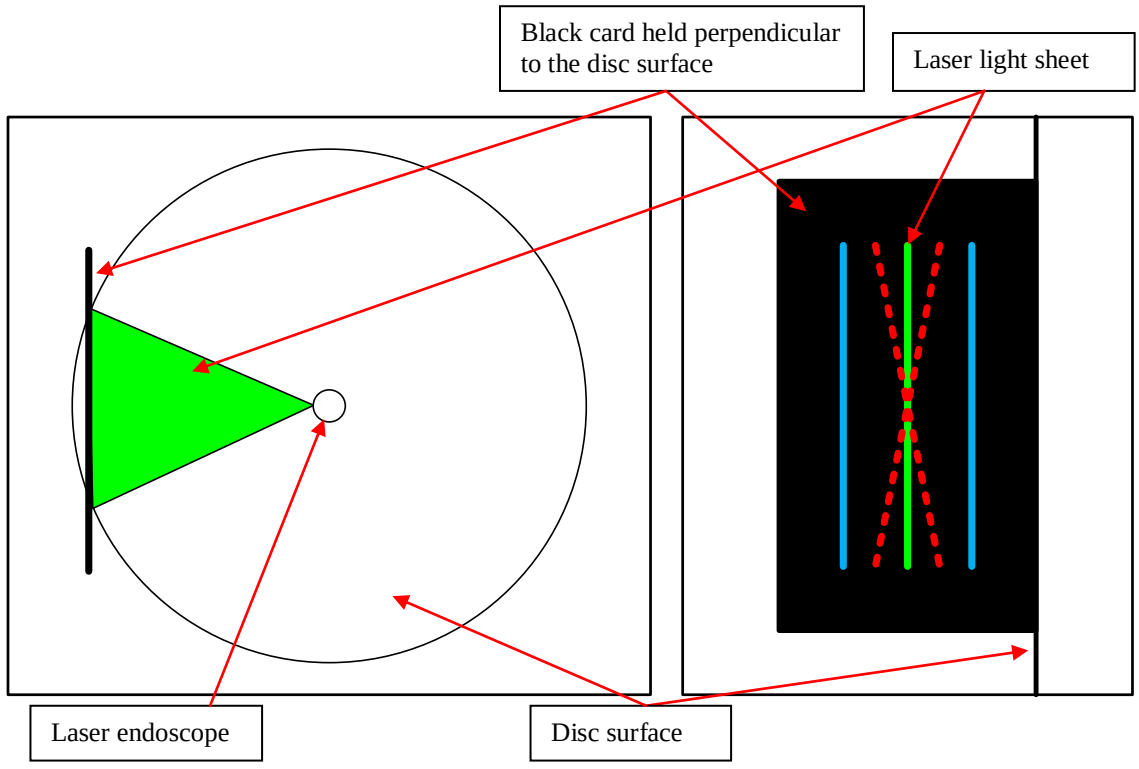

Figure 9.4 – (a) Diagram showing positioning of card and light sheet for alignment checks. (b) Diagram showing the two type of misalignment of the light sheet, horizontal (red broken lines) and relative to driveshaft axis (blue lines).

The light sheet emerges 3 mm from the tip of the endoscope. With the tapering of the disc (discussed in Section 3.4) this means that, when the endoscope is in the datum position 0,0,0, the light sheet will be 8.5 mm away from the disc surface at the radius of the bolt, r = 0.2 m. In order to check the alignment in the vertical plane, the piece of

card was held perpendicular to the disc surface at the bolt radius and the distance between the laser sheet and the disc surface was measured to ensure it was 8.5 mm. To check the alignment in the horizontal plane, a plumb bob was used to ensure the edge of the light sheet, as viewed on the card, was vertical.

Once the laser endoscope was in the correct position it was necessary to ensure that it could be freely inserted and withdrawn from the cavity during a series of subsequent measurement cycles. The existing point of entry was much larger than the diameter of the endoscope, which would create problems sealing the cavity so a cap was made. To allow the endoscope to enter freely and without interference, the cap had a slightly larger diameter hole than the endoscope shaft and was placed over the endoscope before insertion into the cavity. Once the endoscope was in place, the cap could then be screwed into the existing hole in the inlet pipe. An o ring, also placed around the endoscope shaft before insertion, was pressed up against the cap to seal the gap. Since the pressures within the cavity for the PIV tests were very low (up to a maximum of p = 1.27 bar), this provided adequate sealing.

For the tests with bolts it was necessary to set up a trigger on the drive shaft so that the camera and laser could be synchronised to a specific position on the disc, meaning the bolt would be in the same position for each pair of images. An encoder was positioned adjacent to a suitable section of the driveshaft, as shown in Figure 9.5. The encoder is an HOA709 reflective sensor, which uses an infra red emitting diode alongside a phototransistor. The phototransistor responds to the infra red radiation only when a reflective object passes. A matt black marker was placed on the driveshaft flange as a pick up, as indicated in Figure 9.5, and the signal from the encoder was used to trigger the laser and camera. Once the trigger had been set up, the resulting images were inspected and a time offset was applied, within the PIV software. This delayed the triggering of the laser and camera, so that the bolt was in a suitable position in the images.

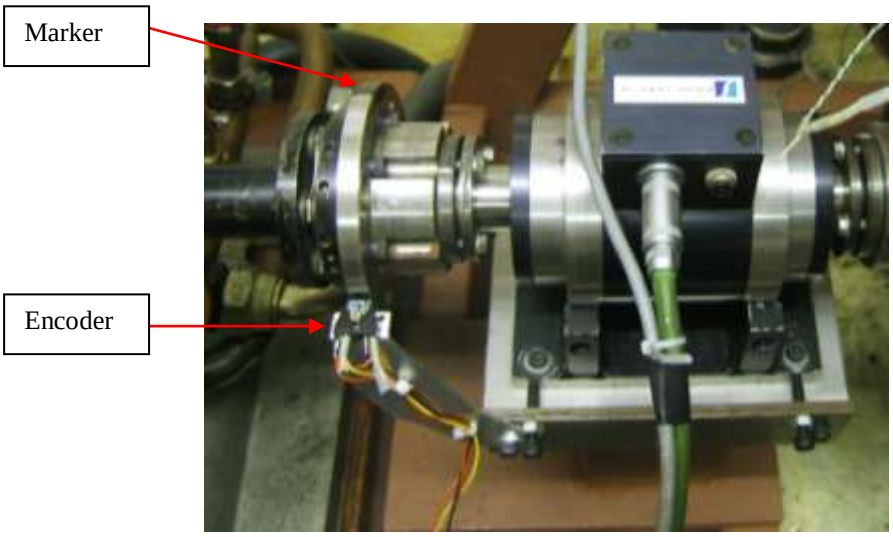

Figure 9.5 – Picture showing encoder for laser and camera triggering.

Measurements were obtained initially, for both the plain disc and with eighteen, 13 mm bolts on the disc surface, with no superimposed throughflow and varying speed 1000 rev/min $\leq N \leq$ 5000 rev/min. Then with throughflow introduced, tests were carried out at a variety of constant throughflow and constant speed conditions covering the ranges $0.053 \times 10^7 \leq Re_\phi \leq 0.172 \times 10^7$, $0.033 \times 10^5 \leq C_w \leq 0.31 \times 10^5$ and $0.041 \leq \lambda_T \leq 0.324$, where $\lambda_T = C_w/Re_\phi^{0.8}$, $C_w = \dot{m}/\mu b$ and $Re_\phi = \rho\omega b^2/\mu$. See Appendix C for the full set of test conditions. The range of λ_T tested includes both rotationally and radially dominant flow conditions. The parameter λ_T was developed by **Owen and Rogers (1989)** from von Kármán's solution for the mass flow entrainment rate for a free disc (see Section 2.2), and is shown in Equation 9.2.

$$\lambda_T = \frac{C_w}{Re_\phi^{0.8}} \qquad \textbf{(9.2)}$$

Where $\lambda_T < 0.219$, all fluid is entrained into the boundary layer of the disc, leaving a core of fluid rotating at a fraction of disc speed (the speed of the core depends on the geometry of the rotor-stator system and is discussed further in Section 2.3). The flow in this case is said to be rotationally dominant. For $\lambda_T > 0.219$, the flow is dominated by the superimposed throughflow. The throughflow slows down the rotating core and the flow is said to be radially dominant.

9.3 Analysis methodology

In order to analyse the data the PIV software, FlowManager 4.71, divides the images into interrogation areas. For each interrogation area the images from both the first and second light pulses are correlated producing a displacement vector for each particle. The vectors for each interrogation area are then brought together to create a vector map for the whole image. The information near the edges of each interrogation area can be lost, since there is an increased risk that the initial or final position of a particle may be outside of the interrogation area. Therefore it is necessary in the analysis of the data to include an overlap of the interrogation areas. By overlapping them the chance of all particle pairs being contained within one interrogation area is increased.

The FlowManager software carries out the analysis in stages, using a large interrogation area initially and then reducing the size in a number of steps specified by the user. For all the plain disc tests, the size of the final interrogation area was specified as 64 pix x 64 pix with 50% overlap. Two refinement steps were used, with an initial interrogation area of 256 pix x 256 pix. Figure 9.6 illustrates the two refinement stages used for the plain disc analysis. Figure 9.6 (a) shows the initial 256 pix x 256 pix interrogation area; Figure 9.6 (b) the first refinement stage, reducing the size of the interrogation areas to128 pix x 128 pix; and Figure 9.6 (c) the final interrogation area, 64 pix x 64 pix. For the tests with eighteen, 13mm bolts an interrogation area of 32 pix x 32 pix was used with a 25% overlap. In this instance three refinement steps were requested in the analysis making the initial interrogation area again 256 pix x 256 pix. The variation between the analysis methods used for the plain disc and the 13 mm bolts is a result of the progression in understanding of the measurement techniques over the testing phase.

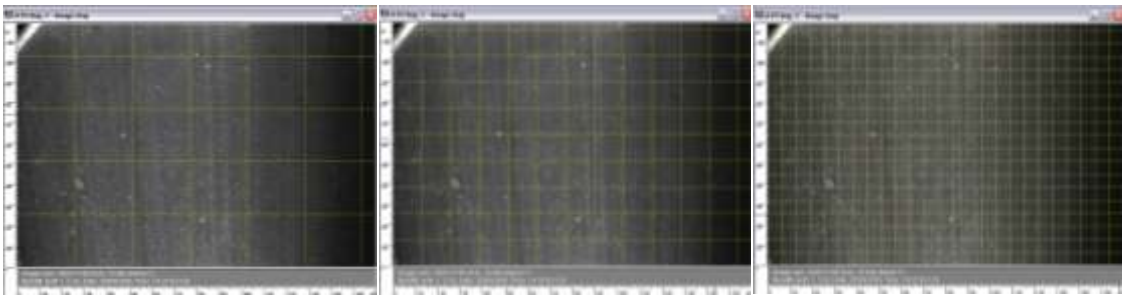

(a) **(b)** **(c)**

Figure 9.6 – Diagrams illustrating the reducing size of the interrogation areas during the three stages of analysis used for the plain disc test result. (a) 256 pix x 256 pix (b) 128 pix x 128 pix (c) 64 pix x 64 pix.

After the initial analysis had created a vector map, two validations were then applied to the data. Firstly, a range validation. Some of the resulting velocities from the initial analysis may be outside of the velocity limits for the flow being assessed. This can happen for a variety of reasons such as too little seeding material, or too low or high light intensity at that point. The range validation identifies velocity vectors outside of the specified range and eliminates them. Figure 9.7 shows an example of a typical range validation. The excluded points are shown in red. For these tests the maximum velocity specified for the range validation was rotor speed, since theory suggests that with radial outflow in a rotor-stator system, the core velocity cannot be faster than the rotor. No minimum boundary was specified.

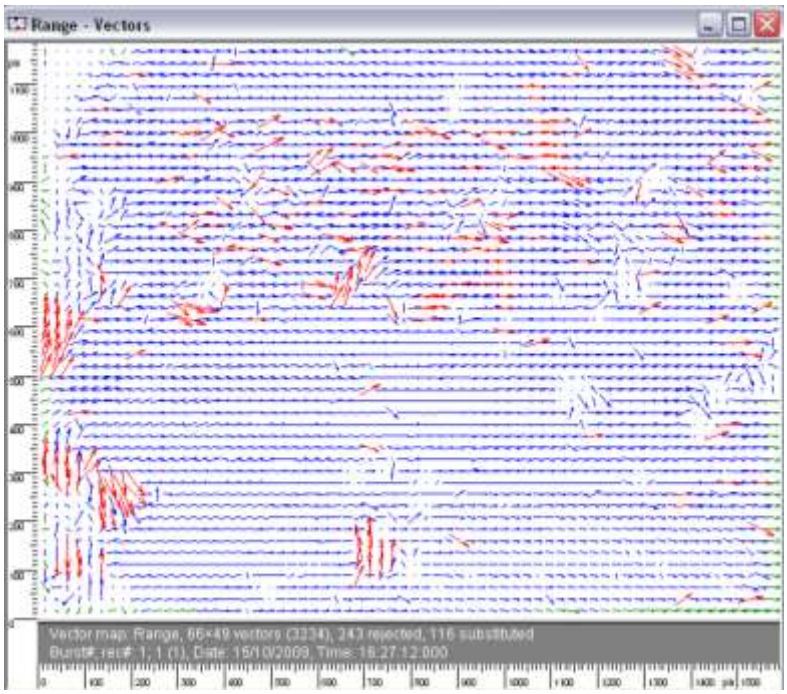

Figure 9.7 – Picture showing a typical range validation (invalid vectors are shown in red).

Secondly, after the range validation, a moving average was then applied. The moving average method validates vectors based on a comparison with neighbouring vectors, and any rejected vectors can then be substituted with a vector estimated from surrounding values. Continuity of the flow is assumed when using the moving average validation. This method is a very useful tool for validation, however it is important to be aware that some of the detail can be lost in areas where the flow structure is particularly varied. Figure 9.8 shows an example of a typical moving average validation. The vectors shown in green are those that have been substituted using an estimate from surrounding values.

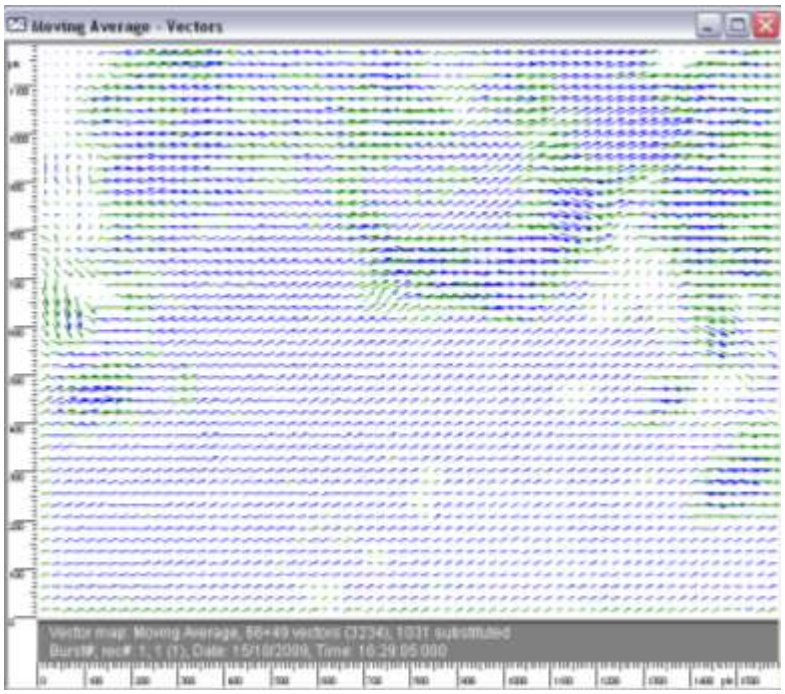

Figure 9.8 – Picture showing a typical moving average validation (substituted vectors are shown in green).

For the plain disc tests a total of 10 image pairs were obtained for the tests where there was no throughflow present, and 20 image pairs for the tests with throughflow. For all the tests with eighteen, 13 mm bolts 40 image pairs were used. After the range and moving average validations, vector statistics were applied to give the mean of the results from all the image pairs in each test. This produces a single vector map for each test condition, an example of which is shown in Figure 9.9. It is the data from this final vector map that is used throughout the results analysis for each test point.

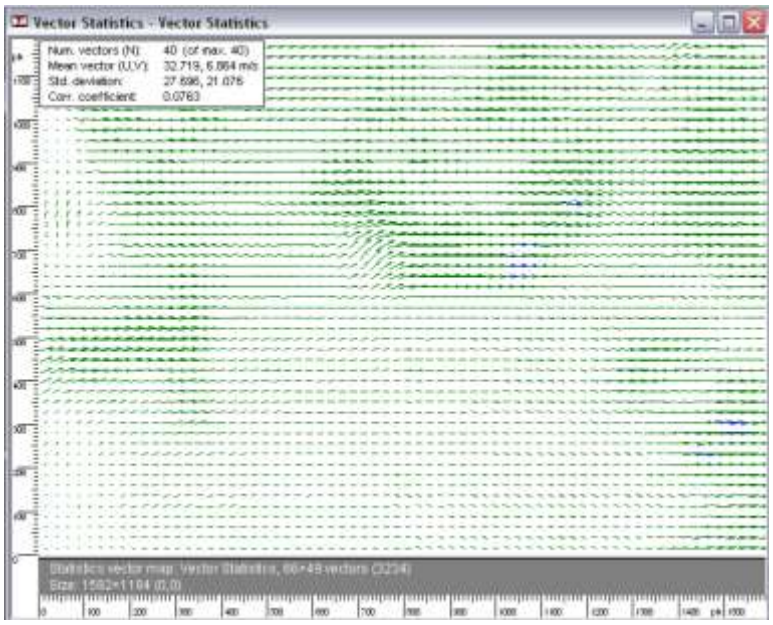

Figure 9.9 – Picture of a typical vector map produced for every test point.

For each test, the flow conditions gave rise to a different range of particle velocities and the choice of time-lapse between the image pairs, δt, therefore had to be set accordingly. It is specified in the FlowManager user guide that to obtain good quality velocity data the displacement of the seeding particles between the two images must be greater than 25% of the final interrogation area and less than 25% of the initial interrogation area. For the plain disc tests with a 64 pix x 64 pix final interrogation area (and 256 pix x 256 pix initial interrogation area), the maximum displacement, d_{max}, must be 16 pix < d_{max} < 64 pix (46.4 μm < d_{max} < 185.6 μm). Using Equation 9.3, where S is the scale factor calculated as 3.67, it is the possible to find the range of δt required for a given velocity of the particles.

$$\delta t = \frac{S d_{\max}}{V_{\max}} \qquad \textbf{(9.3)}$$

Since the velocity of the seeding particles can only be estimated, a set of tests were carried out to identify the optimum time interval required between the images. These tests were carried out with eighteen, 13mm bolts on the rotor, N = 4000 rev/min and C_w = 6000. At these conditions the disc speed would range from U = 73 m/s at the bottom edge of the image and U = 86 m/s at the top edge of the image. Using these velocities, at the bottom edge of the image the time interval should be in the range 2.33 μs ≤ δt ≤

9.28 μs, and at the top edge of the image the range should be 1.98 μs ≤ δt ≤ 7.88 μs. This would be the maximum speed possible for the seeding particles, although it is unlikely that any would actually reach this speed. The particles are likely to be travelling slower than the disc and therefore the δt may need to be larger.

The plots in Figure 9.10 show the velocity profile from the bottom, y = 0 mm, to the top edge of the image y = 31.3 mm, for δt = 5 μs, 10 μs, 20 μs and 30 μs.

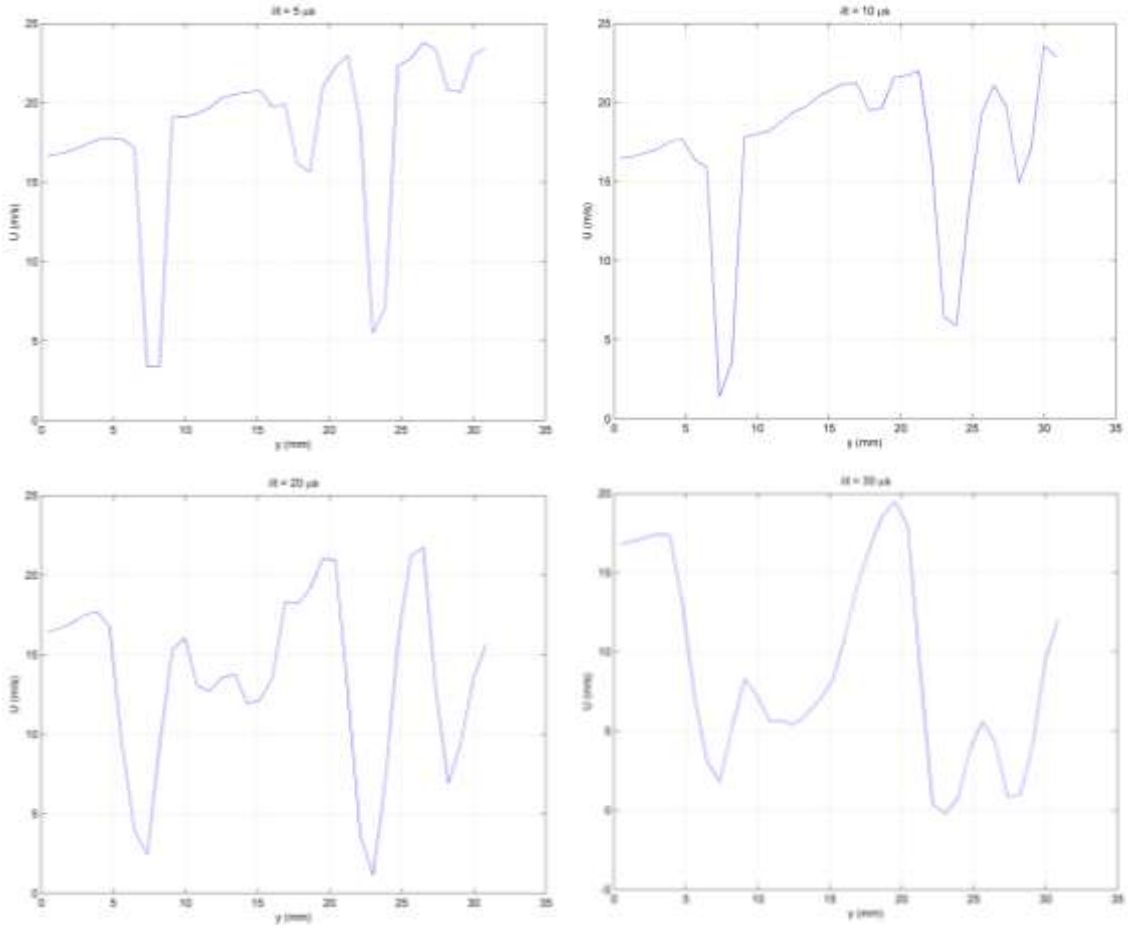

Figure 9.10 – Variation of velocity, U, with y for δt = 5 μs, 10 μs, 20 μs and 30 μs, N = 4000 rev/min and C_w = 6000.

It can be seen from these plots that when δt = 5 μs a clear velocity profile is produced, this is also the case where δt = 10 μs, although to a slightly lesser extent. But as δt increases beyond this, the data becomes very scattered and unreliable. It is with this in mind that the values of δt for all test conditions were calculated using the disc speed at the top edge of the image and set at the top end of the resulting δt range. The large drop

in velocity observed at $y \approx 7$ mm and $y \approx 23$ mm, for $\delta t = 5$ μs, 10 μs and 20 μs, is most likely due to spots of oil on the optical access window, since the erroneous data is located in the same position for each test.

Velocity data obtained from the FlowManager software is given in U and V coordinates, relating to the x and y directions within the image. At the centre of the image these velocities represent V_ϕ and V_r, and $y = r$ since the camera stand was made to sit at an angle such that the horizontal plane matched the tangential direction at the centre of the image. Elsewhere though, U does not equate to V_ϕ, and y is not equal to r. The tangential velocity, is the parameter under investigation therefore it was necessary to analyse the data in terms of V_ϕ and r. To do this, the data was exported from the FlowManager software as text files and a MATLAB routine was written to extract the required data for a user specified x position on the image and convert U and y values into V_ϕ and r. Each text file for the plain disc data, which used a 64 x 64 interrogation area, has velocity data for grid points 32 pixels apart, ranging from 31.5 pix to 1567.5 pix in the x direction, and 31.5 pix to 1151.5 pix in the y direction. For the eighteen, 13 mm bolts data which used a 32 x 32 interrogation area, the velocity data in each text file is for grid points 24 pixels apart, ranging from 15.5 pix to 1575.5 pix in the x direction and 15.5 pix to 1167.5 in the y direction.

Figure 9.11 (a) shows an example of a typical vector map obtained in the FlowManager software, along with a line showing the x position from which the velocity profile is taken. Figure 9.11 (b) shows the resulting tangential velocity profile, calculated using MATLAB, for the position specified in Figure 9.11 (a).

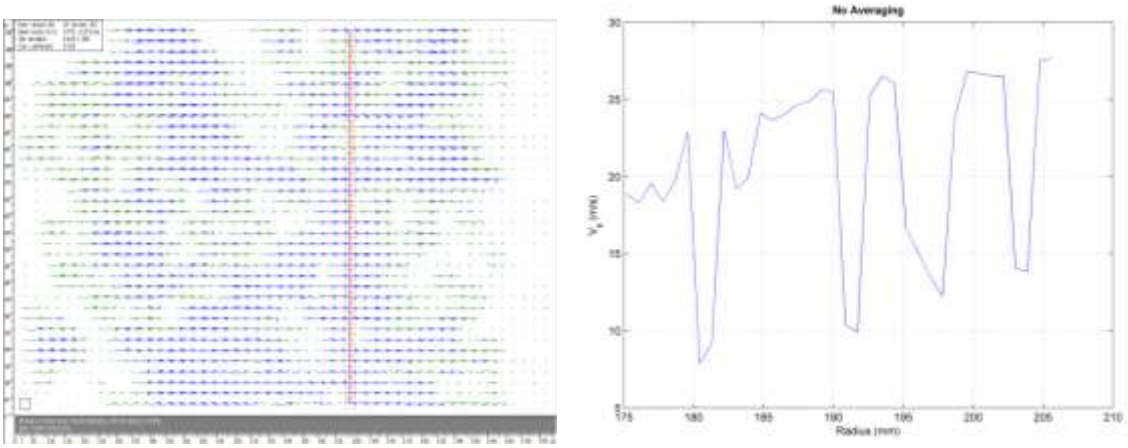

(a) **(b)**

Figure 9.11 – (a) Picture showing an example of the position (in the *x* direction) in a vector map at which the data is taken. (b) Diagram showing the variation of V_ϕ with *r* calculated at the specified position.

It can be seen from Figure 9.11 (b) that the data is quite noisy, meaning a smooth velocity profile is not obtained. A similar effect is observed for the majority of the results obtained. There are many reasons as to why these fluctuations in the data occur. The quantity of seeding material present relative to the light intensity is very important, and either too much or too little seeding in certain areas of the image can affect the data quality. Spots of oil can also build up on the window during testing obscuring the measurement plane, as mentioned previously. To reduce the build up of oil on the window the seeding was only introduced to the flow for small amounts of time during testing and the window was removed and cleaned on a regular basis.

An investigation was carried out to establish the value of averaging data from multiple, adjacent velocity profiles, whilst observing the reduction, if any, in data quality as averaging number increases. To achieve this, plain disc data was analysed for four separate conditions. At constant throughflow where C_w = 10000 and $\mathrm{Re}_\phi = 0.068 \times 10^7$ and 0.137×10^7, and also at constant speed where $\mathrm{Re}_\phi = 0.137 \times 10^7$ and C_w = 3900 and 21500. For each condition a singular velocity profile was compared against the average of 2, 3, 4 and 5 profiles of data. In each case the 2nd, 3rd, 4th and 5th velocity profiles are taken from the right of the position of the non-averaged, singular velocity profile. This is illustrated in Figure 9.12.

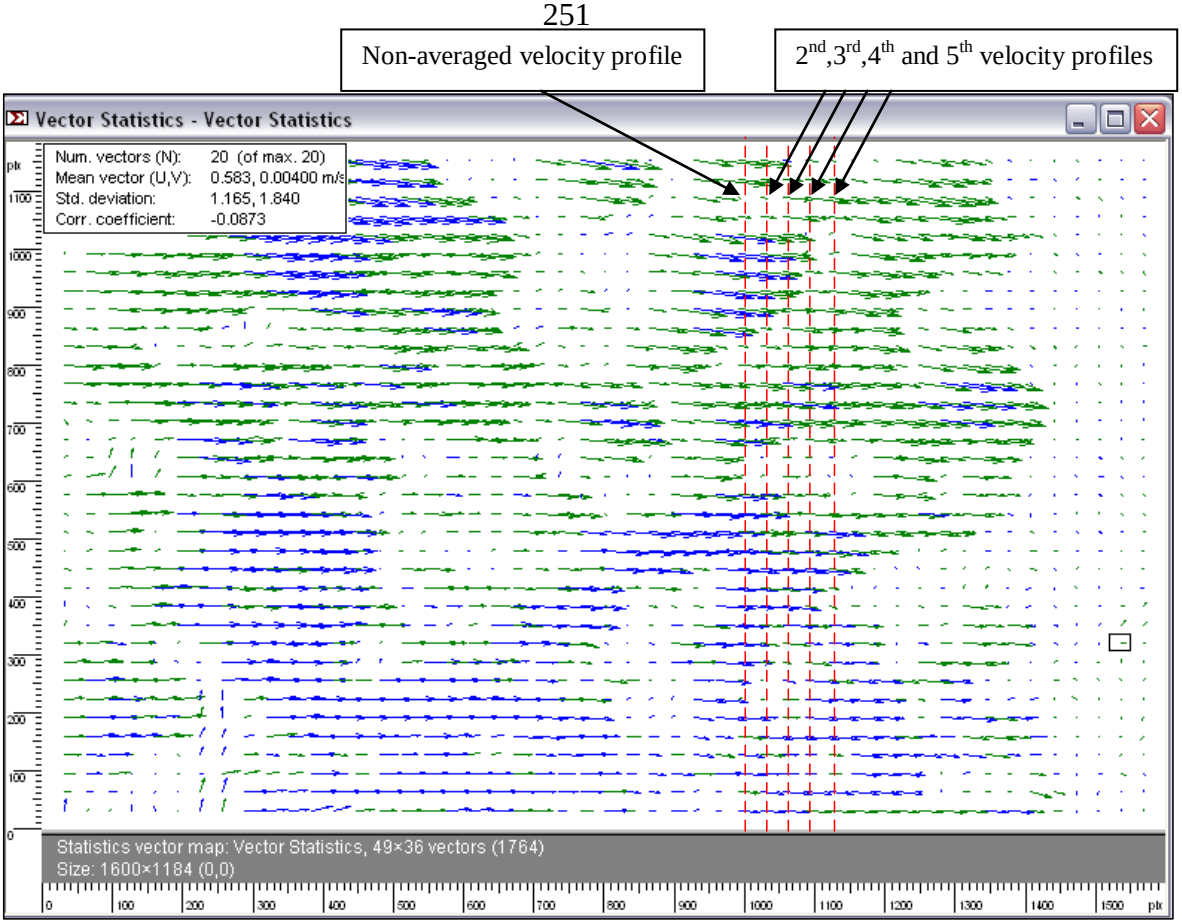

Figure 9.12 – Picture showing the velocity profiles used to investigate the value of averaging multiple adjacent profiles for C_w = 10000 and $Re_\phi = 0.068 \times 10^7$.

The results showed that in all four cases the velocity profile becomes less clear with increasing averaging. Figure 9.13 illustrates the reduction in data quality from the singular velocity profile to the average of five profiles for $Re_\phi = 0.137 \times 10^7$ and C_w = 3000. The complete set of results can be found in Appendix D.

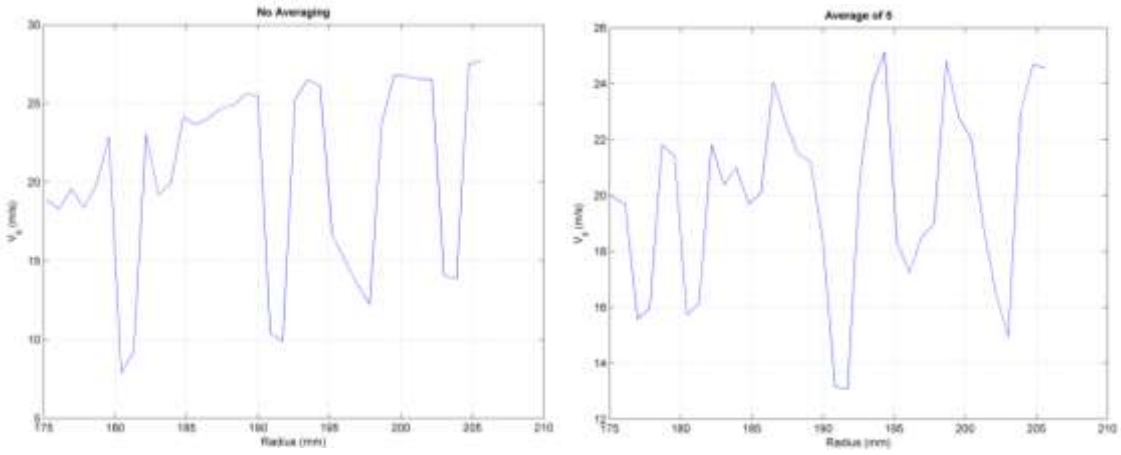

(a) **(b)**

Figure 9.13 – Plots showing the variation of V_ϕ with r for (a) a single velocity profile with no averaging (b) an average of five velocity profiles, $\mathrm{Re}_\phi = 0.137 \times 10^7$ and $C_w = 3900$.

One reason for the degradation of the data quality with averaging is that since the data had to be exported into MATLAB to carry out the evaluation, each velocity profile is 32 pixels (0.87 mm) apart. This means that when averaging five adjacent velocity profiles, the data is spread over 4.35 mm, in which space the data can vary a great deal. This variation in velocity can be seen clearly in Figure 9.12, across the five velocity profiles.

As a result of this investigation it was decided that no average will be taken when analysing the data. In the majority of cases the erroneous data is quite apparent and, if the large fluctuations are ignored such as those at r = 181 mm, 192 mm, 198 mm and 203 mm in Figure 9.13 (a), a velocity profile can still be easily picked out.

9.4 Results

The first objective of these tests was to measure the increase in the tangential velocity of the rotating core within the rotor-stator cavity when bolts are present on the rotor surface. This result was suggested in research by **Kurokawa *et al.* (1978)** who measured the core velocity with a roughness applied to the rotor surface. This work concluded that the core velocity increased with roughness on the rotor, compared with the smooth rotor, by up to 30% where $r/b > 0.9$. Measurements by **Coren (2007)** using

Laser Doppler Anemometry (LDA) showed that the core tangential velocity ratio, where the flow is radially dominant, is increased from an average of $\beta = 0.05$ for the plain disc to $\beta = 0.3$ with 18 bolts. For the case where $\lambda_T < 0.219$, and the flow is rotationally dominant, the core velocity was shown to have increased from $\beta = 0.25$ for the plain disc to a maximum of $\beta = 0.8$ with 18 bolts. The measurements by Coren were obtained at five locations between $0.126 \text{ m} \leq r \leq 0.185 \text{ m}$ and therefore did not include any measurements around the bolts. The current PIV results measure an area between $0.176 \text{ m} \leq r \leq 0.207 \text{ m}$, which encompasses the whole of the bolt, therefore the aim of these measurements is also to be able to identify the effects of the bolt on the flow local to it.

In order to quantify the increase in tangential velocity due to the presence of bolts, measurements were made first with a plain disc. For the initial set of tests $C_w = 0$, and the range of speeds covered by the tests was $1000 \text{ rev/min} \leq N \leq 5000 \text{ rev/min}$, incrementing in 500 rev/min stages. Temperature and pressure data was not obtained during tests with no throughflow. However, using the approximate ambient temperatures and pressures: $T = 21$ °C and $p = 1.01$ bar, the range of rotational Reynolds numbers represented by this range of disc speed is calculated as $0.035 \times 10^7 \leq \text{Re}_\phi \leq 0.174 \times 10^7$. Figure 9.14 shows the variation of V_ϕ with ωr for these tests, where V_ϕ is the tangential velocity of the core flow and ωr is the velocity of the rotor. The position in the image that the data is taken is not critical for the plain disc tests, since the velocity is a function of radius only. Therefore the data for each test condition is taken from a position where the quality of the data is good and not affected by lack of seeding or spots of oil on the window. It can be seen in Figure 9.14 that the data points that do not fit the trend can easily be picked out, as suggested previously in Section 9.3. These erroneous points are clearly marked with red circles.

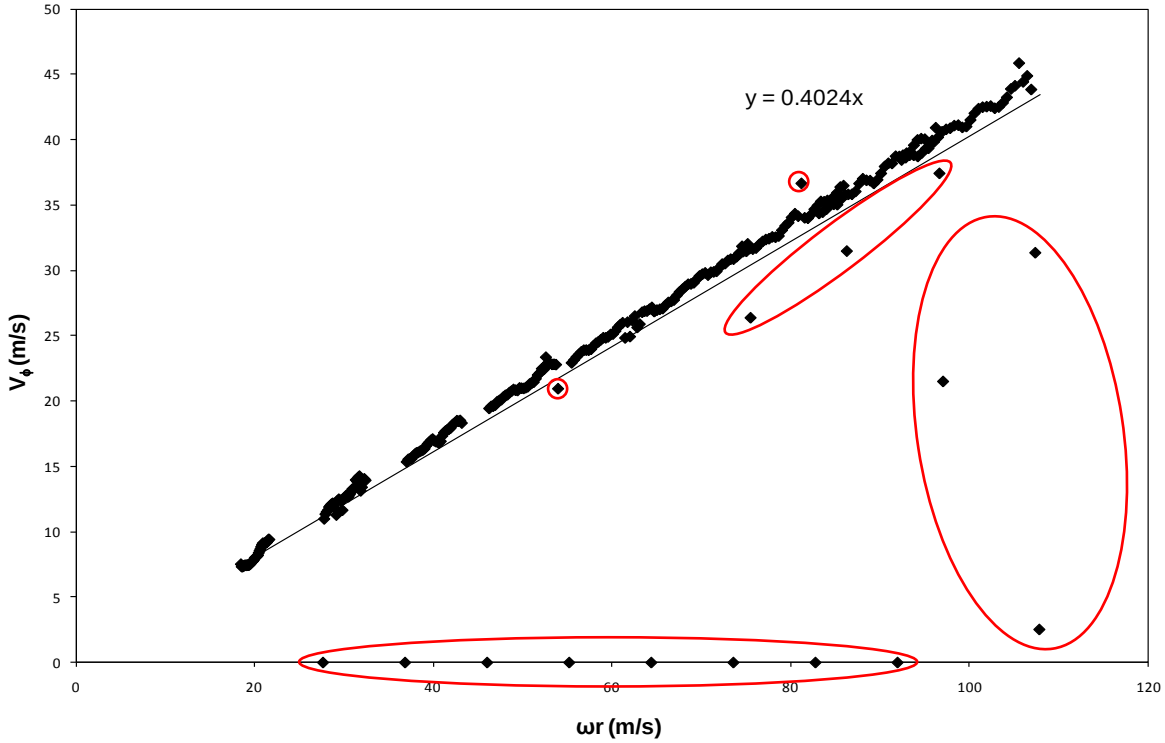

Figure 9.14 – Variation of V_ϕ with ωr for a plain disc, C_w = 0, 1000 rev/min $\leq$ $N \leq$ 5000 rev/min and 0.035 $\leq$ $\mathrm{Re}_\phi \leq$ 0.174 (approx.).

If the erroneous data points are excluded, the results are as shown in Figure 9.15. It can be seen that the data is now closely fitting to a straight line. A selection of tests were repeated and the measurements displayed good repeatability in all cases. Figure 9.16 shows the results from the original and repeat test where N = 4000 rev/min and it can be seen that in both cases the tangential velocity is shown to increase from ~30 m/s at r = 175 mm to ~36 m/s at the r = 206 mm.

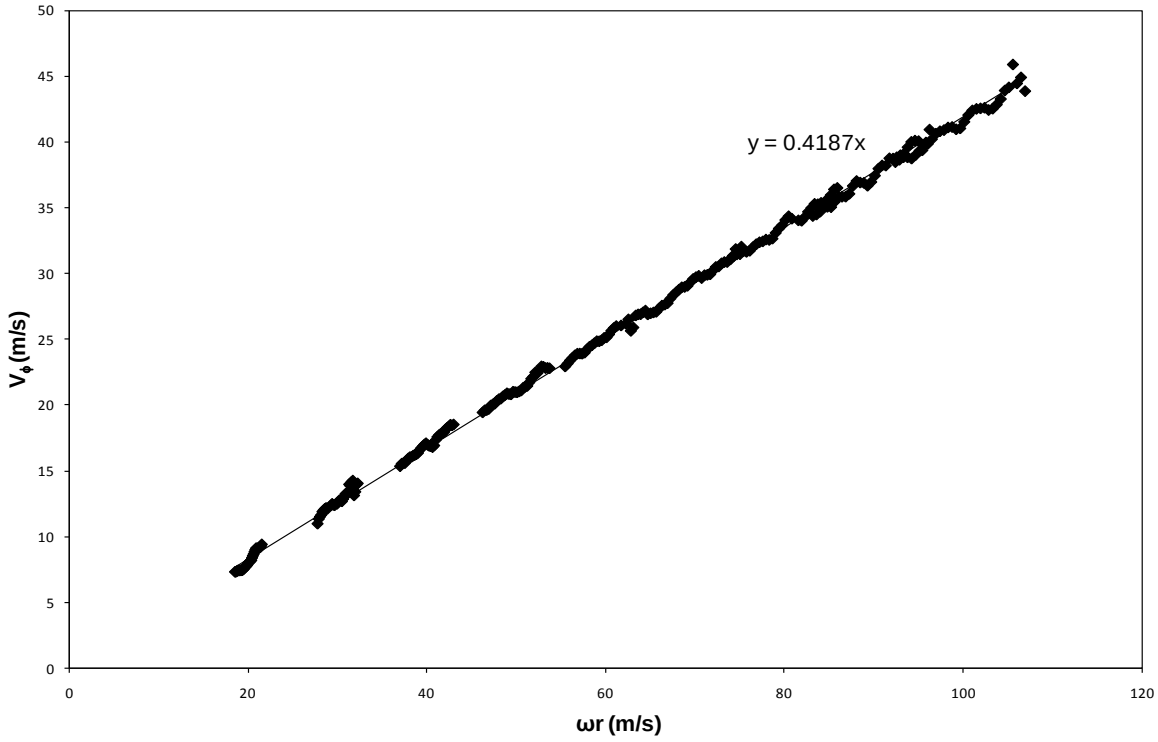

Figure 9.15 - Variation of V_ϕ with ωr for a plain disc with erroneous points removed, C_w = 0, 1000 rev/min $\leq N \leq$ 5000 rev/min and 0.035 $\leq$ Re$_\phi \leq$ 0.174 (approx.).

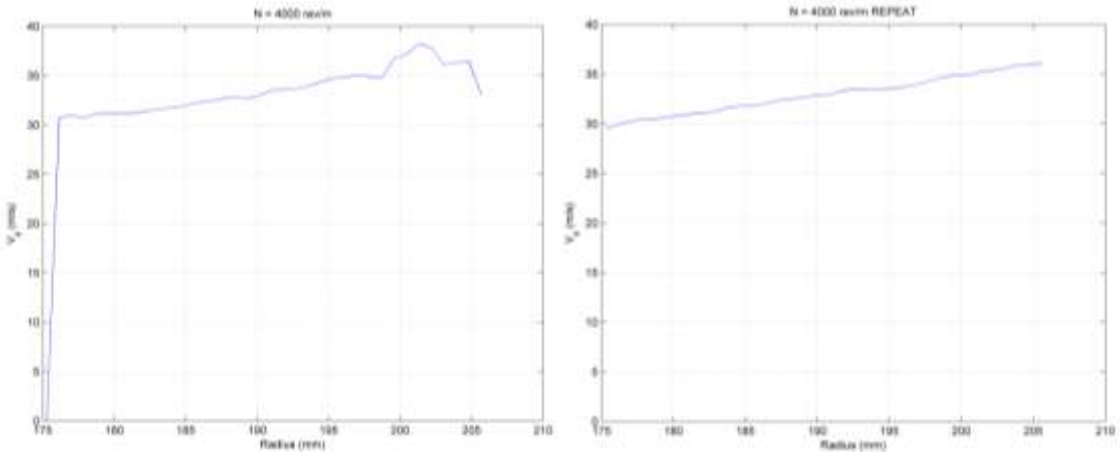

(a) **(b)**

Figure 9.16 – Comparison of the variation of V_ϕ with radius for (a) the original and (b) the repeat test, at N = 4000 rev/min and C_w = 0.

In a rotor-stator system, the fluid to disc tangential velocity ratio is given by the term β, as shown in Equation 9.4.

$$\beta = \frac{V_\phi}{\omega r} \qquad \textbf{(9.4)}$$

Using experimental methods, **Daily and Nece (1960)** found the value of β for a rotor-stator system with no throughflow, and an axial clearance $G = 0.1$, such as the test rig used to obtain these results, to be $\beta = 0.431$. This value is referred to as β^* in the context where there is no superimposed throughflow in the cavity. It can be seen from Figure 9.14 the gradient of the line representing this relationship is calculated as $\beta^* = 0.419$, which is close to the value specified by Owen. This result along with the general lack of scatter (disregarding the few obviously erroneous data points that were excluded) leads to the conclusion that these are good quality, repeatable results instilling confidence in the measurement techniques used.

For the tests with rotor bolts present an encoder was set up to trigger the laser, as described in Section 9.2, so that the bolt appeared in the same position for all captured images. Figure 9.17 shows the position of the bolt within the image.

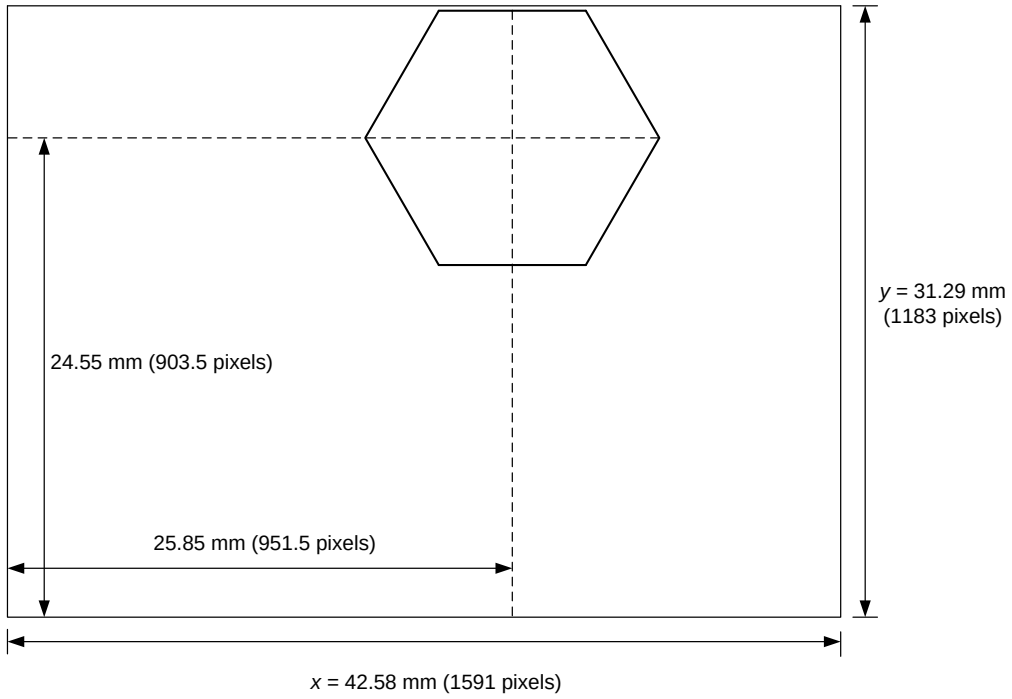

Figure 9.17 – Diagram showing position of bolt in the captured images.

Figure 9.18 shows the variation of V_ϕ with ωr for the tests with eighteen, 13 mm bolts on the rotor surface. As with the plain disc tests there is no superimposed throughflow, and the speed ranged from 1500 rev/min $\leq N \leq$ 5000 rev/min, incrementing in 500 rev/min steps. This represents the range of rotational Reynolds numbers $0.052 \times 10^7 \leq Re_\phi \leq 0.174 \times 10^7$, when calculated using the approximated ambient temperatures and pressures: T = 21 °C and p = 1.01 bar. Again, the data points that do not fit with the trend can easily be picked out. If these are removed, the results are as shown in Figure 9.19. The data for Figures 9.18 and 9.19 is taken from the position x = 25.85 mm (951.5 pix), which represents the centreline of the bolt. Unless otherwise stated, the results for all the rotor bolt tests are taken from this same position within the image. An investigation into the effects of the position from which the data is taken can be found later in this chapter.

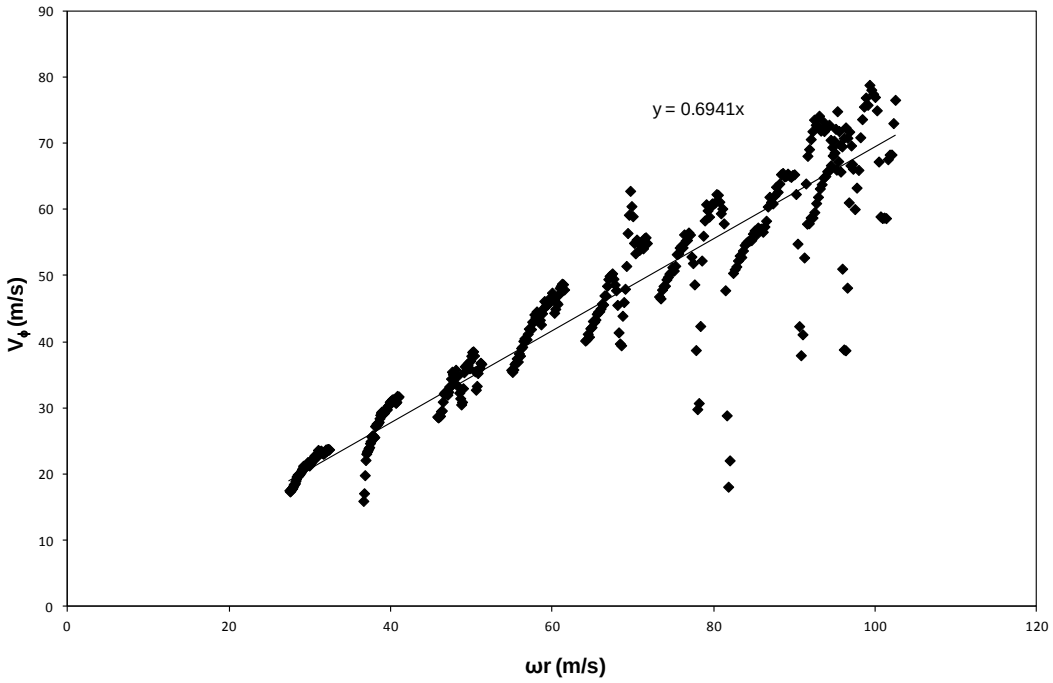

Figure 9.18 – Variation of V_ϕ with ωr for eighteen 13 mm bolts on the rotor, C_w = 0, 1500 rev/min $\leq N \leq$ 5000 rev/min and $0.052 \leq Re_\phi \leq 0.174$ (approx.).

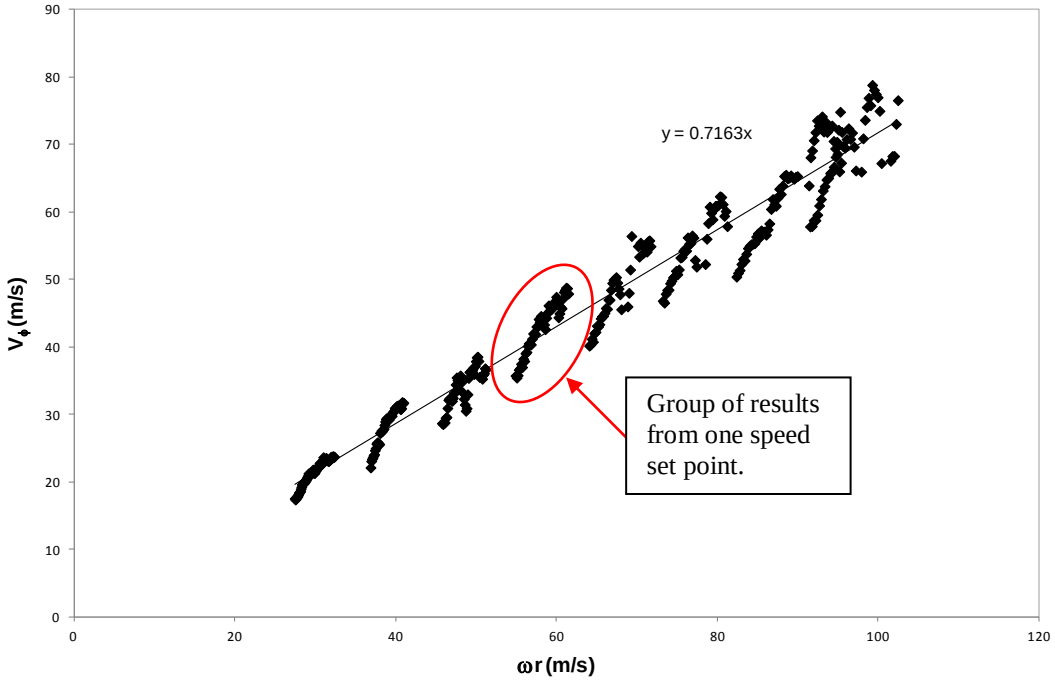

Figure 9.19 - Variation of V_ϕ with ωr for eighteen 13 mm bolts on the rotor with erroneous data points removed, C_w = 0, 1500 rev/min $\leq$ $N \leq$ 5000 rev/min and 0.052 $\leq$ $\mathrm{Re}_\phi \leq$ 0.174 (approx.).

It can be seen from Figure 9.19 that the average value of β has increased dramatically with the introduction of bolts from β^* = 0.419 to β^* = 0.716, an increase of over 70%. The maximum tangential velocity reached in both cases is V_ϕ = 44 m/s for the plain disc and V_ϕ = 79 m/s when bolts are present. This is an 80% increase in tangential velocity, which is the same as that observed by **Coren (2007)**. It is also noted that the variation of the tangential velocity of the fluid between the inner and outermost radii at each speed set point is significant. This is demonstrated by the velocity difference within each group of test points representing each speed set point, as indicated in Figure 9.19. This illustrates that the bolts have a large effect on the flow in their vicinity, since the increase in velocity is much larger than that seen for the plain disc due to increasing radius alone.

The results presented thus far, have quantified the increase in tangential velocity when bolts are present but with no superimposed throughflow. Following this it was important to investigate the effects of introducing throughflow into the cavity. For these tests again, measurements are obtained for both the plain disc as well as with eighteen,

13 mm bolts. The results are plotted using the parameters $\lambda_T(r/b)^{-2.6}$ and β, calculated using Equation 9.4. The parameter $\lambda_T(r/b)^{-2.6}$ is used here instead of the turbulent flow parameter, λ_T , which has predominantly been used in previous chapters. This is because the value of λ_T is constant for each speed set point, whereas the parameter $\lambda_T(r/b)^{-2.6}$ takes into account radial location and therefore varies over the range of velocity data obtained at each speed set point. This parameter is also pertinent to the calculation of β when using the empirical relationship developed by **Daily *et al.* (1964)** shown in Equation 9.5, which is used for comparison throughout this chapter. In this equation C = 12.74 and β^* = 0.431, as specified by Daily **and Nece (1960)** for a gap ratio G = 0.1.

$$\beta = \beta^* \left[1 + \frac{C\lambda_T}{\left(r/b\right)^{2.6}} \right]^{-1} \qquad \textbf{(9.5)}$$

Figure 9.20 shows the variation of β with $\lambda_T(r/b)^{-2.6}$ for the plain disc tests with constant throughflow and varying rotational speed, where C_w = 10100 (±10%) and 1500 rev/min $\leq N \leq$ 5000 rev/min. This represents the range of rotational Reynolds numbers 0.051 x $10^7 \leq \mathrm{Re}_\phi \leq$ 0.214 x 10^7. Also shown are values of β calculated using Equation 9.5.

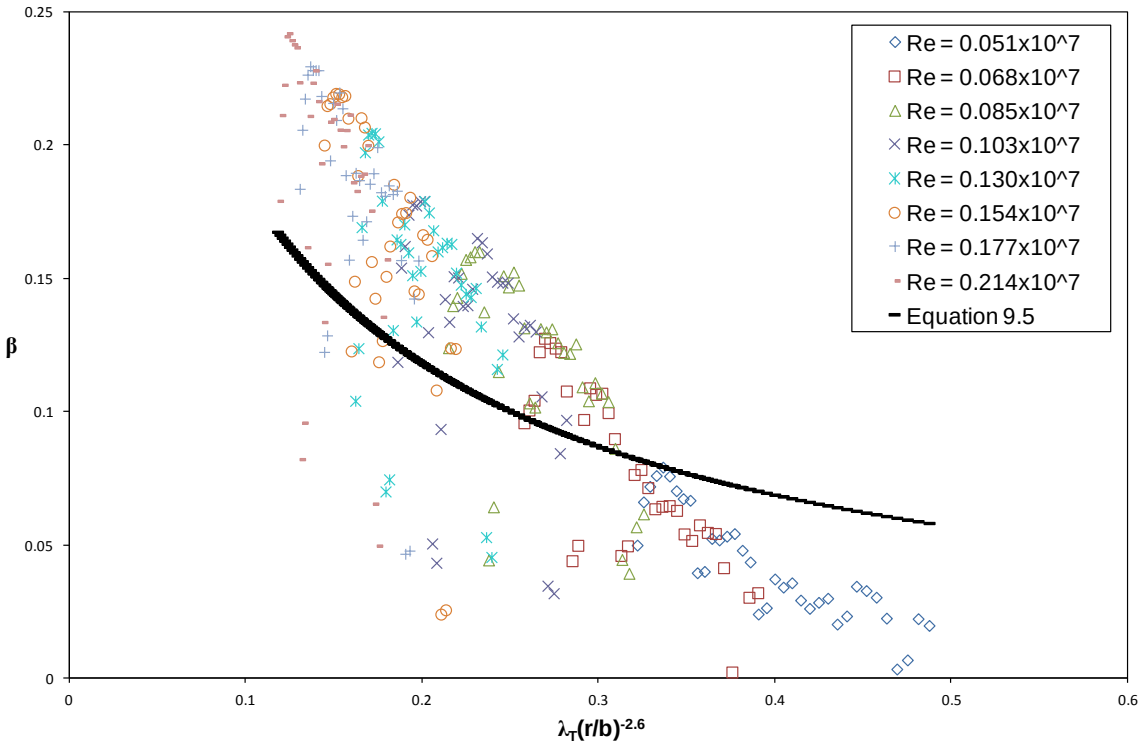

Figure 9.20 – Variation of β with $\lambda_T(r/b)^{-2.6}$ for a plain disc, C_w = 10000 (±10%), 0.051 x $10^7 \leq$ Re$_\phi \leq$ 0.214 x 10^7, 0.094 $\leq \lambda_T \leq$ 0.256, C = 12.74 and β^* = 0.431.

It can be seen from Figure 9.20 the test results are quite different to that predicted by the correlation of Daily *et al*. The value C = 12.74 in Equation 9.5 was chosen by Daily *et al*. to give good agreement with their experimental data at the non-dimensional radius r/b = 0.648. It is stated that their experimental points showed slightly greater values of β than the correlation at r/b = 0.828. Since the range of non-dimensional radius covered by the current experiments is 0.79 $\leq r/b \leq$ 0.92, it would be expected that the results have slightly higher values of β than predicted by Equation 9.5. The values of β measured here, though, are notably higher than predicted where $\lambda_T(r/b)^{-2.6} < 0.3$, by up to 60% for Re$_\phi$ = 0.214 x 10^7. However, the value of β^* assumed by Daily *et al*. when applying the constant C = 12.74, was 0.5 since the experimental results were obtained using the gap ratios G = 0.055 and 0.069. The gap ratio of the current rig is G = 0.1, and the actual value of β^* was measured as 0.419. Daily *et al*. suggest that a 10% reduction in β^* could lead to a 15% reduction in the value of the constant used in Equation 9.5. Using this logic, since β^* = 0.419 is a 16% reduction from β^* = 0.5, the value of the constant, C, could be up to 25% less. Figure 9.21 shows the same as Figure 9.20, except the calculated data from Equation 9.5 is based on β^* = 0.419 and C = 9.56.

It can be seen that the calculated data is a lot closer to the measured results, which is now only 25% higher than the calculated results where $Re_\phi = 0.214 \times 10^7$, rather than 60%.

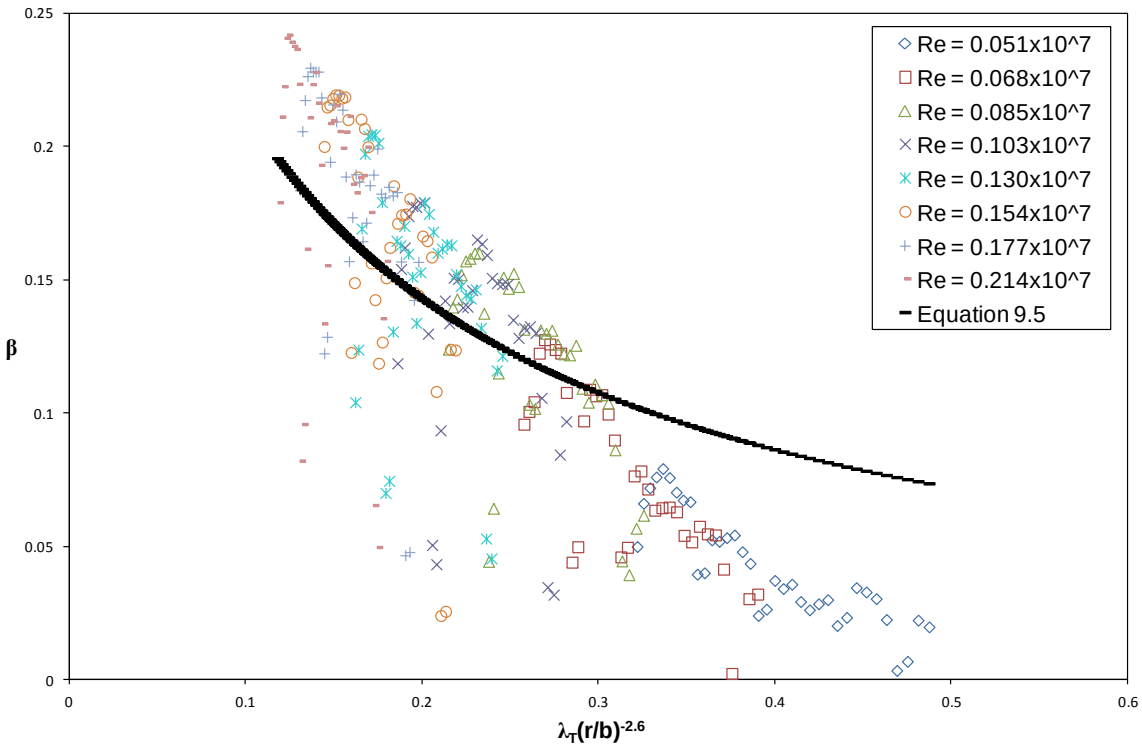

Figure 9.21 – Variation of β with $\lambda_T(r/b)^{-2.6}$ for a plain disc, $C_w = 10000$ (±10%), $0.051 \times 10^7 \leq Re_\phi \leq 0.214 \times 10^7$, $0.094 \leq \lambda_T \leq 0.256$, $C = 9.56$ and $\beta^* = 0.419$.

It is also noted from Figures 9.20 and 9.21, that the measured results are only higher than predicted where $\lambda_T(r/b)^{-2.6} < 0.3$, above this the value of β drops below that predicted by Equation 9.5. The range of experimental data obtained by Daily *et al.* that provides a good approximation to Equation 9.5 is where $\lambda_T < 0.1$. For the current test results where $Re_\phi = 0.214 \times 10^7$, $\lambda_T = 0.094$ and where $Re_\phi = 0.177 \times 10^7$, $\lambda_T = 0.104$, the value of λ_T then increases further with decreasing rotational Reynolds number. The majority of the test results, therefore, are outside the range for which Equation 9.5 has been validated and so would not necessarily be expected to agree.

Figure 9.22 shows the variation of β with $\lambda_T(r/b)^{-2.6}$ for plain disc tests with constant speed and varying throughflow, where $Re_\phi = 0.14 \times 10^7$ (±4%) and $3900 \leq C_w \leq 27400$. The results from Daily *et al.*'s correlation are also shown, calculated using $\beta^* =$

0.419 and C = 9.56. For these tests, it is only when $C_w \leq$ 8500 that $\lambda_T \leq$ 0.1. Figure 9.22 shows that the experimental results have higher values of β, where $\lambda_T(r/b)^{-2.6} < 0.3$, than that predicted using Equation 9.5. This is consistent with the constant throughflow results seen in Figures 9.20 and 9.21.

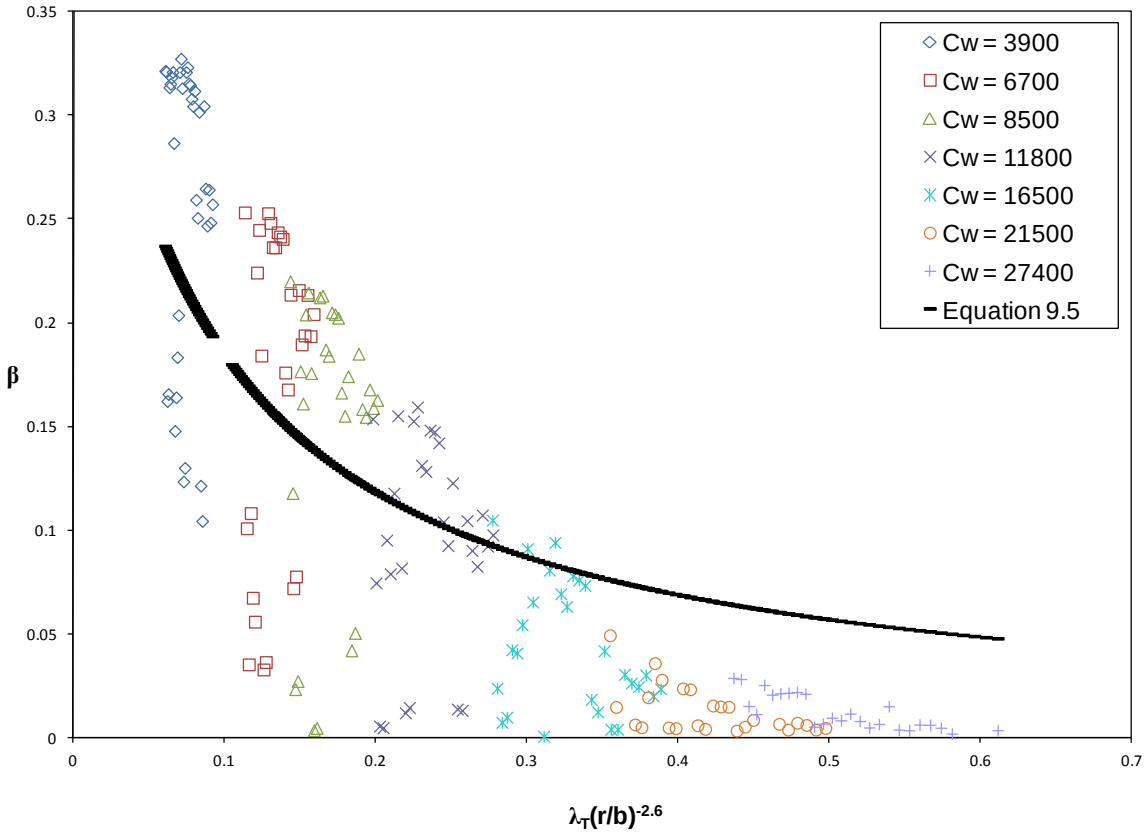

Figure 9.22 – Variation of β with $\lambda_T(r/b)^{-2.6}$ for a plain disc, Re_ϕ = 0.14 x 10^7 (±4%), 3900 $\leq C_w \leq$ 27400, 0.048 $\leq \lambda_T \leq$ 0.321, C = 9.56 and β^* = 0.419.

Figure 9.23 shows the variation of β with $\lambda_T(r/b)^{-2.6}$ for the complete set of plain disc measurements with superimposed throughflow. It can be seen here that the results from the constant speed and constant throughflow tests align well and, disregarding the obviously erroneous data points, a clear trend between the tangential velocity ratio and the parameter $\lambda_T(r/b)^{-2.6}$ is observed.

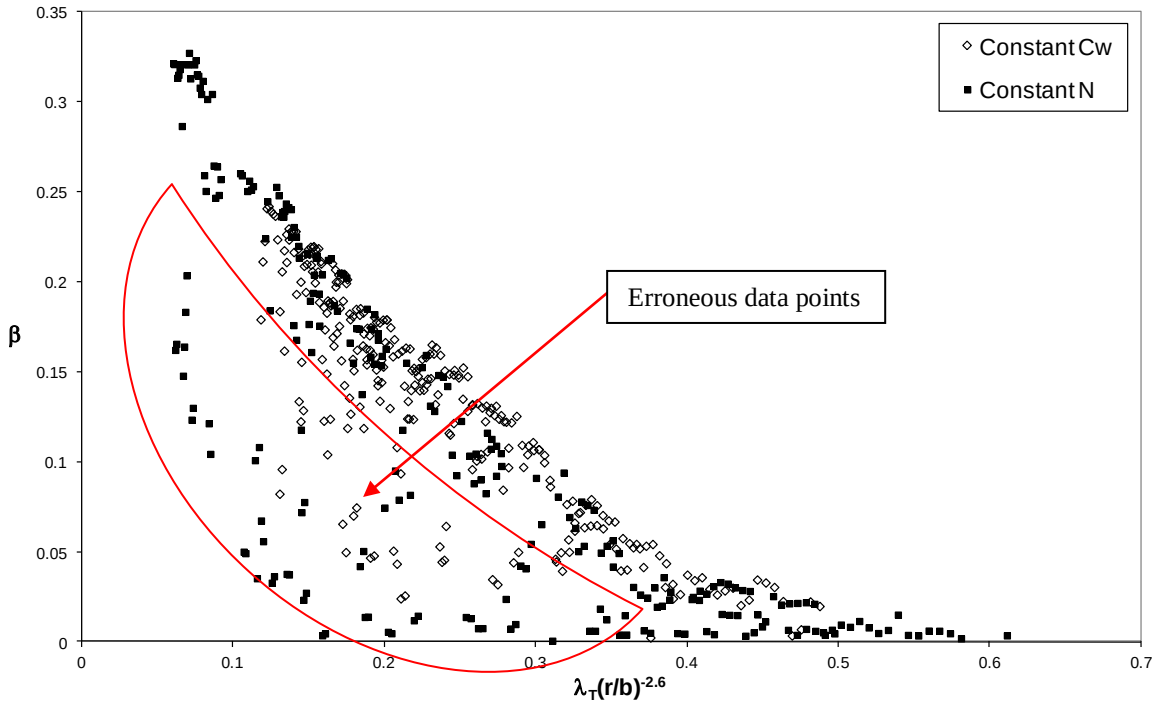

Figure 9.23 - Variation of β with $\lambda_T(r/b)^{-2.6}$ for all plain disc results, $3900 < C_w < 27400$, $0.051 \times 10^7 \leq Re_\phi \leq 0.214 \times 10^7$ and $0.048 \leq \lambda_T \leq 0.321$.

Figure 9.24 shows the variation of β against $\lambda_T(r/b)^{-2.6}$ for tests with eighteen 13 mm bolts, constant throughflow, $C_w = 10100$, and varying speed 1500 rev/min $\leq N \leq$ 5000 rev/min, representing the range of rotational Reynolds numbers $0.053 \times 10^7 \leq Re_\phi \leq 0.172 \times 10^7$. The tangential velocity ratio calculated using Equation 9.5 is also shown to highlight the increase in β when bolts are introduced.

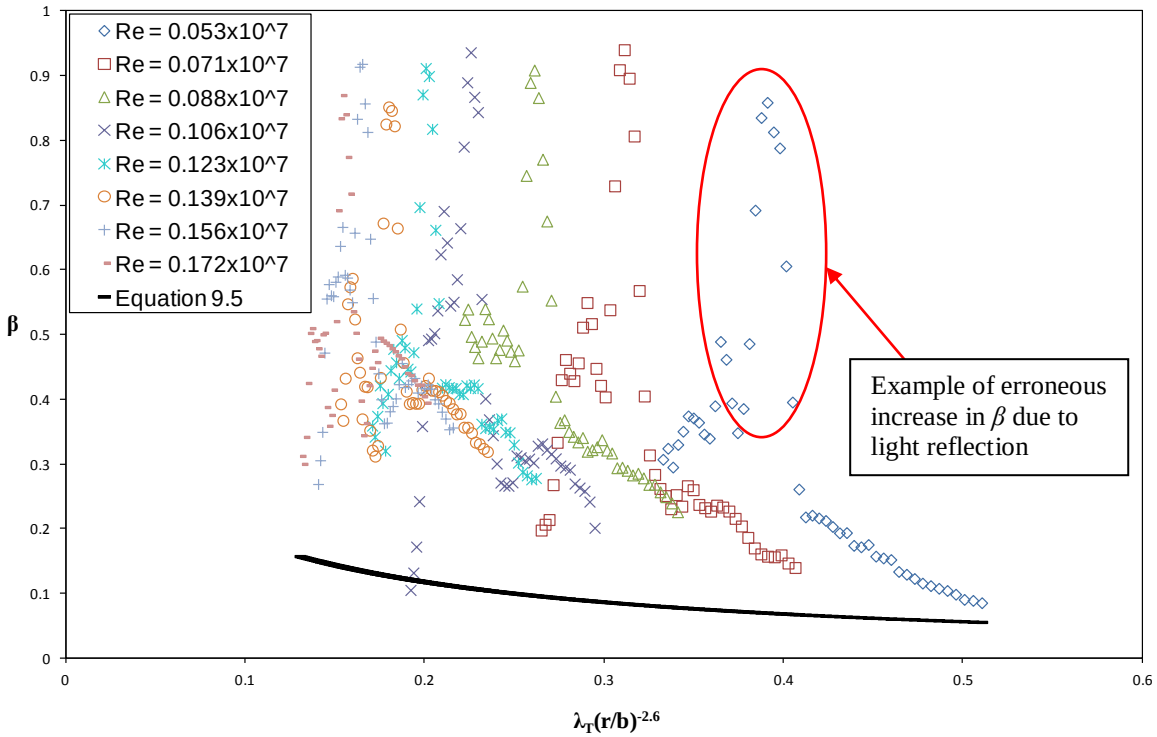

Figure 9.24 - Variation of β with $\lambda_T(r/b)^{-2.6}$ for eighteen 13 mm bolts on the rotor, C_w = 10100, $0.053 \times 10^7 \leq \mathrm{Re}_\phi \leq 0.172 \times 10^7$ and $0.104 \leq \lambda_T \leq 0.256$.

It can be seen from Figure 9.24 that there is consistently a sharp increase in β at a similar position in the image for each set of data obtained. This is indicated on Figure 9.24 for the set of data obtained at $\mathrm{Re}_\phi = 0.053 \times 10^7$. It is likely that this is caused by a reflection of light in the images coming from the bottom edge of the bolt. This reflection can be seen in Figure 9.25. When the bolt is attached to the rotor, the hole in the cap screw is filled with plaster of paris to give a smooth surface. Black paint is then sprayed over the bolts and disc to ensure good PIV measurements. It is clear that in this case the black paint has not completely covered the plaster of paris, resulting in the small patch of white reflecting the light from the laser. This small defect in the paint surface is consistent throughout the 13 mm bolt tests, and causes the same apparent increase in tangential velocity throughout these results.

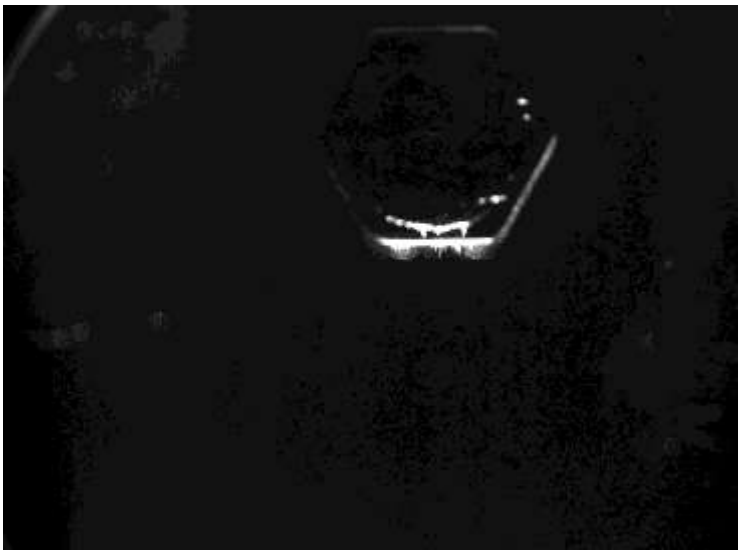

Figure 9.25 – Picture showing light reflections due to white plaster of paris showing past the black paint.

It can be seen in Figure 9.24 that the tangential velocity of the core is much faster when bolts are present than the calculated plain disc data. In general the tangential velocity ratio with bolts present is almost triple that of the plain disc. Where $\lambda_T(r/b)^{-2.6} = 0.28$ and $Re_\phi = 0.088 \times 10^7$ ($\lambda_T = 0.17$) it has increased from $\beta = 0.12$ to $\beta = 0.34$. At the highest values of Re_ϕ though, the increase is slightly less. Where $\lambda_T(r/b)^{-2.6} = 0.18$ and $Re_\phi = 0.172 \times 10^7$ ($\lambda_T = 0.1$) the tangential velocity ratio increases from $\beta = 0.2$ to $\beta = 0.48$, which is just under 2.5 times greater. All test points in Figure 9.24 where $Re_\phi \geq 0.071 \times 10^7$ represent rotationally dominant flow. However, where $Re_\phi = 0.053 \times 10^7$ the flow is radially dominant, since $\lambda_T = 0.256$. The value of β in this case is more than four times greater with bolts than without at $\lambda_T(r/b)^{-2.6} = 0.5$, which is a position far away from the bolt at $r \approx 0.18$ m. Closer to the bolt radius, at $\lambda_T(r/b)^{-2.6} = 0.35$ ($r \approx 0.2$ m), the tangential velocity ratio is more than five times bigger, increasing from $\beta = 0.07$ to $\beta = 0.37$.

Figure 9.26 shows the variation of β with $\lambda_T(r/b)^{-2.6}$ for the tests with 13 mm bolts at constant speed, $N = 4000$ rev/min and varying throughflow $3300 \leq C_w \leq 31300$. The rotational Reynolds number at this speed varies between $0.138 \times 10^7 \leq Re_\phi \leq 0.170 \times 10^7$. The values of β for the plain disc, calculated using Equation 9.5, are once again shown.

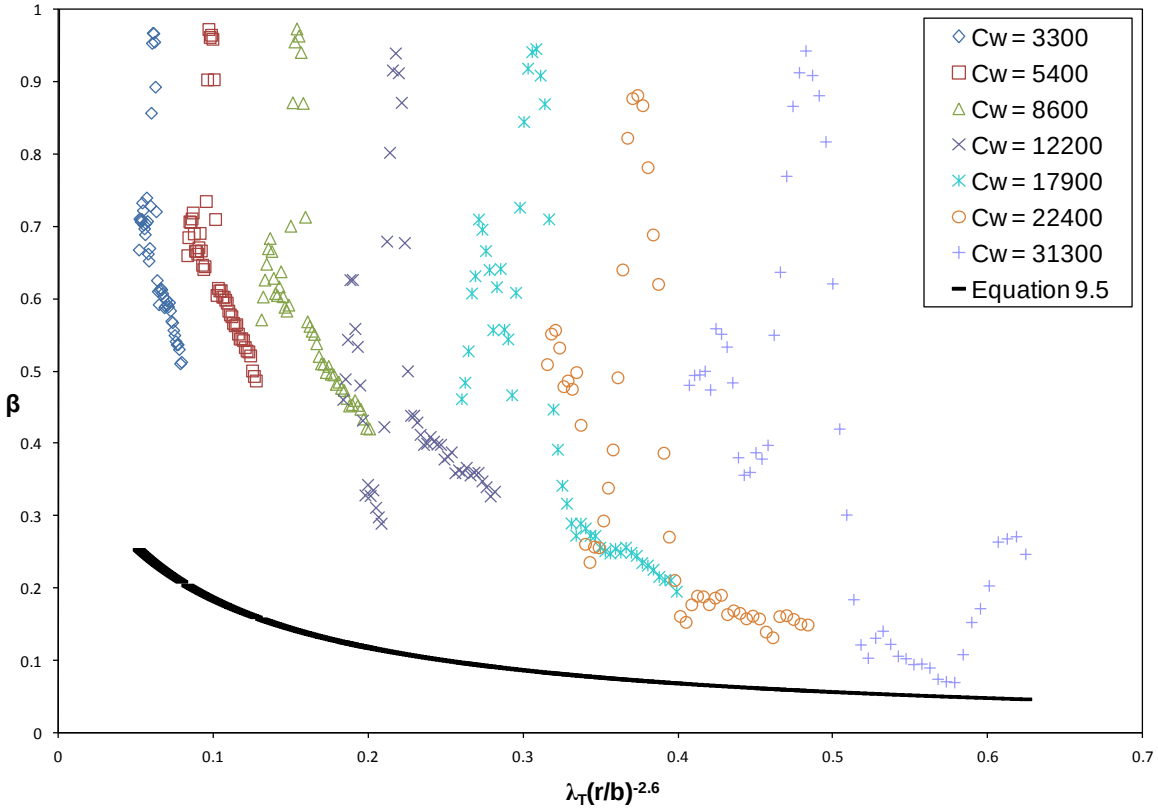

Figure 9.26 – Variation of β with $\lambda_T(r/b)^{-2.6}$ for eighteen 13 mm bolt on the rotor, N = 4000 rev/min, 0.138 x $10^7 \leq$ Re$_\phi \leq$ 0.170 x 10^7, 3300 $\leq C_w \leq$ 31300 and 0.041 $\leq \lambda_T \leq$ 0.324.

Again, a large increase in the tangential velocity ratio, β, is seen in Figure 9.26 over that of the plain disc, similar to the results shown in Figure 9.24. The large spikes in the tangential velocity ratio, observed for all values of C_w, are due to the light reflection mentioned previously. Where C_w = 12200 and λ_T = 0.12, a rotationally dominant flow condition, β has again almost tripled, from β = 0.145 to β = 0.4 at $\lambda_T(r/b)^{-2.6}$ = 0.24. For the radially dominant flow conditions, $C_w \geq$ 22400, β increases at least four times the plain disc value where bolts are present. Where $\lambda_T(r/b)^{-2.6}$ = 0.57 the increase is as much as twelve fold. For the case where C_w = 31300 there is also an area of increased tangential velocity where $\lambda_T(r/b)^{-2.6} \geq$ 0.6 in Figure 9.26, which is radially inward of the bolt. This is assumed to be an anomaly since this does not occur at any of the other values of C_w. This could be the result of a lack of seeding particles in this area.

Figures 9.24, and 9.26 show that with the introduction of throughflow, the bolts generate a much larger increase in the tangential velocity of the fluid than when no

throughflow is present. When $C_w = 0$, the tangential velocity ratio is increased by around 80% as a results of the bolts, but when $C_w > 0$ the tangential velocity is generally almost tripled. In the case of radially dominant flow, it is at least four times greater with bolts present than without, and can reach as high as twelve times greater. To understand the mechanism behind the larger increases in tangential velocity in the presence of throughflow, further measurements are required in order to obtain torque measurements for all test conditions.

An investigation was carried out to determine how the flow behaves in varying positions relative to the bolt, other than the centreline. It was decided that two positions of interest would be both slightly upstream and slightly downstream of the bolt, so the effects of the bolt on its immediate surroundings could be identified. This required the chosen positions to be more than 7.5 mm from the centreline, in either direction, since the diameter of the bolt point to point is 15 mm. One position further downstream was also thought necessary to capture the extent of any wake formation. Positions at the far edges of the images were thought to be of little use since the data in these areas is often unreliable due reduced light intensity. Figure 9.27 shows the positions investigated, given in multiples of bolt diameter, *D*. Each position is given a reference which will be used for the remainder of this chapter when referring to the data. These references, D2, D1, CL and U1, corresponding to: farthest downstream; downstream; centreline of the bolt; and upstream, are shown below the image.

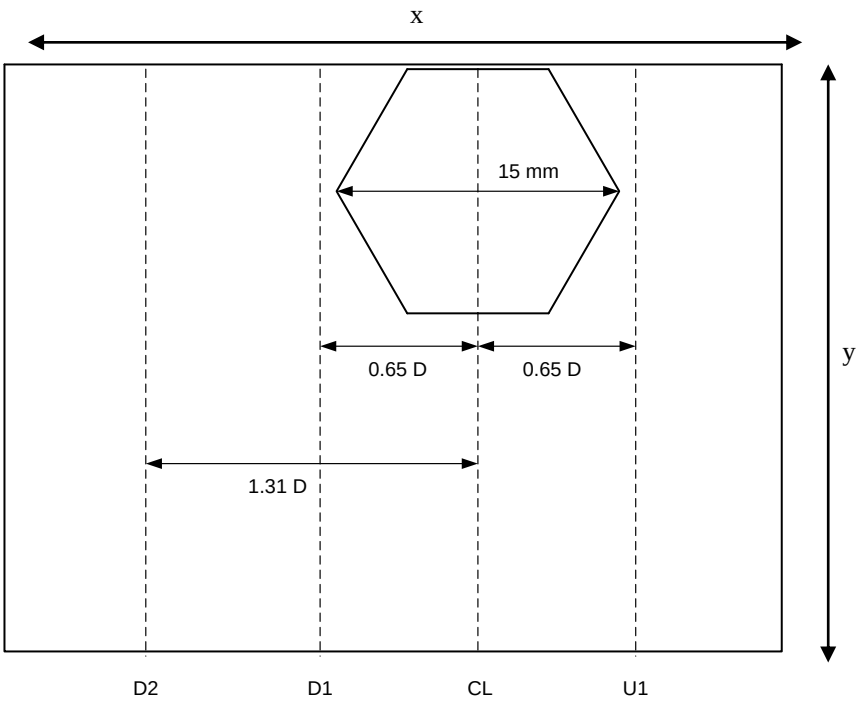

Figure 9.27 – Diagram showing the four positions in the *x* direction of the captured image that measured data is analysed.

The data from each position in the image was then plotted for six flow conditions: two with no throughflow; two with constant throughflow; and two with constant speed, as shown in Table 9.1.

C_w	*N (rev/min)*	$\mathbf{Re}_\phi$
0	2500	~0.087
	5000	~0.174
10100	2500	0.088
	5000	0.172
3300	4000	0.138
22400		0.154

Table 9.1 – Table showing the six flow conditions used for investigating data taken from varying positions in the image.

Figures 9.28 and 9.29 show the variation of β with y for the tests with no superimposed throughflow and speeds of N = 2500 rev/min and 5000 rev/min respectively (relating to Re_ϕ = 0.087 and 0.174 respectively based on ambient temperature and pressure). As

shown in Figure 9.27, *y* is the vertical position in the captured image and in Figures 9.28 to 9.33, 0 mm represents the bottom edge of the image and 31.33 represents the top edge. All four positions: D2, D1, CL and U2 are shown in Figures 9.28 and 9.29, as well as markings showing the bottom and top edge of the bolt as seen in the images.

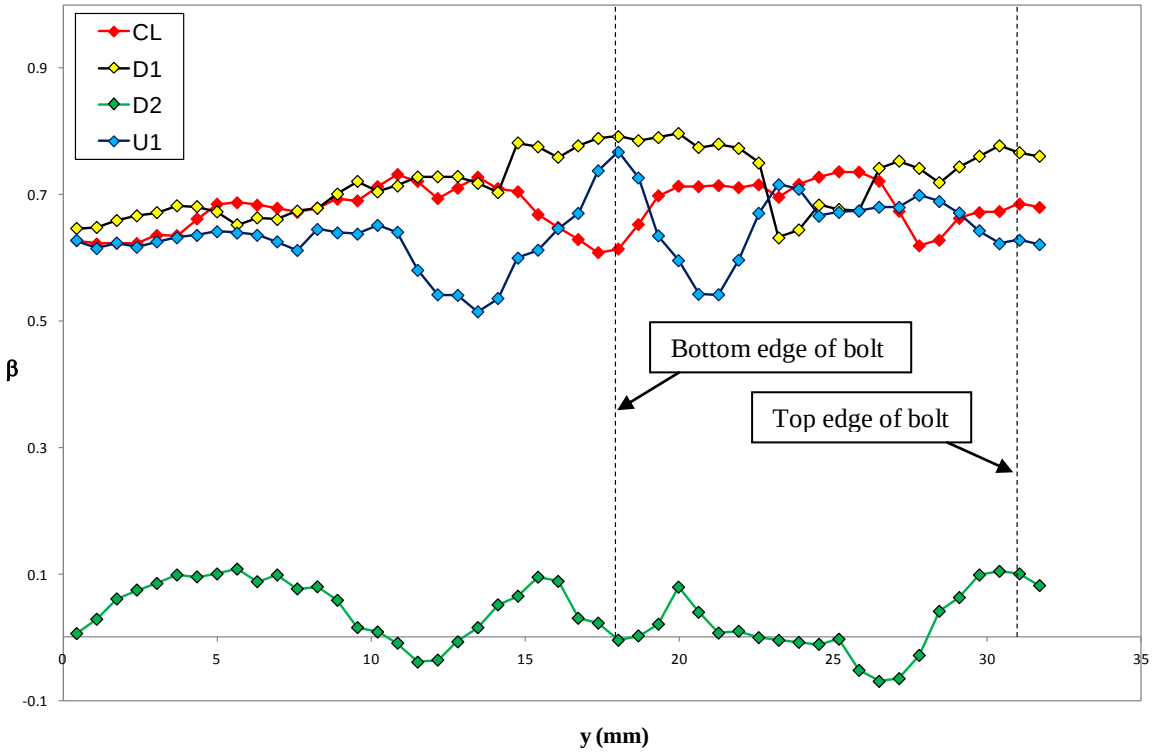

Figure 9.28 – Variation of β with y, $C_w = 0$, $N = 2500$ rev/min and $\mathrm{Re}_\phi = 0.087$ (approx.).

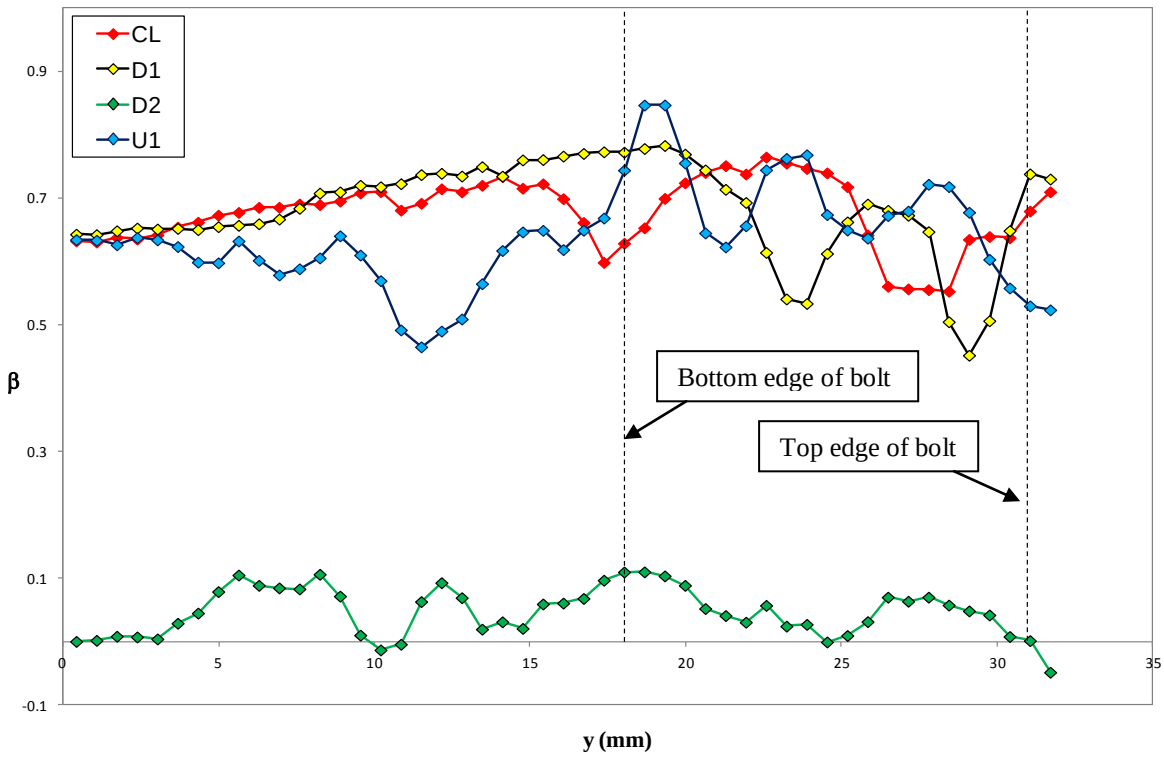

Figure 9.29 – Variation of β with y, $C_w = 0$, $N = 5000$ rev/min and $\mathrm{Re}_\phi = 0.174$ (approx.).

It is clear in both cases that the data from the farthest downstream position, D2, is vastly different to the other three positions and suggesting that the tangential velocity is close to zero. This is most likely due to lack of seeding material in that area, or lack of light, but it is possible that it is the result of wake formation behind the bolt. This, however, is unlikely since if this were the case, it would be expected that the velocities for the position closer behind the bolt, D1, would be lower than the velocities further downstream. This is the behaviour observed from the experimental results of **Payne (2011)**, but is clearly not the case here. The results from the other three positions are similar, although radially inwards of the bolt (0 mm < y < 18 mm) the centreline, CL and downstream position, D1, show little variation. Upstream of the bolt, U1, the tangential velocity varies more in this area. Over the cross section of the bolt however, the velocities fluctuate a great deal at all three positions, between $\beta = 0.45$ and $\beta = 0.85$ where $N = 5000$ rev/min.

Figures 9.30 to 9.33 show the variation of β with y for tests with superimposed throughflow. Figures 9.30 and 9.31 show the constant throughflow tests and Figures

9.32 and 9.33 the constant speed tests. It can be seen that for all four conditions that the tangential velocities for the point farthest downstream, D2, are now similar to the other three positions. This would suggest that the difference seen in Figures 9.28 and 9.29 was due to lack of seeding or light, rather than a result of wake formation. In order to help analyse the data it is important to note that Figures 9.30 to 9.32 are rotationally dominant flow conditions, where λ_T = 0.177, 0.104 and 0.041 respectively. Figure 9.33 is a radially dominant flow condition, where λ_T = 0.251.

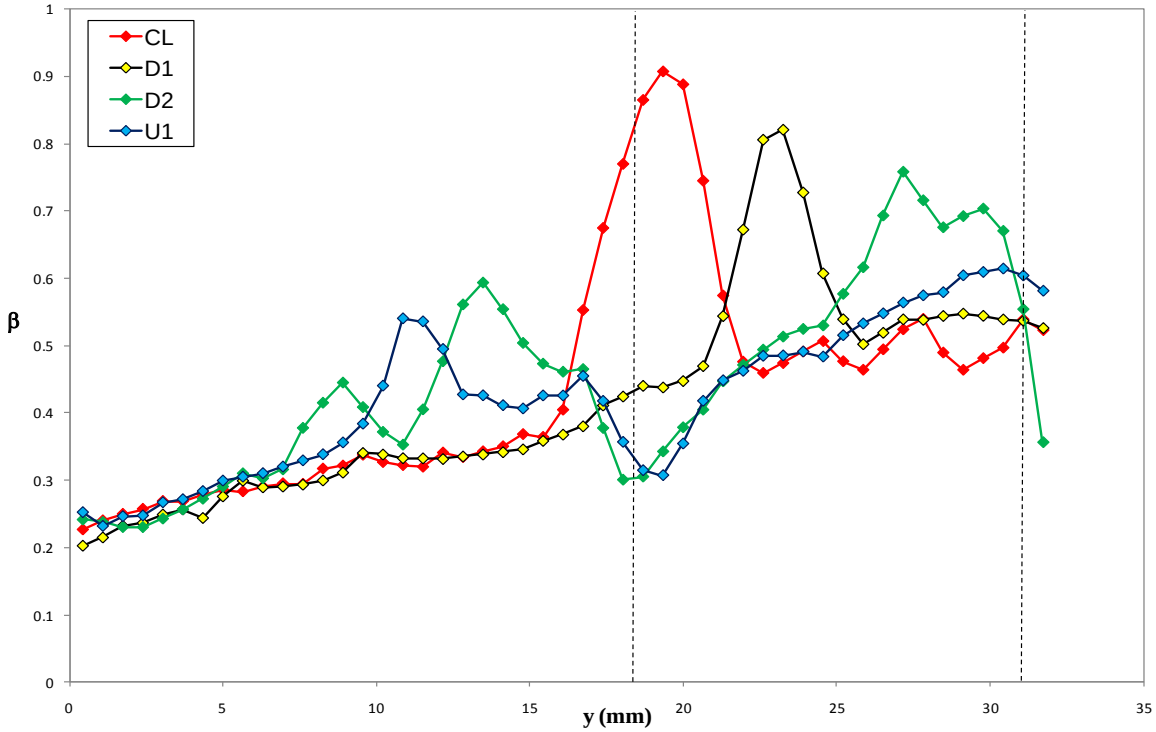

Figure 9.30 – Variation of β with y, C_w = 10100, Re_ϕ = 0.088 and λ_T = 0.177.

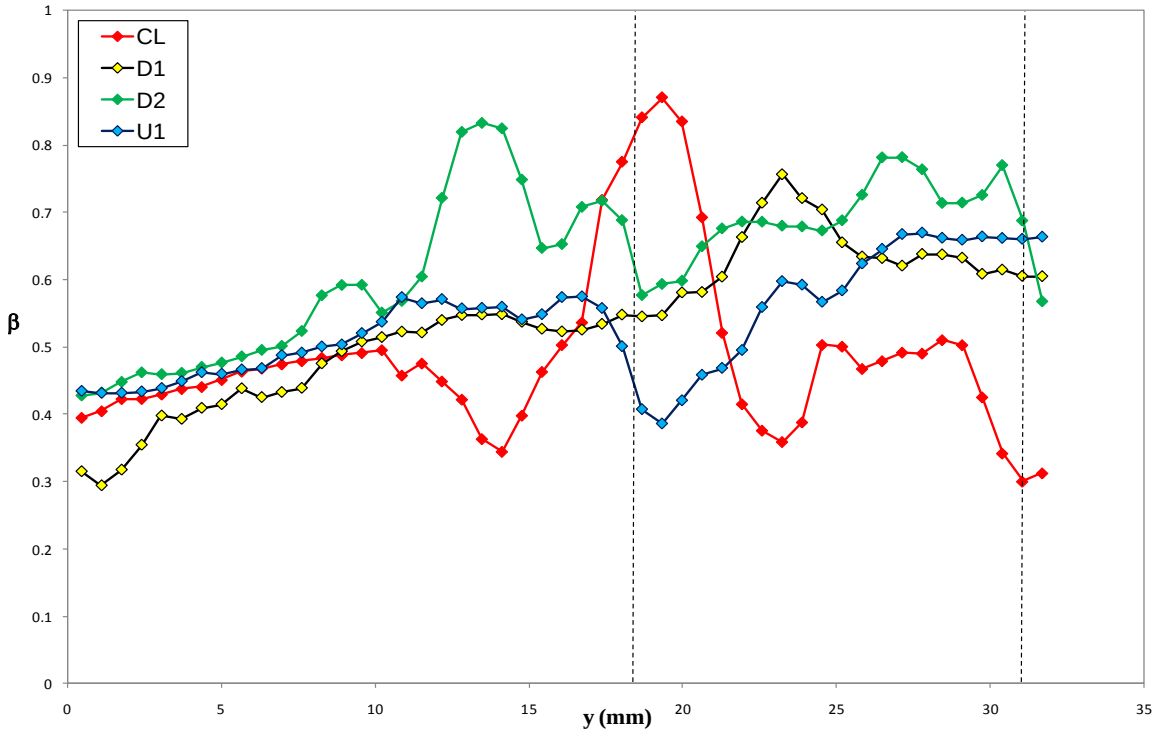

Figure 9.31 – Variation of β with y, C_w = 10100, Re_ϕ = 0.172and λ_T = 0.104.

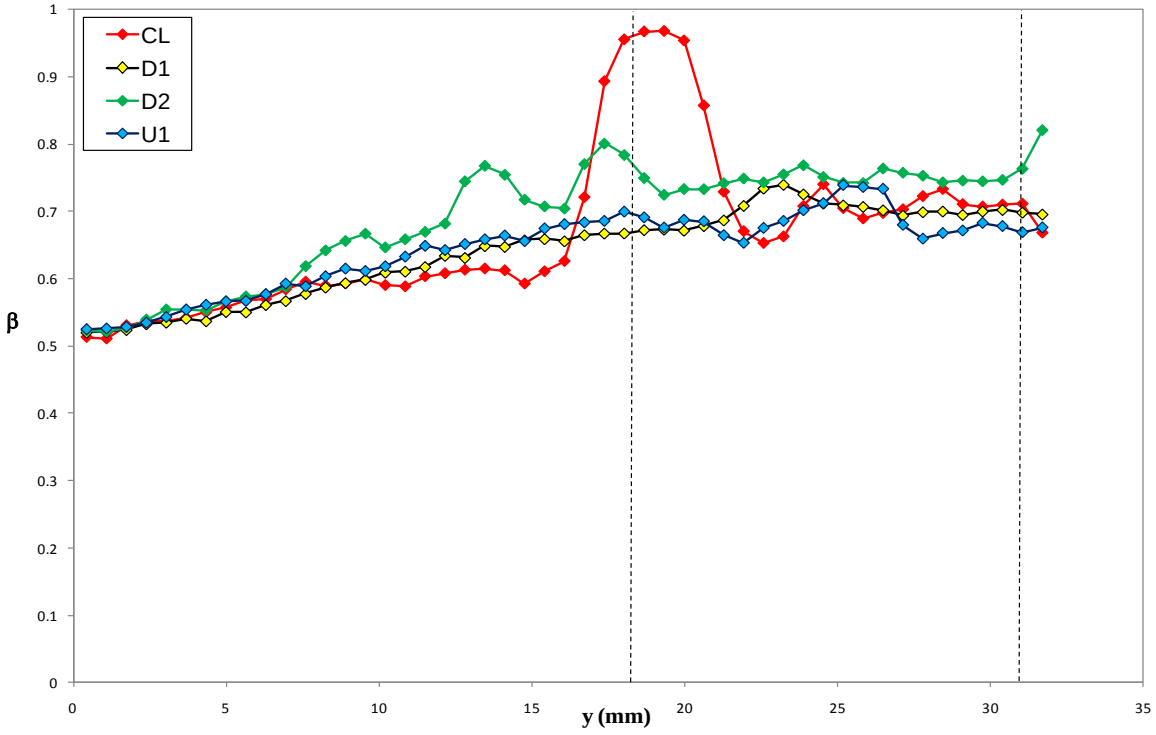

Figure 9.32 – Variation of β with y, C_w = 3300, Re_ϕ = 0.138 and λ_T = 0.041.

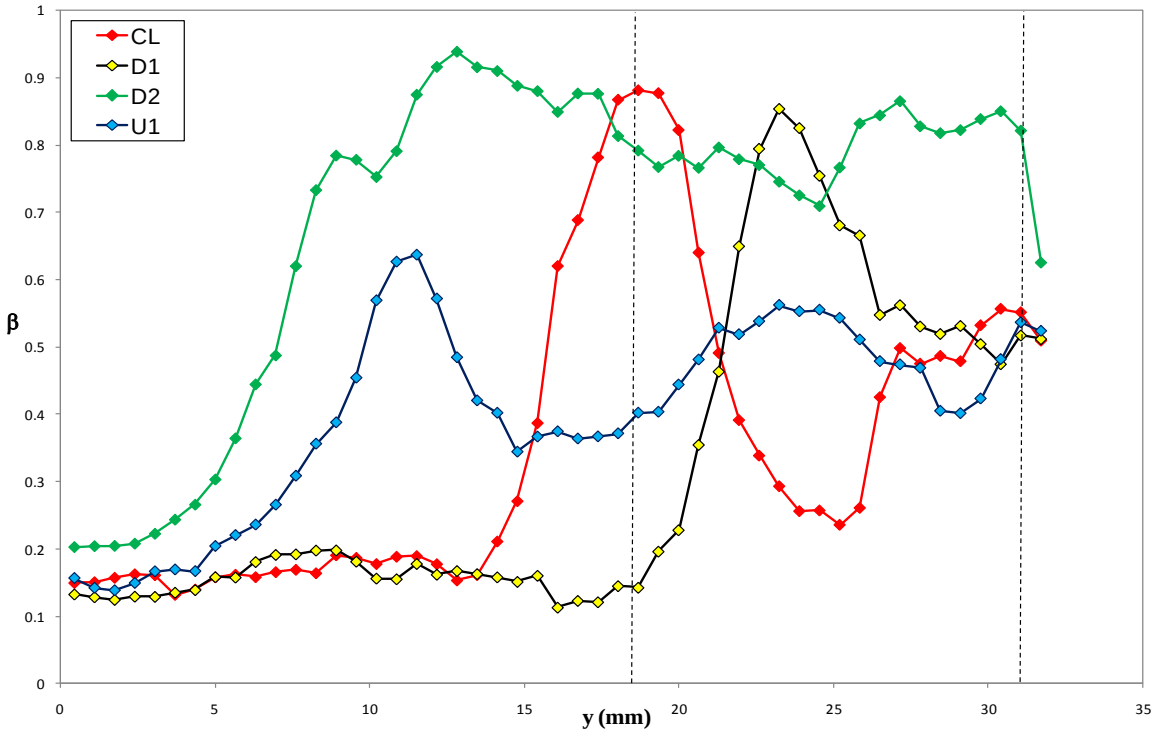

Figure 9.33 – Variation of β with y, C_w = 22400, Re_ϕ = 0.154 and λ_T = 0.251.

It can be seen that for all the rotationally dominant conditions (Figures 9.30 to 9.32), between 0 mm < y < 8 mm, the tangential velocity ratio, β, is consistent for all positions in the image. It is also increasing with decreasing λ_T, as would be expected from increasing rotational dominance. In Figure 9.33 however, it can be seen that the tangential velocity of the core where y < 5 mm is very low, just 10% to 20% of disc speed, due to the superimposed radial flow dominating the flow conditions. Where y > 5 mm though, this radial dominance is quite substantially affected by the tangential velocity of the bolt, particularly at the position farthest downstream, D2, which would not necessarily be expected. It can be seen however that the tangential velocity varies quite substantially over the bolt area, particularly for the centreline, CL, and closest downstream, D1, positions. The large variation observed at the centreline of the bolt, where $y \approx 18$ mm, is attributed to the reflection mentioned previously at the bottom edge of the bolt (see Figure 9.25). This is also the case in Figures 9.30 to 9.33. The large variation observed at the downstream position, D1, however might suggest that wake formation creates much larger instabilities in radially dominant flow than in rotationally dominant flow.

An additional piece of testing was also carried out involving measurements with no throughflow and a disc speed of N = 4000 rev/min (Re_ϕ = 0.174 (approx.)), spanning the cavity in the axial direction, z. The measurements start from a position level with the top of the bolt head and are then obtained in 0.5 mm stages across the cavity to 10 mm above the bolt head, as shown in Figure 9.36.

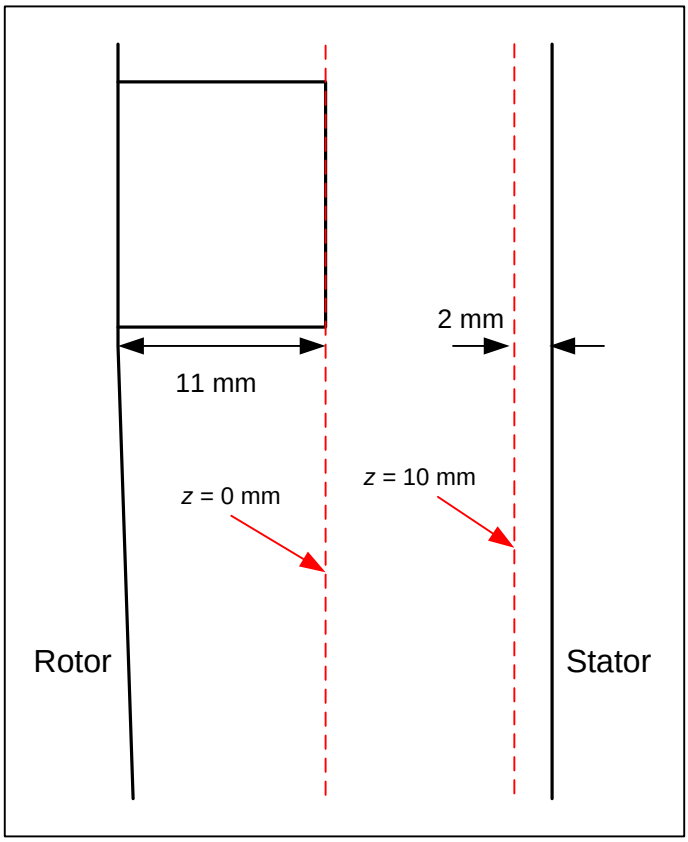

Figure 9.36 – Diagram showing the range of axial traverse measurements.

The purpose of these tests was to investigate the existence of Taylor columns within the cavity as the bolts move through the rotating core. The existence of Taylor columns was predicted by the Taylor-Proudman theorem and has been demonstrated extensively in laboratory experiments. The theorem states that where there are small relative velocities in geostrophic flows in an incompressible fluid, there can be no velocity gradients in the direction parallel to the axis of rotation. A geostrophic flow is one where the Coriolis forces are large compared to the inertial and viscous forces, leading to a balance between the Coriolis and pressure forces. The flow in the core between the rotor and the stator in the current test facility could be approximated as geostrophic if

the rotation is strong and the relative velocity between the rotor and the core were small enough. It is possible that this could be the case since it has been shown that the bolts can speed up the core velocity by up to 80% faster than if no bolts are present.

If Taylor columns were to exist, then the tangential velocity of the fluid above the bolt (in the z direction) would be the same as the bolt across the axial extent of the cavity. This would create a horizontal column of fluid between the rotor and the stator moving at bolt speed. Figure 9.37 shows the tangential velocity, V_ϕ, at the centreline of the bolt in both the x and y direction (x = 25.85, y = 24.55), with the distance, z, across the cavity relative to the top of the bolt head. The top of the bolt head is z = 0, as shown in Figure 9.36. The velocity of the bolt at the centre is 84 m/s at N = 4000 rev/min, therefore it can be seen clearly from Figure 9.37 that Taylor columns do not exist in these conditions. This is likely to be due to the relative velocity between the rotor and the core being too large.

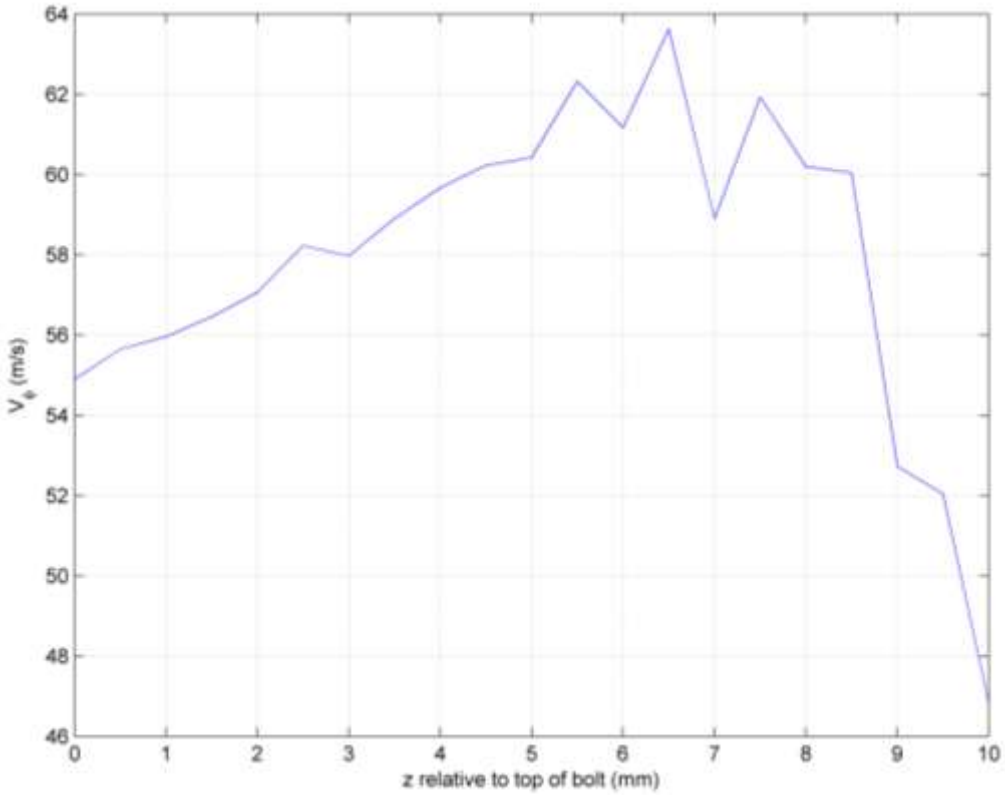

Figure 9.37 – Variation of V_ϕ with z, the axial position in the cavity relative to the top of the bolt head, C_w = 0, Re_ϕ = 0.174 (approx.) and N = 4000 rev/min.

9.5 Summary

The PIV measurements showed up to an 80% increase in the core tangential velocity compared with the plain disc when bolts are present with no superimposed throughflow. The introduction of throughflow increases the effect that bolts have on the tangential velocity of the fluid in the rotor-stator cavity. When flow is rotationally dominant, the tangential velocity ratio more than doubles with bolts present, but for radially dominant flow an increase of up to twelve times that of the plain disc has been observed. The plain disc results with superimposed throughflow were compared to the correlation developed by **Daily *et al.* (1964)**. The difference was found to be less than 25%, when the variations in test facility and measurement location were accounted for, in the region $\lambda_T < 0.1$ where the correlation is valid.

The investigation of the flow at various positions in the PIV images, showed the tangential velocity in the region of the bolt, $0.194 \text{ m} \leq r \leq 0.207 \text{ m}$, to fluctuate a great deal in comparison to the flow radially inward of the bolt. This result was expected from the assumption of wake formation behind the bolts. Experiments to detect the existence of Taylor columns in the rotor-stator cavity when bolts are present showed that they do not exist. This is likely to be due to the relative velocity between the rotor and the core being too large.

Chapter 10. Conclusions and Recommendations for Future Work

10.1 Conclusions

The plain disc test results compare well with those obtained in a previous test phase by **Coren (2007)** on the same test rig. The results were also compared with free disc results from open literature as well as existing analytical and empirical correlations for rotor-stator systems. In most cases there was good agreement found, once any assumptions or variation in the test facilities had been accounted for. The variation found between the test results and any one correlation was shown to be less than the variation between the correlations themselves. These factors led to confidence in the results obtained as well as the future results in the remainder of the test program.

The stator bolt results showed that where $\lambda_T < 0.1$ there is a large increase in both windage and rotor surface temperature, of up to 28%. This particular condition is closest to that found in a typical gas turbine engine, and an increase in disc temperature of this size could significantly reduce the life of a turbine disc. The increase in windage is a direct result of an increase in viscous friction, since the form drag and pumping loss components of the moment coefficient are either not measured, or negligible for the stator bolt tests. From previous data it is clear that there is a large increase in moment coefficient at all conditions when rotor bolts are present. This would suggest that that the contribution to the total moment coefficient from viscous friction is small relative to the contribution from form drag and pumping losses. For all conditions where $\lambda_T > 0.1$ any increase in windage or surface temperature due to the presence of stator bolts, is not measureable with the current instrumentation set up.

The hexagonal rotor bolt tests showed there to be a general trend of increased windage with an increase in bolt diameter. However, the increase in windage is not always consistent with the uniform increase in bolt diameter from 10 mm to 13 mm to 16 mm. Relating the flow around the bolts to the flow around a circular cylinder would suggest that the majority of the tests take place in the transitional region between laminar and turbulent separation. Calculations based on this theory show that the conditions where there is an inconsistent increase in windage with increasing bolt diameter, reside in this transitional region, whereas the conditions where a consistent increase is found sit in the fully turbulent region. Testing also proved that, although λ_T is a useful tool for comparing data, varying moment coefficients can be realised for a constant value of λ_T. A single value of λ_T can be reached via different combinations of Re_ϕ and C_w and tests showed that the moment coefficient is also dependant on the values of these individual parameters. From the complete set of windage results, a correlation was produced to determine the resulting moment coefficient, in a rotor-stator cavity with throughflow, from the number and size of bolts present. This new correlation is important since it allows turbomachinery engineers to assess the windage contribution for a much wider range of conditions than had previously been possible.

Tests comparing bi-hexagonal and hexagonal rotor bolts showed that in most cases there is no measureable difference between the bolts shapes. Only for the condition where the measured quantities were at their largest, was there a reduction observed for the bi-hexagonal bolts. An 8% reduction in moment coefficient was observed at $\lambda_T = 0.192$ (±5%), which was the highest measured torque by over 70%. A 10% reduction in surface temperature reduction was observed where $\lambda_T = 0.064$ (±6%), where the highest surface temperatures were measured. This temperature reduction was thought to be a significant finding, since this condition is close to that found in a modern jet engine. Further testing at low values of λ_T, however, showed that this temperature reduction is limited to this condition and not to low values of λ_T in general. The reduction in both windage and surface temperature is thought to be due to a reduction in form drag due to a smaller wake, in width and length. Clearly though, this small reduction in form drag is only measureable, with the current instrumentation, where the measured variables are large.

Testing with rotor surface cavities showed that the rotor surface temperature increased by up to 14%, where $\lambda_T < 0.1$. An increase in moment coefficient of up to 20% above that of the plain disc was found where $\lambda_T = 0.168$ (±3%), it was also shown to increase with an increasing number of cavities. At all other conditions, however, any increase in moment coefficient or rotor surface temperature, due to the surface cavities, is lost in the uncertainty of the measurement.

The PIV measurements have shown up to an 80% increase in the core tangential velocity ratio, when bolts are present and there is no superimposed throughflow, compared with the plain disc. The introduction of throughflow, however, increases the effect that bolts have on the tangential velocity of the fluid in the rotor-stator cavity. When flow is rotationally dominant, the tangential velocity ratio was shown to more than double with bolts present, but when the flow is radially dominant an increase of up to twelve times that of the plain disc has been observed. Torque measurements at all test conditions would be required, however, if the underlying mechanism behind the larger increase in tangential velocity in the presence of throughflow is to be properly explained. The plain disc results with superimposed throughflow were compared to the correlation developed by **Daily *et al.* (1964)**. The difference was found to be less than 25%, when the variations in test facility and measurement location were accounted for, in the region $\lambda_T < 0.1$ where the correlation is valid. The investigation of the flow at various positions in the PIV images, showed the tangential velocity in the region of the bolt ($0.194\ \text{m} \leq r \leq 0.207\ \text{m}$) to fluctuate a great deal in comparison to the flow radially inward of the bolt. This result was expected from the assumption of wake formation behind the bolts. Experiments to detect the existence of Taylor columns in the rotor-stator cavity when bolts are present showed that they do not exist. This is likely due to the relative velocity between the rotor and the core being too large.

10.2 Recommendations for Future Work

Continuation of the Particle Image Velocimetry testing is a key area of further work. Of particular importance is to extend the investigation with bolts present on the rotor surface to include bolts on the stator surface. Measurements of the core velocity are required to investigate the theory that the core is slowed down due to the stator bolts,

resulting in an increase in the viscous friction between the core and the rotor due to the increased relative velocity. Temperature measurements of the rotor surface were obtained with stator bolts present in order to investigate the increase in viscous friction (see Section 6.3), however the effect was only measurable where $\lambda_T < 0.1$. It is thought that at this condition there is a large increase in the relative velocity, making it measureable as an increase in disc surface temperature. The PIV measurements, therefore, might show the smaller changes in core velocity, so that the effect over a wider range of flow conditions can be observed.

The structure of wakes has been investigated using PIV by **Payne (2011)**. This work investigated only the laminar flow regime, due to the limitations of the wind tunnel used. Extension of this work to the transitional and turbulent regimes could help to further understand the non-consistent increase in windage with increasing bolt size. A PIV investigation of the rotational case with different diameter bolt heads on the rotor surface, could also help explain this unexpected result from the windage measurements presented in Section 7.3.

Further testing is required to investigate the large reduction in rotor surface temperature that was observed, with bi-hexagonal rather than hexagonal rotor bolts, at $\lambda_T = 0.064$. This testing should investigate in the range $0.05 \leq \lambda_T \leq 0.1$, but using a variety of Re_ϕ and C_w values to obtain each value of λ_T. Achieving $\lambda_T = 0.064$ with a variety of Re_ϕ and C_w, may produce data to help explain the reason for the large reduction in disc surface temperature, and whether it is actually limited to this value of λ_T. Wind tunnel experiments using PIV could also be used to investigate this phenomenon, if the work by Payne was extended to include the transitional and turbulent regimes.

A second disc was manufactured at the same time as the one used in the current testing, but with a solid, protruding ring machined at $r = 0.2$ m, matching the bolt radius on the current test disc. This was made to investigate the phenomenon observed by **Millward and Robinson (1989)**, whereby fully shrouded bolts reduced windage compared with un-shrouded bolts and also, in some conditions, the plain disc. The disc with a solid ring was balanced in preparation for testing however, the tests were not carried out due to time constraints. It was intended that this work would also be extended to investigate the "slip-streaming" effect predicted by **Zimmerman *et al.* (1986)**. Once the full ring had been tested, a large number of discrete protrusions could be machined, and then the

number of protrusion reduced at each stage of testing. A CFD investigation by **Pett (2007)** found no such slip-streaming effect to occur, even with 60 bolts, where they are too close together to be practical in reality. It would therefore be interesting to investigate the validity of the CFD model created.

References

Batchelor, G. K., 1950.
Notes on a Class of Solutions of the Navier-Stokes Equations Representing Steady Rotationally Symmetric Flow.
Quarterly Journal of Mechanics and Applied Maths. Vol. 4, Pt 1.

Bayley, F. J. And Conway, L., 1964.
Fluid Friction and Leakage between a Stationary and a Rotating Disc.
Journal of Mechanical Engineering Science, Vol. 6, pp.164-172.

Bayley, F. J. and Owen, J. M., 1969.
Flow Between a Rotating and Stationary Disc.
Aeronautical Quarterly, Vol. 20, pp.330-354.

Bayley, F. J. and Owen, J. M., 1970.
The Fluid Dynamics of a Shrouded Disc System with a Radial Outflow of Coolant.
Journal of Engineering for Power. July 1970.

Betts, D. B., Clarke, F.J.J., Cox, L.J. and Larkin, J. A., 1985.
Infra Red Reflection Properties of Five Types of Black Coating for Radiometric Detectors.
Journal of Physics E-Scientific Instruments. Vol. 18, Issue 8 pp.689-696.

British Standards Institution.
Measurement of Flow in Closed Conduits.
BS 1042-1.4:1992.

Cheah, S.C., Iacodives, H., Jackson, D. C., Ji, H. and Launder, B. E., 1994.
Experimental Investigation of Enclosed Rotor-Stator Disc Flows.
Experimental Thermal and Fluid Science, Vol. 9, pp.445-455.

Cochran, M., 1934.
The Flow due to a Rotating Disc.
Proc. Cambridge Phil. Soc. Vol. 30, pp.365-375.

Coren, D., 2007.
Windage due to Protrusions in Rotor-Stator Systems.
Thermo-Fluid Mechanics Research Centre, University of Sussex, D. Phil Thesis.

Coren, D., Childs, P. R. N. and Long, C. A., 2008.
Windage Sources in Smooth-Walled Rotating Disc Systems.
Proc. IMechE Part C: J. Mechanical Engineering Science, Vol. 223, Issue 4, pp 873 – 888.

Daily, J. W. and Nece, R. E., 1960.
Chamber Dimension Effects of Induced Flow and Frictional Resistance of Enclosed Rotating Discs.
Journal of basic engineering, Vol. 82, pp.217-232.

Daily, J. W., Ernst, W. D. and Asbedian, V., 1964.
Enclosed Rotating Discs with Superposed Throughflow.
Dept. of Civil Engineering, MIT, Report No. 64.

Daniels, W. A., Johnson, B. V. and Graber, D. J., 1991.
Aerodynamic and Torque Characteristics of Enclosed Co/Counter-rotating Discs.
Journal of Turbomachinery, Vol. 113, pp. 67-74.

Dibelius, G., Radtke, F. and Ziemann, M., 1984.
Experiments on Friction, Velocity and Pressure Distribution of Rotating Discs.
Heat and mass transfer in rotating machinery (A89-24451 09-34). Washington DC, Hemisphere Publishing Corp., 1984, pp.117-130.

Dorfman, L, A., 1957.
Turbulent Boundary Layer on a Rotating Disc.
Izv. Akad. Nauk SSSR, Otd. tekh. nauk, No.7, pp.138-142.

Dorfman, L. A., 1958.
Hydrodynamic resistance and the heat loss of rotating solids.
1st Edition, Oliver and Boyd.

Gan, X. P. and MacGregor, S. A., 1995.
Experimental Study of the Flow in the Cavity between Rotating Discs.
Experimental Thermal and Fluid Science, Vol. 10, pp.379-387.

Gartner, W., 1997.
A Prediction Method for the Frictional Torque of a Rotating Disc in a Stationary Housing with Superimposed Radial Outflow.
ASME international gas turbine & aero engine conference paper 97-GT-204.

Gartner, W., 1998.
A Momentum Integral Method to Predict the Frictional Torque of a Rotating Disc with Protruding Bolts.
ASME international gas turbine & aero engine conference paper 98-GT-138.

Geis, T., Ebner, J., Kim, S. and Wittig, S., 2001.
Flow Structures Inside a Rotor-Stator Cavity.
International Journal of Rotating Machinery, Vol. 7, Pt. 4, pp.285-300.

Goldstein, S., 1935.
On the Resistance to the Rotation of a Disc Immersed in a Fluid.
Proceedings of the Cambridge Philosophic, Vol. 31, Pt. 2, pp 232-241.

Gregory, N., Stuart, J. T. and Walker, W. S., 1955.
On the Stability of Three Dimensional Boundary Layers with Application to the Flow due to a Rotating Disc.
Philosophical Transactions of the Royal Society, A248, 155-199.

Haynes and Owen, J 1975.
Heat Transfer from a Shrouded Disc System with a Radial Outflow of Coolant.
Journal of Engineering for Power, Transactions of the ASME. Vol. 97, Issue 1, pp.28-35.

International Organization for Standardization (ISO).
Guide to the expression of uncertainty in measurement.
ISBN 92-67-01075-1, 1993.

International Organization for Standardization (ISO).
Measurement of fluid flow by means of pressure differential devices inserted in circular cross-section conduits running full - Part 1: General principles and requirements.
ISO 5167-1:2003(E), 2nd edition, March 2003.

von Kármán, T., 1921.
Technical Memorandum on Laminar and Turbulent Friction.
National advisory committee for aeronautics, Report No. 1092.

Kistler, A. L. and Tan, F. C., 1967.
Some Properties of Turbulent Separated Flows
The Physics of Fluids, Vol. 10, Issue 9, Pt.2.

Kurokawa, J., Toyokura, T., Shinjo, M. and Matsuo, K., 1978.
Roughness effects on the flow along an enclosed rotating disc.
Bulletin of the JSME. Vol. 21, pp.1725-1732.

Launder, B., Poncet, S. and Serre, E., 2010.
Laminar, Transitional, and Turbulent Flows in Rotor-Stator Cavities.
Annual Review of Fluid Mechanics 2010 42:229-48.

Marks, K. 2007.
Qantas celebrates 60 years of the 'Kangaroo Route'.
The Independent, 30th November 2007 p.34.

Miles, A. L., 2008.
Progress Report on Turbine Disc Bolt Windage Experimental Work.
Thermo-Fluid Mechanics Research Centre, University of Sussex, Report No. 08/TFMRC/TR277.

Millward, J. A. and Edwards, M. F., 1994.
Windage Heating of Air Passing Through Labyrinth Seals.
ASME international gas turbine & aero engine conference paper, 94-GT-56.

Millward, J. A. and Robinson, P. H., 1989.
Experimental Investigation into the Effects of Rotating and Static Bolts on Both Windage Heating and Local Heat Transfer Coefficients in a Rotor-Stator Cavity.
Gas turbine and aeroengine congress and exposition paper, 89-GT-196.

Moghaddam, E. R., Coren, D., Long, C. A. and Sayma, A., 2011.
A Numerical Investigation of Moment Coefficient and Flow Structure in a Rotor-Stator Cavity with Rotor Mounted Bolts.
Proceedings of ASME Turbo Expo 2011 conference paper, GT2011-45588.

Nece, R. E. and Daily, J. W., 1960.
Roughness Effects on Frictional Resistance of Enclosed Rotating Discs.
Journal of basic engineering, pp. 553 – 562.

Owen, J. M., 1987.
An Approximate Solution for the Flow between a Rotating and a Stationary Disc.
Thermo-Fluid Mechanics Research Centre, University of Sussex, Report 86/TFMRC/86b.

Owen, J. M. and Rogers, R. H., 1989.
Flow and Heat Transfer in Rotating Disc Systems, Volume 1: Rotor-Stator Systems.
Research Studies Press, ISBN: 0-86380-090-4.

Payne, D., 2011.

PIV Studies – Flow around bolts and cylinders.

Department of Engineering and Design, University of Sussex, M. Eng individual project report.

Picha, K. G. and Eckert, E. R. G., 1958.

Study of the Air Flow between Coaxial Discs Rotating with Arbitrary Velocities in an Open or Enclosed Space.

Proc. 3rd U.S. Nat. Congr. Appl. Mech., American Society for Mechanical Engineering, June 1958, pp.791-797.

Poncet, S., Chauve, M. and Schiestel, R., 2005.

Batchelor Versus Stewartson Flow Structures in a Rotor-Stator Cavity with Throughflow.

Physics of Fluids, Vol. 17, Issue 7.

Rogers, G. F. C. and Mayhew, Y. R., 1995.

Thermodynamic and Transport Properties of Fluids.

5th Edition, Blackwell Publishers Ltd.

Roshko, A., 1955.

Some Measurements of Flow in a Rectangular Cutout.

National advisory committee for aeronautics, Report No. 3488.

Schlicting, H., 1979.

Boundary Layer Theory.

4th Edition, McGraw Hill.

Schultz-Grunow, F., 1935.

The Frictional Resistance of Rotating Discs in Housings.

ZAMM – Journal of applied mathematics and mechanics, Vol. 15, Part 4, pp. 191-204.

Soong, C., Wu, C., Liu, T. and Liu, T., 2003.
Flow Structure Between Two Co-Axial Discs Rotating Independently.
Experimental Thermal and Fluid Science, Vol. 27, Issue 3, pp295-311.

Stewartson, K., 1952.
On the Flow between Two Rotating Coaxial Discs.
Proc. Camb. Phil. Soc., Vol. 49, pp.333-341.

Taniguchi, S., Sakamoto, H. and Arie, M., 1981.
Flow Around Circular Cylinders of Finite Height Placed Vertically in Turbulent Boundary Layers.
Bulleting of the JSME, Vol. 24, No. 187.

Taniguchi, S., Sakamoto, H. and Arie, M., 1982.
Interference between Two Circular Cylinders of Finite Height Vertically Immersed in a Turbulent Boundary Layer.
Journal of Fluids Engineering, Vol. 104, Issue 4, pp.529-536.

Theodorsen, T. and Regier, A., 1944.
Experiments on Drag of Revolving Discs, Cylinders and Streamlined Rods at High Speeds.
National advisory committee for aeronautics, Report No.793.

Zimmerman, H., Firsching, A., Dibelius, G. H., and Ziemann, M., 1986.
Friction Losses and Flow Distribution for Rotating Discs with Shielded and Protruding Bolts.
ASME international gas turbine conference paper 86-GT-158.

Appendices

Appendix A – Scanivalve measurement positions

DSA 5174

TFMRC label	Channel no.	Position on rig
00016	1	Casing inlet test side
00017	2	Cavity test side r = 232 mm
00018	3	Cavity test side r = 210 mm
00019	4	Cavity test side r = 168 mm
00020	5	Cavity test side r = 148 mm
00021	6	Cavity test side r = 125 mm
00022	7	Cavity test side r = 100 mm
00023	8	Cavity test side r = 76 mm
00024	9	Cavity test side r = -76 mm
00025	10	Cavity test side r = -100 mm
00026	11	Cavity test side r = -125 mm
00027	12	Cavity test side r = -148 mm
00028	13	Cavity balance side r = 76
00029	14	Cavity balance side r = 148
n/a	15	UNUSED
n/a	16	UNUSED

DSA 5176

TFMRC label	Channel no.	Position on rig
00030	1	Inlet orifice test side (upstream)
00031	2	Inlet orifice balance side (upstream)
00032	3	Outlet orifice test side (upstream)
00033	4	Outlet orifice balance side (upstream)
n/a	5	Atlas supply pressure
n/a	6	UNUSED
n/a	7	UNUSED
n/a	8	UNUSED

Appendix B – AutoCAD drawings

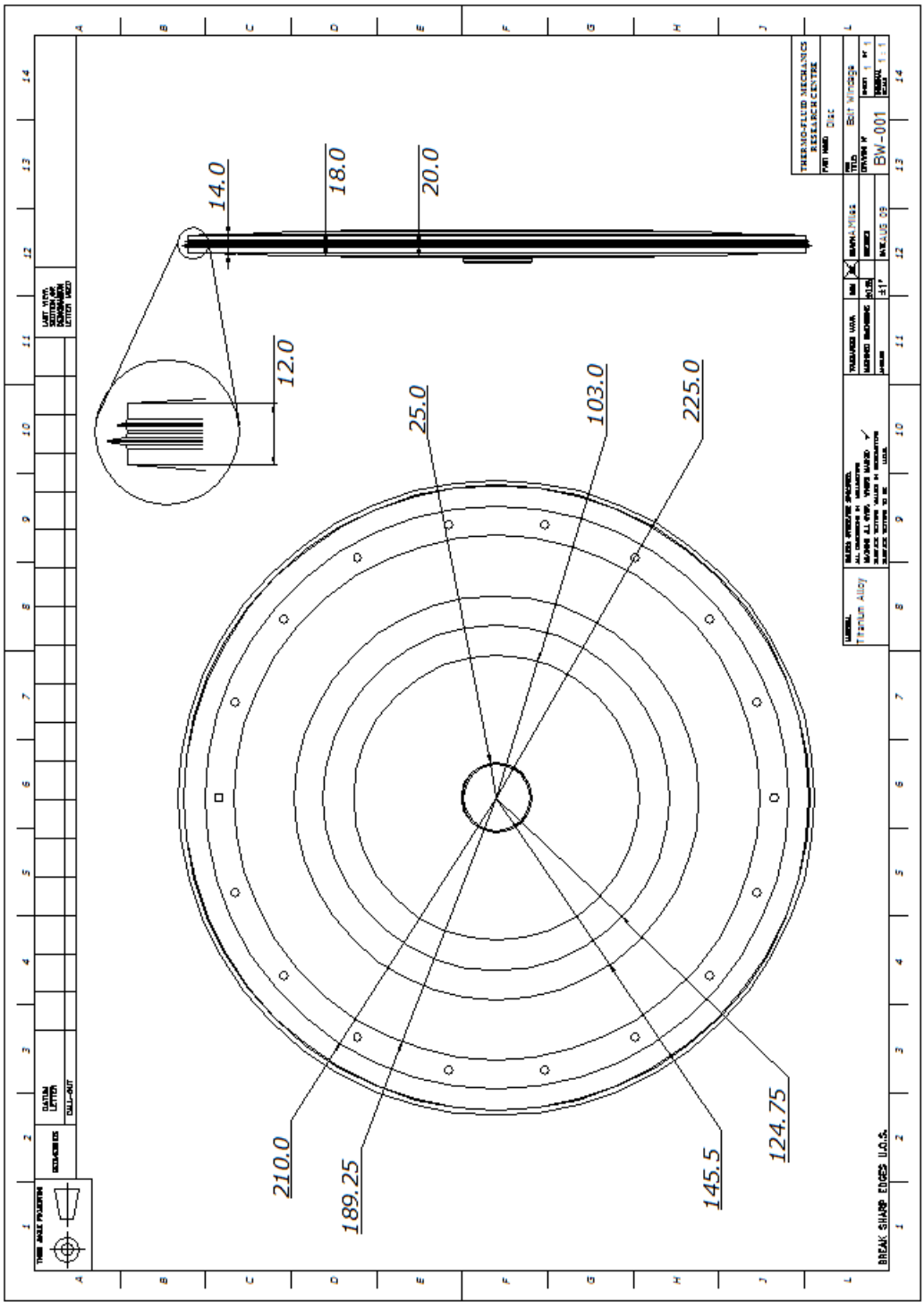

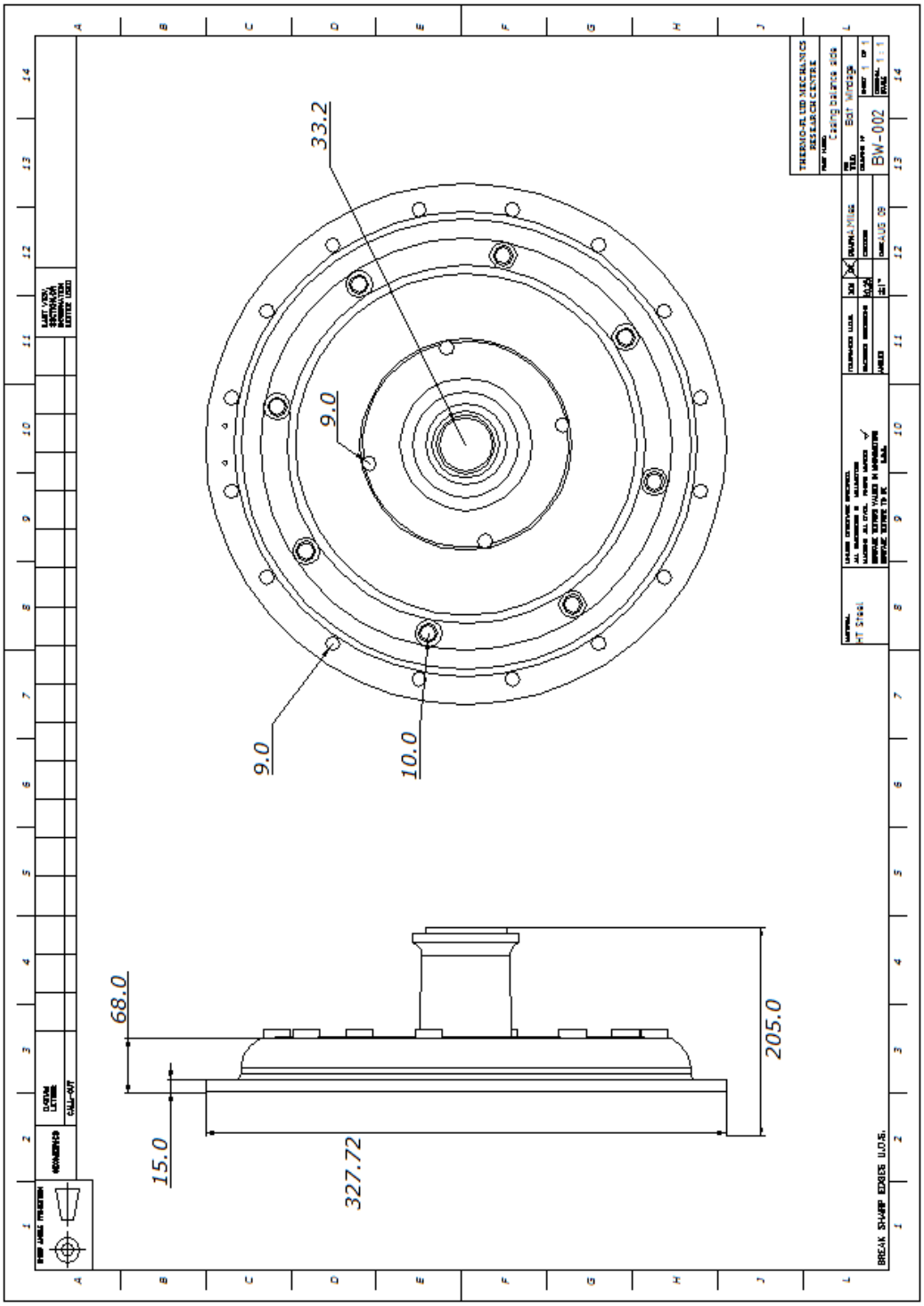
33.2
9.0
9.0
10.0
68.0
15.0
327.72
205.0
BW-002
Bell Mouth
Casing balance pipe
BREAK SHARP EDGES U.O.S.

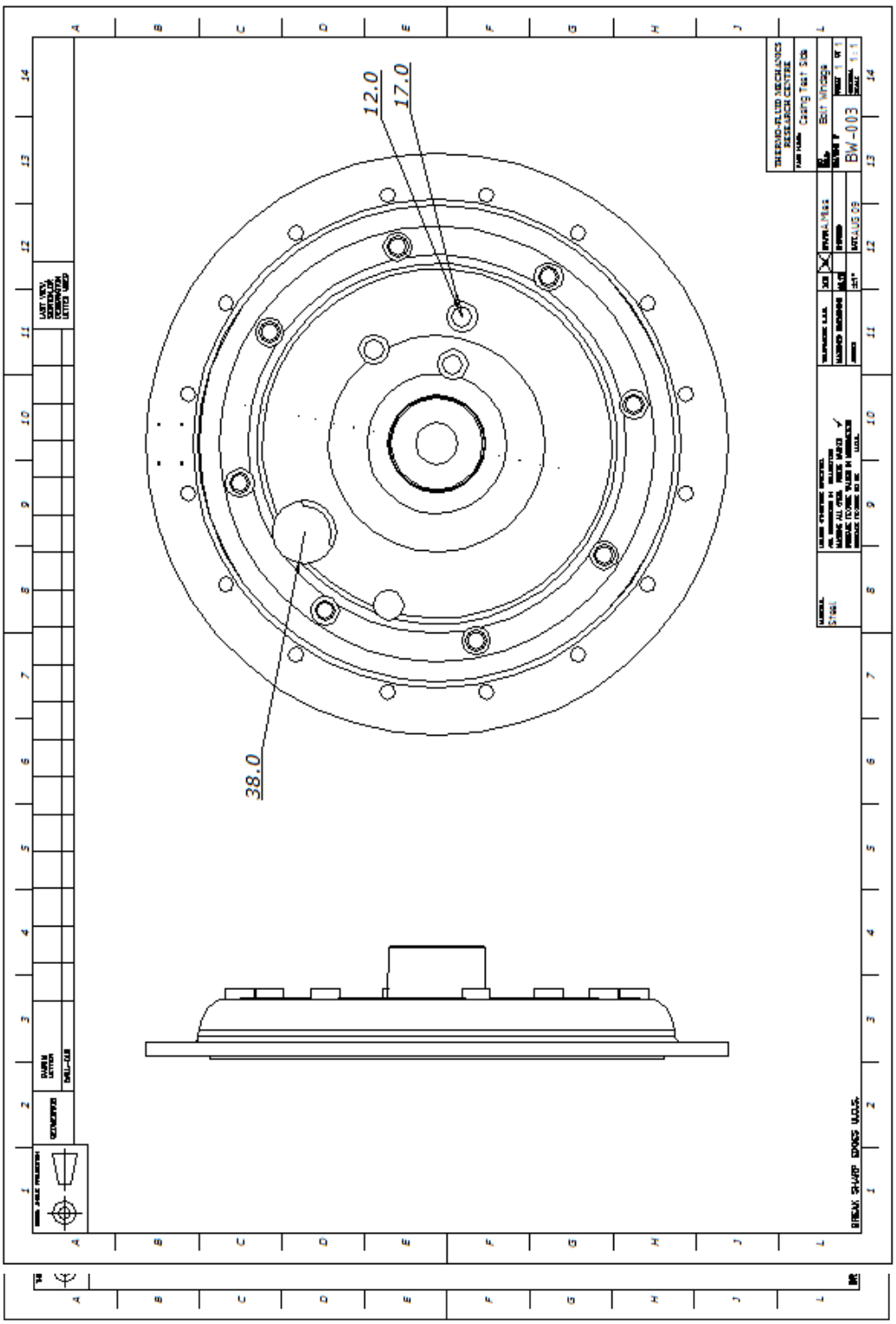
12.0
17.0
38.0
BW-003

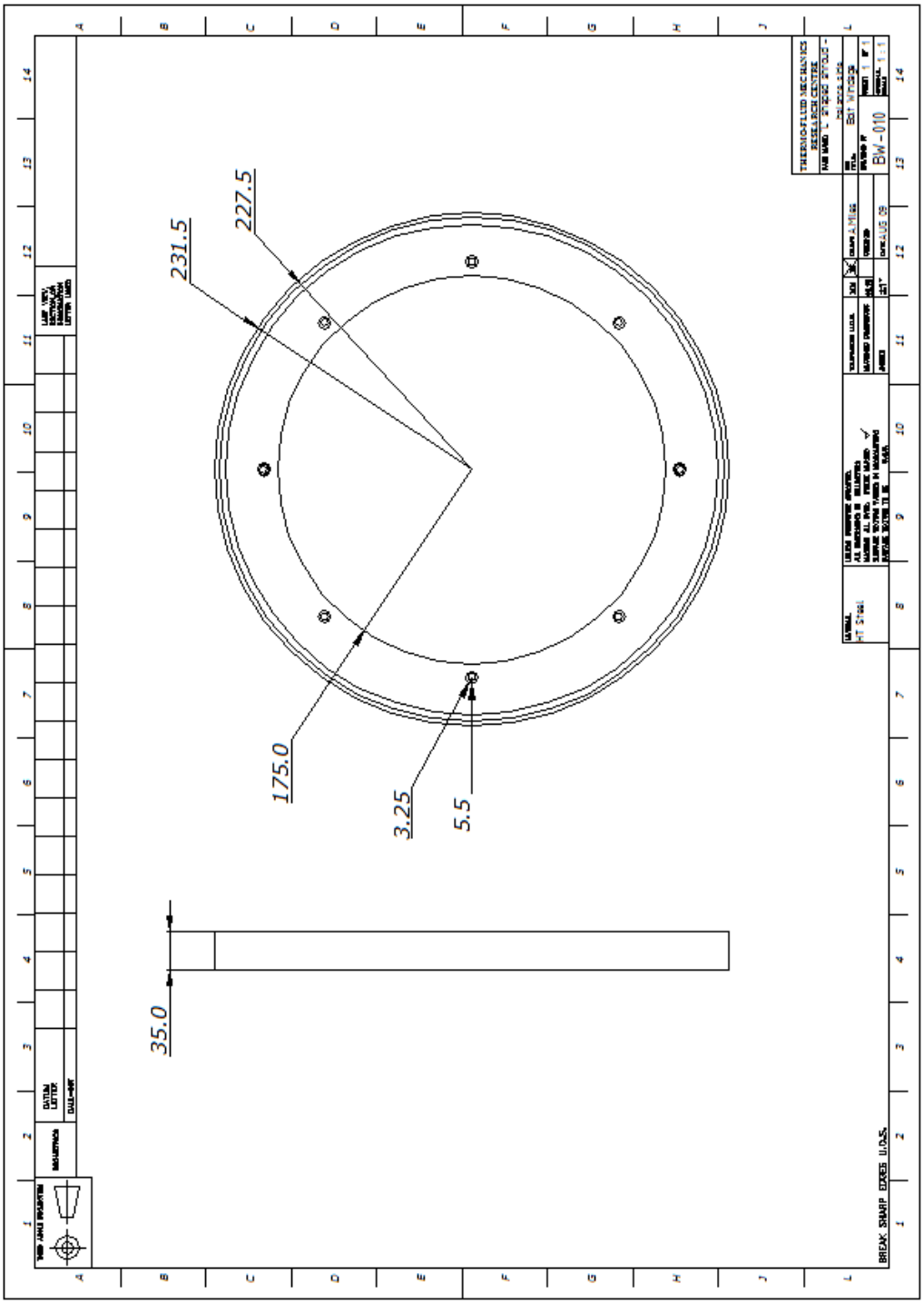
227.5
231.5
175.0
3.25
5.5
35.0
BW-010
BREAK SHARP EDGES U.O.S.

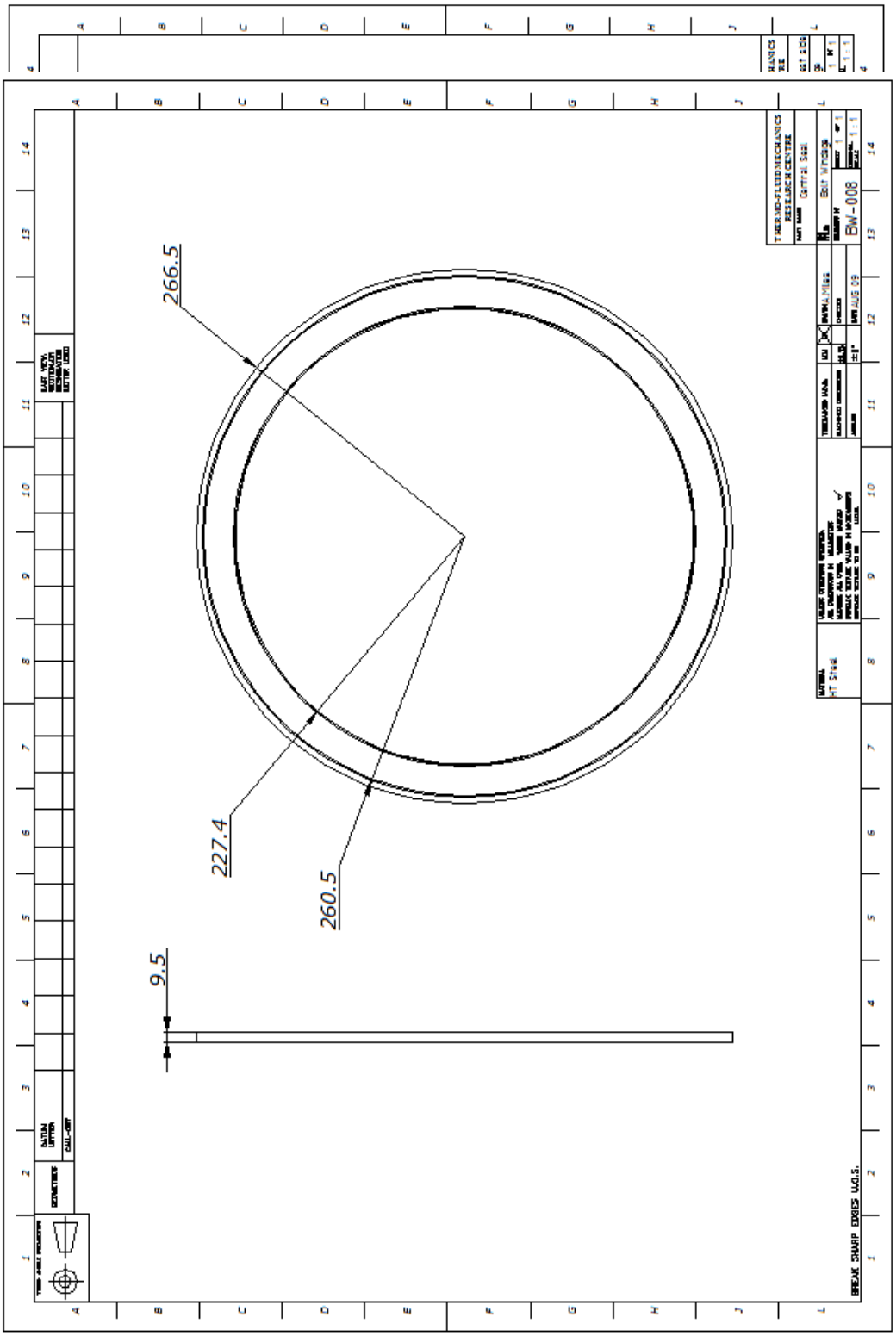
266.5
227.4
260.5
9.5
BW-008
Bell Nozzle
Central Slot
BREAK SHARP EDGES
DIMENSIONS

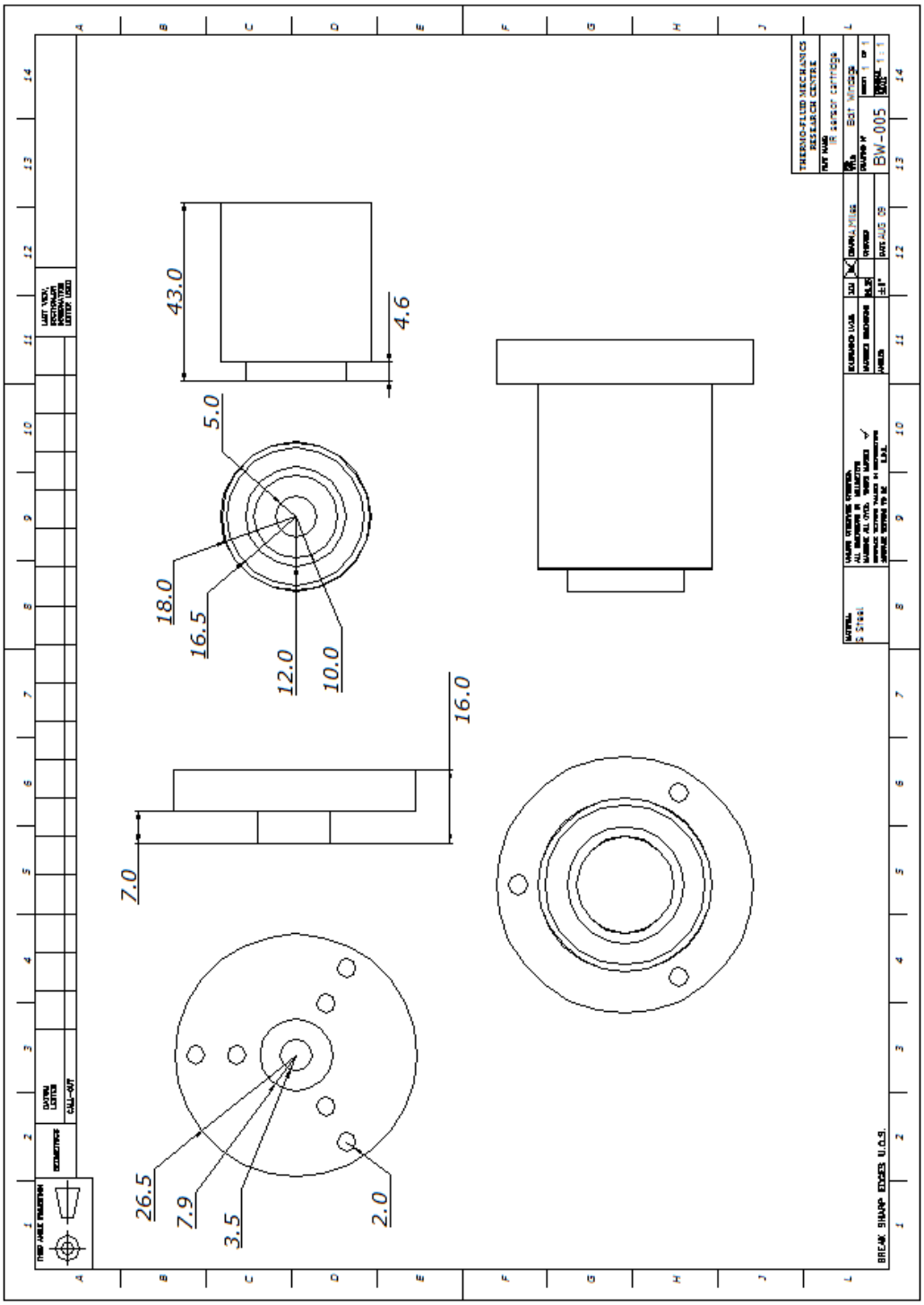
43.0
4.6
5.0
18.0
16.5
12.0
10.0
16.0
7.0
26.5
7.9
3.5
2.0
BW-005
THERMO-FLUID MECHANICS RESEARCH CENTER
BREAK SHARP EDGES
DRAWING
DRAWN
CHECKED
MATERIAL
DATE

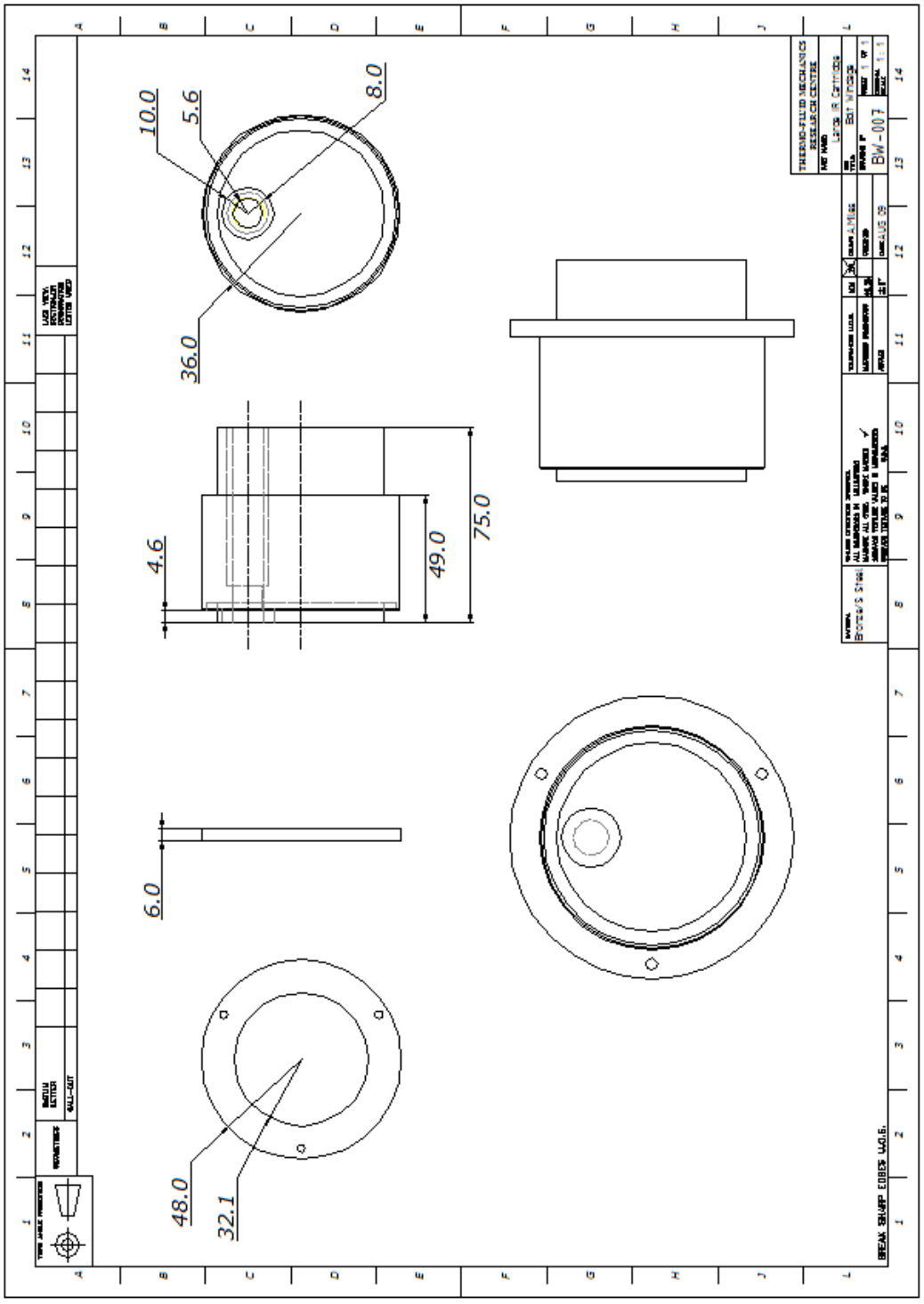
10.0
5.6
8.0
36.0
4.6
49.0
75.0
6.0
48.0
32.1
BREAK SHARP EDGES M.O.S.
BW-007

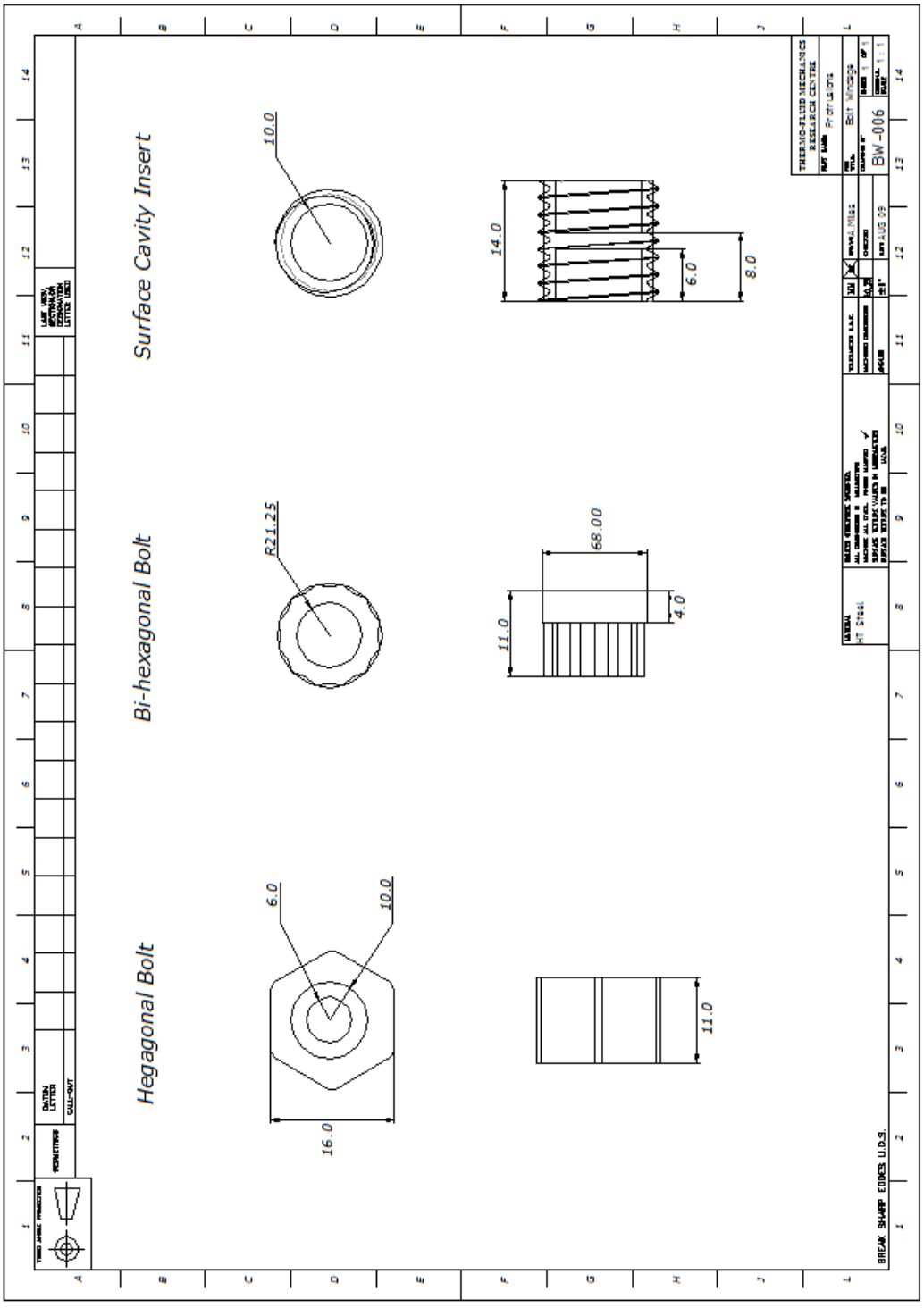
Surface Cavity Insert
Bi-hexagonal Bolt
Hegagonal Bolt
10.0
R21.25
6.0
10.0
16.0
14.0
6.0
8.0
68.00
11.0
4.0
11.0
BW-006
Bolt Wedge
Promotions
BREAK SHARP EDGES U.O.S.

Appendix C – Test Conditions

Plain disc

Bolt Windage Test Matrix - *Plain Disc*

Target *m*	Target casing pressure	Target N	Measured ω	Measured *m*	Measured Dimensionless values			Measured M	Corrected M	Casing pressure
kg/s	bar (abs)	rev/min	rad/sec	kg/s	Re_ϕ (x10^7)	C_ω (x10^5)	λ_T	N m	N m	bar (abs)
0.120	2.000	2500.000	261.900	0.126	0.171	0.310	0.320	0.910	0.710	1.970
		3000.000	317.600	0.127	0.211	0.314	0.274	1.110	0.870	2.010
		3900.000	407.900	0.122	0.271	0.300	0.214	1.490	1.210	2.040
		5900.000	606.700	0.122	0.394	0.296	0.157	2.490	2.100	2.040
	3.000	3900.000	409.400	0.123	0.392	0.302	0.160	1.740	1.460	2.980
		5900.000	617.100	0.124	0.578	0.299	0.116	3.150	2.760	3.020
		8700.000	915.700	0.123	0.802	0.284	0.085	5.780	5.170	3.040
	4.000	10100.000	1057.400	0.123	1.167	0.286	0.063	8.610	7.890	4.040

Target *m*	Target casing pressure	Target N	Measured ω	Measured *m*	Measured Dimensionless values			Measured M	Corrected M	Casing pressure
kg/s	bar (abs)	rev/min	rad/sec	kg/s	Re_ϕ (x10^7)	C_ω (x10^5)	λ_T	N m	N m	bar (abs)
0.400	3.000	10100.000	1061.000	0.413	1.035	0.992	0.242	9.970	9.250	3.110
	5.000	2000.000	207.500	0.414	0.348	1.029	0.601	1.280	1.100	5.010
		3900.000	415.400	0.419	0.680	1.029	0.352	3.120	2.840	4.990
		5900.000	628.100	0.419	1.012	1.018	0.253	5.790	5.390	5.000
		7250.000	768.300	0.419	1.223	1.011	0.216	8.010	7.510	5.030
		8700.000	912.200	0.418	1.420	1.000	0.190	10.510	9.910	5.050
		10100.000	1060.600	0.418	1.610	0.986	0.169	13.560	12.840	5.090

Stator Bolts

Bolt Windage Test Matrix - *3 Bolts on Stator*

Target $\dot{m}$	Target casing pressure	Target N	Measured ω	Measured $\dot{m}$	Measured Dimensionless values			Measured M	Corrected M	Casing pressure
kg/s	bar (abs)	rev/min	rad/sec	kg/s	Re_ϕ (x10^7)	C_{w1} (x10^5)	λ_T	N m	N m	bar (abs)
0.120	2.000	3900.000	406.400	0.115	0.270	0.280	0.200	1.720	1.560	2.070
	3.000	5400.000	563.100	0.117	0.520	0.280	0.119	3.020	2.840	2.960
		8600.000	899.600	0.117	0.760	0.260	0.081	6.480	6.220	2.960
	4.000	10100.000	1058.400	0.113	1.090	0.250	0.059	9.270	8.930	3.970

Target $\dot{m}$	Target casing pressure	Target N	Measured ω	Measured $\dot{m}$	Measured Dimensionless values			Measured M	Corrected M	Casing pressure
kg/s	bar (abs)	rev/min	rad/sec	kg/s	Re_ϕ (x10^7)	C_{w1} (x10^5)	λ_T	N m	N m	bar (abs)
0.400	5.000	2000.000	208.700	0.414	0.350	1.020	0.593	1.650	1.480	5.160
		3900.000	410.200	0.415	0.630	0.990	0.360	3.480	3.320	4.850
		5900.000	617.700	0.413	0.960	0.990	0.257	6.040	5.860	5.030
		8600.000	899.500	0.403	1.390	0.920	0.178	11.060	10.810	5.080
		10100.000	1057.900	0.404	1.590	0.900	0.156	14.340	13.990	5.140

Bolt Windage Test Matrix - *9 Bolts on Stator*

Target *m*	Target casing pressure	Target N	Measured ω	Measured *m*	Measured Dimensionless values			Measured M	Corrected M	Casing pressure
kg/s	bar (abs)	rev/min	rad/sec	kg/s	Re_ϕ (x10^7)	C_ω (x10^5)	λ_T	N m	N m	bar (abs)
0.120	2.000	3900.000	410.000	0.125	0.267	0.301	0.217	1.460	0.590	2.030
		5900.000	617.500	0.124	0.395	0.298	0.157	2.500	1.690	2.050
	3.000	5900.000	617.500	0.122	0.553	0.292	0.118	3.170	2.360	2.940
		8600.000	899.800	0.122	0.756	0.280	0.088	5.790	5.000	2.970
	4.000	10100.000	1058.500	0.110	1.090	0.260	0.061	9.260	8.360	4.060

Target *m*	Target casing pressure	Target N	Measured ω	Measured *m*	Measured Dimensionless values			Measured M	Corrected M	Casing pressure
kg/s	bar (abs)	rev/min	rad/sec	kg/s	Re_ϕ (x10^7)	C_ω (x10^5)	λ_T	N m	N m	bar (abs)
0.400	3.000	10100.000	1058.500	0.394	1.030	0.944	0.232	9.990	9.080	3.160
	5.000	2000.000	208.700	0.419	0.328	1.025	0.628	1.280	0.470	4.830
		3900.000	410.200	0.418	0.640	1.016	0.365	3.040	2.180	4.820
		5900.000	617.500	0.417	0.951	1.007	0.263	5.750	4.930	4.830
		8600.000	899.800	0.426	1.409	1.016	0.194	10.850	10.050	5.070

Bolt Windage Test Matrix - *18 Bolts on Stator*

Target *m*	Target casing pressure	Target N	Measured ω	Measured *m*	Measured Dimensionless values			Measured M	Corrected M	Casing pressure
kg/s	bar (abs)	rev/min	rad/sec	kg/s	Re_ϕ (x10^7)	C_ω (x10^5)	λ_τ	N m	N m	bar (abs)
0.120	2.000	2500.000	262.800	0.123	0.166	0.297	0.314	1.030	0.190	1.990
		3900.000	410.100	0.125	0.271	0.301	0.215	1.520	0.650	2.090
	3.000	3900.000	407.100	0.126	0.383	0.311	0.168	1.810	0.940	2.960
		8600.000	899.500	0.122	0.790	0.279	0.085	6.070	5.270	3.090
	4.000	10100.000	1058.600	0.112	1.127	0.250	0.057	9.620	8.720	4.070

Target *m*	Target casing pressure	Target N	Measured ω	Measured *m*	Measured Dimensionless values			Measured M	Corrected M	Casing pressure
kg/s	bar (abs)	rev/min	rad/sec	kg/s	Re_ϕ (x10^7)	C_ω (x10^5)	λ_τ	N m	N m	bar (abs)
0.400	3.000	10100.000	1058.200	0.399	0.981	0.941	0.240	9.880	8.970	3.090
	5.000	2000.000	209.400	0.423	0.345	1.042	0.613	1.550	0.730	5.000
		3900.000	400.300	0.422	0.652	1.032	0.365	3.230	2.370	5.010
		5900.000	617.600	0.422	0.988	1.020	0.259	5.960	5.150	5.020
		8600.000	899.800	0.413	1.364	0.981	0.192	11.080	10.290	4.980

Hexagonal Rotor Bolts

Bolt Windage Test Matrix - *3 x 10 mm Bolts on Rotor*

Target *m*	Target casing pressure	Target N	Measured ω	Measured *m*	Measured Dimensionless values			Measured M	Corrected M	Casing pressure
kg/s	bar (abs)	rev/min	rad/sec	kg/s	Re_ϕ ($x10^7$)	C_{ω} ($x10^5$)	λ_T	N m	N m	bar (abs)
0.120	2.000	3900.000	408.900	0.120	0.274	0.300	0.212	3.240	2.380	1.990
	3.000	8800.000	924.900	0.120	0.802	0.279	0.084	8.920	8.110	3.020
	4.000	10100.000	1060.900	0.118	1.077	0.266	0.063	12.020	11.110	3.940

Target *m*	Target casing pressure	Target N	Measured ω	Measured *m*	Measured Dimensionless values			Measured M	Corrected M	Casing pressure
kg/s	bar (abs)	rev/min	rad/sec	kg/s	Re_ϕ ($x10^7$)	C_{ω} ($x10^5$)	λ_T	N m	N m	bar (abs)
0.400	5.000	3900.000	411.000	0.415	0.715	1.043	0.343	5.940	5.070	5.060
		5900.000	620.200	0.413	1.048	1.024	0.248	10.380	9.560	5.070
		8600.000	905.200	0.414	1.434	0.996	0.188	17.630	16.840	5.100

Bolt Windage Test Matrix - *3 x 13 mm Bolts on Rotor*

Target *m*	Target casing pressure	Target N	Measured ω	Measured *m*	Measured Dimensionless values			Measured M	Corrected M	Casing pressure
kg/s	bar (abs)	rev/min	rad/sec	kg/s	Re_ϕ (x10^7)	C_ω (x10^5)	λ_T	N m	N m	bar (abs)
0.120	2.000	3900.000	409.700	0.121	0.282	0.301	0.208	3.210	2.350	2.030
	3.000	8600.000	904.600	0.121	0.802	0.283	0.085	8.470	7.670	3.020
	4.000	10100.000	1061.700	0.119	1.117	0.268	0.062	11.950	11.030	4.020

Target *m*	Target casing pressure	Target N	Measured ω	Measured *m*	Measured Dimensionless values			Measured M	Corrected M	Casing pressure
kg/s	bar (abs)	rev/min	rad/sec	kg/s	Re_ϕ (x10^7)	C_ω (x10^5)	λ_T	N m	N m	bar (abs)
0.400	5.000	3900.000	408.400	0.412	0.725	1.043	0.339	5.790	4.920	5.100
		5900.000	620.300	0.416	1.085	1.036	0.244	10.390	9.580	5.170
		8600.000	905.300	0.415	1.491	1.004	0.183	17.780	16.980	5.230

Bolt Windage Test Matrix - *3 x 16 mm Bolts on Rotor*

Target *m*	Target casing pressure	Target N	Measured ω	Measured *m*	Measured Dimensionless values			Measured M	Corrected M	Casing pressure
kg/s	bar (abs)	rev/min	rad/sec	kg/s	Re_ϕ (x10^7)	C_ω (x10^5)	λ_τ	N m	N m	bar (abs)
0.120	2.000	3900.000	408.300	0.121	0.277	0.301	0.211	3.470	2.610	2.010
	3.000	8600.000	898.800	0.120	0.784	0.280	0.085	8.970	8.170	3.020
	4.000	10100.000	1055.600	0.116	1.093	0.259	0.061	12.660	11.740	4.040

Target *m*	Target casing pressure	Target N	Measured ω	Measured *m*	Measured Dimensionless values			Measured M	Corrected M	Casing pressure
kg/s	bar (abs)	rev/min	rad/sec	kg/s	Re_ϕ (x10^7)	C_ω (x10^5)	λ_τ	N m	N m	bar (abs)
0.400	5.000	3900.000	409.000	0.413	0.711	1.040	0.343	6.160	5.300	5.010
		5900.000	619.600	0.415	1.052	1.028	0.248	11.080	10.270	5.080
		8600.000	903.500	0.414	1.435	0.993	0.187	19.160	18.360	5.130

Bolt Windage Test Matrix - *9 x 10 mm Bolts on Rotor*

Target *m*	Target casing pressure	Target N	Measured ω	Measured *m*	Measured Dimensionless values			Measured M	Corrected M	Casing pressure
kg/s	bar (abs)	rev/min	rad/sec	kg/s	Re_ϕ (x10^7)	C_ω (x10^5)	λ_τ	N m	N m	bar (abs)
0.120	2.000	3900.000	404.000	0.122	0.274	0.301	0.213	4.010	3.150	2.050
	3.000	8800.000	927.200	0.120	0.775	0.274	0.084	10.900	10.100	3.050
	4.000	10100.000	1067.300	0.117	1.050	0.258	0.062	15.090	14.170	4.070

Target *m*	Target casing pressure	Target N	Measured ω	Measured *m*	Measured Dimensionless values			Measured M	Corrected M	Casing pressure
kg/s	bar (abs)	rev/min	rad/sec	kg/s	Re_ϕ (x10^7)	C_ω (x10^5)	λ_τ	N m	N m	bar (abs)
0.400	5.000	3900.000	405.400	0.403	0.686	1.005	0.341	7.900	7.030	5.060
		5900.000	616.500	0.403	1.015	0.991	0.246	13.430	12.620	5.100
		8800.000	927.300	0.403	1.411	0.956	0.182	23.400	22.590	5.150

Bolt Windage Test Matrix - *9 x 13 mm Bolts on Rotor*

Target *m*	Target casing pressure	Target N	Measured ω	Measured *m*	Measured Dimensionless values			Measured M	Corrected M	Casing pressure
kg/s	bar (abs)	rev/min	rad/sec	kg/s	Re_ϕ (x10^7)	C_ω (x10^5)	λ_T	N m	N m	bar (abs)
0.120	2.000	3900.000	410.900	0.123	0.278	0.304	0.213	4.270	3.400	2.040
	3.000	8800.000	916.000	0.125	0.802	0.286	0.086	11.300	10.500	3.150
	4.000	10100.000	1060.700	0.119	1.080	0.262	0.062	15.510	14.590	4.160

Target *m*	Target casing pressure	Target N	Measured ω	Measured *m*	Measured Dimensionless values			Measured M	Corrected M	Casing pressure
kg/s	bar (abs)	rev/min	rad/sec	kg/s	Re_ϕ (x10^7)	C_ω (x10^5)	λ_T	N m	N m	bar (abs)
0.400	5.000	3900.000	408.700	0.421	0.711	1.044	0.345	8.090	7.230	5.140
		5900.000	619.400	0.423	1.003	1.039	0.260	13.780	12.970	4.960
		8800.000	923.200	0.426	1.392	1.007	0.194	24.580	23.770	5.050

Bolt Windage Test Matrix - *9 x 16 mm Bolts on Rotor*

Target *m*	Target casing pressure	Target N	Measured ω	Measured *m*	Measured Dimensionless values			Measured M	Corrected M	Casing pressure
kg/s	bar (abs)	rev/min	rad/sec	kg/s	Re_ϕ (x10^7)	C_ω (x10^5)	λ_T	N m	N m	bar (abs)
0.120	2.000	3900.000	409.400	0.121	0.272	0.294	0.209	4.240	3.380	2.020
	3.000	8600.000	889.200	0.120	0.747	0.275	0.087	11.160	10.370	3.060
	4.000	10100.000	1060.000	0.113	1.040	0.244	0.059	15.940	15.020	4.160

Target *m*	Target casing pressure	Target N	Measured ω	Measured *m*	Measured Dimensionless values			Measured M	Corrected M	Casing pressure
kg/s	bar (abs)	rev/min	rad/sec	kg/s	Re_ϕ (x10^7)	C_ω (x10^5)	λ_T	N m	N m	bar (abs)
0.400	5.000	3900.000	411.200	0.403	0.683	1.004	0.342	8.920	8.060	4.950
		5900.000	619.400	0.404	0.994	0.987	0.249	15.100	14.280	4.990
		8800.000	919.300	0.404	1.338	0.947	0.188	25.790	24.990	5.010

Bolt Windage Test Matrix - *18 x 10 mm Bolts on Rotor*

Target *m*	Target casing pressure	Target N	Measured ω	Measured *m*	Measured Dimensionless values			Measured M	Corrected M	Casing pressure
kg/s	bar (abs)	rev/min	rad/sec	kg/s	Re_ϕ (x10^7)	C_ω (x10^5)	λ_T	N m	N m	bar (abs)
0.120	2.000	2500.000	265.600	0.125	0.177	0.312	0.313	3.270	2.420	1.970
		3900.000	410.800	0.125	0.268	0.308	0.222	4.550	3.680	1.970
	3.000	8600.000	903.500	0.119	0.716	0.268	0.088	11.930	11.140	2.920
	4.000	10100.000	1060.100	0.117	0.941	0.249	0.066	16.490	15.770	4.040

Target *m*	Target casing pressure	Target N	Measured ω	Measured *m*	Measured Dimensionless values			Measured M	Corrected M	Casing pressure
kg/s	bar (abs)	rev/min	rad/sec	kg/s	Re_ϕ (x10^7)	C_ω (x10^5)	λ_T	N m	N m	bar (abs)
0.400	5.000	2000.000	212.100	0.416	0.366	1.048	0.588	4.610	3.790	5.010
		3900.000	408.700	0.416	0.676	1.005	0.345	9.070	8.790	5.320
		5900.000	618.500	0.416	1.007	1.014	0.253	16.680	15.870	5.050
		8800.000	920.800	0.411	1.341	0.966	0.192	27.890	27.090	5.010

Bolt Windage Test Matrix - *18 x 13 mm Bolts on Rotor*

Target *m*	Target casing pressure	Target N	Measured ω	Measured *m*	Measured Dimensionless values			Measured M	Corrected M	Casing pressure
kg/s	bar (abs)	rev/min	rad/sec	kg/s	Re_ϕ (x10^7)	C_ω (x10^5)	λ_T	N m	N m	bar (abs)
0.120	2.000	2500.000	262.200	0.124	0.179	0.309	0.307	3.490	2.650	2.020
		3900.000	408.200	0.125	0.272	0.310	0.221	4.860	3.990	2.010
	3.000	8600.000	901.600	0.123	0.751	0.281	0.089	12.630	11.830	3.060
	4.000	10100.000	1058.900	0.118	0.957	0.255	0.066	17.030	16.320	4.080

Target *m*	Target casing pressure	Target N	Measured ω	Measured *m*	Measured Dimensionless values			Measured M	Corrected M	Casing pressure
kg/s	bar (abs)	rev/min	rad/sec	kg/s	Re_ϕ (x10^7)	C_ω (x10^5)	λ_T	N m	N m	bar (abs)
0.400	5.000	2000.000	209.500	0.421	0.355	1.059	0.609	4.540	3.730	4.880
		3000.000	408.500	0.419	0.674	1.021	0.352	8.640	8.360	5.200
		5900.000	618.700	0.419	0.987	1.023	0.260	16.740	15.930	4.910
		8800.000	923.100	0.420	1.332	0.978	0.195	29.000	28.190	4.970

Bolt Windage Test Matrix - *18 x 16 mm Bolts on Rotor*

Target *m*	Target casing pressure	Target N	Measured ω	Measured *m*	Measured Dimensionless values			Measured M	Corrected M	Casing pressure
kg/s	bar (abs)	rev/min	rad/sec	kg/s	Re_ϕ (x10^7)	C_ω (x10^5)	λ_τ	N m	N m	bar (abs)
0.120	2.000	2500.000	264.500	0.125	0.177	0.311	0.312	3.590	2.740	1.990
		3900.000	411.000	0.124	0.272	0.307	0.219	4.980	4.110	2.010
	3.000	8600.000	902.500	0.119	0.716	0.268	0.088	13.050	12.250	2.990
	4.000	10100.000	1060.100	0.115	0.933	0.242	0.064	18.130	17.410	4.080

Target *m*	Target casing pressure	Target N	Measured ω	Measured *m*	Measured Dimensionless values			Measured M	Corrected M	Casing pressure
kg/s	bar (abs)	rev/min	rad/sec	kg/s	Re_ϕ (x10^7)	C_ω (x10^5)	λ_τ	N m	N m	bar (abs)
0.400	5.000	2000.000	211.900	0.410	0.362	1.022	0.579	5.170	4.350	5.070
		3900.000	409.500	0.415	0.668	1.017	0.353	10.280	10.010	5.060
		5900.000	618.800	0.412	0.999	0.994	0.250	18.320	17.510	5.130
		8600.000	889.500	0.412	1.323	0.963	0.193	29.860	29.070	5.100

Extra 18x16 mm Hexagonal Rotor Bolts

λ_T = 0.09				
Measured ω	Measured Dimensionless values			Casing pressure
rad/sec	Re_ϕ	C_ω	λ_T	bar (abs)
334.9	4688786	19957	0.092	4.7
556.1	5138585	21510	0.092	2.87
582.8	5879126	23696	0.091	3.19
674.8	6537055	25835	0.091	3.15
702	7217075	27847	0.091	3.45
764.5	7784233	29840	0.092	3.5
789.5	8614309	32230	0.091	3.82
817.9	9949833	36278	0.091	4.36
876	10383639	37680	0.092	4.35
902	11207820	39889	0.091	4.67
926.7	12489847	43622	0.092	5.17

λ_T = 0.18				
Measured ω	Measured Dimensionless values			Casing pressure
rad/sec	Re_ϕ	C_ω	λ_T	bar (abs)
327.7	4019659	35297	0.184	3.71
340.9	4807784	40665	0.184	4.29
431.8	5464368	45156	0.184	3.89
447.2	6319376	50615	0.184	4.39
538.4	6915756	53595	0.181	4.05
557.3	7611168	58342	0.182	4.35
639	8330881	64966	0.189	4.22
620.3	8407360	63347	0.183	4.39
691.4	9332065	68603	0.182	4.44
706.9	10091780	72887	0.182	4.75
724	11273496	79786	0.182	5.21
834.9	12756871	88296	0.183	5.28

$\lambda_T = 0.26$

Measured ω	Measured Dimensionless values			Casing pressure
rad/sec	Re_ϕ	C_ω	λ_T	bar (abs)
263.7	3590360	46357	0.264	4.17
312.4	3938546	50053	0.265	3.85
361.1	4392591	54432	0.264	3.71
372.5	5096725	61360	0.264	4.17
382.4	5750996	67541	0.264	4.59
432.8	6214806	71783	0.264	4.41
438.5	6616403	75553	0.264	4.64
449.2	7351127	82113	0.264	5.05
512	8541725	92112	0.262	5.21
500.5	7742613	85185	0.263	4.81
562.9	9452160	99840	0.262	5.3
621.2	9938673	103361	0.261	5.12

$\lambda_T = 0.22$

Measured ω	Measured Dimensionless values			Casing pressure
rad/sec	Re_ϕ	C_ω	λ_T	bar (abs)
271.7	3945076	42320	0.224	4.31
277.3	4413164	46412	0.224	4.73
297.2	4587797	47751	0.224	4.59
370.6	5161831	52373	0.223	4.17
384.2	5817250	58050	0.225	4.55
392.9	6494909	63481	0.225	4.98
437.7	6771804	65347	0.224	4.69
510.9	7103625	67239	0.222	4.3
521.4	7827844	72744	0.222	4.65
561.9	7935594	73729	0.223	4.41
577.4	9037206	82041	0.223	4.91
590.8	9933685	88406	0.223	5.31
693.6	10842346	94211	0.222	5.04
711	11801995	100635	0.221	5.43

Bi-hexagonal Rotor Bolts

Bolt Windage Test Matrix - 3 *x* 13 *mm Bi-Hex Bolts on Rotor*

Target *m*	Target casing pressure	Target N	Measured ω	Measured *m*	Measured Dimensionless values			Measured M	Corrected M	Casing pressure
kg/s	bar (abs)	rev/min	rad/sec	kg/s	Re_ϕ (x10^7)	C_ω (x10^5)	λ_T	N m	N m	bar (abs)
0.120	2.000	3900.000	412.600	0.124	0.272	0.304	0.216	3.190	2.320	2.020
	3.000	8600.000	902.100	0.120	0.780	0.277	0.085	8.400	7.600	3.020
	4.000	10100.000	1053.500	0.117	1.100	0.264	0.061	11.740	10.830	4.040

Target *m*	Target casing pressure	Target N	Measured ω	Measured *m*	Measured Dimensionless values			Measured M	Corrected M	Casing pressure
kg/s	bar (abs)	rev/min	rad/sec	kg/s	Re_ϕ (x10^7)	C_ω (x10^5)	λ_T	N m	N m	bar (abs)
0.400	5.000	3900.000	413.700	0.418	0.708	1.042	0.345	5.820	4.960	5.080
		5900.000	621.900	0.419	1.036	1.032	0.252	9.900	9.090	5.100
		8600.000	902.900	0.418	1.432	0.996	0.188	16.670	15.880	5.180

Bolt Windage Test Matrix - 9 *x 13 mm Bi-Hex Bolts on Rotor*

Target *m*	Target casing pressure	Target N	Measured ω	Measured *m*	Measured Dimensionless values			Measured M	Corrected M	Casing pressure
kg/s	bar (abs)	rev/min	rad/sec	kg/s	Re_ϕ (x10^7)	C_ω (x10^5)	λ_T	N m	N m	bar (abs)
0.120	2.000	3900.000	415.000	0.125	0.280	0.304	0.211	3.940	3.080	2.080
	3.000	8800.000	923.000	0.124	0.773	0.283	0.087	10.680	9.880	3.050
	4.000	10100.000	1057.300	0.118	1.038	0.262	0.064	14.400	13.490	4.020

Target *m*	Target casing pressure	Target N	Measured ω	Measured *m*	Measured Dimensionless values			Measured M	Corrected M	Casing pressure
kg/s	bar (abs)	rev/min	rad/sec	kg/s	Re_ϕ (x10^7)	C_ω (x10^5)	λ_T	N m	N m	bar (abs)
0.400	5.000	3900.000	412.100	0.422	0.701	1.049	0.350	7.850	6.980	5.080
		5900.000	621.700	0.421	1.015	1.032	0.256	13.580	12.760	5.060
		8800.000	921.700	0.418	1.396	0.987	0.190	22.860	22.050	5.140

Bolt Windage Test Matrix - *18 x 13 mm Bi-Hex Bolts on Rotor*

Target *m*	Target casing pressure	Target N	Measured ω	Measured *m*	Measured Dimensionless values			Measured M	Corrected M	Casing pressure
kg/s	bar (abs)	rev/min	rad/sec	kg/s	Re_ϕ (x10^7)	C_ω (x10^5)	λ_τ	N m	N m	bar (abs)
0.120	2.000	2500.000	265.500	0.124	0.181	0.308	0.304	3.130	2.280	2.040
		3900.000	412.100	0.124	0.275	0.303	0.214	4.390	3.530	2.040
	3.000	8600.000	901.900	0.120	0.725	0.272	0.088	11.550	10.760	3.020
	4.000	10100.000	1058.900	0.122	0.972	0.263	0.068	16.400	15.680	4.020

Target *m*	Target casing pressure	Target N	Measured ω	Measured *m*	Measured Dimensionless values			Measured M	Corrected M	Casing pressure
kg/s	bar (abs)	rev/min	rad/sec	kg/s	Re_ϕ (x10^7)	C_ω (x10^5)	λ_τ	N m	N m	bar (abs)
0.400	5.000	2000.000	210.600	0.423	0.345	1.052	0.619	3.770	2.950	4.880
		3900.000	407.700	0.416	0.680	1.027	0.351	8.750	8.480	5.090
		5900.000	613.900	0.423	0.952	1.021	0.267	15.540	14.730	4.930
		8800.000	918.400	0.423	1.303	0.980	0.199	27.000	26.200	4.980

Extra 13 mm Bi-hexagonal/hexagonal Rotor Bolts

Bolt Windage Test Matrix - *18 x 13 mm Hex extra tests*

Target *m*	Target casing pressure	Target N	Measured ω	Measured *m*	Measured Dimensionless values			Measured M	Corrected M	Casing pressure
kg/s	bar (abs)	rev/min	rad/sec	kg/s	Re_ϕ ($x10^7$)	C_ω ($x10^5$)	λ_T	N m	N m	bar (abs)
0.12	3.000	8600.000	900.900	0.123	0.719	0.280	0.092	11.710	11.120	3.070
		10100.000	1057.700	0.120	0.725	0.262	0.085	14.150	13.430	2.920
		11400.000	1196.900	0.120	0.750	0.251	0.079	16.930	16.110	2.950
	4.000	7800.000	816.800	0.120	0.888	0.275	0.076	11.640	11.110	4.130
		8800.000	922.600	0.119	0.932	0.264	0.070	13.910	13.300	4.140
		10100.000	1058.900	0.118	0.972	0.251	0.064	17.030	16.320	4.170
		10100.000	1058.900	0.118	0.957	0.255	0.066	17.030	16.320	4.080
	5.000	8200.000	859.200	0.115	1.050	0.259	0.063	13.680	13.120	4.950
		9500.000	996.200	0.114	1.104	0.247	0.057	17.040	16.370	4.990

Bolt Windage Test Matrix - *18 x 13 mm Bi-Hex extra tests*

Target *m*	Target casing pressure	Target N	Measured ω	Measured *m*	Measured Dimensionless values			Measured M	Corrected M	Casing pressure
kg/s	bar (abs)	rev/min	rad/sec	kg/s	Re_ϕ (x10^7)	C_ω (x10^5)	λ_T	N m	N m	bar (abs)
0.12	3.000	8600.000	900.400	0.119	0.721	0.271	0.088	10.870	10.270	3.050
		10100.000	1058.800	0.121	0.752	0.267	0.084	13.690	12.970	2.970
		11400.000	1195.900	0.121	0.784	0.257	0.078	16.340	15.520	3.010
	4.000	7800.000	817.000	0.117	0.886	0.266	0.074	11.130	10.600	4.100
		8800.000	921.400	0.116	0.940	0.258	0.068	13.260	12.650	4.130
		10100.000	1058.900	0.122	0.972	0.263	0.068	16.400	15.680	4.020
	5.000	8200.000	859.700	0.113	1.078	0.255	0.060	13.480	12.920	5.030
		9500.000	955.600	0.113	1.147	0.244	0.055	16.880	16.220	5.140

Surface Cavities

Bolt Windage Test Matrix - 3 *x Surface Cavities*

Target *m*	Target casing pressure	Target N	Measured ω	Measured *m*	Measured Dimensionless values			Measured M	Corrected M	Casing pressure
kg/s	bar (abs)	rev/min	rad/sec	kg/s	Re_ϕ (x10^7)	C_ω (x10^5)	λ_T	N m	N m	bar (abs)
0.120	2.000	3000.000	316.200	0.214	0.218	0.309	0.263	1.830	0.960	2.040
		3900.000	411.200	0.214	0.277	0.298	0.209	2.270	1.400	2.020
		5900.000	621.500	0.122	0.407	0.298	0.154	3.410	2.600	2.020
	3.000	5900.000	618.000	0.123	0.599	0.297	0.112	4.060	3.250	3.050
		8600.000	903.400	0.123	0.815	0.288	0.085	6.500	5.710	3.060
	4.000	10100.000	1057.800	0.119	1.179	0.271	0.060	9.520	8.610	4.140

Target *m*	Target casing pressure	Target N	Measured ω	Measured *m*	Measured Dimensionless values			Measured M	Corrected M	Casing pressure
kg/s	bar (abs)	rev/min	rad/sec	kg/s	Re_ϕ (x10^7)	C_ω (x10^5)	λ_T	N m	N m	bar (abs)
0.400	3.000	3900.000	409.600	0.409	0.427	1.021	0.507	3.060	2.190	3.060
	5.000	3900.000	410.100	0.412	0.695	1.027	0.345	3.830	2.970	5.040
		5900.000	619.300	0.412	1.035	1.017	0.249	6.570	5.750	5.050
		7250.000	760.500	0.412	1.257	1.010	0.211	8.810	8.030	5.080
		10100.000	1053.500	0.412	1.671	0.986	0.164	14.830	13.920	5.150

Bolt Windage Test Matrix - *9 x Surface Cavities*

Target *m*	Target casing pressure	Target N	Measured ω	Measured *m*	Measured Dimensionless values			Measured M	Corrected M	Casing pressure
kg/s	bar (abs)	rev/min	rad/sec	kg/s	Re_ϕ (x10^7)	C_ω (x10^5)	λ_T	N m	N m	bar (abs)
0.120	2.000	3000.000	314.800	0.123	0.211	0.307	0.268	1.340	0.480	2.000
		3900.000	418.800	0.123	0.278	0.305	0.213	1.810	0.950	2.000
		5900.000	619.400	0.122	0.399	0.299	0.157	2.950	2.130	2.000
	3.000	5900.000	619.400	0.122	0.584	0.296	0.114	3.690	2.880	2.990
		8800.000	920.500	0.121	0.797	0.285	0.086	6.670	5.870	3.000
	4.000	10100.000	1053.900	0.120	1.121	0.276	0.063	9.520	8.610	4.040

Target *m*	Target casing pressure	Target N	Measured ω	Measured *m*	Measured Dimensionless values			Measured M	Corrected M	Casing pressure
kg/s	bar (abs)	rev/min	rad/sec	kg/s	Re_ϕ (x10^7)	C_ω (x10^5)	λ_T	N m	N m	bar (abs)
0.400	3.000	3900.000	409.100	0.412	0.412	1.021	0.521	2.760	1.890	3.050
	5.000	3900.000	408.800	0.413	0.681	1.025	0.350	3.610	2.750	5.070
		5900.000	618.400	0.413	1.014	1.015	0.252	6.700	5.890	5.090
		7250.000	760.100	0.414	1.230	1.012	0.215	9.300	8.520	5.120
		10100.000	1054.000	0.413	1.620	0.986	0.168	15.730	14.830	5.170

Bolt Windage Test Matrix - *18 x Surface Cavities*

Target *m*	Target casing pressure	Target N	Measured ω	Measured *m*	Measured Dimensionless values			Measured M	Corrected M	Casing pressure
kg/s	bar (abs)	rev/min	rad/sec	kg/s	Re_ϕ (x10^7)	C_ω (x10^5)	λ_τ	N m	N m	bar (abs)
0.120	2.000	3000.000	314.800	0.124	0.211	0.308	0.269	1.380	0.520	2.010
		3900.000	408.900	0.124	0.273	0.307	0.218	1.910	1.050	2.010
		5900.000	618.900	0.124	0.401	0.302	0.158	3.250	2.440	2.020
	3.000	5900.000	618.500	0.123	0.586	0.297	0.114	4.030	3.220	3.000
		8800.000	918.200	0.122	0.801	0.284	0.085	7.260	6.460	3.020
	4.000	10100.000	1055.400	0.117	1.114	0.264	0.061	10.470	9.560	4.050

Target *m*	Target casing pressure	Target N	Measured ω	Measured *m*	Measured Dimensionless values			Measured M	Corrected M	Casing pressure
kg/s	bar (abs)	rev/min	rad/sec	kg/s	Re_ϕ (x10^7)	C_ω (x10^5)	λ_τ	N m	N m	bar (abs)
0.400	3.000	3900.000	408.700	0.413	0.420	1.023	0.514	2.910	2.040	3.060
	5.000	3900.000	408.700	0.418	0.672	1.036	0.358	3.830	2.970	4.970
		5900.000	618.400	0.419	1.010	1.024	0.255	7.330	6.520	5.040
		7250.000	760.500	0.418	1.217	1.008	0.216	10.050	9.270	5.060
		10100.000	1054.400	0.417	1.594	0.978	0.169	17.240	16.330	5.130

Appendix D – PIV averaging velocity profiles

Plain Disc C_w = 3000, N = 4000 rev/min

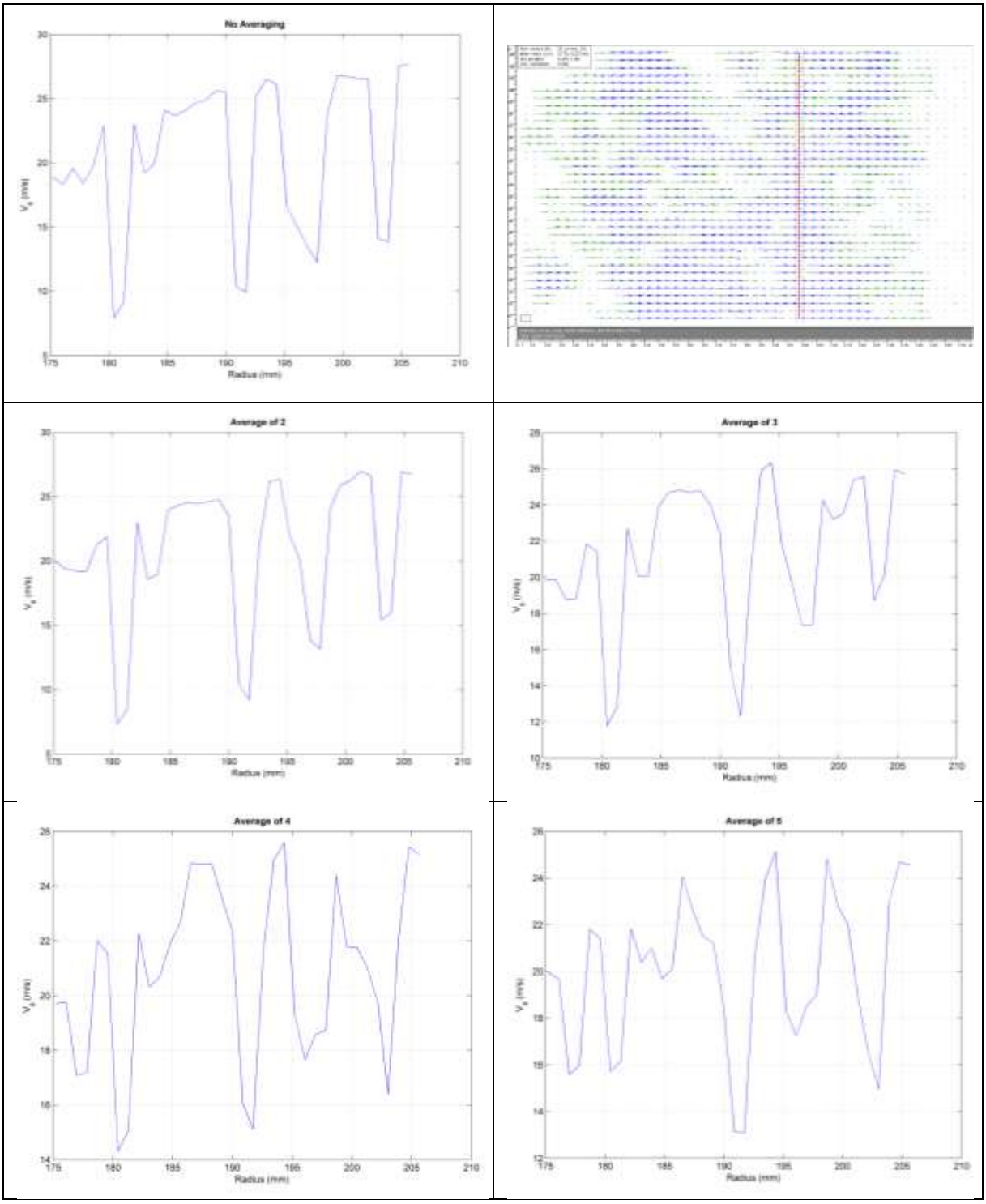

Plain Disc C_w = 22500, N = 4000 rev/min

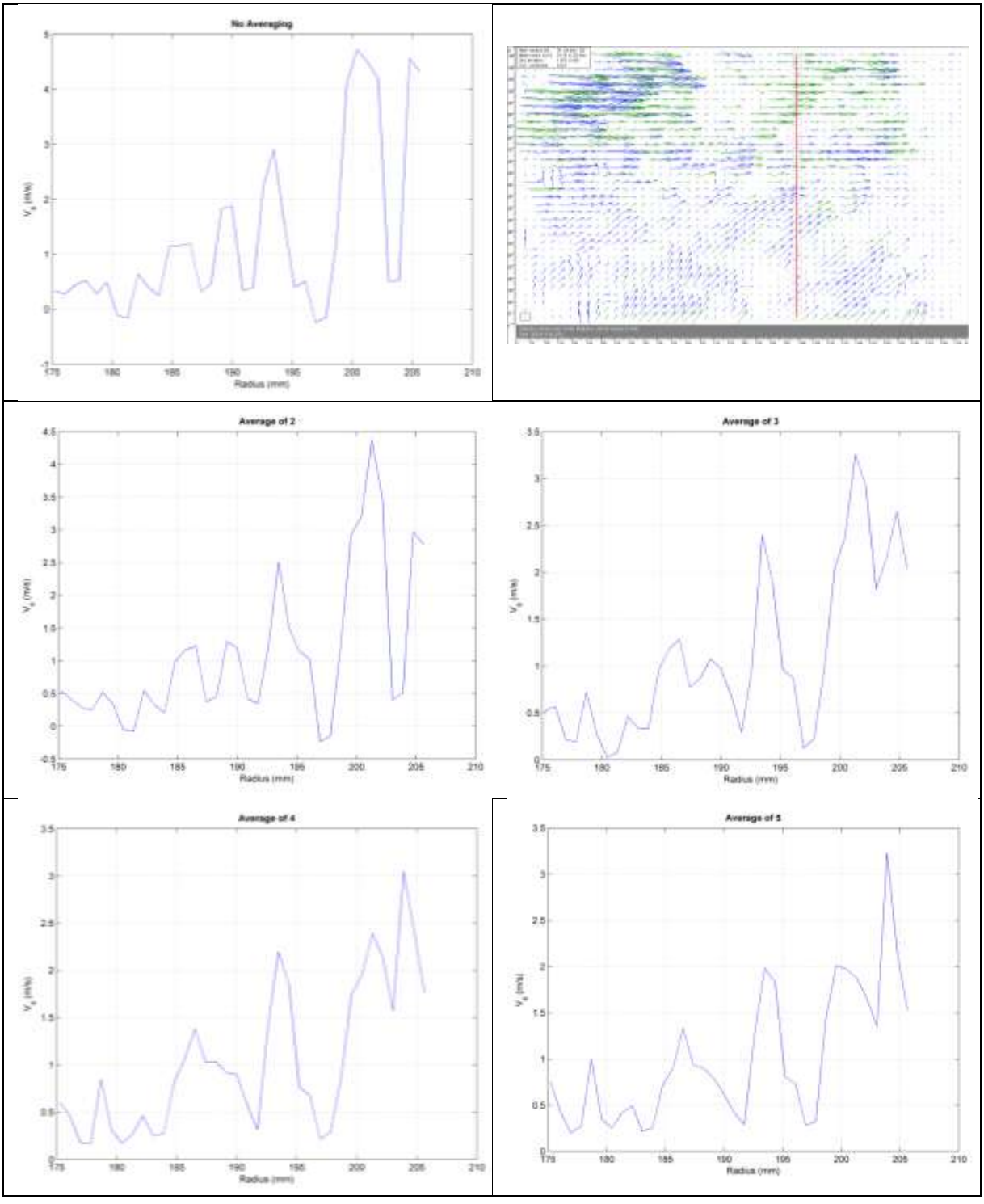

Plain Disc, C_w = 10000, N = 2000 rev/min

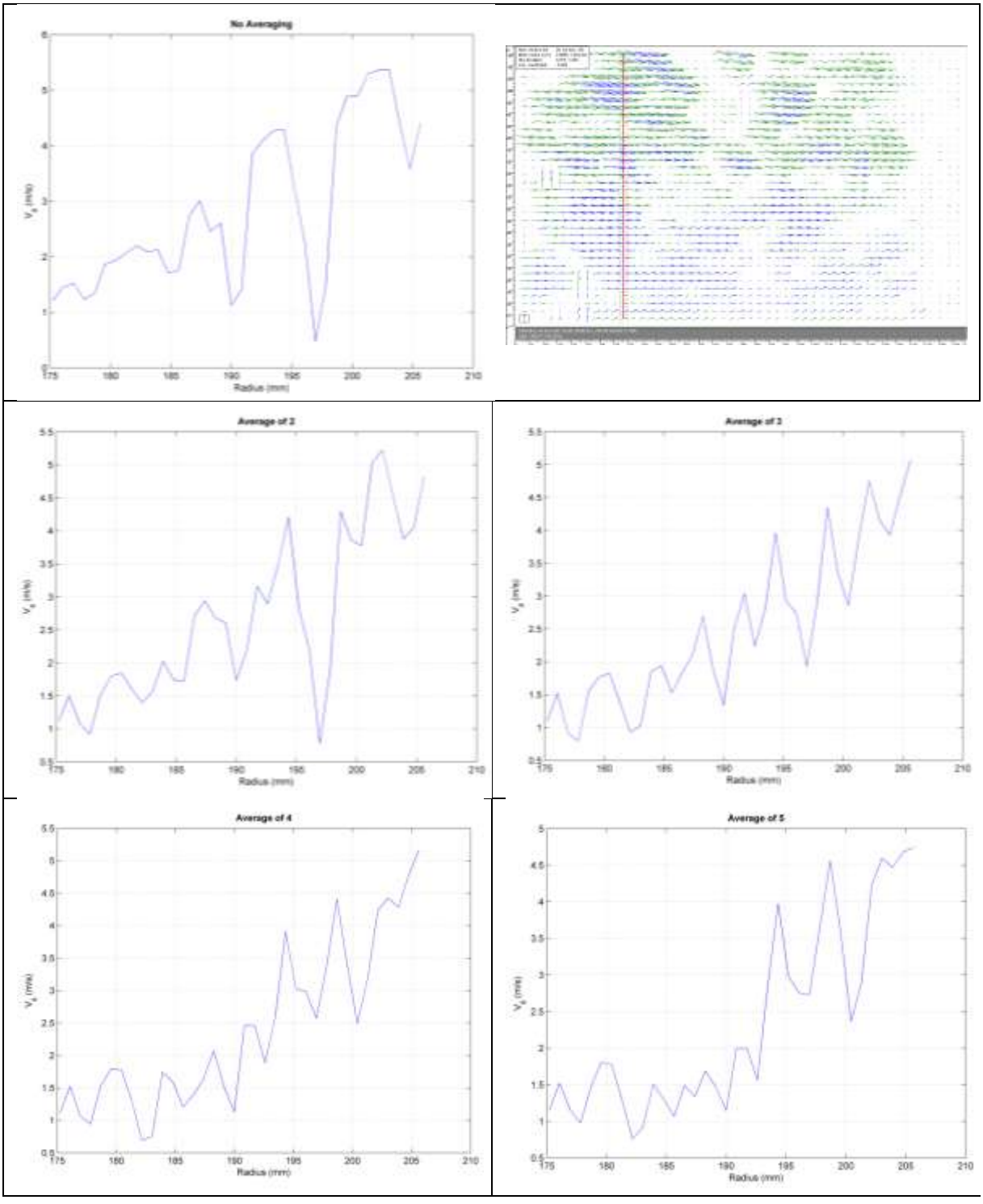

Plain Disc, C_w = 10000, N = 5000 rev/min

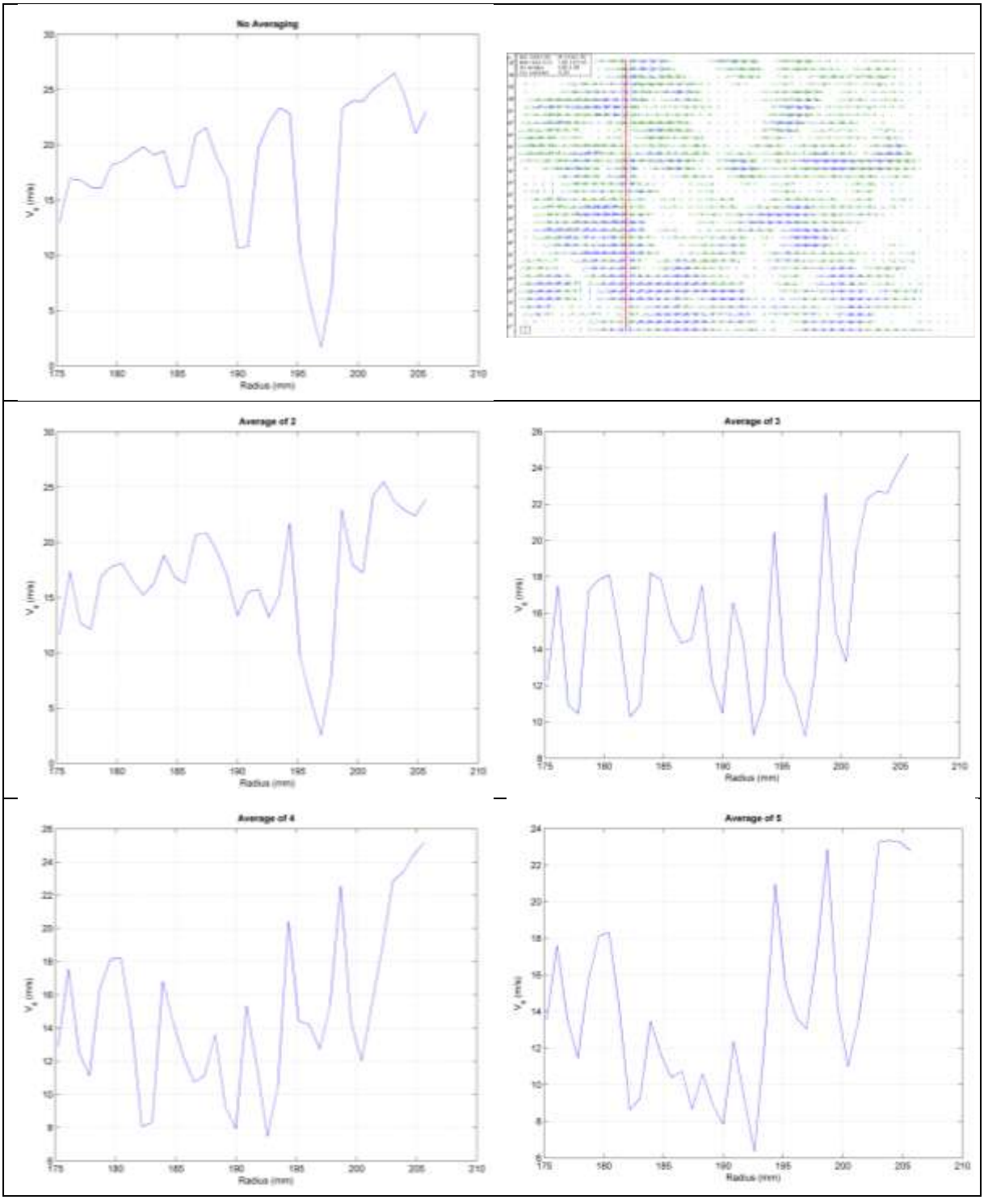

Appendix E – TFMRC Internal Report 08/TFMRC/TR277

University of Sussex

Progress Report on Turbine Disc Bolt Windage Experimental Work

REPORT NO. 08/TFMRC/TR277

A.L. Miles

TFMRC

University of Sussex

Contents

1. Introduction

This report discusses the test results to date for the plain disc tests on the bolt windage rig. Also included is an account of the investigations carried out in order to understand an apparent change in the characteristics of the rig since tests were previously carried out by Coren (2007).

2. Test Rig

Figure 1 shows a general assembly of the test rig. The rig consists of a shaft mounted Titanium alloy turbine disc of radius 0.225 m that is enclosed within a sealed steel casing. Around the outer rim of the disc is a labyrinth seal with a stator mounted shroud encasing the cavities on either side of the disc. The disc is driven by 5 kW motor through a 5:1 step up gearbox. Mounted between the gearbox and the disc is an in line torquemeter with friction grip coupling at either end.

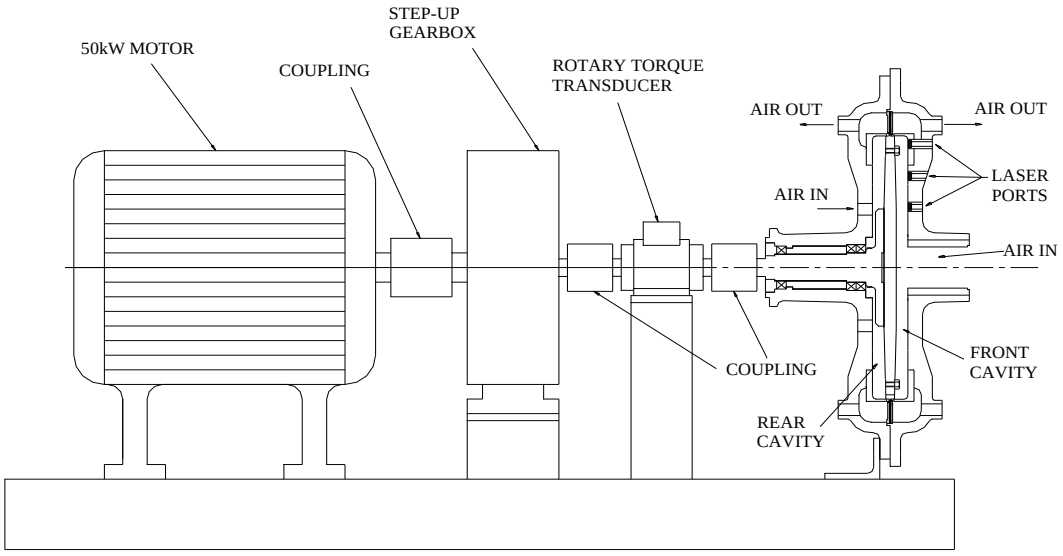

Figure 1 – Test rig assembly

The test side of the disc (the right hand side in Figure 1) has the majority of the pressure and temperature instrumentation whereas the balance side (the left side) has enough instrumentation to enable balancing of the flow conditions on both sides of the disc.

A superimposed axial air flow enters the rig centrally on the test side, flows radially outward through the cavity and exits through the labyrinth seal at the perimeter. On the balance side the air enters through four inlet pipes equally spaced around the central shaft. There are four orifice plates positioned upstream and downstream of the test rig on both the test and balance side in order to calculate the mass flow of air through the rig as well as to ensure both sides of the disc are balanced. The air is supplied at pressures up to 7.5 bar (absolute) and mass flows of 0.82 kg/s by an Atlas Copco screw type compressor. The air is then passed through an Atlas Copco air conditioning unit to provide dry air at a consistent temperature to the rig.

3. Testing

In September 2006 testing began on the bolt windage rig with a set of plain disc tests. Five test points were selected to match a range of conditions from the previous plain disc data obtained by Coren (2007). The two sets of results were then compared in order to ensure that they were matching, within the limits of uncertainty. The reason for doing this was to ensure that any new data obtained with the bolts on the stator can confidently be compared to the plain disc data already available. The five tests were carried out at the conditions shown in Table 1:

Mass Flow (kg/s)	Casing Pressure (bar, abs)	Disc Speed (rpm)
0.12	2	5900
0.24	2	5900
0.4	5	3900
0.4	5	5900
0.4	5	8500

Table 1 – Plain disc test conditions

Once these tests had been carried out it was clear that the new results were not comparable to the previous results. Figure 1 and Figure 2 show the variation of the moment coefficient C_m with the parameters λ_T and Re_φ respectively for the high mass flow (0.4 kg/s), high pressure (5 bar) tests. It can be seen that the measured torque, and therefore the moment coefficient, was consistently higher than it had been previously, by a larger amount than could be considered within the limits of uncertainty.

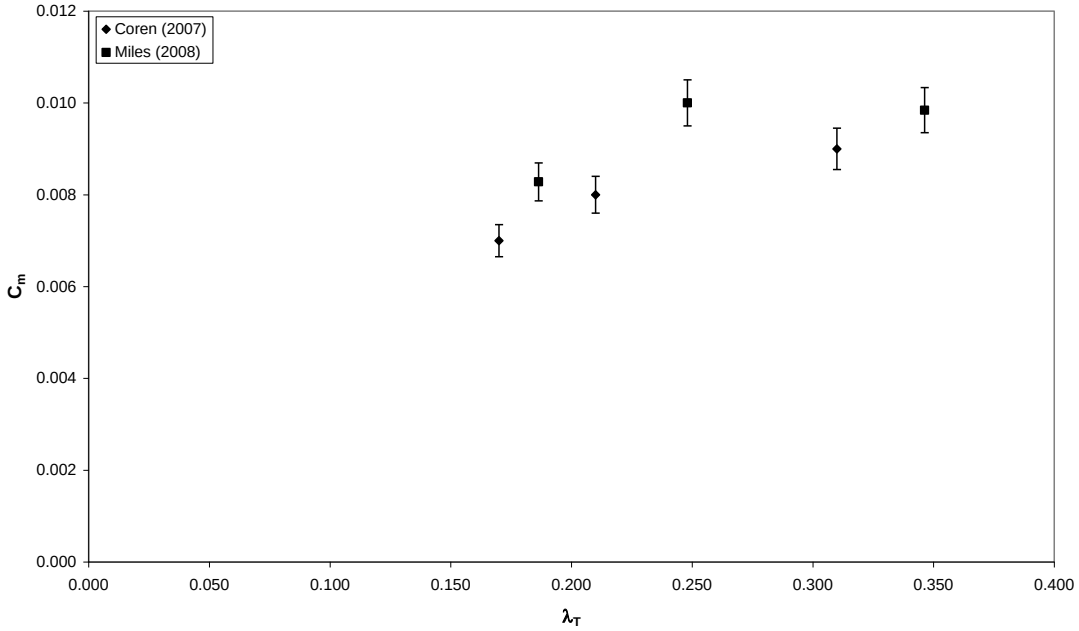

Figure 1 – Variation of C_m with λ_T

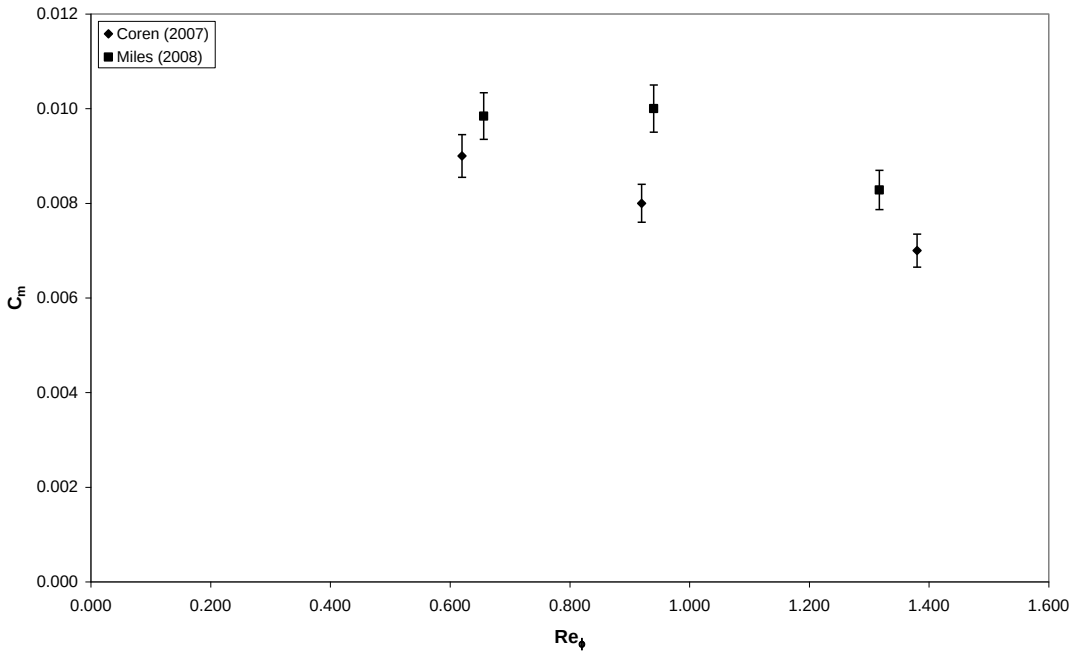

Figure 2 – Variation of C_m with Re_φ

Table 2 shows both sets of measured torque values from the conditions shown in Figures 1 and 2, as well as the torque calculated from the enthalpy rise within the casing.

Disc Speed (rpm)	Old corrected torque meter readings (Nm)	New corrected torque meter readings (Nm)	% increase	Old enthalpy torque (Nm)	New Enthalpy torque (Nm)	% increase
3900	2.46	2.72	10.6	2.80	3.43	22.5
5900	4.83	6.13	26.9	5.09	5.65	11.0
8500	9.80	11.10	13.3	9.89	11.00	11.2

Table 2 – Torques recorded and calculated from both old and new sets of data

After these initial tests were carried out it was necessary to dismantle the rig in order to drill holes in the stationary casing on the balance side if the rig, to match those already on the test side, ready for the upcoming stator tests. During this period the torquemeter was sent to Young Calibration for calibration to ensure the validity of the torque readings obtained from the recent plain disc tests. The shaft bearings were replaced at this point also. Before the rig was reassembled, various checks were made to ensure there was no excess friction throughout the driveshaft. The labyrinth seals were checked for circularity and sign of excessive rubbing and the carbon seals checked for circularity and concentricity with the bearing housings. A small amount of rubbing was detected from the carbon seal around the shaft near the rear bearing, at the point indicated below in Figure 3. This seal was cleaned up so that any future rubbing of the seal could be detected.

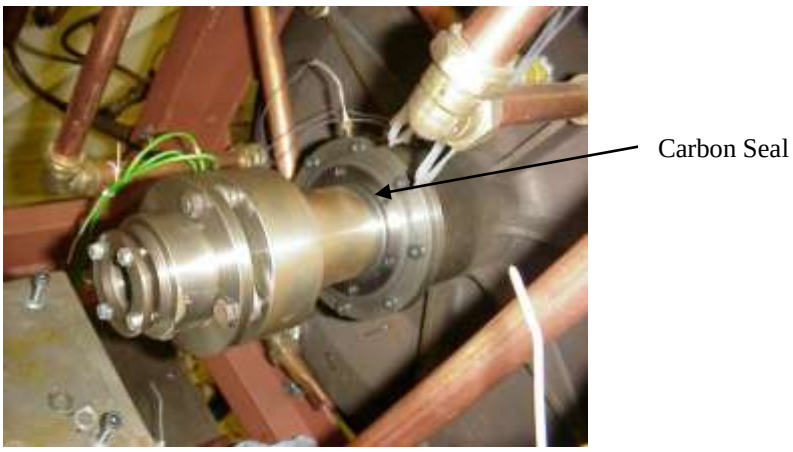

Figure 3 – Picture showing position of carbon seal

Once the rig was re-commissioned in March 2007, another set of plain disc test were carried out to check if the problem with higher torques still existed or if the steps taken to rectify the problem had been successful. Due to the fact that, previously, the difference in the results was much larger in the high mass flow, high pressure tests;

these conditions were repeated for this set of tests. This means that the rig was set up with a mass flow of 0.4 kg/s, pressure of 5 bar absolute and results were recorded at speeds of 3900, 5900 and 8500 rpm. Figures 4 and 5 show the results from these tests.

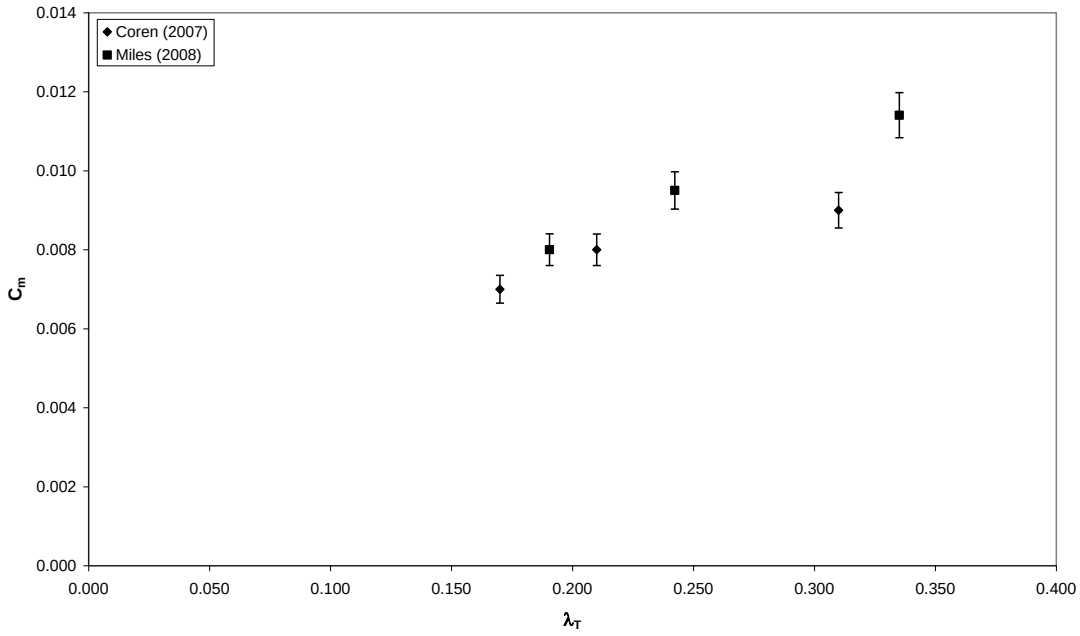

Figure 4 – Variation of C_m with λ_T

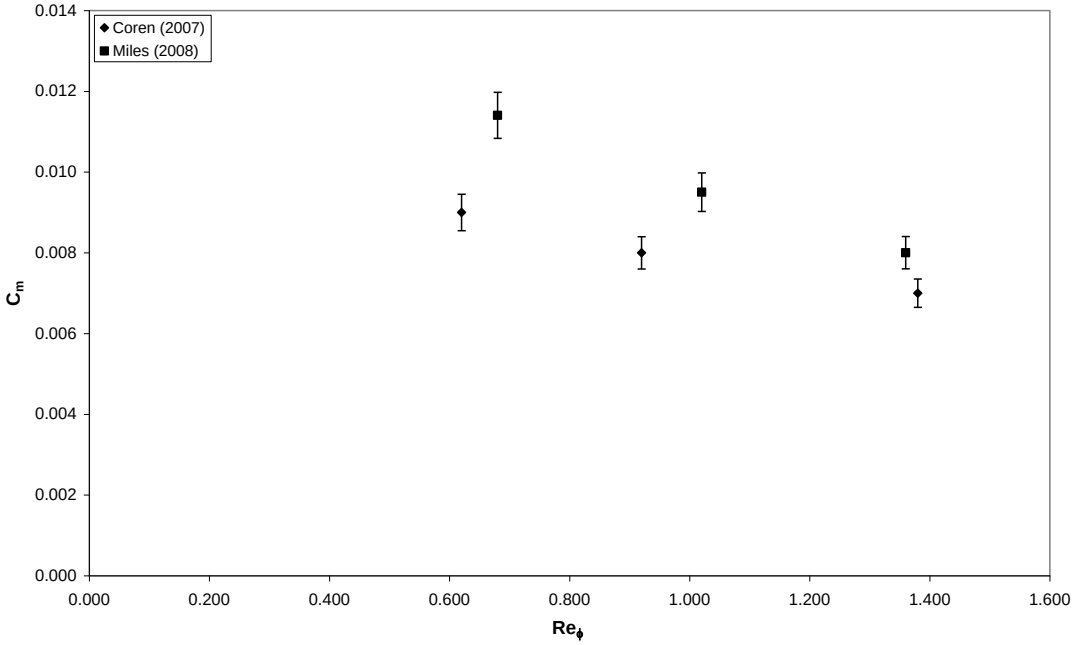

Figure 5 - Variation of C_m with Re_φ

Table 3 shows the increase in torque for the conditions shown in Figures 4 and 5, both recorded from the torquemeter as well as calculated from the enthalpy rise in the fluid.

Disc Speed (rpm)	Old corrected torque meter readings (Nm)	New corrected torque meter readings (Nm)	% increase	Old enthalpy torque (Nm)	New Enthalpy torque (Nm)	% increase
3900	2.46	3.26	32.5	2.80	3.55	26.8
5900	4.83	6.20	28.4	5.09	5.59	9.8
8800	9.80	10.83	10.5	9.89	10.55	6.7

Table 3 – Torques recorded and calculated from both old and new sets of data

This table shows that the torque has actually increased more since the tests in September 2006, and that this is more prominent at the lower speeds. Unfortunately during these tests it was found that there was some leakage from the casing so the results are not fully reliable. However, the leak was around the periphery of the casing, meaning that the correct mass flow of air was passing over the disc and so should not effect the windage over the disc. But even accounting for a small error in the windage torque measurements the results were still significantly higher than they had been previously.

Due to some high bearing temperatures noted during the last set of tests, the test rig was run a few times in order to ensure that the new bearings were bedding in appropriately. A low windage disc was fitted to the test rig, which was left un-pressurised with the front casing removed. It was then run at 6250 rpm on four separate occasions for 1 hour at a time. The results from these runs showed that the bearing temperatures recorded seemed to be a little high, settling at temperatures around 40 °C rather than just under 30 °C, as had been the case before they were replaced. However, they were nevertheless maintaining consistent values throughout the tests confirming that the bearings were fine.

It seemed appropriate at this point to carry out some tests on the driveline to check for a change in characteristics here. In order to test the driveline losses, the test rig was again un-pressurised with the front casing left open. It was run at 6 speeds leaving it for 10 minutes at each of these speeds in order to gain a representative average torque value. This test was repeated four times and the results showed a consistently higher torque

value throughout the range of speeds. Figure 6 shows the driveline loss results obtained by Coren (2007).

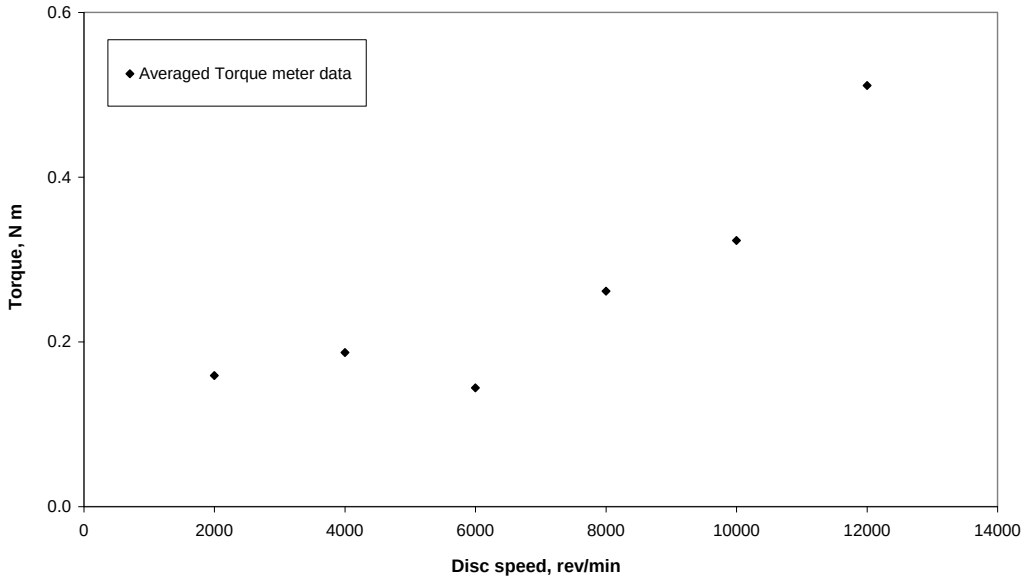

Figure 6 – Variation of driveline loss torque with speed.

It can be seen that the average driveline torque across the range of speeds from 2000 rev/min to 10000 rev/min is about 0.22 Nm. Figure 7 shows the driveline loss torque for the new tests. The average now for the speed range 2000 rev/min to 10000 rev/min is 0.83 Nm. The uncertainty of the torquemeter itself is ± 0.3 Nm which is a large proportion of these values. However even though the measured torques are very low, there is a definite indication that there is some excess friction in the driveline that had not been there previously.

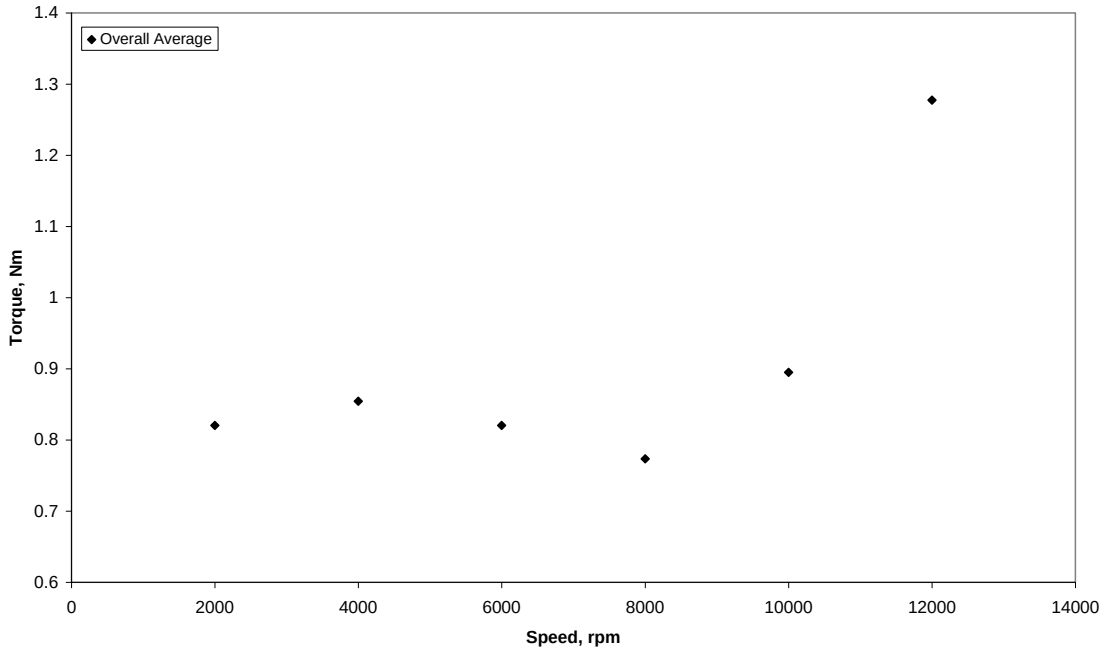

Figure 7 – Variation of driveline loss torque with speed

Throughout April the test rig was run, on four separate occasions, at a mass flow of 0.4 kg/s and 5 bar absolute pressure, at speeds of 3900, 5900 and 8500 rev/min in order to test the repeatability of the results. Figures 8 and 9 show the variation of C_m with both λ_T and Re_φ for the results from Coren (2007) and the four recent, identical tests. It is clear that although the new torque results are higher than those acquired by Coren (2007), there is a high level of repeatability from the four tests.

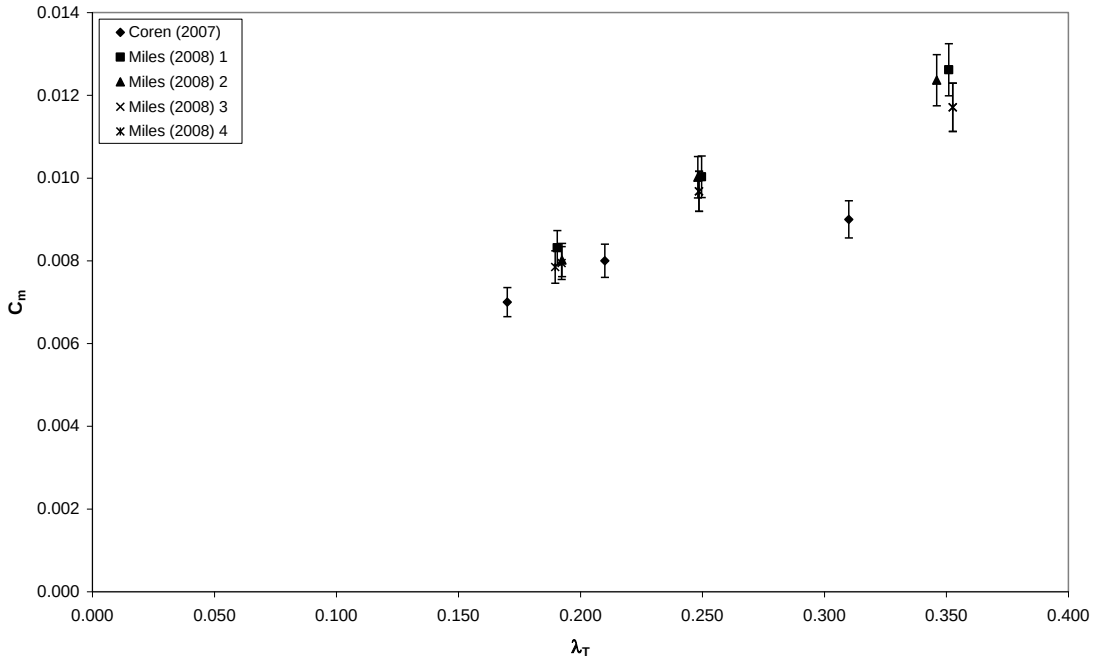

Figure 8 - Variation of C_m with λ_T

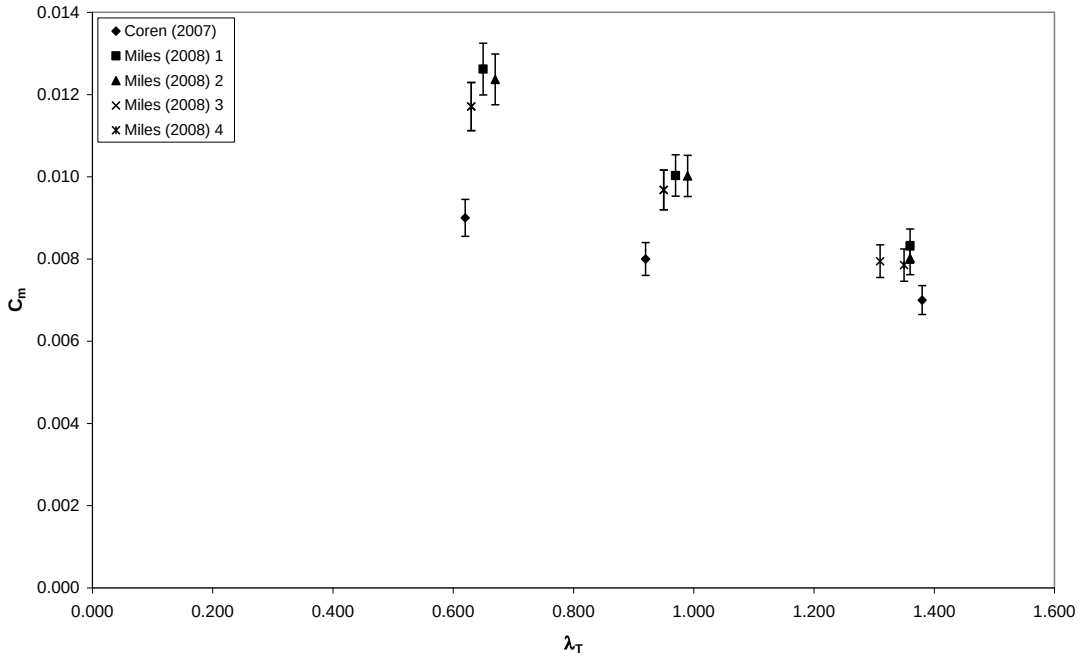

Figure 9 - Variation of C_m with Re_φ

At this point it was starting to look as though there was no physical reason for the higher torques being measured. So one final check was made in order to make quite sure there was nothing wrong with the test rig. It was taken apart once again and the

shaft was measured for concentricity using a dial test indicator and the carbon seals were also re-checked to see if there had been any more rubbing since they were cleaned. After this, one last set of plain disc test were carried out, again at a high mass flow, 5 bar absolute casing pressure and 3900, 5900 and 8500 rev/min. The mass flow this time, however, was adjusted to match the actual mass flows of the original tests and not the target mass flow of 0.4 kg./s, therefore this last set of tests were carried out with a mass flow of 0.35 kg/s. One of the tests was discarded due to an anomalous result at a speed of 5900 rev/min. Figures 10 and 11 show these results from these tests.

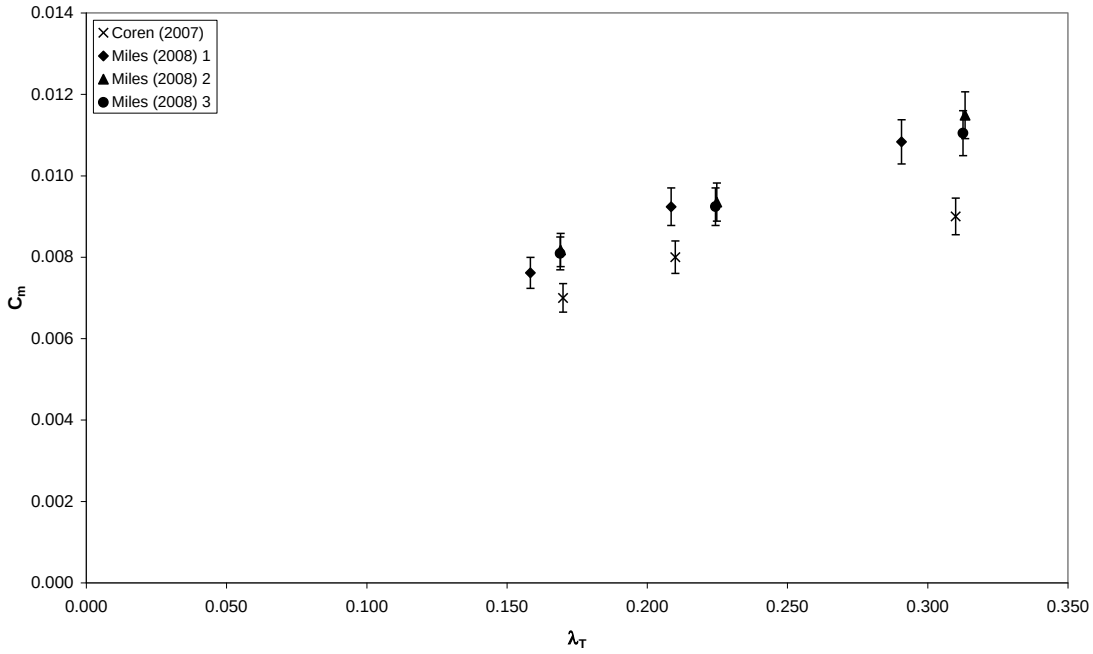

Figure 10 - Variation of C_m with λ_T

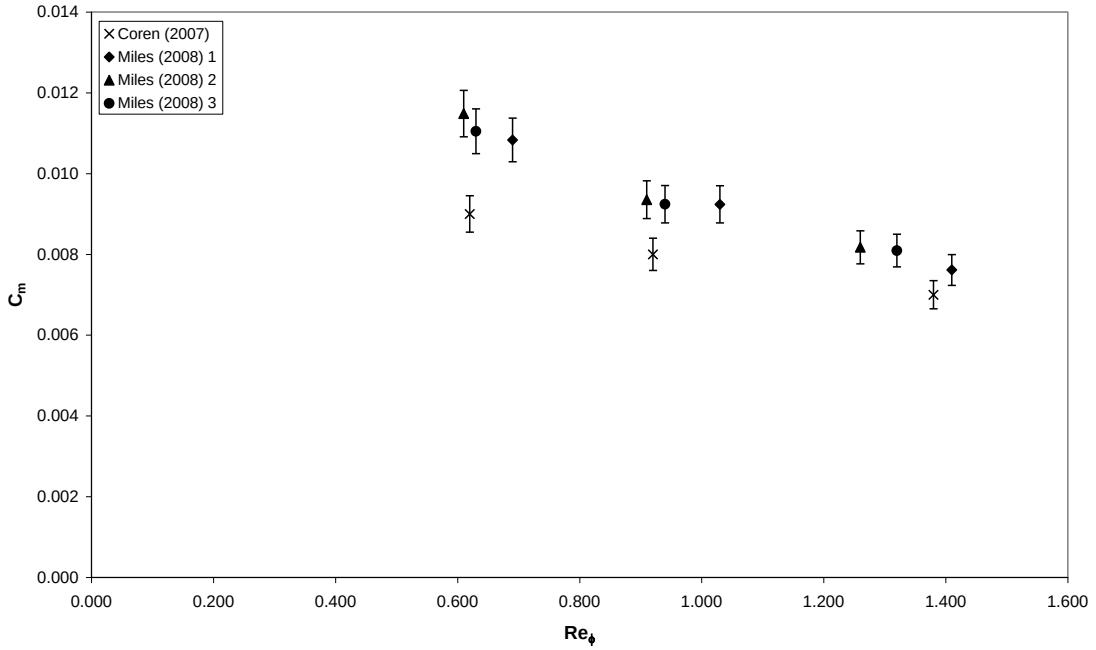

Figure 11 – Variation of C_m with Re_φ

Figures 10 and 11 show that, again, the moment coefficients are significantly higher than the original results but also very consistent with each other making the tests highly repeatable. Table 4 shows the actual torque increase in both the measured and calculated torque values.

Disc Speed (rpm)	Old corrected torque meter readings (Nm)	New corrected torque meter readings (Nm)	% increase	Old enthalpy torque (Nm)	New Enthalpy torque (Nm)	% increase
3900	2.46	2.93	19.1	2.80	2.9	3.57
5900	4.83	5.56	15.1	5.09	5.28	3.73
8500	9.80	10.27	4.8	9.89	10.17	2.8

Table 4 - Torques recorded and calculated from both old and new sets of data

You can see here that the measures torque has decreased a little compared to the higher mass flow tests but still the percentage increase on the old results is, on average, more than 10 %. The enthalpy calculations, on the other hand, seem to have dropped quite significantly. However, the enthalpy calculations are not very accurate as the test rig is not insulated and so is not isenthalpic, therefore these calculations can only be used as an estimate. The torquemeter reading are accurate to ± 0.3 Nm and so are more reliable.

4. Conclusion

Thorough inspections and tests have been carried out in order to investigate the cause of this increased torque, but nothing could be found. Therefore it was decided that the new results were reliable enough to be used even if they did not agree with the original set carried out by Coren (2007). As a result a whole new set of plain disc tests will be carried out in order to cover a complete range of engine representative test conditions with which to compare all future data to.

References

Coren, D., 2007,
Windage due to Protrusions in Rotor-Stator Systems
Thermo-Fluid Mechanics Research Centre, University of Sussex, D.Phil. thesis